Developing Additive Manufacturing Methodology Towards the *In Situ* Repair of Articular Cartilage Defects

By

Ailsa Mummery

A thesis submitted to
the University of Birmingham
for the degree of
DOCTOR OF PHILOSOPHY

Biomedical Engineering Research Group
School of Engineering
College of Engineering and Physical Sciences
University of Birmingham
February 2024

Abstract

In situ additive manufacturing as a next step in the development of technologies towards repair of articular cartilage defects to treat a younger, more active population, and to delay full knee replacement.

The main steps in the in situ AM workflow are explored in depth to investigate best-practice and technologies available for development. This thesis covers 3D optical scanning, alignment of conformal prints, toolpath development for in situ additive manufacture of surface additions and filling of surface defects, and in situ additive manufacture of PLA constructs onto 'known' and 'unknown' surfaces.

Investigation of the 3D scanning parameters presents lighter coloured objects as more accurately captured (compared to darker objects) by the EinScan-SP 3D scanner. The optimum print parameters for dimensional accuracy for additive manufacture of thermally bonded polylactic acid were 40 mm/s print speed and 200 °C. For scan dimensional accuracy, a print speed between 30 and 60 mm/s, and print temperature of 200 °C produced maximum dimension deviations of 0.2 mm.

A series of surfaces successfully underwent in situ conformal additive manufacture on the top surface, or the base of a surface defect. First, basic cuboids previously 3D printed, with varying complexity of top surface geometry. Next, clay approximations of the radius of curvature of human knee articular surfaces. Finally, an "unknown" surface (Sawbone bone model).

In conclusion, this thesis provides in depth proof-of-concept for the development of a technique for additive manufacturing in situ for conformal additive manufacturing onto 'unknown' surfaces.

Dedication

I dedicate this thesis to the Birmingham extended Queer and Disabled STEM community, which has supported me throughout this journey. In particular to those who were not able to finish their own journeys.

Acknowledgements

My deepest appreciation to my supervisors, Prof. Duncan Shepherd and Dr Lauren Thomas-Seale, as well as my collaborator Barnaby Hawthorn.
Additionally, this endeavour would not have been possible without the support of the UKRI Engineering and Physical Sciences Research Council (EPSRC) through funding to complete this research.

Contents

List of Figures

List of Tables

Acronyms

3MF	3D Manufacturing Format
AC	Articular Cartilage
ACI	Autologous Chondrocyte Implantation
ADSCs	Adipose Derived Stem Cells
AM	Additive Manufacturing
AMF	Additive Manufacturing File Format
CAD	Computer-Aided Design
CT (scan)	Computed Tomography (scan)
DICOM	Digital Imaging Communications in Medicine
DOF	Degrees of freedom
ECM	Extra-Cellular Matrix
FDM	Fused Deposition Modeling *(see MEX-TRB)*
FFF	Fused Filament Fabrication *(see MEX-TRB)*
GelMa	Gelatin methacrylate
GelMa/HAMa	Gelatin-methacrylamide/hyaluronic acid-methacrylate
HDR	High Dynamic Range
HU	Hounsfield unit
ICRS	International Cartilage Repair Society
IPFP	Infra-patellar fat pad
LAP	Lithium-acylphosphinate
M-ACI	Matrix-Assisted Autologous Chondrocyte Implantation
MEX-TRB	Material extrusion additive manufacture with thermal reaction bonding
MRI	Magnetic Resonance Imaging
MSC	Mesenchymal stem cells
OA	Osteoarthritis
OAT	Osteochondral Auto-Graft
OR	Operating Room
PDMS	Polydimethylsiloxane
PI	Photoinitiator
PLA	Poly(lactic) acid
ROC	Radius of curvature
SSFG	Specifically shaped fiducial guide
STL	Standard Triangle / Tessellation Language, Stereolithography
TCP	Tool centre point
Tukey's HSD	Tukey's Honestly Significant Difference
UV	Ultraviolet
VS	Viscosupplementation

Chapter 1

Introduction

In-situ additive manufacturing (AM) technology could be the next step in patient specific implants. The development of surgical techniques incorporating in-situ additive manufacturing could achieve better host-graft match, shorten patient-clinic interaction, and reduce the need for further surgeries and treatments. In situ AM describes the process of 3D printing, by depositing a material in a layer-by-layer fashion, but building onto an already existing non-planar surface instead of the flat bed of the printer. This could be used to fill a recess, build a surface feature, or extend the surface geometry.

Tissue engineering techniques using additive manufacturing have been shown to offer enhanced precision and control [1] and increase the potential for regenerating biological tissues such as bone and cartilage [2, 3]. Scaffolds for chondral repair have been manufactured using 3D printing, pre-made in the laboratory and subsequently implanted during surgery [4, 5, 6, 7]. Despite modelling these implants on pre-operative medical scans, the process of surgery to access the chondral surface alters the patients anatomy [8]. Any mechanical mismatch between the implanted scaffolds and surrounding tissues can inhibit cartilage regeneration at defect sites leading to implant failure [9].

As we have progressed through The Fourth Industrial Revolution, additive manufacturing technologies have grown exponentially. As individual techniques and equipment developed separately, different names have been coined and have evolved in the way they are used. As of the 2021 BS EN ISO/ASTM 52900 guidelines (Additive Manufacturing - General Principles - Fundamentals and vocabulary) Additive Manufacturing is defined as *"the process of joining materials to make parts from 3D model data, usually, layer by layer, as opposed to subtractive and formative manufacturing technologies."* [10]. The guidelines further standardise the terminology for describing specific types of additive manufacturing. Historical terms include, but are not limited to: additive fabrication, additive processes, additive techniques, additive layer manufacturing, layer manufacturing, solid freeform fabrication, fused filament fabrication, fused deposition manufacturing, and freeform fabrication. For this thesis, unless quoting from previous works, the 2021 standards of terminology are used. The main type of additive manufacturing discussed in this work is MEX-TRB/P/PLA, which describes additive manufacturing with material extrusion deposition of PLA (polylactic acid) plastic, with thermal bonding between the layers.

The main part of the research explored in this thesis is based upon developing a reliable workflow for in situ conformal additive manufacturing towards repair of articular cartilage

(AC) defects (Figure 1.1). Replication of the specific bone contour geometry and the layered structure of articular cartilage tissue provide two specific challenges to be met appropriately via additive manufacture. Furthermore, the application of in situ additive manufacturing could be a solution to graft-host mismatch, which is a significant factor in the long-term success or failure of a surgical articular cartilage injury treatment [9]. This informs objective 4 towards specialisation of the in situ techniques towards articular cartilage defect repair. The application of this workflow would involve scanning the damaged section of articular cartilage in the knee, and additive manufacturing in situ into that defect to fill and repair it, as the next step up from manufacturing a scaffold outside the body and implanting it in. The specific processes for this are not standardised nor able to be reliably replicated. Current research into this application has "black boxes" at the extraction and toolpath stages where the scan data is input and a functional toolpath is output. While presenting results which demonstrate the feasibility of in situ AM for cartilage implants, current research does not present or explore the toolpath development for printing in situ (Li et al (2017) [11], Ma et al (2020) [12]). Thus, the objectives of this project, specifically objectives 2 and 3 enable the toolpath development to be explored, and a methodology of toolpath design to be formulated to fill this knowledge gap. Project objectives 1 and 5 enable the subsequent objectives to be undertaken, and evaluation of the workflow produced, respectively.

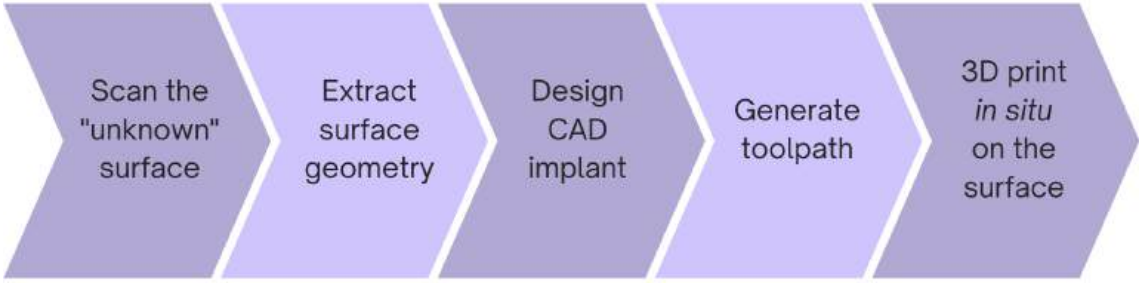

Figure 1.1: Standardised Primary Workflow for In Situ Conformal Additive Manufacturing.

The overall project aim is to develop a technique for additive manufacturing *in-situ* based on the developments of biomedical applications of AM in the human body. The overall aim is achieved with the following objectives:

1. Evaluate methods for imaging the geometry that will be printed upon.
2. Formulate a method for extracting the surface geometry from the scan data.
   (a) Extract the surface to be manufactured onto.
   (b) Extract the geometry which is to be replicated.
3. Develop methods for additive manufacturing onto a non-flat surface.
   (a) Generate the toolpath for in situ AM.
   (b) Additive manufacture in situ onto additive manufactured basic geometric shapes.
   (c) Additive manufacture in situ onto non-AM, in-house manufactured bases.
   (d) Additive manufacture in situ onto unknown surfaces with bone surface geometry.
4. Formulate techniques to use in situ additive manufacturing for specific surgical procedure(s)

(a) Repair of articular cartilage defects in the knee.

5. Evaluate the proposed workflow.

The structure of this thesis begins with a systemic review of the current literature surrounding additive manufacturing technologies and biomedical applications, before walking the reader through the workflow for in situ conformal AM. Finally, discussion and conclusions to be taken from this research are presented, alongside the new work that could be built upon these foundations.

Chapter 2

Background

2.1 Introduction

In situ in vivo additive manufacturing for repair of articular cartilage defects involves combining knowledge and techniques from a wide range of engineering and science disciplines. The literature review was therefore of great breadth, and includes:

- Current writing on the structure and function of human articular cartilage in the knee
- Injuries to the cartilage which cause articular cartilage defects
- Traditional treatments of articular cartilage defects and their efficacy
- Current Additive Manufacturing technologies
- Current biomedical applications for additive manufacturing
- Current research for *in situ* conformal additive manufacturing
- Specific applications for additive manufacturing for repair of articular cartilage defects

The aim of this chapter is to inform the reader on the current state of the art of in situ additive manufacturing, and support the decisions stated in this thesis with literature. This background chapter forms the basis from which the methodology given in this thesis is built upon. The objectives to achieve this aim are:

1. Understand the additive manufacturing technologies available that meet the requirements of this research project.
2. Collate the current research knowledge base on the structure and function of the articular cartilage which is to be replicated.
3. Summarise current treatments for articular cartilage defects, and their limitations.
4. Highlight where in situ additive manufacturing can fill the gaps left by these limitations.
5. Evaluate current state of the art in situ additive manufacturing technologies, and highlight where the research compiled in this thesis can develop the current technologies.

2.2 Articular Cartilage Structure and Properties

Articular cartilage (also known as hyaline cartilage) is a highly specialised connective tissue with a complex structure that enables its specific properties [8]. Articular cartilage provides a smooth, low friction articulating surface for joint movement, and displays good resistance to compressive and shear loading. Distinct features of articular cartilage include its 3D collagen fibre arrangement [8], and layered internal structure [13]. Cartilage is made up of chondrocytes and the extracellular matrix (ECM), which contains the collagen and proteoglycans [14]. Cartilage has no neural or vascular tissue, and therefore research suggests that the tissue relies on diffusion for nutrition and homeostasis [8, 13, 14, 15]. 80% of cartilage wet weight is water [16, 17]. The layered structure of articular cartilage is presented in Figure 2.1. The main cartilage layers, from the articulating surface down, are the Tangential Zone, Transitional zone, and Radial Zone [13].

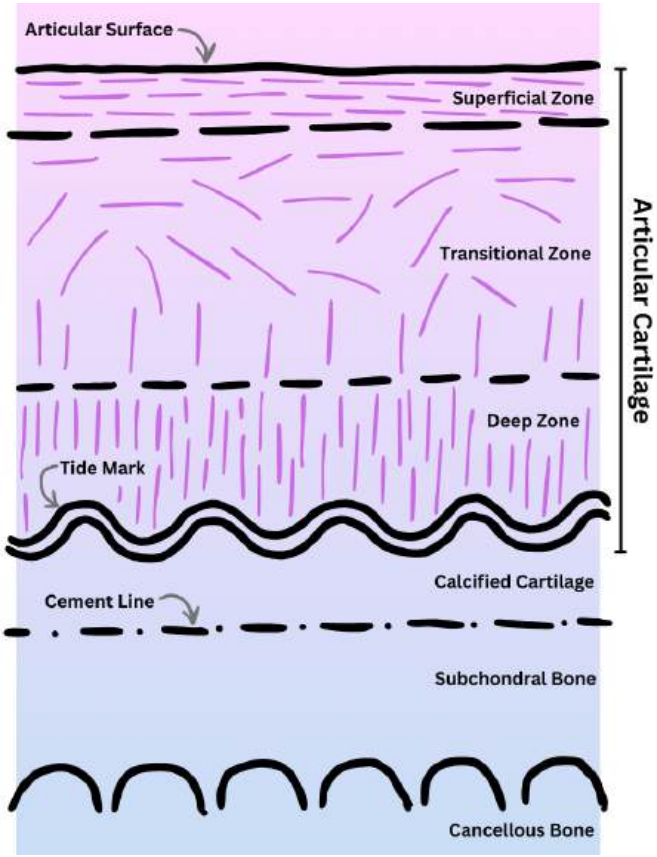

Figure 2.1: Cartilage layer structure. Image created with reference to images from Moore, D.W. (2023) [18]

The superficial layer, or Tangential Zone, accounting for approximately 10 % of the cartilage thickness, resists most of the applied shear stress. This is due to the collagen fibres being oriented parallel to the joint articular surface. Beneath this zone is the Transitional Zone, approximately 50 % of the thickness of the cartilage. This layer has a transitional structure between the superficial layer above and the radial zone below. The Radial Zone, often referred to as the Deep or Basal Zone, functions to resist the high compressive loads applied to the knee joint. The collagen fibres in this zone are oriented perpendicular to the joint

articular surface. This zone is approximately 30 % of the cartilage thickness.

The structure of articular cartilage enables durable stiffness to compression, and the ability to sustain the loads applied to the joint and distribute them evenly, minimising peak stresses transmitted to the underlying subchondral bone [8, 15]. The mechanical properties of articular cartilage are in between muscle and bone though closer in rigidity to bone [14]. Articular cartilage is said to be viscoelastic, and research places the Young's modulus of human femoral condyle articular cartilage around 1.00 MPa (1.03 ± 0.48 [19], 0.70 (indentation) [20], 0.85 ± 0.35 (unrestricted compression) [21]). Antons et al. (2018) describe the Elastic modulus increasing through the height of the cartilage, from 0.02 ± 0.003 to 6.44 ± 1.02 MPa (from superficial zone to calcified layer) [22]. Furthermore, Kabir et al. (2020) state the compressive modulus of 10.60 ± 3.62 MPa, and Poisson's Ratio of 0.4 ± 0.1 [19]. Although articular cartilage is just 2 to 3mm thick [15, 23, 24], being aneural and avascular limits its ability to repair itself [8, 13, 14, 15].

Articular cartilage transitions to bone via the calcified cartilage layer, attaching to the subchondral plate via the cement line. Near the bone-cartilage interface, there is a transitional region from chondrocytes (the main cell type in articular cartilage) to osteoblasts (a cell type found in bone tissue) [14]. The subchondral plate is the barrier between the articular cartilage and the cancellous bone (tissue) which houses the marrow cells within the bone (organ). The subchondral bone plate itself is the bony lamellar (cortical endplate) immediately under the calcified cartilage layer, and displays notably variable anatomy between individuals [25, 26]. The subchondral bone plays a role in how articular cartilage behaves during loading. Cartilage and bone work together - cartilage bearing the mechanical loads, and bone as structure and shock absorber [27]. The subchondral bone absorbs significantly more shock under impact compression where fracture occurs, sparing the overlying cartilage from immediate injury [28]. However, this risks long-term degeneration of the underlying bone [28], and the function of the articular cartilage relies on the mechanical properties of the underlying bone [29]. The articular cartilage on the distal femur is the articular cartilage of interest for the repair considered as the basis for the research contained in this thesis. Figure 2.2 presents the gross anatomy of the distal femur. The distal end of the femur (thigh bone) presents in two curved condyles - the medial and lateral [30].

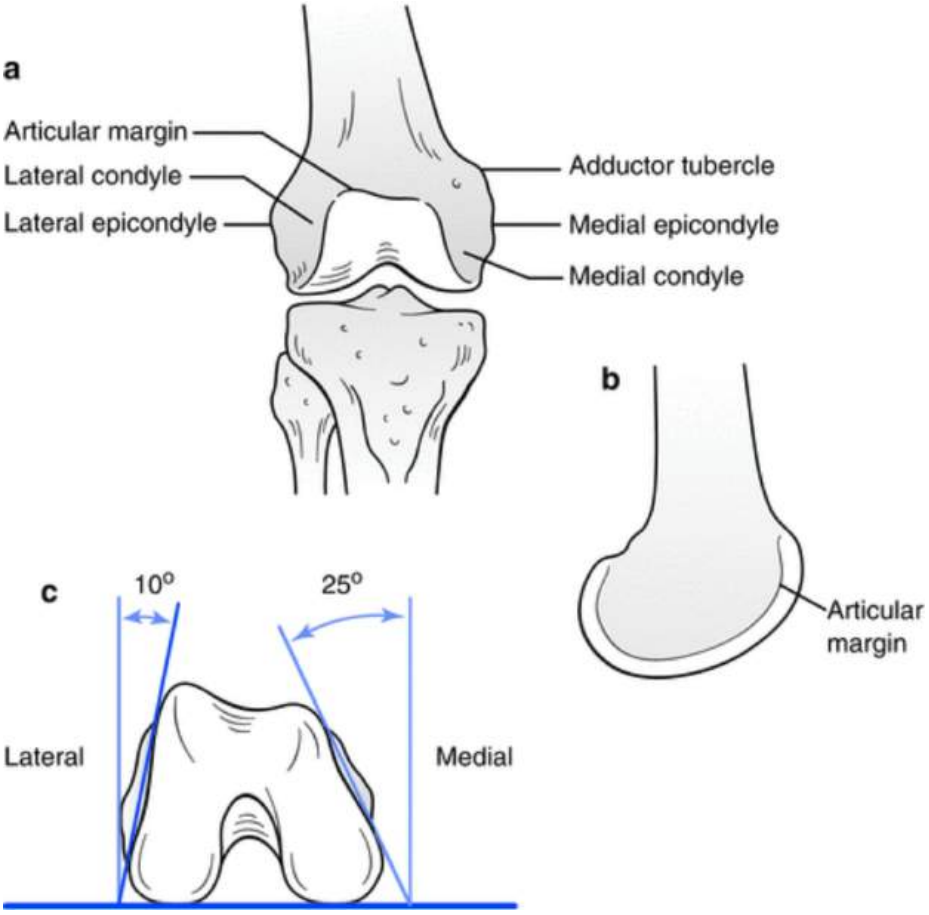

Figure 2.2: Anatomy of the distal femur. Image reused with permission from Springer Nature and Aneja & Graves (2015) [31].

2.3 Articular Cartilage Injuries

Cartilage injuries are a source of significant morbidity and pain [13] and can lead to loss of function of the joint, and develop into osteoarthritis (OA) [8, 32] which is a leading cause of disability in developed countries [33]. Chondral defects result in higher contact stresses in the healthy adjacent cartilage, which can lead to degenerative knee arthritis [13]. As the average age of the population continues to rise [34], knee injury patients are increasingly younger and living longer with more active lives [35]. Individuals with isolated chondral surface damage are therefore often younger, more active, and less willing to accept limitations in activities [13]. Therefore it is necessary to explore new treatments and procedures with the aim to restore normal / near normal hyaline like cartilage, and enable long lasting normal function of healthy articular surfaces in knee joints.

The mechanisms of mechanical injury to articular cartilage are discussed by Buckwalter in Mechanical Injuries of Articular Cartilage. Excessive joint loading and / or blunt trauma can result in the joint being subject to intense compressive and shear forces, causing mechanical injury to the cartilage. Substantial force is required to disrupt normal articular cartilage with a single impact. Loads exceeding 25 MPa are required to cause chondrocyte death and matrix fissures in human articular cartilage [15]. In a "closed" articular surface injury, the cartilage

matrix and cells are damaged, altering the mechanical properties without visible tissue disruption. These types of injury do not penetrate or expose the interior of the joint, and are very difficult to diagnose [15] (Figure. 2.3, ICRS grade 1A). If trauma to the joint ruptures the cartilage matrix and causes visible defects in the articular surface, i.e. chondral fracture, this is an "open" articular surface injury (Figure. 2.3, ICRS grade 2 and above). These types of injury occur less often than closed injuries. If the fracture extends through the cartilage into the subchondral bone, this is called an osteochondral fracture [15] (Figure. 2.3, ICRS grade 4).

A 'critical size' AC defect will not fully heal spontaneously without intervention [8, 36]. Classification of chondral lesions are based on the condition of the articular cartilage surface, as well as the depth, diameter, and location of the defect [15]. Defect 'size' is the surface area at the articular surface, and 'depth' is classified as partial, full, or extending into the subchondral bone [37]. Medial femoral condyle (MFC) is the most frequent site of deep grade III and IV lesions [23]. The AC at this location has a mean thickness of 2.35 mm [24], and lesions can range from 0.5 to 12 cm^2 [23]. Various sources define a 'small' defect in the knee is one less than 2 cm^2 [13, 38], and Thomas F. Moyad defines a large defect as one with a surface area greater than 6 cm^2 [13].

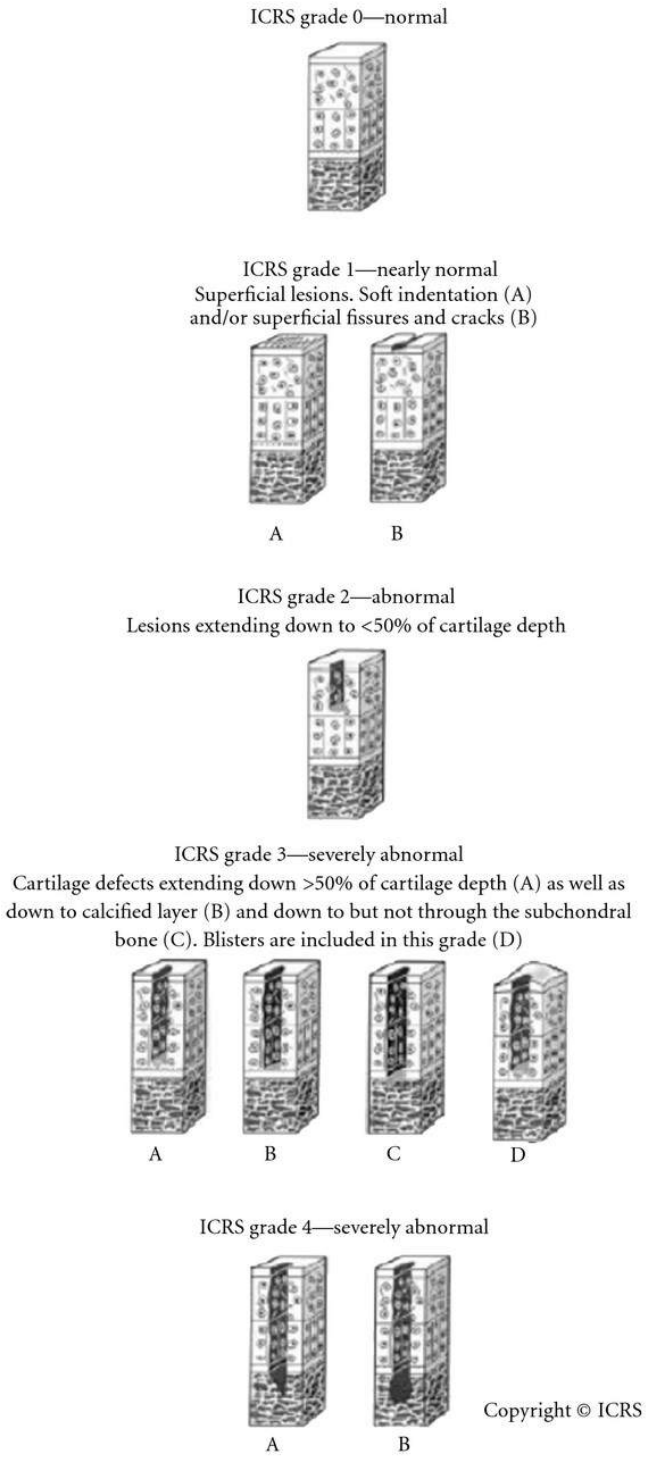

Figure 2.3: Visual representation of the ICRS grading criteria for cartilage defects. Copyright 2012 Olivier A. van der Meijden et al. [39]

2.4 Treatment of Articular Cartilage Injuries

Multiple factors contribute to the decision on the repair technique used, including age and activity levels of patient, and location and size of defect. Initial treatment of osteoarthritis, a leading cause of articular cartilage defects, includes viscosupplementation (VS) [40] whereby a viscoelastic solution is injected into the intra-articular space of the joint to replace, or reinforce, the rheological properties of the synovial fluid. Should the condition progress, reparative surgical treatments can be used. These techniques are referred to as Marrow Stimulation procedures, and utilise the body's own pluripotent bone marrow stem cells to generate reparative fibrocartilage tissue [13]. Examples of these techniques are Microfracture [41], Abrasion Chondroplasty [13, 15], and Subchondral Drilling [13]. The procedures involve creating small holes, or fractures, in the subchondral bone plate. This allows blood, bone marrow stem cells, and growth factors to "leak out" and fill the cartilage defect, and stimulate formation of fibrocartilage repair tissue. These techniques are relatively simple, low cost, and can effectively relieve s0ymptoms [13, 40]. Fibrocartilage, however, is not the same as hyaline cartilage; it is tougher, and less flexible.

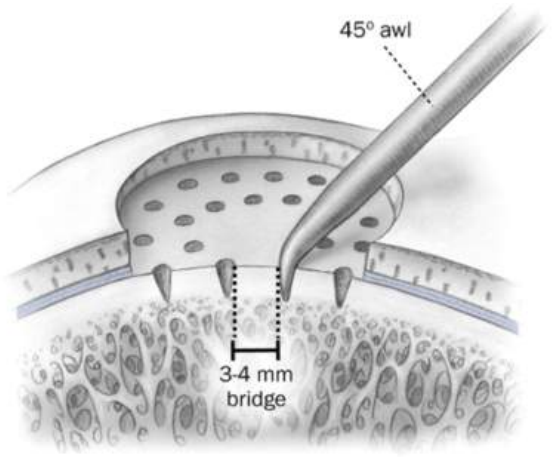

Figure 2.4: Microfracture diagram. Included with permission from Mithoefer, K. et al. [42]

Marrow Stimulation techniques appear to simulate the natural biological response following osteochondral fractures. The process of the healing of an osteochondral fracture without intervention is as follows. Following the fracture, blood escapes into the defect and forms a hematoma that temporarily fills the injury site. Fibrin forms within the hematoma, and platelets bind to fibrillar collagen to establish hemostasis. A continuous fibrin clot fills the bone defect, and extends for a variable distance into the cartilage defect. Undifferentiated mesenchymal cells migrate into the clot, proliferate, and synthesise a new matrix. Some of the cells assume the form of chondrocytes and synthesise a matrix that contains type II collagen and a high concentration of proteoglycans, producing regions of hyaline-like cartilage in both the chondral and bone portions of the defect [15].

The chondral portions of the defect rarely fill completely with repair tissue, averaging approximately 2/3 filled in large osteochondral defects [15]. This repair tissue rarely replicates the same level of specialised structure of normal articular cartilage, with a composition in between that of hyaline cartilage and fibrocartilage. Fibrocartilage is a tougher, more dense,

less flexible form of cartilage, which in articular cartilage healing presents as a type of scar tissue. Without the distinctive orientation of collagen fibrils seen in native articular cartilage, the repair tissue demonstrates inferior mechanical properties. This includes lack of stiffness and poor response to shear and compressive forces [32, 33], which appears to make it frequently susceptible to degeneration due to increased loading of the macromolecular framework during joint use, resulting in progressive structural damage to the matrix collagen and proteoglycans. It is suggested that the lack of durability of the repaired tissue can lead to the development of osteoarthritis [8].

Following progression of chondral injury, replacement surgical treatments are offered, such as Cartilage Resurfacing procedures [13]. Also known as biological resurfacing of cartilage defects, these techniques aim to restore normal (or near-normal) joint cartilage and the articular contour of the joint, to provide a more resilient, hyaline-like cartilage surface. These procedures involve more demanding operations than Marrow Stimulation, with increased costs, longer patient rehabilitation, and higher risk of complications. Treatments included in this stage are Osteochondral Auto-graft (OAT), Osteochondral Allograft, and Autologous Chondrocyte Implantation (ACI).

Osteochondral Auto-grafts [13] are a single stage procedure where healthy cartilage plugs are removed from "limited weight-bearing" areas in the joint, and reimplanted into the chondral defects. This is presented in Figure 2.5. Due to it being the patient's own tissue there are no issues such as donor tissue rejection, however there is the potential issue of donor site morbidity. No site in the knee joint is truly non-weight-bearing and therefore the loss of cartilage in the donor site(s) can cause damage to the surrounding healthy articular cartilage or the subchondral bone due to increased applied loads following the procedure.

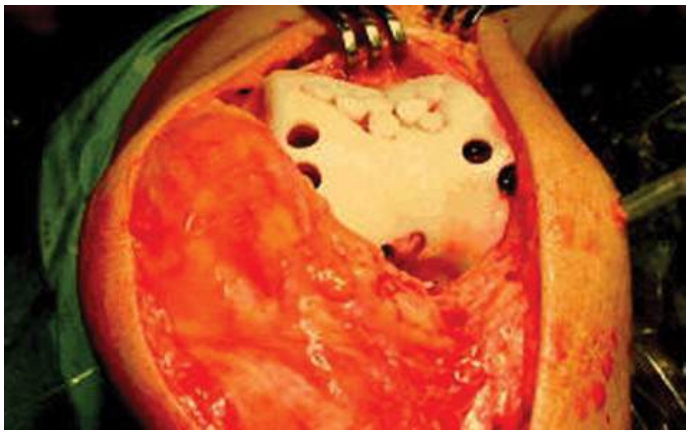

Figure 2.5: Photograph demonstrating the OAT procedure. Note the donor sites and the defect filled with the healthy cartilage plugs. (Thomas F. Moyad, copyright 2011) [13]

Osteochondral allografts [13, 32] also known as particulate cartilage allograft transplantation, is a similar procedure using cadaveric donor tissue from another person. The donor cartilage is minced and placed into the chondral defect and covered using a patch and fibrin glue. This procedure carries no risk of donor site morbidity for the patient, however, there is the chance of tissue rejection because the cartilage is from a donor. Autologous Chondrocyte Implantation [8, 13, 33] is a two stage procedure. Stage 1 is the initial arthroscopic cartilage

biopsy, and stage 2 is the surgical reimplantation of expanded adult chondrocytes. During the initial surgery, damaged cartilage layers are removed without violating the subchondral plate, and healthy articular cartilage is excised from "low-weight-bearing" areas of the joint [11]. Chondrocytes from the healthy cartilage are cultured *in vitro*, and the cultured tissue is implanted into the cartilage defects during the second surgery [8, 13, 40]. Figure 2.6 presents the patch graft securing, with sutures and fibrin glue, the autologous chondrocyte implant.

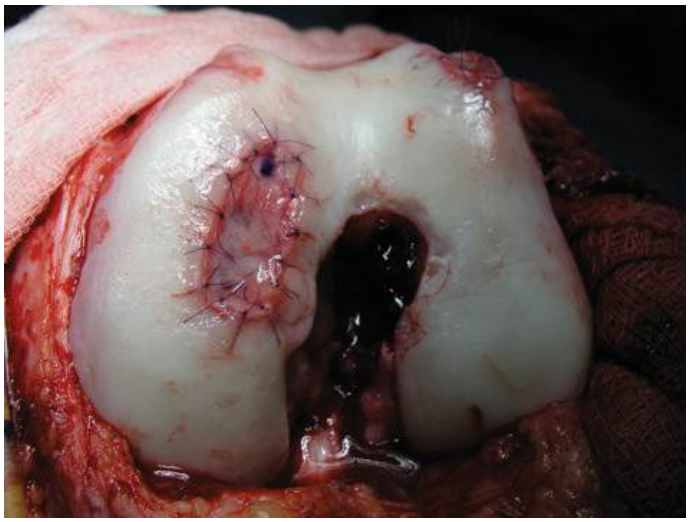

Figure 2.6: Photograph showing the patch graft secured with stitches and fibrin glue. (Thomas F. Moyad, copyright 2011)[13]

Matrix-Assisted Autologous Chondrocyte Implantation (M-ACI) takes ACI one step further and involves the healthy chondrocytes being cultured onto a collagen scaffold *in vitro* before being re-implanted into the defect(s) [8, 13]. Surgical techniques using cartilage "plugs" implanted into the defect, such as OAT, often have graft-site mismatch, with size-depth mismatch being more frequent compared to other procedures. This mechanical mismatch can disrupt the smooth articular surface contour, inhibit cartilage regeneration, and cause implant failure [8]. There are also issues with poor integration of the graft with the host cartilage, resulting in the breakdown of tissue at the host-graft interface [32]. Autogenous transplantation procedures (i.e. OAT and ACI) present fewer complications of infection, but face issues with limited availability of donor sites, tissue harvesting problems, and donor site morbidity [43]. The final type of procedure, a knee arthroplasty, involves removing the damaged parts of the joint and replacing them with implants. This can be a total or unicompartmental replacement [40].

2.5 CAD Topologies

2.5.1 Solid Modelling vs Surface Modelling

Solid modelling produces a 3D model, of a calculable volume, via additive and subtractive operations [44]. Solid modelling can be constructed from 2D dimensions (i.e. a sketch), 3D dimensions such as wireframes, and basic geometric shapes such as cubes and spheres [45]. The model will have a wall-thickness or solid volume [46], and can be distinguished from

wireframe and surface modelling by being 'complete', 'unambiguous', 'valid', and 'solid', as defined by Dassault Systemes 'Glossary' [45]:
"Complete - various points of an object within the modeling environment can be classified as inside or outside (giving a more accurate representation of the object and its surfaces).
Valid - Vertices, faces and edges are properly connected for a complete view of the object.
Unambiguous - [there is a] singular interpretation of all design aspects of the object (this means that there is certainty and clarity in the design of the object - you can see what it will actually look like in reality).
Solid - [the model] consists of geometric and topological data (weight, shape, size, connectivity of nodes/edges/faces)."
Surface modelling produces a 3D model via defining the faces that the geometry is comprised of [44]. These models have no thickness [46]. Types of surface modelling include Polygonal modelling, Non-Uniform Rational B-Spline (NURBS) modelling, and Subdivision modelling [47, 48].

2.5.2 Polygon Modelling

Polygon modelling, also referred to as polygon mesh modelling, is 3D Surface modelling consisting of vertices, edges, and polygons. The vertices are essentially coordinates within the modelling environment, the edges are straight lines connecting neighbouring vertices, and the resulting faces are polygons which form the surface. Triangles and quadrilaterals are the most commonly used polygons [49, 50, 51]. Smoother curves are generated in polygonal modelling by increasing the number of polygons which represent the model (Figure 2.7). If a polygon mesh model with a low number of polygons is enlarged, curved surfaces are revealed to be angular [50].

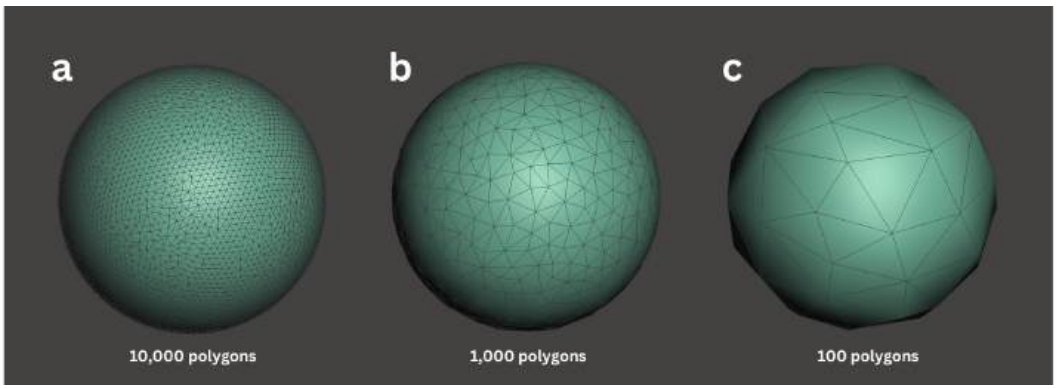

Figure 2.7: A sphere modelled in Autodesk Meshmixer software (Autodesk, USA) [52] with different polygon counts. Model a - 10,000 polygons, model b - 1000 polygons, model c - 100 polygons.

2.5.3 Parametric Modelling

Parametric surfaces are generated by mathematical equations which define the shape of the surface [48, 53]. Parameters can include length, width, radius and angle, which can be adjusted to change the surface shape [48]. Unlike polygon / mesh models, parametric modelling uses mathematical instruction to produce a single contour, as opposed to joining many flat polygons. Thus, parametric models can be considered to have "infinite resolution";

scalable without any loss of surface quality [50, 54]. Parametric surfaces are standard for designing CAD (Computer-Aided Design) shapes such as cylinders and cones, but can also be used to generate more complex geometries [48].

2.5.4 NURBS Surfacing

NURBS, a type of Bezier curve, are mathematical representations of 3D geometry, and NURBS curves can be used to generate NURBS surfacing [48, 55, 56]. NURBS curves are defined by control points and knots, and offer a high level of control and precision [48, 55]. An example NURBS curve is presented in Figure 2.8. NURBS can be used to represent many types of geometry, from standard lines, spheres and toruses, to free-form geometry such as the human body [56]. A NURBS curve on its own is not a surface, but a set of NURBS curves together can define the shape of a surface [48, 55]. Converting a polygon mesh model to a NURBS model is called reverse engineering (Figure 2.9) [50]. As with all parametric models, compared to polygon mesh models, enlarging a NURBS surface 3D model does not impact curve smoothness, as the curves are recalculated to fit the new scale using the software algorithms [48, 50].

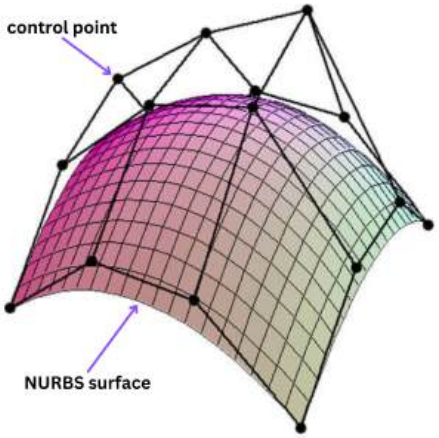

Figure 2.8: An example NURBS surface [55].

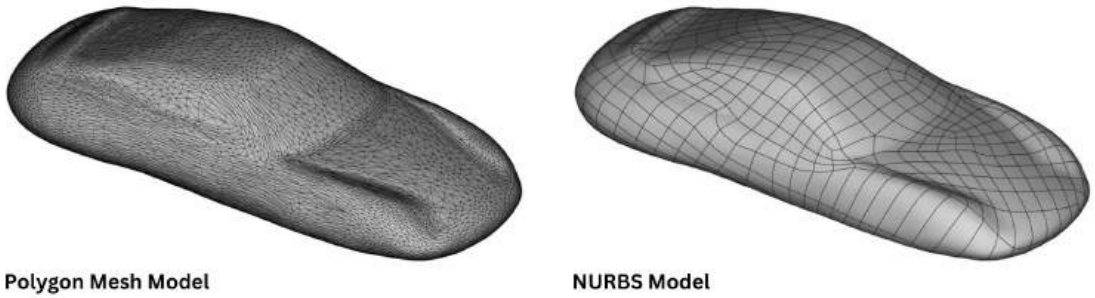

Figure 2.9: While a polygon mesh model is calculated from polygons, a NURBS surface model is calculated as splines [55]. Image courtesy of Rack (2020) [50].

2.5.5 Subdivisional Surfacing

Subdivisional surfacing can be considered a combination of NURBS and polygon mesh modelling, allowing generation of smooth contour approximations from course polygon mesh (Figure 2.10) [57, 58]. The shape of the contour, called the inner mesh, is calculated from, and thus can be controlled by editing, the coarse mesh, called the control cage or outer mesh [57]. This is similar to B-splines (used in NURBS) in that the final curve is defined by the vertices of the initial mesh [59]. Most subdivisional surfacing methods iteratively subdivide the control mesh polygon faces to a denser mesh (more polygon faces) which better approximates the smooth contour [57]. Each iteration is called a subdivision level, starting at zero (no subdivision) [60]. Subdivisional surfacing is not considered useful for creating geometrically accurate models, but is an appropriate organic surface modelling technique [61]. The opposite process, reducing the number of polygons, is called un-subdividing [60].

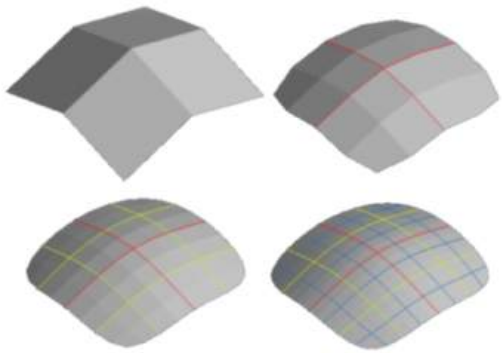

Figure 2.10: An example of the Catmull-Clark subdivisional surfacing method [62]. Image courtesy of Kemiyatorn (2009) [63].

2.6 Additive Manufacture

The British Standards Institute defines Additive Manufacturing as the "process of joining materials to make parts from 3D model data, usually layer upon layer, as opposed to subtractive manufacturing and formative manufacturing methodologies" [10]. There are many different types of AM processes. Considering in situ AM, Material Extrusion (MEX) and Material Jetting (MJT) of bioinks are the most applicable technologies. Other types of AM such as Binder Jetting (BJT), Powder Bed Fusion (PBF), and Vat Polymerisation (VPP) are commonly used in the wide range of industries that have adopted some form of AM into their production process(es) [64]. MEX is defined as an "[AM] process in which material is selectively dispensed through a nozzle or orifice", and MJT as an "[AM] process in which droplets of feedstock material are selectively deposited" [10]. The research presented in this thesis focused on MEX AM, specifically of thermoplastics and hydrogels.

The process of generating a part by AM requires a CAD model. The CAD model is converted to an additive manufacturing file format , sliced digitally into cross-sectional layers during preprocessing, and the information is sent to the 3D printer where the part is built layer by layer [65, 66]. An Additive Manufacturing File (AMF) is a file format for communicating AM model data including a description of the 3D surface geometry with native support for colour, materials, lattices, textures, constellations, and metadata [10]. Traditionally the STL

(standard triangle / tessellation language, stereolithography) file was the standard file type for AM processes. This files type is limited and only describes the surface 3D geometry of an object. Other files formats have emerged such as the 3MF (3D Manufacturing Format) file type, an open source file format designed specifically for AM. The 3MF file can hold more information, provides a clear definition of manifoldness, cannot have 'non-manifold' edges, and is more compressed than an STL file. The file creation process descritises the continuous geometry in the CAD file into a header, small triangles, or coordinate triplet list of x, y, z coordinates and the normal vector to the triangles. This process is inaccurate, but the smaller the triangles, the closer the AMF file is to the CAD model [10, 67].

Frunzaverde et al. (2022) investigated the effect of print temperature and colour of PLA filament on the dimensional accuracy of additive manufactured items, and found optimal dimensional accuracy between 200 and 220 °C for natural and black PLA. Notably, their measure of dimensional accuracy was the volume of the printed cuboid, thus not specific to top-surface conformal printing applications [68]. Alsoufi et al. (2019) investigated the effect of temperature on dimensional accuracy. They observed that all the printed dimensions for the length and width of the cuboids were smaller than the CAD dimensions, and there was difficulty assigning a consistent trend with regard to varied temperature (195 to 250 °C). The colour of the PLA used was grey, and a slower print speed (15 mm/s) was used for the top, bottom, and walls [69].

EinScan-SP scanners have been used to validate the quality of the prints created by a MakerBot FFF (Fused Filament Fabrication) printer (MakerBot Industries, USA) [70] and an Ultimaker 3 Ext. FFF printer (Ultimaker B.V., The Netherlands) [71], by comparing the CAD dimensions to the scanned model dimensions. Unfortunately, the dimensions of the print were not taken or compared as far as can be seen in the papers. The EinScan-SP scanner is a model of structure light scanner, able to register the local surface geometry of an object using the way 'flat' 2D patterns are distorted when projected onto a 3D object. If the object is flat, for example the side of a cube that is perpendicular to the direction of projection of the image, the projected image is the same as the 2D original image. If the object is different, the projected image will be distorted. For example, if an image of two parallel lines is projected onto the curved surface of a ball, the lines will no longer display as parallel, they will diverge and converge as shown in Figure 2.11. The rate of divergence/convergence would depend on the curvature of the surface of the ball. The scanner utilises this phenomenon by projecting a well-defined 2D pattern (consisting of parallel and perpendicular lines) onto the object, and observing the distortion of the pattern. The displacement of a line can be converted into 3D coordinates. Using this, it attempts to reconstruct the surface geometry of the scanned object [72]. If required, the pattern projection and recognition process is repeated at different angles, and then these multiple point clouds can be joined together to build the full geometry of the whole object's surface. An example of the structured light scanning process is presented in Figure 2.12. 3D scan point clouds are typically converted to, and exported as, a polygon mesh [50] (Section 2.5.2) for 3D modelling use. Recreational user experience for the Einscan-SP (with ExScanS v3.0.0.0) advises that the balance between increasing frequency of turntable steps to increase accuracy, and the resultant increase in time taken to scan, is optimised at 16 turntable steps per 360° rotation [73].

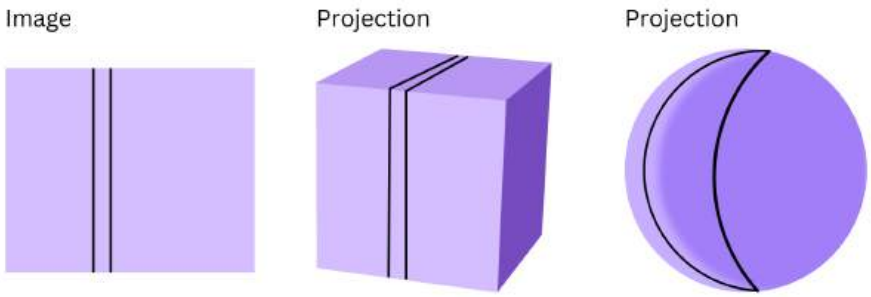

Figure 2.11: Diagram presenting the theory of optical scanner projection.

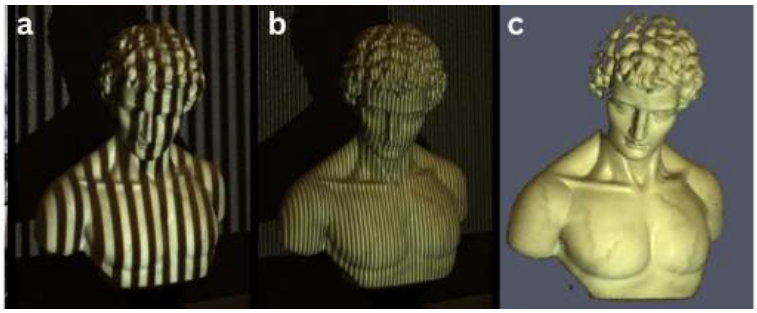

Figure 2.12: An example of structured light 3D scanning on a bust model. a) Wide vertical stripe pattern projecting onto the bust, b) narrow vertical stripe pattern projecting onto the bust, c) the point cloud generated in the 3D scanner virtual environment [74].

2.7 Biomedical Applications of Additive Manufacture

The main benefit of AM processes over conventional manufacturing, with regards to biomedical applications, is the ability to create implants with specific macro-, micro-, and nano-scale structures in a single build platform, which are specific to the patient anatomy, type of injury, and surgical technique used [67, 75, 76, 77, 78]. While the resolution is limited to what the AM machine is capable of printing [75], AM offers the ability to produce parts with gradient compositions and mechanical properties [14, 79, 80]. This is significant when engineering implants to replace articular cartilage, enabling structures such as biphasic scaffolds to reproduce the anatomy of complex articular surfaces [81].

The process of AM for medical implants involves various steps, such as the imaging of the patient anatomy, segmentation, and manufacturing phases. Each of these steps introduces a source of error [82]. Collaboration between engineers, radiologists and surgeons is necessary to correctly image the selected anatomy, achieve good segmentation, and create an accurate model [77]. There is currently a lack of standardisation of additive manufactured implants. As AM becomes more widely used, there need to be procedures outlined for optimal conversion of DICOM (Digital Imaging and Communications in Medicine [43, 81, 82]) files to 3D models, appropriate file preparation, and selection of suitable AM technology and parameters [66].

The process of AM of an implant can be summarised in a few steps: capture the internal medical data of the patient with CT (Computed Tomography) and MRI (Magnetic Resonance Imaging) scans, convert the collected images into CAD models, finalise the implant CAD

model and visualise the fit through simulation software, and finally the print file is generated [66]. Many current clinical applications of AM focus around high quality cranial and maxillofacial bone implants. AM produces implants that fit better and are easier to insert and secure; reducing procedure time, and improving cosmetic results [67]; however, these are low weight bearing applications.

Preoperative imaging of the anatomy generates CT and MRI scan data which is segmented by medical image processing software such as Mimics (Materialise, Belgium) [77, 79]. The data is used to model the anatomical defect, and this model is used to design the implant geometry [32, 34, 66, 76, 77, 78, 80, 83, 84, 85, 86]. A highly detailed image of the defect is required, and the imaging resolution places an upper limit on the achievable fit of the implant [8, 32]. Furthermore, the imaged anatomy is likely altered by surgical debridement before implantation, causing inevitable graft-host mismatch of pre-constructed implants [8, 32].

For high accuracy imaging of large cranial defects, a spiral scanning technique allowing full volume CT imaging has been utilised. With this technique, Jardini *et al* (2014) [77] were able to generate a large number of slices of recommended thickness (between 1 and 2 mm). The data was obtained in DICOM format and converted into a 3D virtual model using InVesalius software (ProMED project developed at CTI). The bone structure was isolated from the surrounding tissues through segmentation, and the STL file exported. Virtual modelling of internal structures of the human body requires very good segmentation with high resolution, and small pixel size. Magics 15.0 software (Materialise, Belgium) was used to edit the STL to minimise surface imperfections. Solidworks software was used to develop the implant CAD model.

A workflow for 3D modelling and additive manufacture of patient specific medical implants is suggested by Salmi *et al* (2011) [87]. The methods described involved CT imaging of the facial bone defect, with a slice thickness of 1.25 mm. The medical 3D model was created from the tomography images using OsiriX 2.7.5 Open Source Software [82, 87].

Moiduddin *et al* (2017) [43] also obtained cranial image data using CT scan images saved in DICOM format. Mimics 17.0 software was used to convert the DICOM files into a 3D model [79]. Segmentation and region growing techniques were applied with a Hounsfield unit (HU) value in the range of 310-2850 (skull model segmented using 500 HU value [82]) for segmentation of hard and soft tissues, and saved as STL. The STL was imported in 3-Matic 9.0 software to design the reconstruction implant using mirror imaging of the original anatomy, superimposing, and Boolean operation. The implant bulk design file was imported into Magics 18.03 structural module, and a validation model of the implant was fabricated through polymer based FDM (Fused Deposition Modeling) using a Stratasys FDM machine.

Singare *et al* (2004) [88] generated a 3D model of a bony defect from helical CT data. A General Electric CT scanner with a 1.3 mm slice thickness and slice reconstruction interval of 0.6 mm with a resolution of 512 x 512 image matrix was used. The CT scan data was imported into Mimics software. Initial Graphic Exchange Specification (IGES) representation of the segmented region was generated using CTM (Materialise Medical software) and exported to reverse engineering software Digisurf for surface reconstruction. The data was then converted to a mesh based surface representation format (a STL file).

Ciocca *et al* (2009) [81] used a CT scan of a mandible performed with a GE Healthcare BrightSpeed instrument, with slice thickness 0.625 mm and image resolution of 512 x 512 pixels. This yielded 243 slices, which were stored in DICOM files. Using this data, a 3D digital model of the mandible was reconstructed. The soft tissue data was segmented by setting a suitable threshold value using Amira 3.1.1 (Mercury Computer Systems, Chelmsford, MA), a software tool for 3D visualisation, data analysis and geometry reconstruction. Manual operations such as filling holes and deleting erroneous polygon data were completed to obtain a watertight mesh in STL format. Refinement editing operations were performed using Rapidform XOS2 software for 3D scanners (INUS technology, Seoul Korea). Finally the models were fabricated using a Stratasys Dimension SST (Soluble Support Technology) 3D printer (FDM based) with a layer thickness of 0.254 mm [81].

The slicing process introduces inaccuracy to the file because the algorithm replaces the continuous contour with discrete stair steps [67]. This is mitigated by making the slices have minimal thickness - e.g. 3D model sliced horizontally with layers of thickness 0.127 - 0.331 mm [83]. Bausch *et al* (2016) [89] describes the process of tool path planning after slicing the object; the print manoeuvre tool path was created and amended with ISO-hops. This includes "non-print manoeuvres" such as advancing to the next layer, and avoiding collisions with previously printed paths.

Most recently, Perez et al. (2023) investigated the ability of the EinScan-SP to accurately record the gross anatomy of a tumour that was removed from a patient during surgery [90]. The high-resolution, photo-realistic, scanned model was considered comparable to viewing and inspecting the gross specimen in real life, whilst also offering a solution for long-term storage of biological specimens, and improving communication between the examining pathologist and the rest of the clinical care team (or anyone wishing to examine the case in the future).

The use of 3D scanner technology in the operating room (OR) has been investigated by He et al. as part of bone recognition for computer- and robotic- assisted orthopaedic surgeries. The EinScan-SP 3D scanner on its own [72], and combined with rapid-setting impression moulding techniques [91], was compared to the paired-point technique [92], and intraoperative CT scanning. The shape of the scanned bone was compared to the preoperative CT scan image and a surface matching algorithm [93] correlates the corresponding location of the scanned bone with the preoperative image, thus registering the bone. It offered an inexpensive and compact method of bone registration, without the use of further ionising radiation from intraoperative CT scanning. Furthermore, a specifically shaped fiducial guide (SSFG) technique was developed that enabled the bone area to be registered, and also tracked in real time after registration, allowing the surgeon to move the operative extremity in space [91].

Bone registration techniques for orthopaedic surgery have been explored widely. Registration for surgical applications of computer-assisted surgery involve the spatial alignment of the patient anatomy, the computer-aided model/ surgical plan, and the coordinate frames of the robot / automated system assisting in the procedure. Registration must be maintained during the entire process of the surgery [94]. The two main methods of maintaining registration, and thus accuracy, during surgery are immobilisation and tracking [94]. Immobilisation, relative or absolute, is often necessary to maintain the alignment of these, and is suitable for many orthopaedic procedures due to the rigid structure of the larger bones in the body [94, 95].

In terms of tracking, a key element in registration is the use of fiducial markers. A fiducial marker is an object in the field of view of an imaging system which appears in the image produced, for use as a point of reference or a measure [94, 96]. Fiducial markers, or fiducials, are either artificial (extrinsic registration) or natural / anatomic (intrinsic registration) [95]. Typically a highly contoured surface is designed, or chosen, for the fiducial marker [94]. Extrinsic registration refers to artificial fiducials that are secured to the area of the procedure. For orthopaedic surgical applications, this could be a frame / reference object on the outside of the body, or something placed inside the body, such as a screw or a radiological marker [95]. Artificial fiducials have arbitrary shape, and are designed to be high contrast and clearly visible on the preoperative images and during the procedure [97]. Extrinsic registration is fast, relatively easy, and can often be automated [98, 99]. In a 2016 review on extrinsic registration methods for medical imaging, Alam et al (2016) [98] summarise the comparisons of moulds and frames (non-invasive registration) to invasive registration methods (stereotactic frames and screw fiducial markers) and other non-invasive registration methods (skin fiducial markers). Tightly secured moulds and holder frames have been used for image guided surgery on the head, and surround the area with non-invasive fiducial markers. They are considered suitable for efficient image-guided surgery, and offer accuracy without use of complex optimisation and image registration computation. While patient movement can potentially dislocate the markers, greatly affecting accuracy of registration, the advantages of speed and decreased invasiveness are notable. The methods are considered reliable, robust, and widely available [98]. Robot-assisted surgical systems mostly use artificial fiducials as they are the most easily recognised [94]. Intrinsic registration refers to the geometry of the patient's anatomy, and is thus more complicated [95]. However, anatomical markers do not involve the process of attaching the artificial marker rigidly to the patient's anatomy, which is often an invasive procedure to secure the marker to their bone [94, 100].

Fiducials can be further categorised as point, spatial, linear, or planar. This refers to the ability of a single fiducial marker to define the coordinate frame, and this is determined by their geometry. Point and spatial fiducials are the most common. A single point fiducial provides an x, y, and z coordinate (three of the six constraints needed to define a coordinate frame), and thus a minimum of three point fiducials are needed to fully define the coordinate frame. Spatial fiducials are able to provide all six coordinate frame constraints [94]. A disadvantage of optical tracking with fiducial markers is that the markers can be covered and the registration geometry 'lost' during the procedure [100]. Combining bone registration techniques with in-situ conformal 3D printing could advance computer- and robotic- assisted surgeries further.

2.8 Additive Manufacture and Repair of Articular Cartilage Defects

When exploring the possibilities of additive manufacture for cartilage implants, the processes and materials which may be suitable must be considered. The structure should be biocompatible, biomimetic, and biodegradable if used as a support for integration of native cells. For this application, biocompatible means that the material(s) used should not significantly affect the host body in an adverse way. Examples of adverse effects on the human body of implanted materials include toxicity and thrombogenicity (the tendency of a

material to induce blood clotting [101, 102]. Biomimetic, in this application, considers the ability of the constituent and gross material(s) to replicate the appearance, structural function, and mechanical function of the articular cartilage tissue that the implant is replacing. Referring to the structure and mechanical properties of AC (Section 2.2), does the structure effectively resist and distribute the applied shear stresses and compressive loads applied to the articular cartilage of the knee. The geometry must fit the defect, and should possess mechanical properties capable of bearing the loads encountered in vivo [81]. Finally, considering the biodegradability of the structure involves designing either for the structure to remain as a permanent scaffold (bioinert) or for it to be broken down by the host body over time as the native tissue grows into the structure to replace it (bioresorbable [103]). If the material is bioresorbable, then its products of degradation should be biocompatible as well. This lends itself to biocompatible polymers and hydrogels.

AM MEX-TRB is a common form of material extrusion additive manufacturing technology [66, 75, 80, 86, 83, 104]. The process uses thermoplastic filaments or biopolymers [85, 105] and pneumatic or mechanical (piston / screw) dispensing systems to extrude continuous material [14] to deposit the layers of the print with thickness (z-axis resolution) of 0.1 - 0.25 mm [67, 106]. AM MEX-TRB is inexpensive compared to other AM processes, and can be used with commercially available biodegradable filaments [80]. FDA cleared materials for AM biomedical applications (including articular cartilage, knee joint bearing surfaces, and scaffolds) include polymethylmethacrylate (PMMA), polyethylene (PE), and polyetheretherketone (PEEK) [66]. AM MEX-TRB has been used to create porous PEEK tissue engineering scaffolds [14].

AM processes are also being used in tissue engineering, with the aim of manufacturing biological tissues layer by layer, with or without plastic polymer structural support. Biofabrication is the process of producing complex living and non-living biological 3D constructs from raw materials such as living cells, molecules, extra-cellular matrix, and biomaterials [85, 107]. The combination of AM technology and biofabrication produces Bioprinting - the simultaneous deposition of structural biomaterials and living cells [32]. Bioprinters can be AM MEX printers that dispense hydrogels or hydrogel-cell mixtures [85]. Hydrogels often have variable viscosity so extrusion systems are effective [80], however, hydrogels have low mechanical strength, so are often paired with other polymers for their structural properties [85]. The mechanical properties of a tissue scaffold determine its integrity post-processing, the ease of handling, and the biological behaviours of cells within itself [107].

2.8.1 *In Situ* Additive Manufacture for Articular Cartilage Repair

In 2016 a core group of researchers at the ARC Centre of Excellence for Electromaterials Science (Intelligent Polymer Research Institute, Innovation Campus, University of Wollongong, Australia) and the University of Melbourne (Australia) developed the Biopen - a handheld 3D bioprinting device. The Biopen was designed to utilise dual extrusion of material - a 'Core' of hydrogel containing cells, and a 'Shell' of hydrogel that could be UV cured to provide the structural mechanical properties of the scaffold. The Biopen presented a new approach to using freeform biofabrication in surgery while considering the practical constraints of the operating theatre, enabling the deposition of living cells and biomaterials in a manual

directwrite fashion [33].

The original design for the Biopen had co-linear extrusion of the 'core' and 'shell' side by side, with the 'shell' extruded simultaneously as a second layer on top of the 'core'. This enabled it to protect the cell-laden 'core' underneath while receiving the curing effects of the UV light. The base of both the 'core' and 'shell' was GelMa/HAMa hydrogel (Gelatin-methacrylamide / hyaluronic acid-methacrylate). The 'core' also contained human infra-patellar fat pad (IPFP) derived adipose stem cells. A photo-initiator (PI) was added to the 'shell' bioink - for the initial experiments this was VA086 [33].

The Biopen was developed into co-axial extrusion of the 'core' and 'shell' bioinks, and underwent large animal model testing of the ability to repair full thickness chondral defects in the lateral and medial condyles of the femurs of sheep [32]. The cells used in the 'core' for this experiment were adipose-derived mesenchymal stem cells (MSC) from sheep. The experiment compared the Biopen against implantation of preconstructed bench-printed bioscaffolds, microfracture treatment, and control (no treatment of the defects).

Co-currently, investigation was made into the most appropriate PI to use for the Biopen application [108]. The Biopen system requires a bioink that sets rapidly enough to allow handheld application, generates a construct of sufficient stiffness to immediately withstand the forces within the intra-articular environment, and delivers viable cells with the ability to form chondral tissue. The co-axial extrusion Biopen was used with sheep infrapatellar adipose-derived mesenchymal stem/stromal cells (ADSCs) in the 'core' hydrogel, and different PIs were added to the 'shell' hydrogel. The 'implants' were bioprinted into PDMS (Polydimethylsiloxane) molds (1 cm diameter, 1 mm depth), and the 'shell' bioink was cured using 365 nm UV light at 700 mW/cm^2 intensity. The volume of the mold was less than 2 cm^2 which is suggested to be a critical size from previous papers [8, 36, 38]. The resulting implant discs underwent mechanical compression testing (unconfined). From the results, LAP (lithium - acylphosphinate) was chosen as the recommended PI for this application. IRGACURE2959 and VA086 were also tested.

Further experimentation validated the survival and proliferation of human adipose-derived mesenchymal stem cells (hADSCs) within the bioprinted implants over 8 weeks, analysing the formation of hyaline-like neocartilage [8]. The hADSCs were harvested from the infra-patellar fat pad (IPFP) of donor patients affected by osteoarthritis. PDMS molds (1 cm diameter, 1 mm thickness) again were used as structures for the implants to be bioprinted into. The PI was LAP, and the curing was with 365 nm UV at 700 mW/cm^2 for 10 seconds. The resulting implants were cultured and the formation of human hyaline-like neocartilage was validated [8].

Although the experimental results with the Biopen are positive, and the group discuss the move towards larger scale testing before it becomes a regulated medical instrument, there are elements of uncertainty. For one, the 'toolpath' of the implant is left entirely up to the operating surgeon (or researcher in these experiments). Therefore the consistency in the repeatability of their tests comes under question - how was it made confident that the 'toolpath' was the same in all their experimental samples. Furthermore, the toolpath and orientation of the hydrogel as it is deposited may impact its material and bio-mechanical properties [109, 110].

In Nanjing, China, a group were also experimenting with *in situ* repair of bone and cartilage using 3D scanning and printing. In 2017, Li *et al* [11] tested the feasibility of *in situ* bioprinting for the repair of a large bone defect, a full thickness ICRS Grade IV cartilage defect (approx 0.42 cm^2), and a cylindrical osteochondral defect (diameter 6 mm, depth 3 mm). They scanned the femurs (from sacrificed rabbits and pig) using a handheld EinScan-Pro 3D scanner (Shining3D, China), and exported the scans to Magics 21 software (Materialise, Belgium) as STL files.

The scanned virtual models were used to print resin models of the biological samples for printing onto during the experiment, and to design the implant geometries to repair the defects. The printer used was a modified Bio-Architect 3D printer (Regenovo, China), which used UV cured hydrogels to fill the defects. The resin models were set in plastic foam on the print bed, with the bottom surface of each defect parallel to the print bed. After printing, the models were scanned and the virtual models analysed using Geomagic Studio 12 (Geomagic, USA) and 3-Matic STL 9.0 (Materialise, Belgium). The hydrogel prints were considered successful and accurate in filling the defects and replicating the functional geometry.

Whilst providing evidence on the feasibility of the technology, there is no discussion or explanation of the toolpath development for printing in situ. Furthermore, it is not stated how the 3D printer has been modified, or why. While there is some discussion of the accuracy of the resulting implant prints, the error analysis is limited and there is no statistical analysis of the accuracy provided or discussed.

In 2020, the process was developed to include a 6 DOF robotic arm for robotic-assisted *in situ* 3D printed cartilage regeneration [12]. This experiment tested a fast tool centre point (TCP) calibration method for the robot. A HAMA hydrogel with added PI for UV curing was used again to 3D print onto a resin model. This model was generated from Micro CT images of a rabbit femoral condyle, with a cylindrical defect (5 mm diameter, 4 mm depth) mimicking osteochondral injury. The same scanning and analysis methods were used as before [11]. Furthermore, this procedure was then repeated on a live rabbit femur - in vivo printing to fill an ICRS grade IV defect made by mosaicplasty. The nozzle was manually positioned at the starting point of the print path.

The TCP calibration method showed a decrease in the error of the prints. Surface error of less than 30 μm was reported. It was stated that this is significant due to the superficial zone of human AC having a thickness of approximately 200 μm*, which is suggested to be almost impossible to repair manually.

*This measurement is assumed from the superficial zone being defined as the top 10 % of the AC tissue thickness, which is measured at an average of 2.4 mm (for healthy medial femoral condyles of cadavers aged 23 to 49) [111].

Again, the development of the toolpath is not expanded upon, and limits to the technology are suggested by the manual operation of moving the print head to the implant print 'origin' before printing. Furthermore, minimal error analysis is presented with no obvious statistical significance testing.

2.9 Summary

The key insights from the review of the current literature are thus. Articular cartilage is a highly specialised, complex, layered, biological structure. The distal femoral anatomy, where articular cartilage defects are common, presents specific contour geometry that needs to be replicated accurately to provide a successful articulating surface for joint function. Critical sized articular cartilage defects will not heal fully without intervention, and current interventions generate fibrocartilage to replace the damaged / lost hyaline cartilage, or require implantation of donor hyaline cartilage. The inferior mechanical properties of fibrocartilage under normal joint loading, articular surface contour mismatch, and graft-host mismatch, are the main factors limiting the effectiveness of current interventions. Additive manufacturing, combined with 3D scanning, has been used to manufacture implants for low load bearing medical interventions. AM MEX-TRB of thermoplastic filament or biopolymers is considered suitable to apply to the manufacture of an articular cartilage implant. While current in situ additive manufacturing research has developed a unique 'filament' for articular cartilage repair in the form of the Biopen Shell/Core system, gaps remain in the current research regarding the steps taken from scanning the cartilage defect, to the implant being manufactured in situ via additive manufacturing. There is little to no information presented in the literature on: how the scan data is developed into the 3D printer toolpath, how the printer(s) were modified for the experiments undertaken, and the accuracy / methodology of manual initial position of the print head at the print origin.

To be able to bridge the gaps evidenced between the scan data and the toolpath, a method of imaging will need to be developed (Objective 1) that produces scan data that can be manipulated (Objective 2) to produce CAD modelling of (and thus AM toolpaths for (Objective 3)) a variety of implant experiments. Once the toolpath generation process is understood, the methodologies can be developed for applying the technology to repair of articular cartilage defects (Objective 4).

A successful proof of concept result for in situ additive manufacturing for repair of articular cartilage defects will consist of: a method outlined for converting the scanned object data into a functional AM toolpath for an in situ AM implant, and an object additively manufactured in situ on the surface of another object. An essential aspect of this success will be conformal surface matching between the implant and the scanned object, with no damage to the underlying surface of the scanned object.

Desirable outcomes would be that an in situ AM print is completed into a recess that is considered an approximation of an AC defect, for example a 10 mm diameter cylindrical recess. Furthermore, the ability for the accurate positioning of the origin of the print within the print volume to be part of the automated AM process (rather than manual positioning before the AM process begins). Finally, for the research presented in this thesis to be able to be combined in future work with the Biopen filament research to produce reliably replicable implants, with functional biomechanical properties, for AC defects.

In summary, considering the combination of additive manufacturing and surgical implants towards conformal bioprinting, the need for a standardised repeatable workflow became abundant. While some groups have been able to move on to proof of concept in vivo 3D printing of biocompatible hydrogel-based implants *in situ*, there is a gap in the underlying

theory and mechanics of the *in situ* process. Filling this gap is significant in enabling a solid foundation for the development of patient-specific, customisable, *in situ* 3D printed implants for the repair of human articular cartilage defects. The work presented in this thesis contributes towards standardisation of the process of *in situ* additive manufacture onto unknown surfaces, helping to bridge that gap and fulfil the novel aspect of the PhD requirements. The first step in the workflow is accurate, reliable capture of the surface geometry to be 3D printed onto.

Chapter 3

Surface Scanning

3.1 Introduction

The first step in a standardised methodology for conformal AM for in situ repair of AC defects is accurately imaging the defect in real time during surgery (Figure 1.1). In order to use additive manufacturing to print onto an "unknown" substrate, instead of the flat, known, bed of a printer, the 3D geometry of the substrate surface needs to be established. An "unknown" surface is defined as a surface which has not been designed or generated through known tool paths. An example would be an anatomical surface in the human body such as a bone. Furthermore, inaccuracy or consistent error in the scanning process needs to be registered and accounted for in the tool path planning for an implant or surface addition.

The scanner available for the early exploratory phase of this research project was an EinScan-SP 3D scanner - a tabletop scanner with a turntable. In a surgical context, this type of scanner would not be appropriate, however Shining 3D also produces handheld 3D scanners which would suit the surgical application. Examples of Shining 3D scanners that should fit the specification for this application (biomedical implant design) include the EinScan HD [112] and EinScan H2 [113]. While the EinScan-SP has been shown to be useful in anatomical 3D scanning for accurate virtual representation of surface geometry, the specific settings for generating usable scan data are not presented in the literature (Section 2.7). To fulfil project objective 1, the parameters of the 3D scanner used for this project required full understanding and clarification. During the preliminary scanning process for the work discussed in this thesis, it became desirable to systematically investigate the EinScan-SP scanner settings to develop a reliable method for generating good quality scan data. To achieve the essential success criteria outlined in Section 2.9, it was necessary to ensure the scan data being used to design the implants further along the workflow was as accurate as possible with the scanner technology available.

The aim of this chapter was to evaluate the EinScan-SP 3D scanner settings to determine the settings that produce good quality scan output, to fulfil project objective 1. The aim was achieved by the following objectives:

1. Evaluate the effect of turntable step frequency on the dimensional accuracy of the 3D scan model produced
2. Investigate the effect of the colour of the scanned object on the dimensional accuracy of the 3D scan model produced

3. Determine the optimum settings for the 3D scanner for dimensional accuracy of the 3D scan model produced

4. Understand the limitations of the EinScan-SP 3D scanner for this project

3.2 Effect of Turntable Step Frequency on Scan Dimensional Accuracy

This work investigated the effect of the frequency of the turntable steps on the scan accuracy and resolution. The EinScan-SP (Shining3D, China) [114] is a structured light 3D scanner (Section 2.6). In its most simple configuration it consists of a scanner 'head' which houses 2 cameras, and a round flat base (bed). The scanner head is originally mounted in a frame which also holds the base. The head can also be mounted separately on a tripod with its conventional attachment, enabling scans from a taller height and more top-down viewing angle. The cable connecting the head to the bed is a length such that it stops the head being outside of the scan distance required by the scanner (standoff distance is 290 to 480 mm [114]). The bed of the scanner can be stationary during the scanning process, or it can rotate (either 180 or 360 degrees) at a set frequency of turntable steps during the scanning process.

Alignment of the point clouds can be manual (undertaken by marking points as coincident on the different scan point clouds) or automatically using settings Turntable Alignment and Coded Turntable Alignment. Coded turntable alignment is suggested to be more accurate as it does not rely on the turntable step accuracy, but on the codes on the bed which remain relative to the model during the scan. Turntable steps alignment relies on the turntable steps being accurate / exactly the same as each other (no step slightly having a bigger or smaller number of degrees).

This preliminary work scanned a section of a bone model (Sawbones, USA) [115] and the aim was to investigate the effect of the frequency of turntable steps of the EinScan-SP 3D scanner on the dimensional accuracy and resolution of the 3D scan output model. A bone model was scanned at various frequencies of turntable steps per one 360-degree revolution of the scanner base plate. The results form the first step towards developing the methodology for in-situ conformal printing onto an 'unknown' object.

3.2.1 Method

A model bone section (Sawbones, USA) [115] of maximum dimensions 81.00 mm (width), 199.90 mm (length), and 45.35 mm (height) was scanned using the EinScan-SP 3D scanner (Shining3D, China) [114]. The truncated end had a sliced defect across the section, of length 30.58 mm and mean width 0.75 mm. This was noted as a 'surface feature' for precise surface geometry investigation. The dimensions were measured with digital Vernier calipers to 2 decimal places.

The bone was scanned at 8, 20, 90, and 180 turntable steps per 360° revolution of the turntable plate. The other settings remained constant: HDR (High Dynamic Range), Turntable Alignment, Texture Scan. HDR brightness offers more accurate scanning output by better capturing the full range of light and dark highlights and shadows when capturing the

object's image. This is especially important for enabling scanning of textured objects or objects with contrasting colours. Texture scan means the colour of the object is also captured. The scanner was mounted in the original frame connected to the turntable, and the device was housed inside a darkbox to reduce the effect of ambient lighting conditions [73, 116] (Figure 3.1).

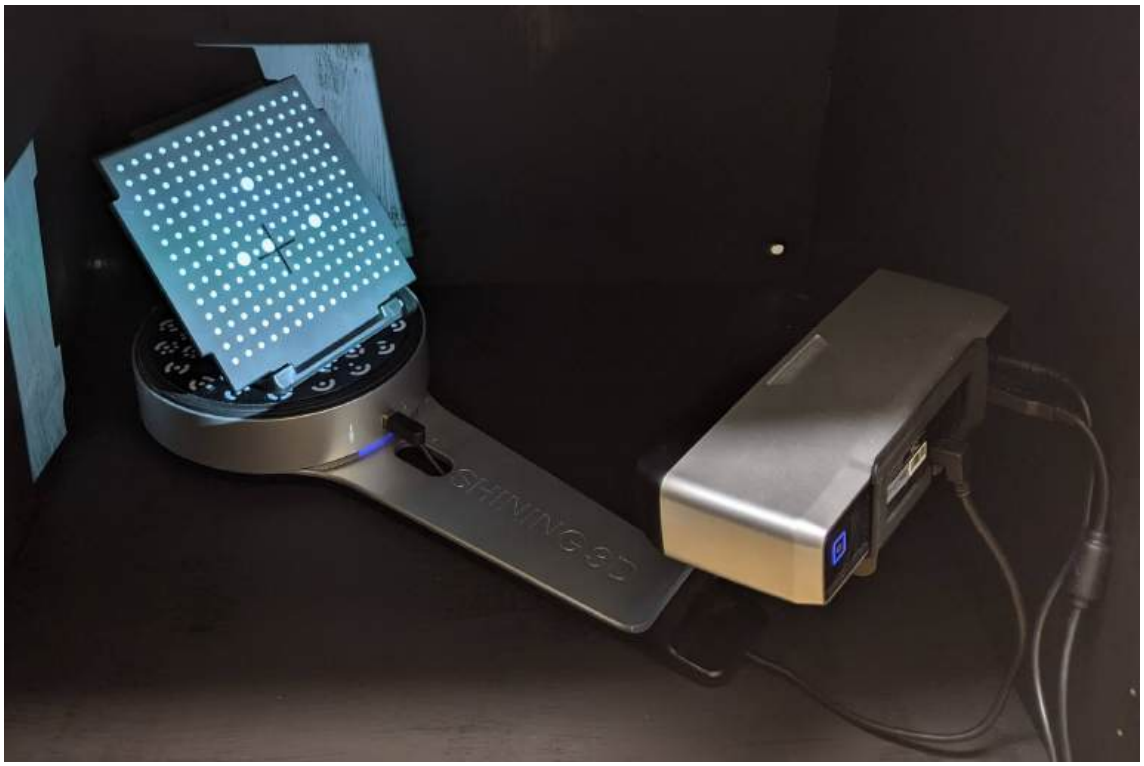

Figure 3.1: The EinScan-SP 3D scanner and turntable in the original mount, with the calibration plate in position on the turntable. The apparatus is housed inside the dark box.

The bone was scanned 3 times at each turntable frequency, for a total of 12 scan models. The companion software for the EinScan-SP (ExScanS V3.0.0.0) was used to record the scan data and convert the point cloud to a mesh - the models were saved as an unwatertight mesh, and a watertight, Medium Detail mesh (Fig. 3.2). An unwatertight mesh connects only the points in the point cloud that are within a certain distance of each other, and does not add in any polygons. A watertight mesh has no holes (missing surface triangles) and no overlaps in the surface. Furthermore, each face has a designated 'inside' and 'outside'. Converting from an unwatertight mesh to a watertight mesh means the software fills in any holes in the model, using the surrounding data to make decisions on how the holes are filled [117, 118]. The watertight models were initially measured to investigate how well the mesh filling abilities of the ExScanS V3.0.0.0 software were able to aid in the areas that were not captured.

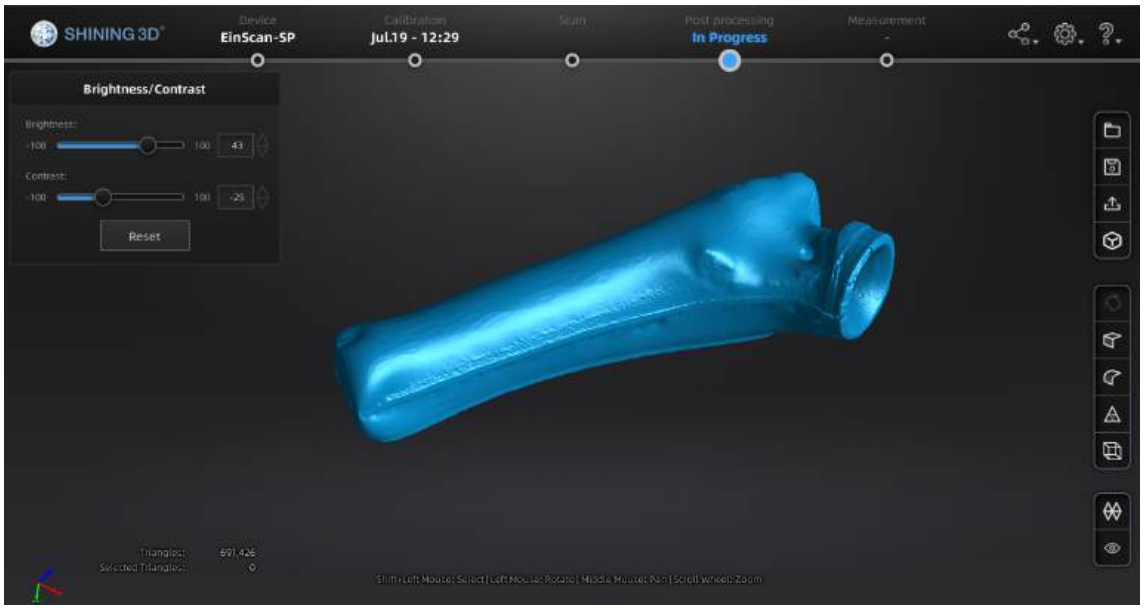

Figure 3.2: Screencapture of the Shining3D software-generated watertight medium detail mesh of the bone model section

The mesh models were saved as .3mf files and exported to Autodesk Meshmixer software (Autodesk, USA) [52] where they were thus converted to .mix files to enable analysis. Meshmixer measuring tool 'Units/Dimensions' was used to determine the overall dimensions of the CAD model (Fig. 3.3), and the tool 'Measure / point to point' was used to determine the length of the recognisable surface feature (Fig. 3.4). The X and Z axes measure the maximum length and width of the model, and the Y axis measures the maximum height of the model. The scan model measurements were compared to the caliper measurements to examine the dimensional accuracy of the scan. The physical and scan models were compared by overall height, width, and length, as well as the length of the surface feature.

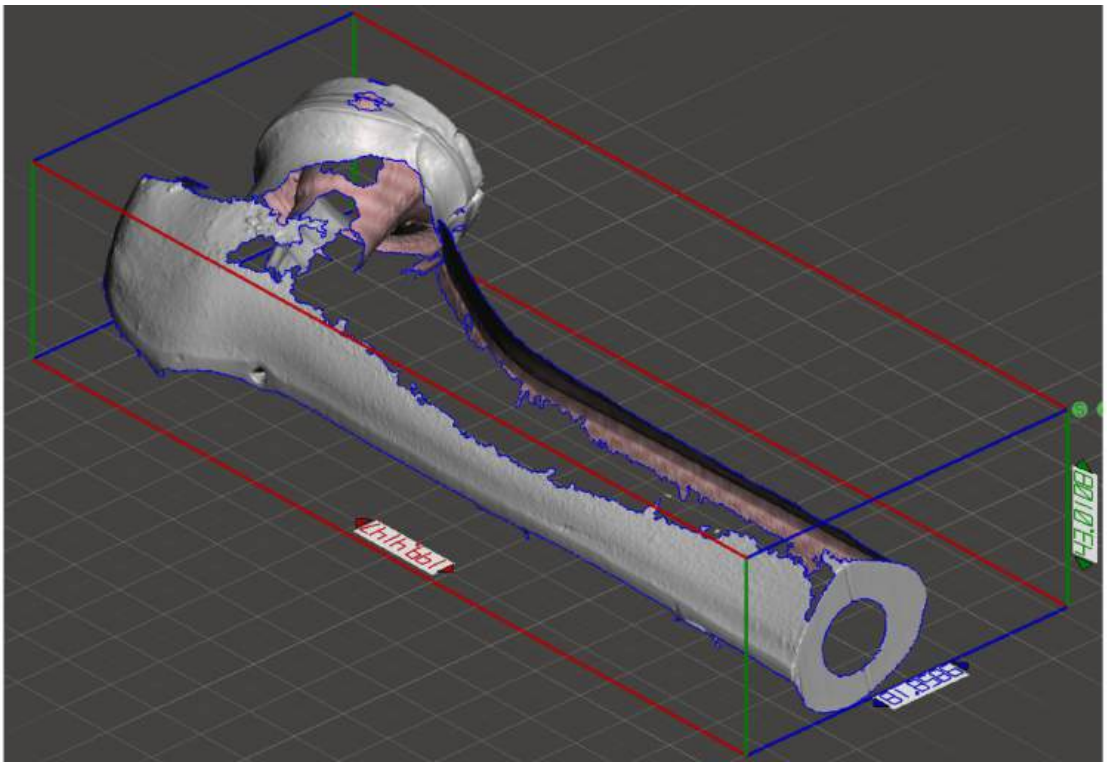

Figure 3.3: The 3D scanned unwatertight mesh model measured in Meshmixer.

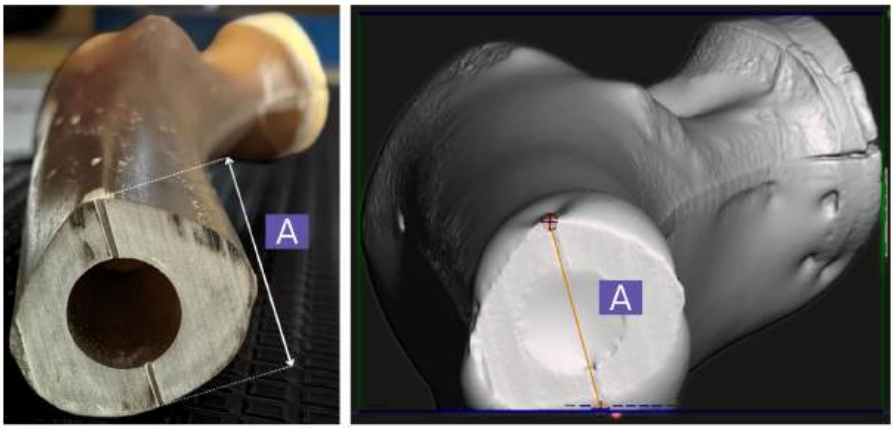

Figure 3.4: Left: Model from the truncated end. The surface feature length is labelled 'A'. Right: The medium watertight 3D model in Meshmixer. The surface feature is outlined with the 'point to point' measuring tool and labelled 'A'.

3.2.2 Statistical Analysis

Primary statistical analysis using One-Way ANOVA was performed to determine if the scanned dimensions for each turntable frequency setting belong to different populations, i.e. are significantly different, $p < 0.05$. If found significant by the One-Way ANOVA testing, further statistical tests were undertaken to find which scan models were significantly different from one another, and to suggest whether the difference was likely to be due to the effect of

the independent variable (or another variable, or error). Tukey's Honestly Significant Difference (HSD) test suggests which of the groups of samples were significantly different to each other. If found to be different, Cohen's f test and the Omega Squared test were undertaken to suggest the size of the effect of the independent variable on this outcome. Further explanation of the statistical formulae used can be found in Appendix A.

3.2.3 Results

Maximum Width Dimensional Accuracy

The average dimension of maximum width of the scan models was compared to the measured maximum width of the bone model. Figure 3.5 presents the maximum width dimensions of the scanned models at the various turntable step frequencies (8, 20, 90, 180), for both the unwatertight meshes and the medium-detail watertight meshes. The figure also presents the model caliper maximum width measurement as a reference line (dark blue) at 81.00 mm. All the scans had a greater maximum width measurement than the bone model.

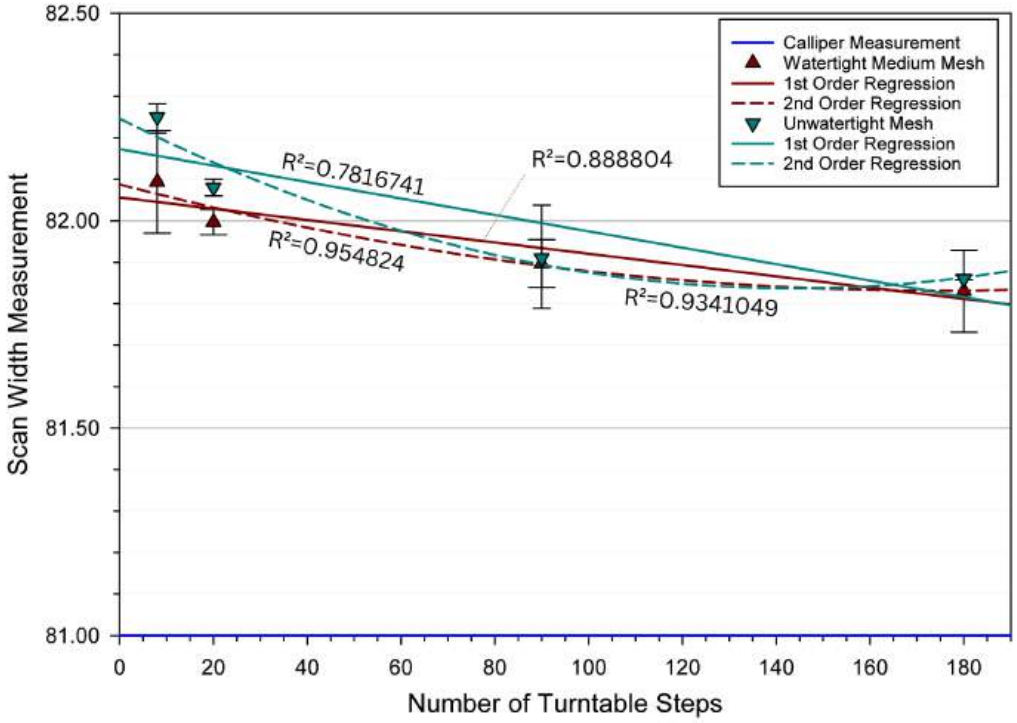

Figure 3.5: Maximum width dimensions. Watertight Mesh: first order regression line of $y = (82.06 \pm 0.15) + (-0.0014 \pm 0.0015)x$ (95% confidence), $R^2 = 0.89$; second order regression line of $y = (82.09 \pm 0.49) + (-0.0029 \pm 0.016)x + (0.0000084 \pm 0.000084)x^2$ (95% confidence), $R^2 = 0.95$. Unwatertight Mesh: first order regression line of $y = (82.17 \pm 0.32) + (-0.0020 \pm 0.0032)x$ (95% confidence), $R^2 = 0.78$; second order regression line of $y = (82.25 \pm 0.91) + (-0.0057 \pm 0.030)x + (0.000020 \pm 0.00016)x^2$ (95% confidence), $R^2 = 0.93$. Caliper measurement (dark blue). Error bars are standard deviation.

Table 3.1: Maximum width of the unwatertight mesh models compared to the caliper measurement, 81.00 mm.

Turntable Step Frequency	Mean Maximum Width (mm)	Difference (mm)	Difference (%)
8	82.23	+1.23	+1.52
20	82.08	+1.08	+1.33
90	82.02	+1.02	+1.26
180	81.88	+0.88	+1.09
All models	82.05	+1.05	+1.30

Considering the unwatertight mesh models, Figure 3.5 presents a first order trendline (green solid) which suggests that the maximum width measurement decreased, towards the caliper measurement, as turntable step frequency was increased. The second order trendline (green dotted) also suggests that the maximum width measurement decreased towards the caliper measurement as the frequency increased, but possibly began to plateau between 90 and 180.

Statistical analysis was undertaken to examine whether the change in maximum width measurement was significant and able to be attributed to the change in turntable step frequency. One-Way ANOVA testing for the 4 groups suggests a significant difference between the means of at least 2 of the groups. Tukey's HSD test suggests that the means for all groups were significantly different to each other, except for comparison between the scans at 20 turntable steps and 90 turntable steps. Post-hoc testing was performed to investigate the size of the effect of the turntable step frequency on these significantly different means. The Cohen's f test and the Omega Squared test both suggested that the effect of the independent variable (turntable step frequency) on the outcome was large.

Table 3.2: Maximum width of the watertight medium-detail mesh models compared to the caliper measurement, 81.00 mm.

Turntable Step Frequency	Mean Maximum Width (mm)	Difference (mm)	Difference (%)
8	82.09	+1.09	+1.35
20	82.00	+1.00	+1.23
90	81.90	+0.90	+1.11
180	81.83	+0.83	+1.02
All models	81.96	+0.96	+1.19

Considering the watertight medium-detail mesh models, Figure 3.5 presents a first order trendline (red solid) which suggests that the maximum width measurement for the watertight model decreased, towards the caliper measurement, as turntable step frequency was increased. The second order trendline (red dotted) also suggests that the maximum width measurement decreased towards the caliper measurement as the frequency increased, but with a shallower gradient, possibly beginning to plateau from 180.

Statistical analysis was undertaken to examine whether the change in maximum width measurement was significant and able to be attributed to the change in turntable step frequency. One-Way ANOVA testing for the 4 groups suggests a significant difference between the means of at least 2 of the groups. Tukey's HSD test suggests that the means for the groups scanned at 8 and 180 turntable step frequency were significantly different from one another, while every other group combination was found to be not significantly different. The Cohen's f test and the Omega Squared test both suggested that the effect of the independent variable (turntable step frequency) on the outcome was large.

Maximum Length Dimensional Accuracy

The average dimension of maximum length of the scan models was compared to the measured maximum length of the bone model. Figure 3.6 presents the maximum length dimensions of the scanned models at the various turntable step frequencies (8, 20, 90, 180), for both the unwatertight meshes and the medium-detail watertight meshes. The figure also presents the model caliper maximum length measurement as a reference line (dark blue) at 199.90 mm. All the scans had a smaller maximum length measurement than the bone model.

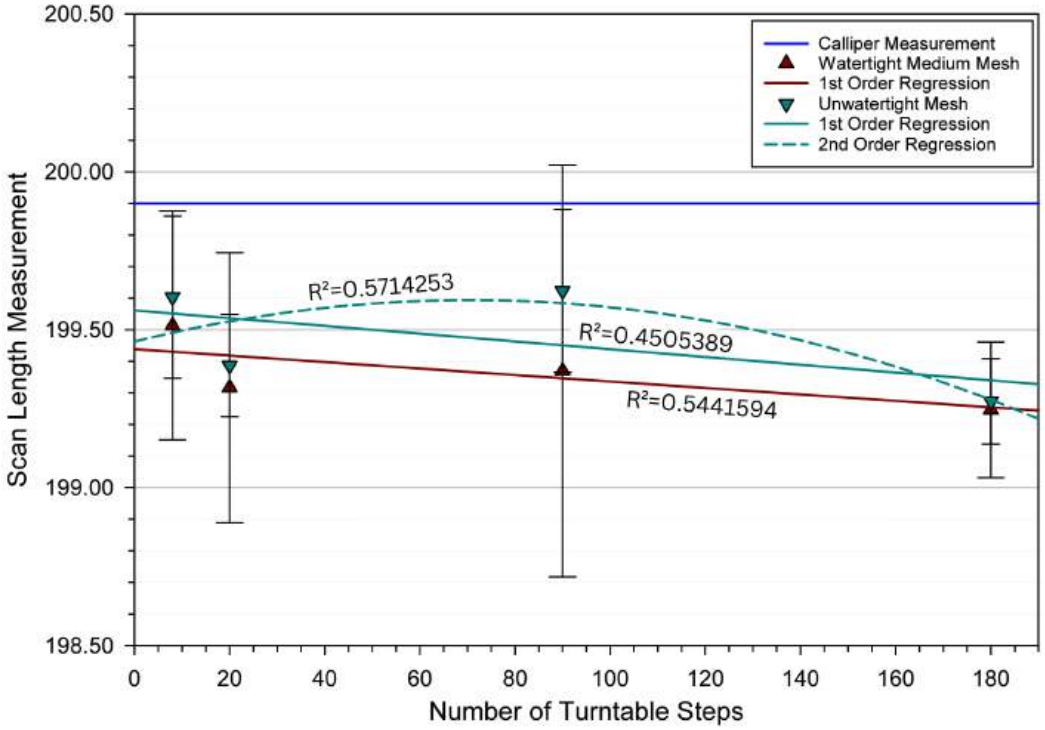

Figure 3.6: Maximum length dimensions. Watertight Mesh: first order regression line of $y = (199.44 \pm 0.29) + (-0.0010 \pm 0.0029)x$ (95% confidence), $R^2 = 0.54$. Unwatertight Mesh: first order regression line of $y = (199.57 \pm 0.47) + (-0.0014 \pm 0.0046)x$ (95% confidence), $R^2 = 0.45$; second order regression line of $y = (199.51 \pm 2.14) + (0.0017 \pm 0.071)x + (-0.000016 \pm 0.00037)x^2$ (95% confidence), $R^2 = 0.57$. Error bars are standard deviation. Caliper measurement (dark blue).

Table 3.3: Maximum length of the unwatertight mesh models compared to the caliper measurement, 199.90 mm.

Turntable Step Frequency	Mean Maximum Length (mm)	Difference (mm)	Difference (%)
8	199.63	-0.27	-0.14
20	199.39	-0.51	-0.26
90	199.56	-0.34	-0.17
180	199.27	-0.63	-0.32
All models	199.46	-0.44	-0.22

Considering the unwatertight mesh models, Figure 3.6 presents a first order trendline (green solid) that suggests that the maximum length measurement decreased, away from the caliper measurement, as turntable step frequency was increased. The second order trendline (green dotted) could present a hyperbolic curve, further from the caliper measurement at the extremes and closer at frequency 90. Conversely, it could present a plateau between 8 and 90, before decreasing away from the caliper measurement at 180. One-Way ANOVA testing for the 4 groups suggests no significant difference between the means of any of the groups.

Table 3.4: Maximum length of the watertight medium-detail mesh models compared to the caliper measurement, 199.90 mm.

Turntable Step Frequency	Mean Maximum Length (mm)	Difference (mm)	Difference (%)
8	199.51	-0.39	-0.20
20	199.32	-0.58	-0.29
90	199.37	-0.53	-0.27
180	199.25	-0.65	-0.33
All models	199.36	-0.54	-0.27

Considering the watertight medium-detail mesh models, Figure 3.6 presents a first order trendline (red solid) which suggests that the maximum length measurement decreased, away from the caliper measurement, as turntable step frequency was increased. No second order regression line is presented as it did not produce a better fit or better R^2 value. One-Way ANOVA testing for the 4 groups suggests no significant difference between the means of any of the groups.

Maximum Height Dimensional Accuracy

The average dimension of maximum height of the scan models was compared to the measured maximum height of the bone model. Figure 3.7 presents the maximum height dimensions of the scanned models at the various turntable step frequencies (8, 20, 90, 180), for both the unwatertight meshes and the medium-detail watertight meshes. The figure also presents the

model caliper maximum height measurement as a reference line (dark blue) at 45.35 mm.

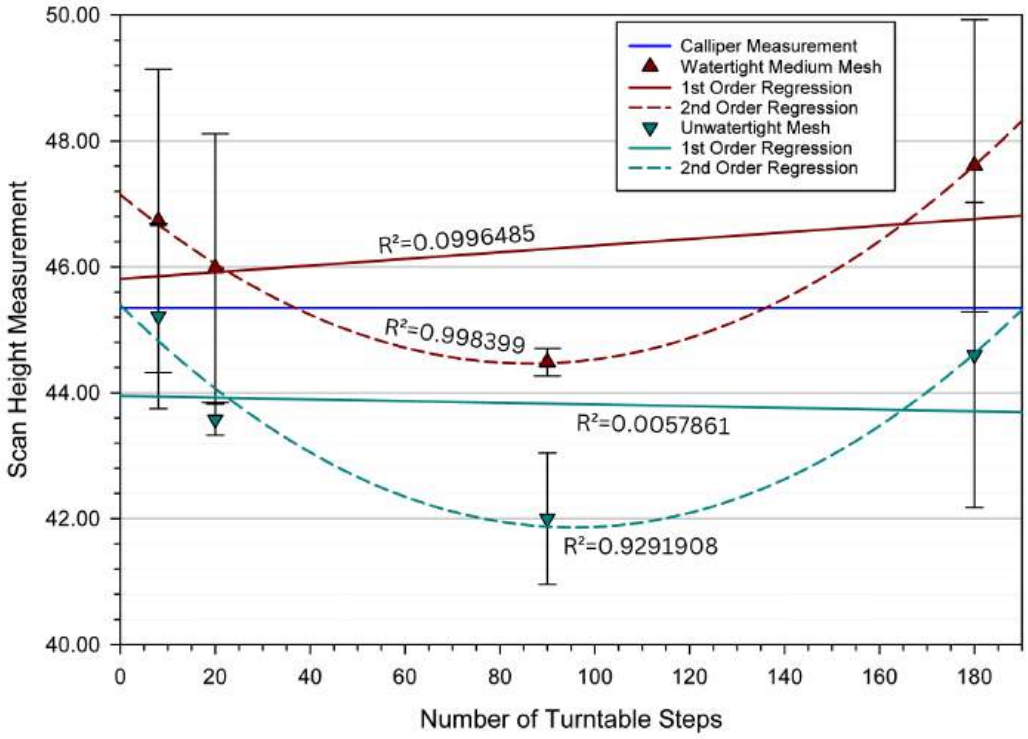

Figure 3.7: Maximum height dimensions. Watertight Mesh: first order regression line of $y = (45.81 \pm 4.87) + (0.0053 \pm 0.048)x$ (95% confidence), $R^2 = 0.10$; second order regression line of $y = (47.15 \pm 1.06) + (-0.062 \pm 0.035)x + (0.00036 \pm 0.00018)x^2$ (95% confidence), $R^2 = 1.00$. Unwatertight Mesh: first order regression line of $y = (43.95 \pm 5.45) + (-0.0014 \pm 0.054)x$ (95% confidence), $R^2 = 0.0058$; second order regression line of $y = (45.39 \pm 7.51) + (-0.074 \pm 0.25)x + (0.00039 \pm 0.0013)x^2$ (95% confidence), $R^2 = 0.93$. Caliper measurement (dark blue). Error bars are standard deviation.

Table 3.5: Maximum height of the unwatertight mesh models compared to the caliper measurement, 45.35 mm.

Turntable Step Frequency	Mean Maximum Height (mm)	Difference (mm)	Difference (%)
8	44.20	-1.15	-2.54
20	43.57	-1.78	-3.93
90	43.36	-1.99	-4.39
180	44.78	-0.57	-1.26
All models	43.98	-1.37	-3.02

Considering the unwatertight medium-detail mesh models, Figure 3.7 presents a first order trendline (green solid) which suggests that the maximum height measurement remained approximately the same at around 43.80 mm, as turntable step frequency was increased. This is smaller than the caliper height measurement. The second order trendline (green dotted)

presents a hyperbolic curve where the extremes are closer to the caliper measurement, and further away at a frequency of 90 steps. One-Way ANOVA testing for the 4 groups suggests no significant difference between the means of any of the groups.

Table 3.6: Maximum height of the watertight medium-detail mesh models compared to the caliper measurement, 45.35 mm.

Turntable Step Frequency	Mean Maximum Height (mm)	Difference (mm)	Difference (%)
8	46.73	+1.38	+3.04
20	45.98	+0.63	+1.39
90	44.49	-0.86	-1.90
180	47.61	+2.26	+4.98
All models	46.20	+0.85	+1.87

Considering the watertight medium-detail mesh models, Figure 3.7 presents a first order trendline (red solid) which suggests that the maximum height measurement increased, away from the caliper measurement, as turntable step frequency was increased. The second order trendline (red dotted) presents a hyperbolic curve with the scan being larger at the frequency extremes, and smaller than the caliper measurement at frequency 90. One-Way ANOVA testing for the 4 groups suggests no significant difference between the means of any of the groups.

Surface Feature Dimensional Accuracy

The average dimension of the surface feature length of the scan models were compared to the measured surface feature length of the bone model. Figure 3.8 presents the surface feature length dimensions of the scanned models at the various turntable step frequencies (8, 20, 90, 180), for both the unwatertight meshes and the medium-detail watertight meshes. The figure also presents the model caliper surface feature length measurement as a reference line (dark blue) at 30.58 mm. Most of the scans had a smaller surface feature length measurement than the bone model.

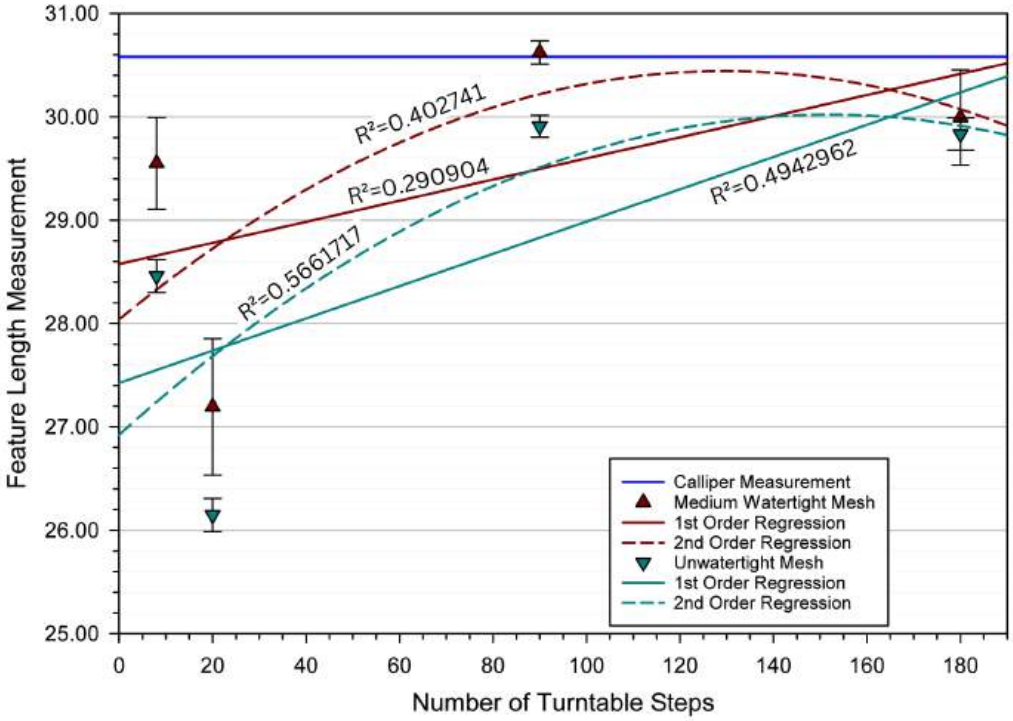

Figure 3.8: Surface feature lengths. Watertight Mesh: first order regression line of $y = (28.58 \pm 4.90) + (0.010 \pm 0.048)x$ (95% confidence), $R^2 = 0.29$, second order regression line of $y = (28.04 \pm 23.21) + (0.037 \pm 0.77)x + (-0.00014 \pm 0.0040)x^2$ (95% confidence), $R^2 = 0.40$; Unwatertight Mesh: first order regression line of $y = (27.42 \pm 4.85) + (0.016 \pm 0.048)x$ (95% confidence), $R^2 = 0.49$, second order regression line of $y = (26.92 \pm 23.20) + (0.041 \pm 0.77)x + (-0.00013 \pm 0.0040)x^2$ (95% confidence), $R^2 = 0.57$. Caliper measurement (dark blue). Error bars are standard deviation.

Table 3.7: Surface feature length for the unwatertight mesh models compared to the caliper measurement, 30.58 mm.

Turntable Step Frequency	Mean Surface Feature Length (mm)	Difference (mm)	Difference (%)
8	28.46	-2.12	-6.93
20	26.15	-4.43	-14.49
90	29.91	-0.67	-2.19
180	29.83	-0.75	-2.45
All models	28.59	-1.99	-6.51

Considering the unwatertight mesh models, Figure 3.8 presents a first order trendline (green solid) which suggests that the surface feature length measurement increased, towards the caliper measurement, as turntable step frequency was increased. The second order trendline (green dotted) also suggests that the surface feature length measurement increased towards the caliper measurement as the frequency increased, but possibly began to plateau between 90 and 180.

One-Way ANOVA testing for the 4 groups suggests a significant difference between the means of at least 2 of the groups. Tukey's HSD test suggests that the means for all groups were significantly different to each other, except for comparison between the scans at 90 turntable steps and 180 turntable steps. The Cohen's f test and the Omega Squared test both suggested that the effect of the independent variable (turntable step frequency) on the outcome was large.

Table 3.8: Surface feature length for the watertight medium-detail mesh models compared to the caliper measurement, 30.58 mm.

Turntable Step Frequency	Mean Surface Feature Length (mm)	Difference (mm)	Difference (%)
8	29.55	-1.03	-3.37
20	27.19	-3.39	-11.09
90	30.62	+0.04	+0.13
180	29.99	-0.59	-1.93
All models	29.34	-1.24	-4.05

Considering the watertight medium-detail mesh models, Figure 3.8 presents a first order trendline (red solid) which suggests that the surface feature length measurement increased, towards the caliper measurement, as turntable step frequency was increased. The second order trendline (red dotted) also suggests that the surface feature length measurement increased towards the caliper measurement as the frequency increased, but possibly began to plateau between 90 and 180, or possibly formed a hyperbolic trend with the peak at frequency 90 and the extremes smaller than the caliper measurement.

One-Way ANOVA testing for the 4 groups suggests a significant difference between the means of at least 2 of the groups. Tukey's HSD test suggests that the mean for the group scanned at 20 turntable step frequency was significantly different to all the other group means, while every other group combination was found to be not significantly different. The Cohen's f test and the Omega Squared test both suggested that the effect of the independent variable (turntable step frequency) on the outcome was large.

3.2.4 Discussion

Maximum Width Dimensional Accuracy

All scan width dimensions were greater than the caliper width dimension (81.00 mm). Both the unwatertight and watertight meshes found significantly different groups as the turntable step frequency was varied. Both presented similar trendline patterns - an overall decrease in the scan width dimension, towards the caliper measurement, as the turntable step frequency increased. The second order trendlines both have strong R^2 values (0.95 for watertight mesh, and 0.93 for unwatertight mesh) which suggest the patterns fits the data points well. Furthermore, the standard deviations presented are all relatively small.

For the unwatertight models, the mean maximum dimension decreased from 82.23 mm (8 steps) to 81.88 mm (180 steps), a change of -0.35 mm. There was a significant difference between all group comparisons, except when comparing scan models at frequency 20 and 90 turntable steps. For the watertight medium-detail models, the mean maximum dimension decreased from 82.09 mm (8 steps) to 81.83 mm (180 mm), a change of -0.26 mm. There was a significant difference between the groups scanned at frequency 8 and 180 only.

This suggests that while the effect of the turntable step frequency on dimensional accuracy is less significant in the middle range of frequency, there is a suggested significant difference in dimensional accuracy when comparing the models scanned at frequency 18 and 180 turntable steps. The scans at frequency 180 were more accurate (the width measurement was closer to the caliper measurement) than the scans at frequency 8. Furthermore, the watertight mesh width was on average found to be more accurate than the unwatertight mesh (+0.96 mm vs +1.05 mm compared to the caliper measurement).

Maximum Length Dimensional Accuracy

All scan length dimensions were smaller than the model's length dimension (199.90 mm). Both the unwatertight and watertight meshes found no significant differences between any of the groups as the turntable step frequency was varied. All the trendlines presented had medium to weak R^2 values (0.45 to 0.57), suggesting poor fit to the data. Furthermore, Figure 3.6 presents relatively large error bars, suggesting large variance within the groups, possibly due to measuring error.

For the unwatertight models, the mean maximum dimension was 199.46 mm, a difference of -0.44 mm compared to the caliper measurement. For the watertight medium-detail models, the mean maximum dimension was 199.36 mm, a difference of -0.54 mm compared to the caliper measurement. Thus the unwatertight model was more accurate in length measurement. This data suggests that there is no effect of the turntable step frequency on the dimensional accuracy of the lengthwise measurement.

Maximum Height Dimensional Accuracy

Scan height dimensions were more variable than the other dimensions, and this potentially contributed to the One-Way ANOVA testing finding no significant difference between any of the turntable step frequencies, due to large in-group variance. Unsurprisingly, the unwatertight mesh models had mean maximum height dimensions smaller than the caliper measurement, and smaller than the watertight medium-detail mesh models. The mean for all the unwatertight models was 43.98 mm, 1.37 mm smaller than the mean calliper measurement. The maximum height measurements for the watertight mesh models had a mean of 46.20 mm, 0.85 mm larger than the mean caliper measurement. This suggests that the watertight mesh models were more accurate, however the large variance within the data set questions the reliability of this inference.

As can be seen in Figures 3.9 and 3.10, the top surface of the model was almost entirely missing from the captured data points. Despite the top surface being the geometry of interest in the scanning process, regardless of brightness settings or positioning of scanner camera

relative to the top surface, it was never captured fully. The top surface geometry generated in the watertight mesh is visually very variable in shape and maximum height, which is explained by the lack of data the model had to generate the surface from.

Surface Feature Dimensional Accuracy

Almost all scans had surface feature lengths smaller than the caliper measurement (30.58 mm). The unwatertight and watertight meshes both found significantly different groups as the turntable step frequency was varied. Both also presented similar trendline patterns, an increase in the scan feature length measurement, towards the caliper measurement, from frequency 8 to 90, and then a possible plateau close to the caliper measurement from frequency 90 to 180. All trendlines have weak R^2 values (0.29 to 0.57) which suggests they do not fit the presented data well, however, the standard deviations are mostly relatively small which suggests small variation within the groups.

For the unwatertight models, there was a significant difference between all group comparisons, except when comparing the scan models at frequency 90 and 180 turntable steps. This supports an increase to frequency 90 then plateau trendline. For the watertight medium-detail models, there was a significant difference between the group scanned at frequency 20 and every other group. Every other group combination was found to not be significantly different.

The most accurate measurement (regardless of watertight or unwatertight mesh model) was for the models scanned at frequency 90. The surface feature length was the most reliable to measure and compare as it is not dependent on accurate orientation of the overall model. Variability in the measurement appears to stem from variability in the proportion of the truncated end surface that was captured by the scan. The majority of the end face was captured, but the edge was captured to varying amounts. When less of the surface geometry was captured, it decreased the diameter of the face in the scanned model, thereby shortening the length of the surface feature. This is shown visually in Figure. 3.10.

Considering All Measurements

Overall, in analysis of the dimensional accuracy of all the maximum dimension measurements as a group, there are recurring sources of possible variation other than the frequency setting. From Figure 3.10 it can be seen that aligning the unwatertight mesh model to "lie flat" on the virtual surface was prone to increased error due to poor ability of the scanner to capture the geometry on the undermost side of the object. With limited geometry to use as boundaries for aligning the mesh model on the virtual surface, the chance of the model being tilted along its axes is increased, thereby altering the measurement that is taken. While the watertight mesh model had lower surface geometry generated, it was created from the point cloud data that was captured by the scanner, and thus is inaccurate due to being based on incomplete data.

Furthermore, from Figure 3.9 it can be seen that the watertight mesh generated a more uneven surface on the truncated end of the bone model. This surface was also used for alignment for measurement in Meshmixer, so increased variability in this surface would increase the chance of error in aligning the model in the same orientation. This could account for misalignment of the virtual model, and make the comparison of the measurements less

reliable.

All mean maximum measurements fall outside the boundary of the 3D scanner 'accuracy', 0.03 mm. All mean maximum measurements, except the surface feature length for the watertight model at scan frequency 90, fall outside the 0.2 mm boundary (layer height for the 3D printer and 'point distance' for the 3D scanner). Considering the range of the differences (between model and scan) across the turntable frequencies, all values were greater than the 3D scanner accuracy. All were greater than the 0.2 mm boundary, but the mean maximum width and length differences for the watertight models had a range of 0.26 mm for both, which could be considered borderline. Scanner specifications such as point distance and how that might affect scan model geometry are discussed in further depth in Section 3.4.

In conclusion, the following patterns were observed:

- For the maximum width measurement, greater turntable step frequency correlated with more accurate measurement.
- For the maximum length and height measurements, there was no significant difference between the scans at different turntable step frequencies.
- For the surface feature length measurement, a turntable step frequency of 90 produced significantly more accurate measurement.

Therefore, for following investigations, a turntable step frequency of 90 is proposed.

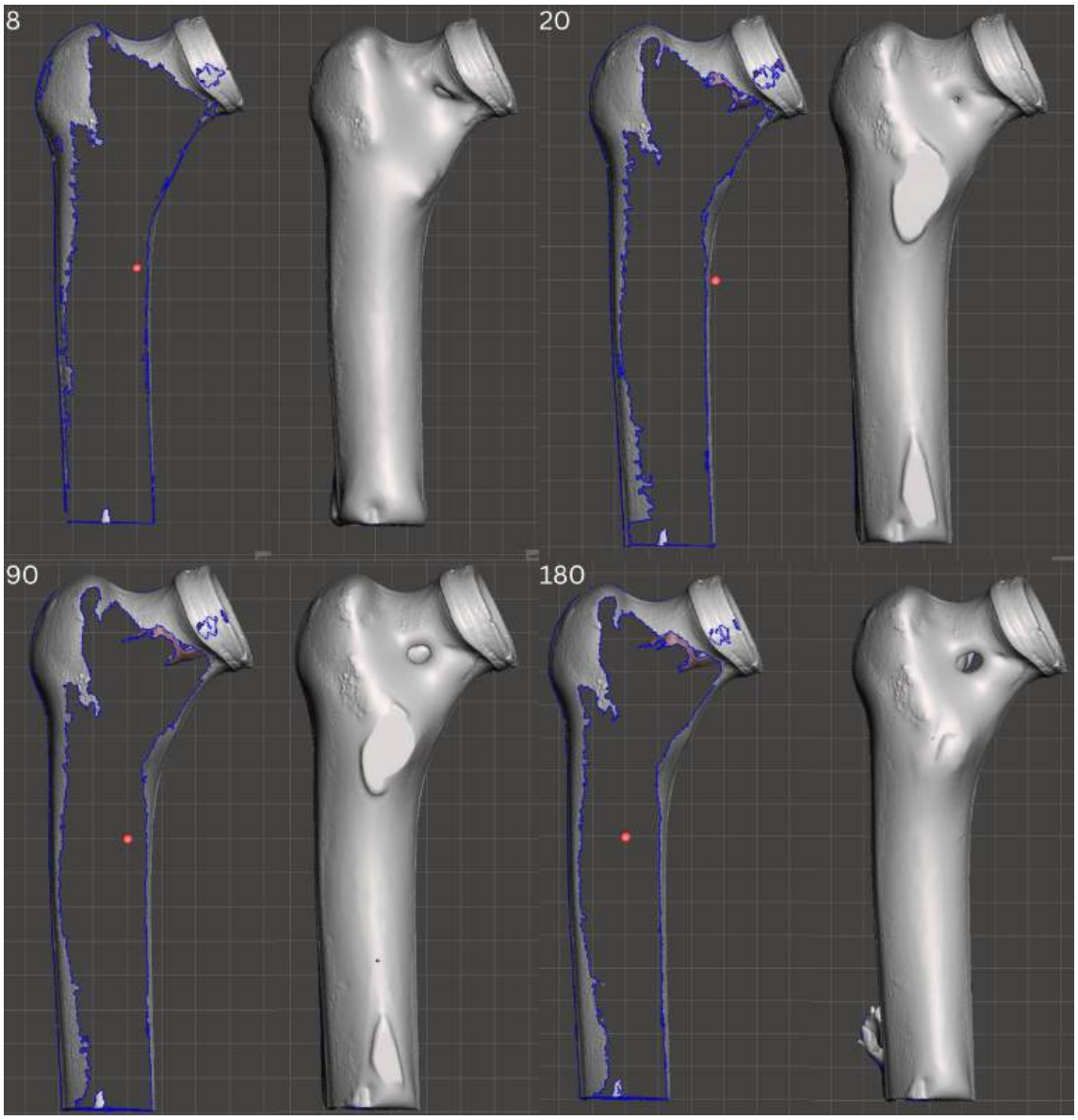

Figure 3.9: Top-down views of the scanned models presented in Meshmixer, for each turntable step frequency (8, 20, 90, 180). The left image for each pair is the unwatertight mesh model, and the right image is the watertight medium-detail mesh model.

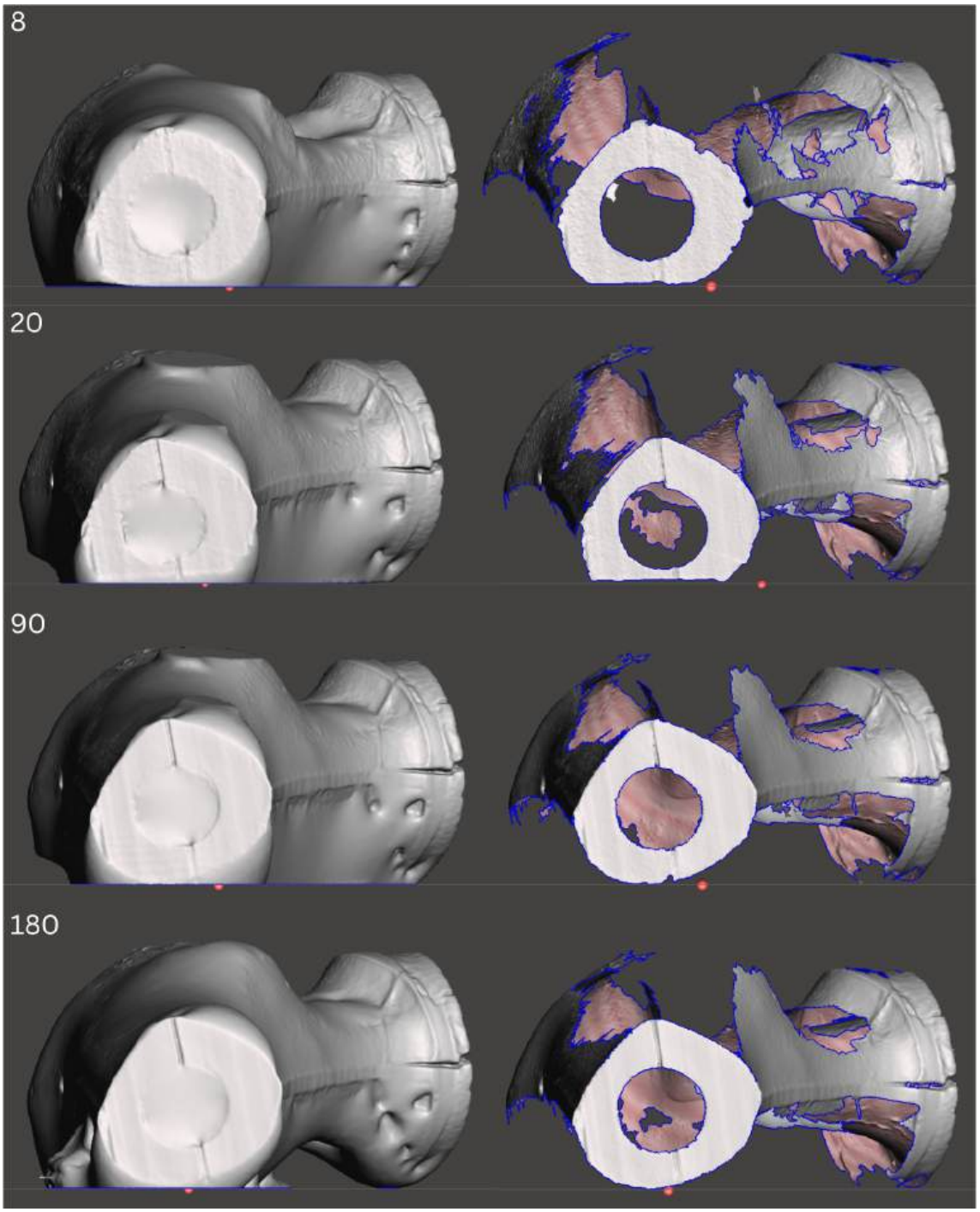

Figure 3.10: Views from the truncated end of the scanned models presented in Meshmixer, for each turntable step frequency (8, 20, 90, 180). The left image for each pair is the watertight medium-detail mesh model, and the right image is the unwatertight mesh model.

3.3 Effect of Object Colour on Scan Dimensional Accuracy

3.3.1 Introduction

Following investigations with the original bone model, it was valuable to investigate the effect of colour of the object being scanned, particularly light and dark surface tones, on the ability of the scanner to capture the geometry of the object, and on the dimensional accuracy of the scanned models generated from the scan data. Furthermore, ExScan software is being regularly updated, and it became valuable to further investigate the effect of the turntable step frequency settings (ExScan V3.1.3.0) on scan dimensional accuracy during this process. The newer version software settings changed the turntable step frequency upper limit from 180 steps to 36 steps, added in a Turntable Speed setting (from 1 to 10), and include the option of selecting a "half" turn of the turntable (180°) alongside the original "one" 360° turn.

3.3.2 Methods

Two bone models from (Sawbones, USA) [115] were scanned using the same EinScan-SP 3D scanner (Shining3D, China) [114]. The dark-colour bone from the investigations in Section 3.2, and a light-colour model bone model of maximum dimensions 78.00 mm (width), 228.00 mm (length), and 60.40 mm (height) (Fig. 3.11). The dimensions were measured with digital Vernier calipers to 2 decimal places.

Figure 3.11: The model bones. Left: dark-colour bone, Right: light-colour bone.

Each bone model was scanned at 8, 17, 26, and 36 turntable steps per 'one turntable turn' (360° revolution of the turntable plate). The other settings remained constant: HDR, turntable coded alignment, non-texture scan, and turntable speed 1. Each object was scanned 3 times at each turntable frequency setting, for a total of 24 scan models. The companion software for the EinScan-SP (ExScanS V3.1.3.0) was used to record the scan data and convert the point cloud to a mesh - the models were saved as an unwatertight mesh.

The mesh models were saved as .3mf files and exported to Autodesk Meshmixer software (Autodesk, USA) [52] where they were thus converted to .mix files to enable analysis. The Meshmixer tool 'Units/Dimensions' was used to determine the overall dimensions of the CAD model (Fig. 3.12). The X and Z axes measure the maximum length and width of the model,

and the Y axis measures the maximum height of the model. The scan model measurements were compared to the caliper measurements to examine the dimensional accuracy of the scan. The physical and scan models were compared by overall height, width, and length. The accuracy of the light and dark models were compared to determine whether the colour had an effect on the scan accuracy.

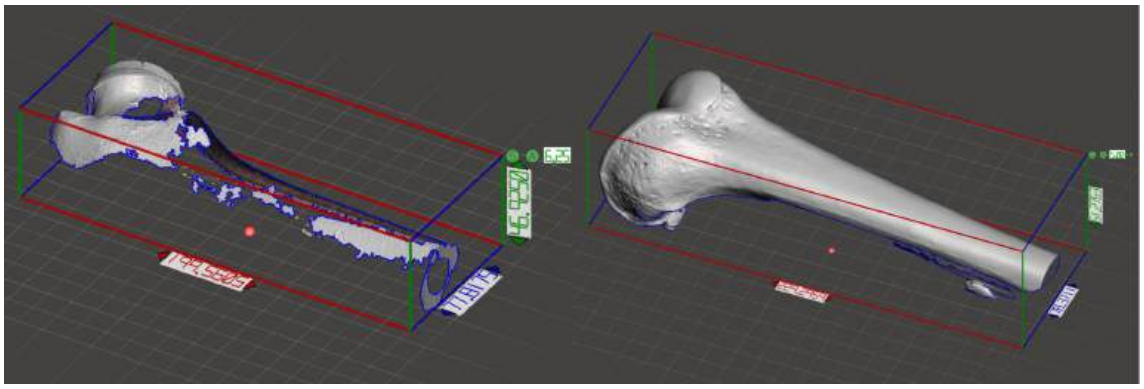

Figure 3.12: Unwatertight mesh models of scanned bone models in Meshmixer. Left: dark-colour bone, Right: light-colour bone.

3.3.3 Statistical Analysis

Primary statistical analysis using One-Way ANOVA was performed to determine if the scan model dimensions for each turntable frequency setting belong to different populations, i.e. are significantly different, $p < 0.05$. If found significant by the One-Way ANOVA testing, further statistical tests were undertaken to find which scan models were significantly different from one another, and to suggest whether the difference was likely to be due to the effect of the independent variable (or another variable, or error). Tukey's HSD test suggests which of the groups of samples were significantly different to each other. If found to be different, Cohen's f test and the Omega Squared test were undertaken to suggest the size of the effect of the independent variable on this outcome. Further explanation of the statistical formulae used can be found in Appendix A.

3.3.4 Results

Maximum Width Dimensional Accuracy

The average maximum width dimensions of the scan models were compared to the measured maximum widths of the bone models. The following figures present the maximum width dimensions of the bone scan models at the various turntable step frequencies (8, 17, 26, 36).

Light colour bone

Figure 3.13 and Table 3.9 present the light-colour bone data. A first order trendline (green solid) (Figure 3.13) suggests that the maximum width measurement decreased as turntable step frequency was increased. The second order trendline (red solid) also suggests that the maximum width measurement decreased as the frequency increased, but possibly remained

fairly constant between 8 and 26 turntable step frequency before decreasing as the frequency increased to 36 steps. One-Way ANOVA testing for the 4 groups suggests no significant difference between the means of any of the groups.

Table 3.9: Maximum width of the light colour bone scan models compared to the caliper measurement, 78.00 mm

Turntable Step Frequency	Mean Maximum Width (mm)	Difference (mm)	Difference (%)
8	78.36	+0.36	+0.46
17	78.35	+0.35	+0.45
26	78.33	+0.33	+0.42
36	78.17	+0.17	+0.22
All models	78.30	+0.30	+0.38

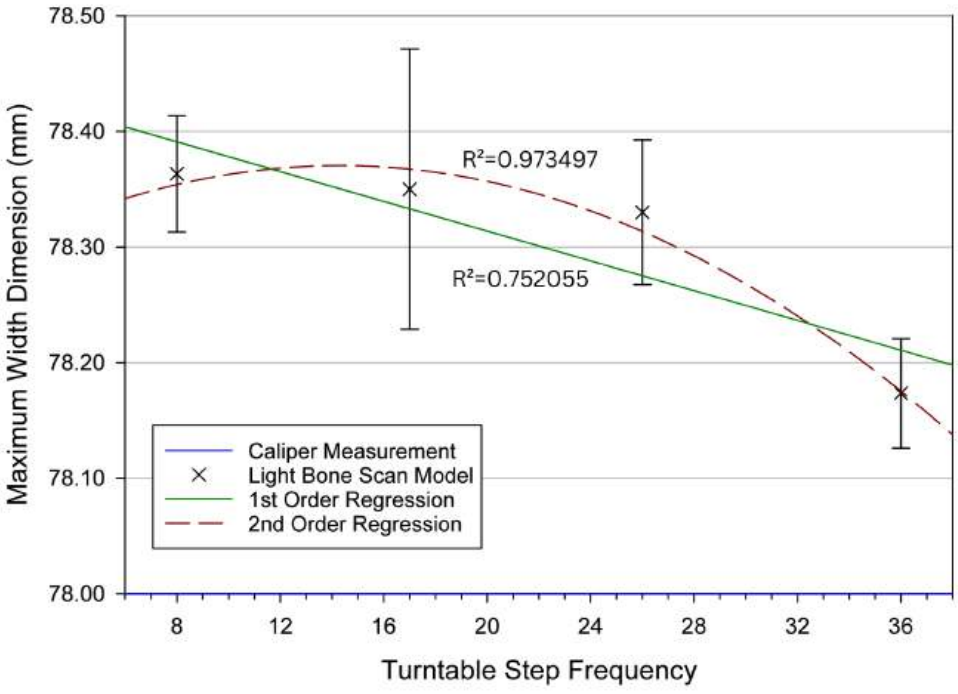

Figure 3.13: Maximum width dimension of the light bone scan models. First order regression line of $y = (78.443 \pm 0.271) + (-0.00644 \pm 0.0112)x$ (95% confidence), $R^2 = 0.75$. Second order regression line of $y = (78.286 \pm 0.740) + (0.0118 \pm 0.0774)x + (-0.000414 \pm 0.00172)x^2$ (95% confidence), $R^2 = 0.97$. Caliper measurement (dark blue). Error bars are standard deviation.

Dark colour bone

Figure 3.14 and Table 3.10 present the dark-colour bone data. A first order trendline (green solid) (Figure 3.14) suggests that the maximum width measurement increased slightly as

turntable step frequency was increased. The second order trendline (red dotted) presents a hyperbolic U curve with a minimum dimension between 17 and 26 turntable step frequency. One-Way ANOVA testing for the 4 groups suggests no significant difference between the means of any of the groups.

Table 3.10: Maximum width of the dark colour bone scan models compared to the caliper measurement, 81.00 mm

Turntable Step Frequency	Mean Maximum Width (mm)	Difference (mm)	Difference (%)
8	77.59	-3.41	-4.21
17	76.81	-4.19	-5.17
26	77.71	-3.29	-4.06
36	77.40	-3.60	-4.44
All models	77.38	-3.62	-4.47

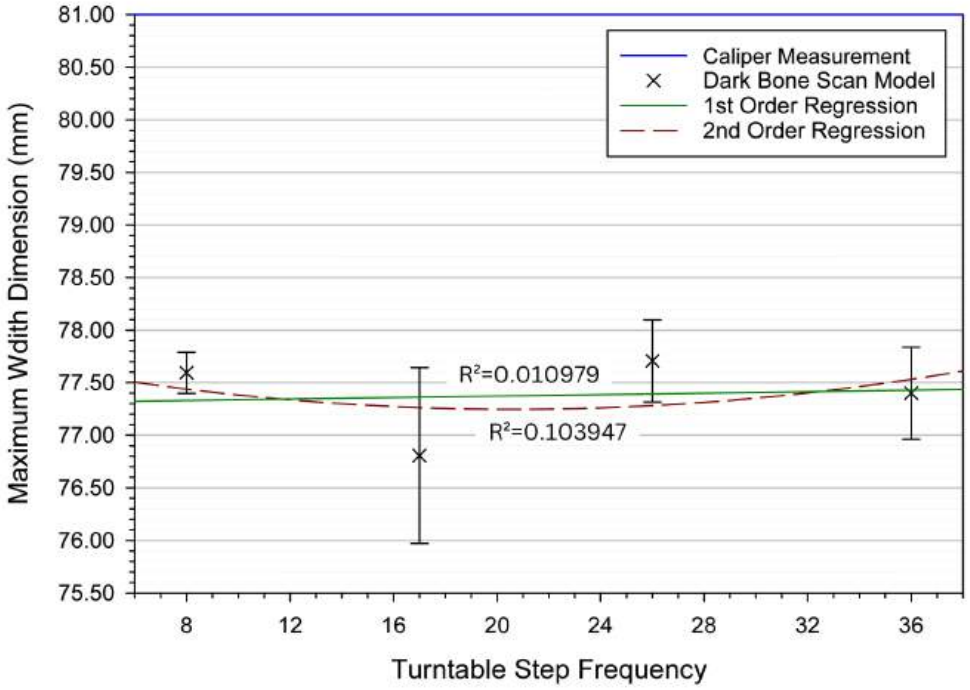

Figure 3.14: Maximum width dimension of dark bone scan models. First order regression line of $y = (77.302 \pm 2.420) + (0.003484 \pm 0.1004)x$ (95% confidence), $R^2 = 0.01$. Second order regression line of $y = (77.756 \pm 19.263) + (-0.04948 \pm 2.015)x + (0.001201 \pm 0.04486)x^2$ (95% confidence), $R^2 = 0.10$. Caliper measurement (dark blue). Error bars are standard deviations.

Maximum Length Dimensional Accuracy

The average dimensions of maximum length of the scan models were compared to the measured maximum lengths of the bone model.

Light colour bone

Figure 3.15 and Table 3.11 present the maximum length dimensions of the scanned models at the various turntable step frequencies (8, 17, 26, 36). A first order trendline (green solid) (Figure 3.15) suggests that the maximum length measurement was fairly constant but slightly increased as turntable step frequency was increased. The second order trendline (red solid) presents a hyperbolic trendline, with the smallest measurements at the extremes, and the largest measurement close to 26 turntable step frequency. One-Way ANOVA testing for the 4 groups suggests no significant difference between the means of any of the groups.

Table 3.11: Maximum length of the light colour bone scan models compared to the caliper measurement, 228.00 mm

Turntable Step Frequency	Mean Maximum Length (mm)	Difference (mm)	Difference (%)
8	229.13	+1.13	+0.50
17	229.27	+1.27	+0.56
26	229.20	+1.20	+0.53
36	229.20	+1.20	+0.53
All models	229.20	+1.20	+0.53

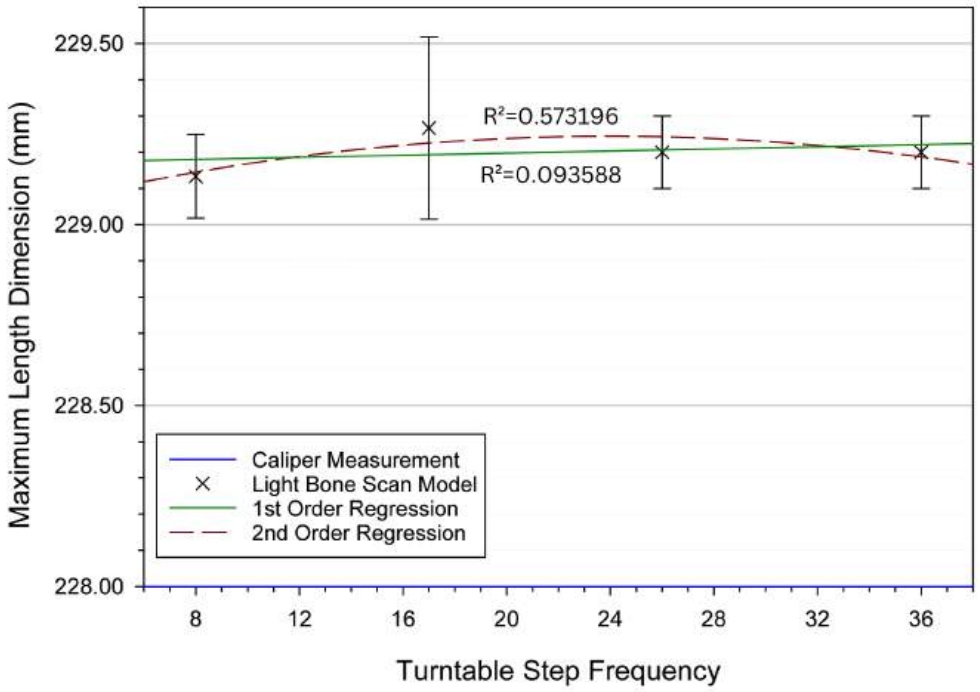

Figure 3.15: Maximum Length dimension of white bone scan models. First order regression line of $y = (229.168 \pm 0.332) + (0.00146 \pm 0.0138)x$ (95% confidence), $R^2 = 0.09$. Second order regression line of $y = (229.021 \pm 1.903) + (0.0187 \pm 0.199)x + (-0.000390 \pm 0.00443)x^2$ (95% confidence), $R^2 = 0.57$. Caliper measurement (dark blue). Error bars are standard deviation.

Dark colour bone

Figure 3.16 and Table 3.12 present the maximum length dimensions of the dark-colour bone models at the various turntable step frequencies (8, 17, 26, 36).
A first order trendline (green solid) (Figure 3.16) suggests that the maximum length measurement decreased as turntable step frequency was increased. The second order trendline (red dotted) presents a hyperbolic curve with a maximum dimension between 17 and 26 turntable step frequency. One-Way ANOVA testing for the 4 groups suggests no significant difference between the means of any of the groups.

Table 3.12: Maximum length of the dark colour bone scan models compared to the caliper measurement, 199.90 mm

Turntable Step Frequency	Mean Maximum Length (mm)	Difference (mm)	Difference (%)
8	199.58	-0.32	-0.16
17	199.53	-0.37	-0.19
26	199.71	-0.19	-0.10
36	199.48	-0.42	-0.21
All models	199.58	-0.32	-0.16

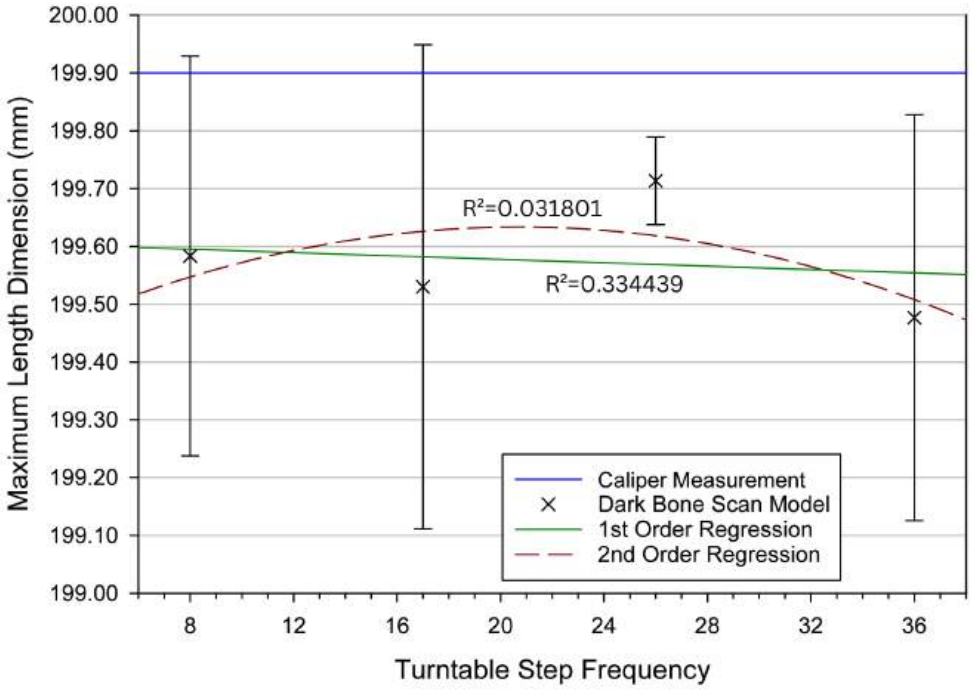

Figure 3.16: Maximum length dimension of dark bone scan models. First order regression line of $y = (199.607 \pm 0.5926) + (-0.001467 \pm 0.02458)x$ (95% confidence), $R^2 = 0.03$. Second order regression line of $y = (199.404 \pm 4.109) + (0.02219 \pm 0.4298)x + (-0.0005363 \pm 0.009569)x^2$ (95% confidence), $R^2 = 0.33$. Caliper measurement (dark blue). Error bars are standard deviation.

Maximum Height Dimensional Accuracy

The average dimensions of maximum height of the scan models were compared to the measured maximum heights of the bone models.

Light colour bone

Figure 3.17 and Table 3.13 present the maximum height dimensions of the light-colour scanned models at the various turntable step frequencies (8, 17, 26, 36). A first order trendline (green solid) (Figure 3.17) suggests that the maximum height measurement decreased as turntable step frequency was increased. The second order trendline (red dotted) also suggests that the maximum height measurement decreased as the frequency increased, or possibly remained fairly constant between 8 and 26 turntable step frequency before decreasing as the frequency increased to 36 steps. One-Way ANOVA testing for the 4 groups suggests no significant difference between the means of any of the groups.

Table 3.13: Maximum height of the light colour bone scan models compared to the caliper measurement, 60.40 mm

Turntable Step Frequency	Mean Maximum Width (mm)	Difference (mm)	Difference (%)
8	61.29	+0.89	+1.47
17	61.17	+0.77	+1.27
26	61.19	+0.79	+1.31
36	60.92	+0.52	+0.86
All models	61.14	+0.74	+1.23

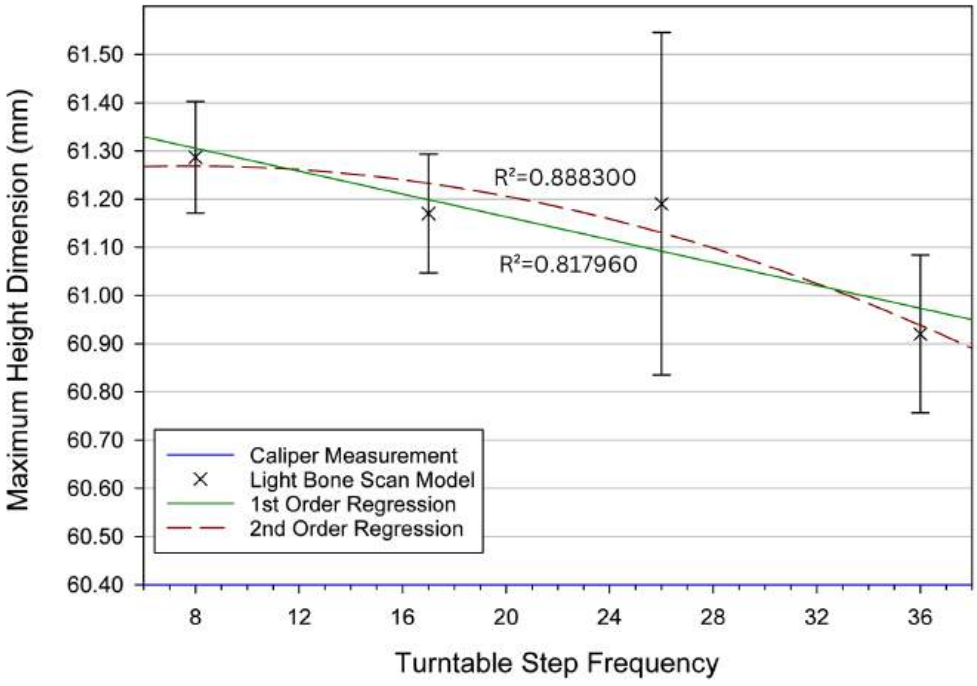

Figure 3.17: Maximum height dimension of white bone scan models. First order regression line of $y = (61.400 \pm 0.409) + (-0.0118 \pm 0.0170)x$ (95% confidence), $R^2 = 0.82$. Second order regression line of $y = (61.245 \pm 2.680) + (0.00631 \pm 0.280)x + (-0.000412 \pm 0.00624)x^2$ (95% confidence), $R^2 = 0.89$. Caliper measurement (dark blue). Error bars are standard deviation.

Dark colour bone

Figure 3.18 and Table 3.14 present the maximum width dimensions of the scanned models at the various turntable step frequencies (8, 17, 26, 36).
A first order trendline (green solid) (Figure 3.18) suggests that the maximum height measurement remained relatively constant as the turntable step frequency was increased. The second order trendline (red dotted) presents a hyperbolic curve with the smallest dimensions at the frequency extremes, and the greatest dimension between frequencies 17 and 26. One-Way ANOVA testing for the 4 groups suggests no significant difference between the

means of any of the groups.

Table 3.14: Maximum height of the dark colour bone scan models compared to the caliper measurement, 45.35 mm

Turntable Step Frequency	Mean Maximum Width (mm)	Difference (mm)	Difference (%)
8	47.88	+2.53	+5.58
17	49.18	+3.83	+8.45
26	47.85	+2.50	+5.51
36	48.37	+3.02	+6.66
All models	48.32	+2.97	+6.55

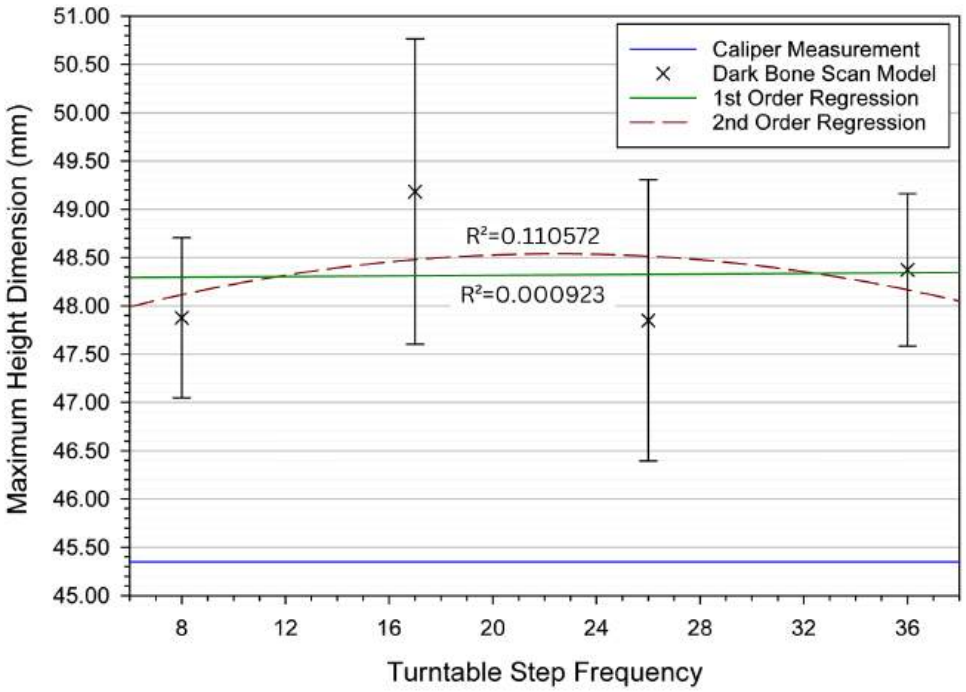

Figure 3.18: Maximum height dimension of dark bone scan models. First order regression line of $y = (48.286 \pm 3.782) + (0.001571 \pm 0.1569)x$ (95% confidence), $R^2 = 0.00$. Second order regression line of $y = (47.519 \pm 29.845) + (0.09102 \pm 3.121)x + (-0.002028 \pm 0.06950)x^2$ (95% confidence), $R^2 = 0.11$. Caliper measurement (dark blue). Error bars are standard deviation.

3.3.5 Discussion

Maximum Width Dimensional Accuracy

For the light bone model, the mean maximum width dimension of the scan was 78.30 mm, larger than the caliper measurement by 0.30 mm (0.38 %). The error bars range from approximately 0.05 mm to 0.15 mm each side. For the dark bone model, the mean maximum width dimension of the scan was 77.38 mm, 3.62 mm smaller than the caliper measurement (4.47 %). As well as an overall larger difference in dimension (both in true measurement, and as a percentage difference of the caliper measurement), the dark bone scan models also had larger error bars (Figure 3.14), ranging from 0.2 mm to 0.8 mm each side.

Maximum Length Dimensional Accuracy

For the light bone model, the mean maximum length dimension of the scan was 229.20 mm, larger than the caliper measurement by 1.20 mm (0.53 %). The error bars range from approximately 0.1 mm to 0.25 mm each side.

For the dark bone model, the mean maximum length dimension of the scan was 199.58 mm, 0.32 mm smaller than the caliper measurement (0.16 %). Although for length there was an overall smaller difference in dimension (both in true measurement, and as a percentage difference of the caliper measurement), the dark bone scan models again presented larger error bars for most of the data (Figure 3.16), ranging from 0.05 mm to 0.4 mm each side.

Maximum Height Dimensional Accuracy

For the light bone model, the mean maximum height dimension of the scan was 61.14 mm, larger than the caliper measurement by 0.74 mm (1.23 %). The error bars range from approximately 0.1 mm to 0.35 mm each side. For the dark bone model, the mean maximum height dimension of the scan was 48.32 mm, 2.97 mm larger than the caliper measurement (6.55 %). As well as an overall larger difference in dimension (both in true measurement, and as a percentage difference of the caliper measurement), the dark bone scan models also had larger error bars (Figure 3.18), ranging from 0.75 mm to 1.55 mm each side.

Considering All Measurements

Considering the effect of the turntable step frequency on the dimensional accuracy of the scanned models in the newer version of the software, no significant difference was found when comparing any of the frequency groups. Thus it is suggested that the turntable step frequency has no effect on the dimensional accuracy of the scanned models.

The light-colour bone model generally had more accurate scan model dimensions, and smaller in group variance at each turntable step frequency. This suggests that the colour of the scanned object can have an effect on the dimensional accuracy of its scans, and that the surface geometry of a lighter coloured object is better captured than that of a darker coloured object, for this particular scanner (EinScan-SP). From Figures 3.19 & 3.20 it can be seen that the surface of the lighter colour model was more completely captured. This supports that the

measurements, particularly for height, for the light colour scan model were more reliable than for the dark colour scan model, as there were more data points captured to measure. The light colour bone model still presented difficulties with caliper measurements due to its highly irregular shape, much the same as the dark colour bone model. Furthermore, difficulties were present with alignment in the virtual environment as the lower sides of the model were, again, not captured well.

All mean maximum measurements fall outside the boundary of the 3D scanner 'accuracy', 0.03 mm. All mean maximum measurements, except the light model width (at frequency 36) and the dark model length (at frequency 26), fall outside the 0.2 mm boundary (layer height for the 3D printer and 'point distance' for the 3D scanner). Considering the range of the differences (between model and scan) across the turntable frequencies, all values were greater than the 3D scanner accuracy, for both bone models. For the 0.2 mm boundary, both models' length measurements and the light colour model width were inside the boundary. Both models' height measurements and the dark colour model width fell outside this boundary. Scanner specifications such as point distance and how that might affect scan model geometry are discussed in further depth in Section 3.4.

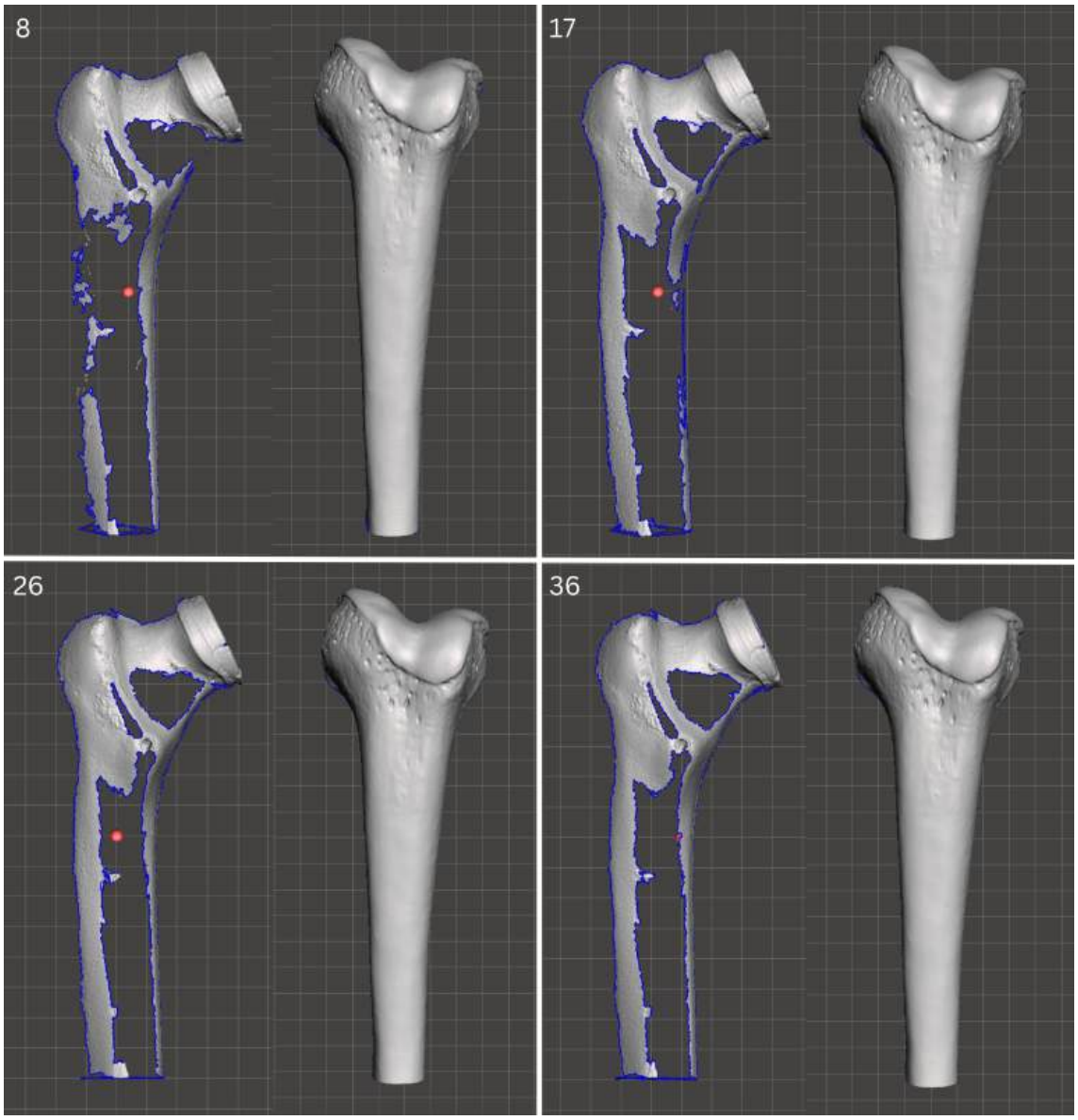

Figure 3.19: Top-down views of the scanned models presented in Meshmixer, for each turntable step frequency (8, 17, 26, 36). The left image for each pair is the unwatertight mesh model for the dark colour bone, and the right image is the unwatertight mesh model for the light colour bone.

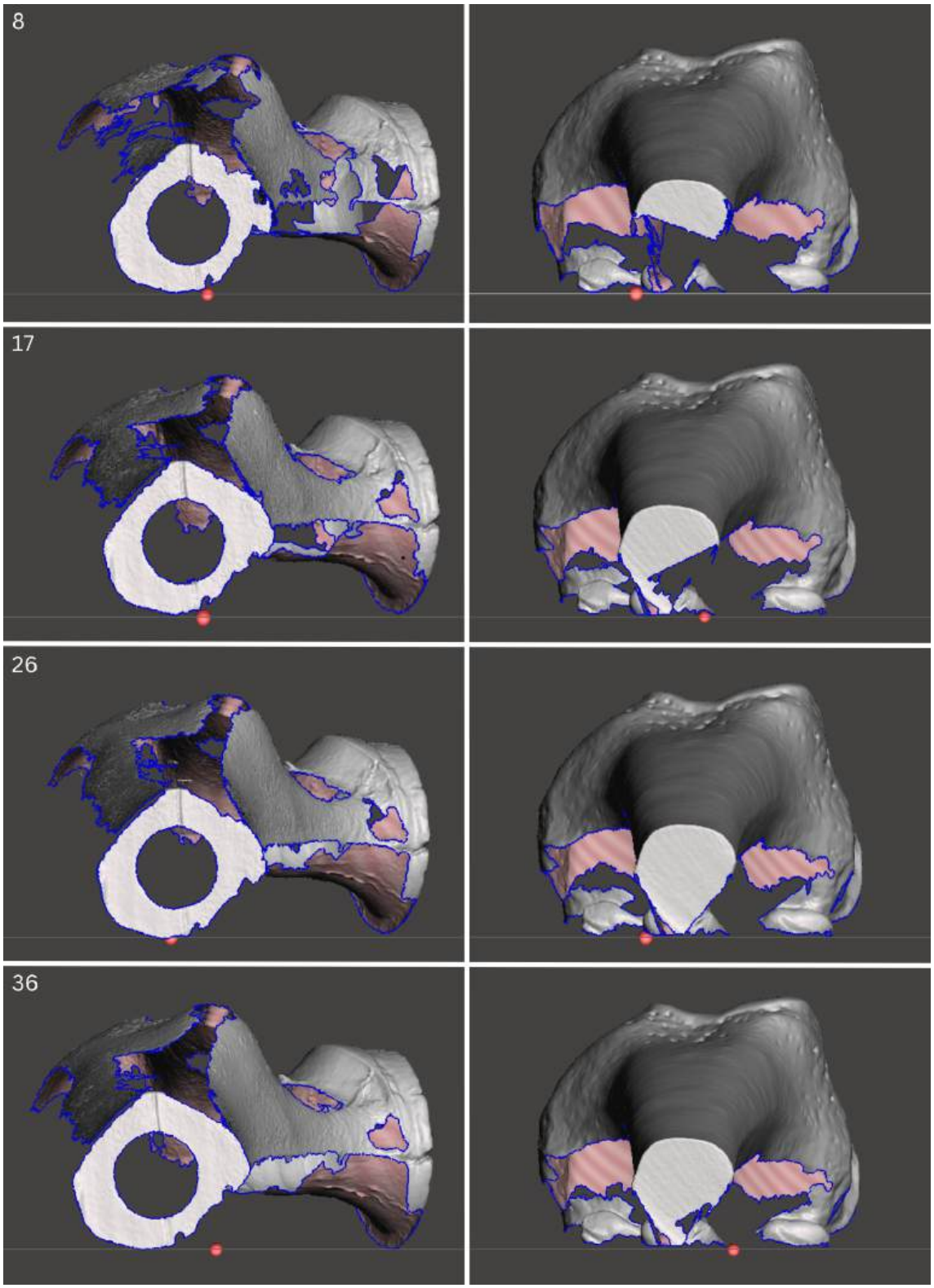

Figure 3.20: Views from the truncated end of the scanned models presented in Meshmixer, for each turntable step frequency (8, 17, 26, 36). The left image for each pair is the unwatertight mesh model of the dark colour bone, and the right image is the unwatertight mesh model of the light colour bone.

In conclusion,

- Lighter colour objects are captured with more dimensional accuracy using the EinScan-SP 3D scanner.
- Differences between the caliper measurements and the scan model measurements could be due to difficulties measuring the bone models with calipers.

Lighter colour models should be utilised for further 3D scanner research where possible, and more reliable methods of in-person measurement of the bone models could be investigated.

Comparison of Dark Bone Results

Comparing the maximum dimensions of the dark colour bone model from both scanning investigations suggests that there is large variation. Lower average dimensional accuracy in the scan model measurements in the Section 3.3 results. This is understandable considering the second investigation was limited to a maximum turntable step frequency of 36 (compared to 180 in investigation one), but raises the question of why the frequency was limited in the newer version of the software if it reduces the dimensional accuracy abilities of the scanner. These results are limited to a single type of surface (bone models from Sawbones) which was very smooth and slightly shiny, and the effect on dimensional accuracy of scanned surface feature geometry when changing the colour of the object being scanned was not explored. Further work presented in Chapter 4 investigated the effect of 3D printing parameters (speed, temperature, and filament colour) on the 3D scan output of 3D printed objects.

Table 3.15: Comparison of overall dimensional accuracy results for dark coloured bone unwatertight mesh model in Section 3.2 and Section 3.3 for turntable step frequency between 8 and 36.

Measurement (mm)	Section 3.2	Section 3.3
Width (difference)	82.16 (+1.16)	77.38 (-3.62)
Length (difference)	199.51 (-0.39)	199.58 (-0.32)
Height (difference)	43.89 (-1.46)	48.32 (+2.97)

3.4 Overall Discussion

Referring back to Section 2.6, Figure 3.21 visually presents an explanation for how the scanner converts the 3D object into a 3D virtual object. The point distance refers to the distance between the measured points that map out the shape on the physical object (Figure 3.21). These points are translated by the scanner and remapped in the virtual environment. The precision of the scan is dictated by the point distance - how small the gap is between 2 points that are being measured. If the scan was 100% accurate, the points mapped on the physical object would be remapped perfectly into the virtual space. The scanner accuracy here relates

to the distance of each remapped point from the theoretical perfectly remapped point in the virtual space (Figure 3.21). The remapped points in the virtual space comprise the 'point cloud', which the scanner software converts into a 3D polygon mesh model by considering the points as vertices and connecting them to generate edges and polygons (Section 2.5.2).

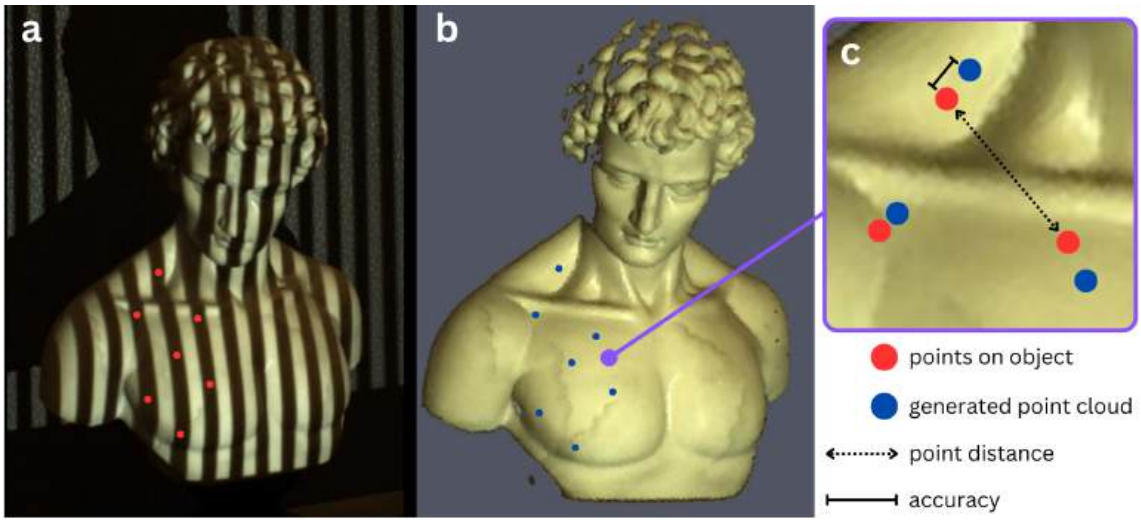

Figure 3.21: Visual explanation for how an object's geometry is mapped into a virtual environment using structured light scanning. a) Wide vertical stripe pattern projected onto the bust. The red markers represent specific measured locations on the physical model. b) The point cloud generated in the virtual environment. The blue markers represent the specific measured points in the cloud. c) Visual explanation of the scanner 'point distance' and 'accuracy'. Bust scanning images courtesy of Taubin et al (2014) [74].

The point distance for structured light scanning is dictated by the thickness of the stripes and/or how much the stripe pattern is plane shifted if repeated phase shift projection [119] is used. The accuracy is the distance of each virtual remapped point from the theoretical perfectly remapped point in the virtual space. This is given by the ability of the camera and algorithms to decide if the projected stripe is white or black. Inaccuracies arise from the ability of the camera and algorithms to perceive and deduce if the white, black or grey shade detected is a stripe projection (direct illumination), which can be difficult on the boundaries between the stripes where there is gradient, if the distorted stripe projection is very thin in width, or where reflected light (global illumination) changes the shade of the black stripes [74, 120, 121, 122].

Specularities, intense highlights on a shiny or reflective surface [123], and shadows are the main issues faced by structured light 3D scanning [124]. Shiny surfaces also present more indirect illumination effects from interreflections [122]. Although attempts were made to mitigate the effect of ambient lighting on the results of the 3D scan, there are questions surrounding the effect of the surface quality and potential reflected light on the outcomes of both investigations. Both bone models were considered to have the same surface finish / quality, however the differences in their scan capture would not be expected just from their colour difference alone. There is the potential that the darker colour of the first model interacted with the reflected light in a significant way, or that the models were actually different in terms of glossy surface texture. Further experimentation exploring different

surface textures and colours would be useful for clarifying the effects presented by the scans in Chapter 3.

Additionally, Nayar & Gupta (2012) propose a method of diffuse structured light to mitigate specularities and shadows when using structured light with linear translational symmetry patterns. They place a linear diffuser between the light source and the object, reducing specularities and shadows by converting the one-dimensional set of light rays into a two-dimensional light field [124]. This method could be used with the bone models to elucidate the effects of the surface quality in the experimental results of Chapter 3.

Inaccuracies are also introduced during the conversion process from point cloud to mesh model. Polygon mesh generation from point clouds is based on the principles of Delaunay triangulation, and Voronoi diagrams. Delaunay triangulation is important as the triangulations are unique for a set of points, except for degenerate cases. This means a mesh of contiguous, non-overlapping triangles can be generated from a dataset of points. Points are connected according to Delaunay's empty circle method (1934) [125, 126] presented visually in Figure 3.22. The method states that no point lies within the interior of any of the circumcircles of the triangles. This results in minimum interior angle being maximised, and the maximum interior angle is minimised. Thus almost equi-angular triangles are generated; avoiding long, thin triangles as much as possible. While Delaunay triangulation connects the vertices of the point cloud, Veronoi polyhedra diagram connects the circumcircles. The Delaunay and Voronoi constructs are interlinked with each other (Figure 3.23).

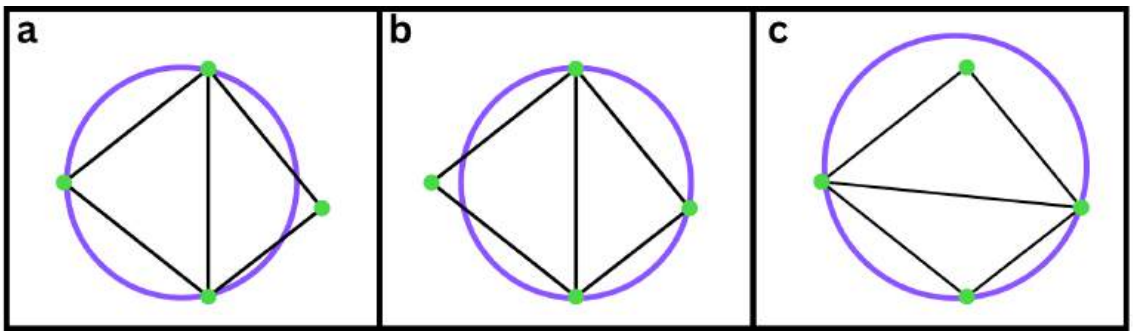

Figure 3.22: Delaunay empty circle visualisation of 4 points is presented in (a) and (b) showing that the circumcircle (purple) associated with each triangle does not have any other points inside it. When the common edge of this pair of triangles is 'flipped' (c), the same set of 4 points are not in Delaunay triangulation - the fourth point is inside the circumcircle of the right hand triangle. Images recreated from MathWorks [127].

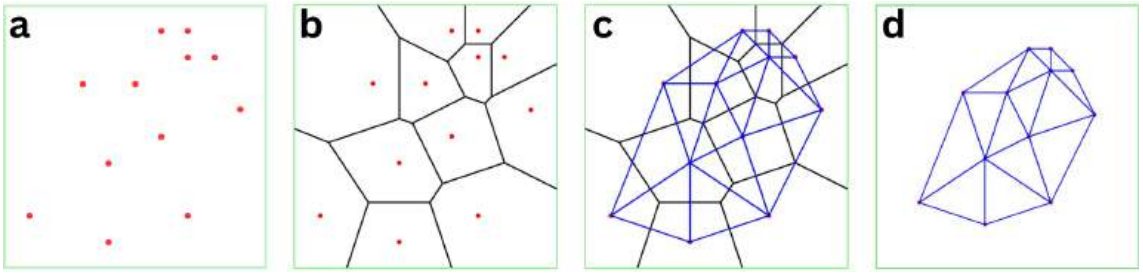

Figure 3.23: (a) A set of points. (b) The Voronoi Diagram for (a). (c) The Delaunay Triangulation and the Voronoi diagram for (a). (d) The Delaunay triangulation for (a). Images courtesy of Gallier (2011) [128].

Red Blob Games presents an interactive visual model for the relationships between Delaunay triangulation and Voronoi polygons on a 3D sphere (Figure 3.24). This simulation presents a transferable example of how the triangulation, and Voronoi region generation, would be generated from a point cloud to create a 3D polygon mesh model of a scanned object. Gallier (2011) presents a mathematical explanation of both principles and their interactions [128].

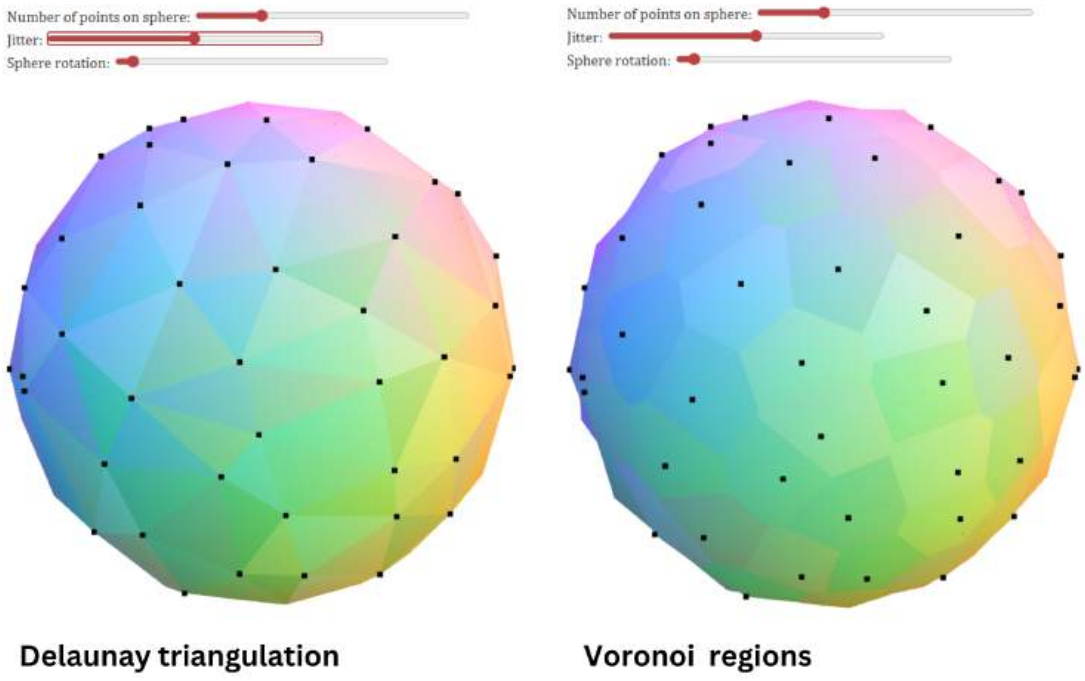

Figure 3.24: Screencaptures of the interactive mapping of Delaunay triangulation and Voronoi regions for a sphere of points [129].

3.5 Conclusion

This chapter explored the effect of turntable step frequency (objective 1), and object colour (objective 2), on scanned model dimensional accuracy. The results of the investigation presented in Section 3.2 presents that turntable step frequency can have a significant effect

on the dimensional accuracy of scanned models. This is particularly noticeable considering overall width measurements, and geometries of surface features. Furthermore, a turntable step frequency of 90 is considered to produce scan models with good dimensional accuracy (objective 3). The investigation in Section 3.3 suggests that the colour of the item being scanned is a significant factor in the dimensional accuracy of the scan model, with lighter colour items more accurately captured by the optical 3D scanner. There are unanswered questions regarding the effect of the surface textures of the bone models on the ability of the scanner to capture their geometries (objective 4). The importance of accurate, reliable orientation in the virtual and physical environments is also highlighted. With reference to Section 2.7, the significance of object recognition, and utility of alignment between the real and virtual 3D spaces is reinforced by these results.

In summary, the EinScan-SP scanner settings were systematically investigated to collate reliable scanning parameters for use in the rest of this study, contributing to project objective 1. In the next chapter, 3D printed items are scanned and the scan models' dimensional accuracy is investigated, to complete the requirements of project objective 1. The effect of different print parameters when manufacturing these items is explored.

Chapter 4

Additive Manufacturing and 3D Scanning

4.1 Introduction

In the previous chapter, the dimensional accuracy of scanned virtual models generated by the EinScan-SP was explored. For Material Extrusion Additive Manufacturing of PLA [10], the printing parameters can have an effect on the accuracy of the printed item when compared to the CAD model they are based on. Discussed in Section 2.6, the effects of print temperature and speed have been explored with regards to dimensional accuracy of the print, but not on the subsequent surface quality of the print with regards to the potential effects on the scan capture [68, 69]. Dimensional accuracy of of 3D print scans compared to their CAD design models has been explored by scanning with EinScan-SP, however there is no investigation of the dimensional accuracy of CAD to print, or print to scan, which leave questions about the true sources of error with regard to dimensional accuracy of scanned 3D prints [70, 71]. Furthermore, the standards used are changeable and sometimes not noted in the methodology. Additionally, different measuring practices are used for different applications, and thus some measurements investigated are unsuitable indicators of accuracy for specific applications such as biomedical implant printing. Conformal AM printing onto an object in-situ requires reliable and accurate knowledge of the dimensions of the object. It is necessary to be aware of the accuracy of the scanned data of the "base" print, as this is used to generate the CAD model of the surface feature "implant" print. It is also useful to be aware of the dimensional inaccuracies of the MEX-TRB/P/PLA AM, in order to anticipate and understand the results of the implant in situ print process contained within project objectives 3b, 3c, and 3d. Structured light 3D scanning has been investigated for its applications in biomedical advances and direct clinical care, and the EinScan-SP 3D scanner (Shining 3D, China) has been shown to be an affordable, commercially available scanner for such purposes (Section 2.7).

The aim of the work contained in this chapter was to investigate how print parameters affect the dimensional accuracy of a 3D printed object, and the dimensional accuracy of 3D scans of the object. For the purpose of this chapter, 'accuracy' is defined as how close the measured dimensions of the 3D print are to the CAD model dimensions, and to the scanned virtual model dimensions. The results of this chapter facilitate fulfilment of project objective 1, and were used to develop MEX-TRB/P/PLA printing parameter standards and guidelines for fulfilling project objective 3. The aim of this chapter was achieved with the following objectives:

1. Investigate the effect of AM print speed on accuracy of 3D scanner dimensional accuracy of AM objects
2. Investigate the effect of AM print temperature on accuracy of 3D scanner dimensional accuracy of AM objects
3. Evaluate the significance of AM print parameters effects on 3D scanning dimensional accuracy of AM objects

4.2 Methods

4.2.1 Printing Settings

Fifty cubes of dimensions 30 x 30 x 30 mm were 3D printed in green PLA filament [130] using UltiMaker S5 FDM printers (UltiMaker B.V., Netherlands). The dimensions were chosen as they meet the minimum object dimensions for scanning, as stated in the specification for the EinScan-SP 3D scanner (Shining 3D, China) [114]. The smallest dimension was chosen as this reduced overall print time for fifty prints, but was also large enough, and an appropriate geometry, for the faces of the cubes to meet the measurement criteria for the research on surface metrology being undertaken by B. Hawthorn and myself [131]. Furthermore, the cuboid shape enabled simplicity of measurements in the X, Y and Z axes, and easiest analysis of directional print effects.

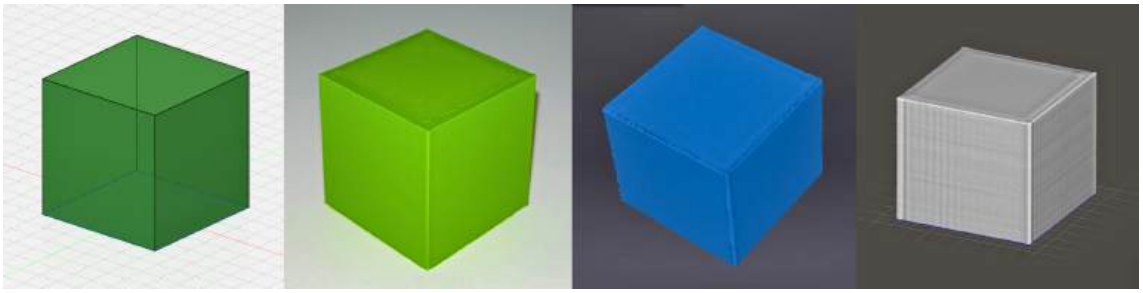

Figure 4.1: From left to right: cube CAD model, 3D printed MEX-TRB/P/PLA cube, Shining3D point cloud, meshed model from the scan data.

The cube design was created in Fusion 360 CAD software (Autodesk, USA), then exported as an STL file to Ultimaker Cura (Ultimaker B.V., Netherlands) where the model was sliced and the print toolpath generated. The Ultimaker S5 printer has a dual extrusion print head (single extrusion was used), and the 0.4 mm nozzle used is stated to produce a print (layer) resolution of 0.02 - 0.2 mm. This printer has operating printing temperatures between 180 and 280 °C, a heated glass build plate which has operating temperatures of 20 to 140 °C, and a stated XYZ resolution of 6.9, 6.9, and 2.5 µm, respectively [132].

The G-code settings were manually updated to ensure 100% flow at all points, and that the parameters presented in Table 4.1 were the same across all 50 printed cubes. To promote consistent surfaces for the prints, there were 5 top and 5 bottom layers, both with 100 % infill at 500 mm/s^2 acceleration, and 5 wall (shell) layers printed at 2000 mm/s^2 . When each complete printed cube was removed from the print bed, the bottom face was labelled for X

and Y print directions.

Table 4.1: Constant print parameters

Parameter	Value
Layer height (z resolution)	0.2 mm
Build plate temperature	60 °C
Print head travel speed	150 mm/s
Initial layer print speed	10 mm/s
Infill	20 %
Acceleration	4000 mm/s²

Two investigations into the effect of different additive manufacturing parameters were conducted. The printing parameters for the effect of print speed (Section 4.3.1 & 4.3.2) are presented in Table 4.2; five models were printed for each speed setting (25 total cubes). The printing parameters for the effect of print temperature (Section 4.3.3 & 4.3.4) are presented in Table 4.3; five models were printed for each temperature setting (25 total cubes).

Table 4.2: Constant print temperature print parameters

Parameter	Value
Print temperature	200 °C
Print speed (infill, walls, top, bottom)	30 - 70 mm/s (10 mm/s increments)

Table 4.3: Constant print speed print parameters

Parameter	Value
Print speed (infill, walls, top, bottom)	50 mm/s
Print temperature	180 - 220 °C (10 °C increments)

4.2.2 Scanning

Each cube was scanned individually using an EinScan-SP 3D Scanner (SHINING 3D, China), housed inside a darkbox (Fig. 4.2) to reduce the effect of ambient lighting conditions [73]. The EinScan-SP has a stated point distance of 0.17 - 0.20 mm, and accuracy of 0.03 mm. The scans used HDR (High Dynamic Range) brightness to generate 'non-texture' scans (the colour of the object was not captured), using coded turntable alignment with 90 turntable steps. HDR offers more accurate scanning output by better capturing the full range of light and dark highlights and shadows. This is especially important for enabling scanning of textured objects or objects with contrasting colours. The scan was post-processed with the companion software for the EinScan-SP (ExScanS V3.0.0.0), and a watertight, high detail

mesh was produced and exported as an .3mf file.

Figure 4.2: A 3D printed cube on the coded turntable of the scanner inside the darkbox.

4.2.3 Measurements

Before scanning, each cube was measured with Vernier calipers to 2 decimal places. The lines of measurement, shown in Fig. 4.3, were midline measurements across the centre point in the X and Y axis directions, and maximum measurements in the X and Y axis directions, for the 'top' face in the XY plane. After scanning, the .3mf files were imported into Autodesk Meshmixer (Autodesk, USA), and thus converted to .mix file format. In Meshmixer, the cubes were 'plane cut' to section a shell of the 'top' face, approximately 1 mm in depth. Note the notation change for the Meshmixer software: the X and Z axis plane is parallel to the base of the cube, whereas for the printed cubes the X and Y axis plane is parallel to the base. Midline measurements across the centre point in the X and Z axis directions, for the top face in the XZ plane, were taken using the 'point to point' measure tool in the X and Z axes directions, respectively (Fig. 4.4a). Maximum measurements in the X and Z axes directions for the top face in the XZ plane were taken using the 'dimensions' measure tool (Fig. 4.4b).

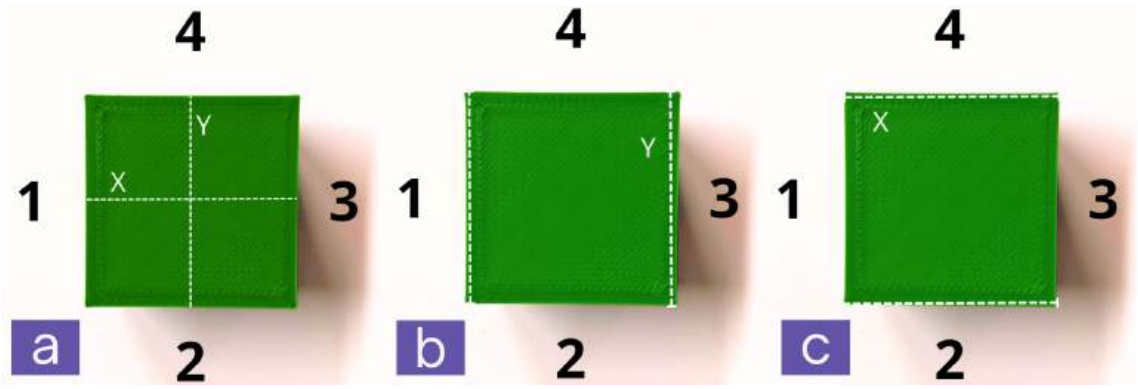

Figure 4.3: Labelled measurement points of printed cube: a) midline measurements in both axis directions, b) maximum measurements in Y axis direction, c) maximum measurements in X axis direction. The sides of the cube are numbered in relation to the print direction during manufacture.

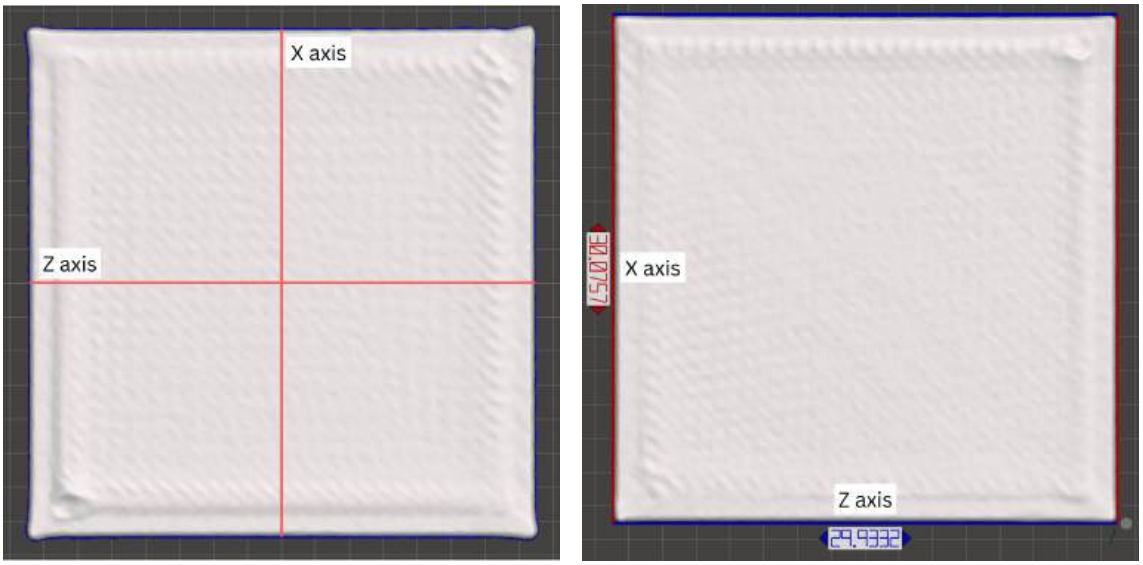

(a) Midline (b) Maximum

Figure 4.4: Dimensions measurement examples, top view, Meshmixer

4.2.4 Statistical Analysis

Primary statistical analysis using One-Way ANOVA was performed to determine if the samples for each print parameter setting belong to different populations, i.e. are significantly different, $p < 0.05$. Further statistical tests were undertaken to find which samples were significantly different from one another, and to suggest whether the difference was likely to be due to the effect of the independent variable (or another variable, or error). Tukey's HSD test suggests which of the groups of samples were significantly different to each other. If found to be different, Cohen's f test and the Omega Squared test were done to suggest the size of the effect of the independent variable on this outcome. Example calculations and further explanation can be found in Appendix A.

4.3 Results

4.3.1 Effect of Print Speed on Printed Dimensions

The CAD cube had dimensions of 30 mm in all axes. Figure 4.5 presents the average dimension for the top face of the printed cubes, for each print speed (30, 40, 50, 60 and 70 mm/s). The figure also presents the CAD dimension as a reference line (pink) at 30 mm. The mean dimension of the top faces of the printed cubes for each print speed was greater than the CAD dimension (30 mm) by 0.13, 0.20, 0.33, 0.27, and 0.43 %, for 30, 40, 50, 60, and 70 mm/s, respectively. The presented trend in Figure 4.5 suggests that as the print speed was increased, the printed dimension increased.

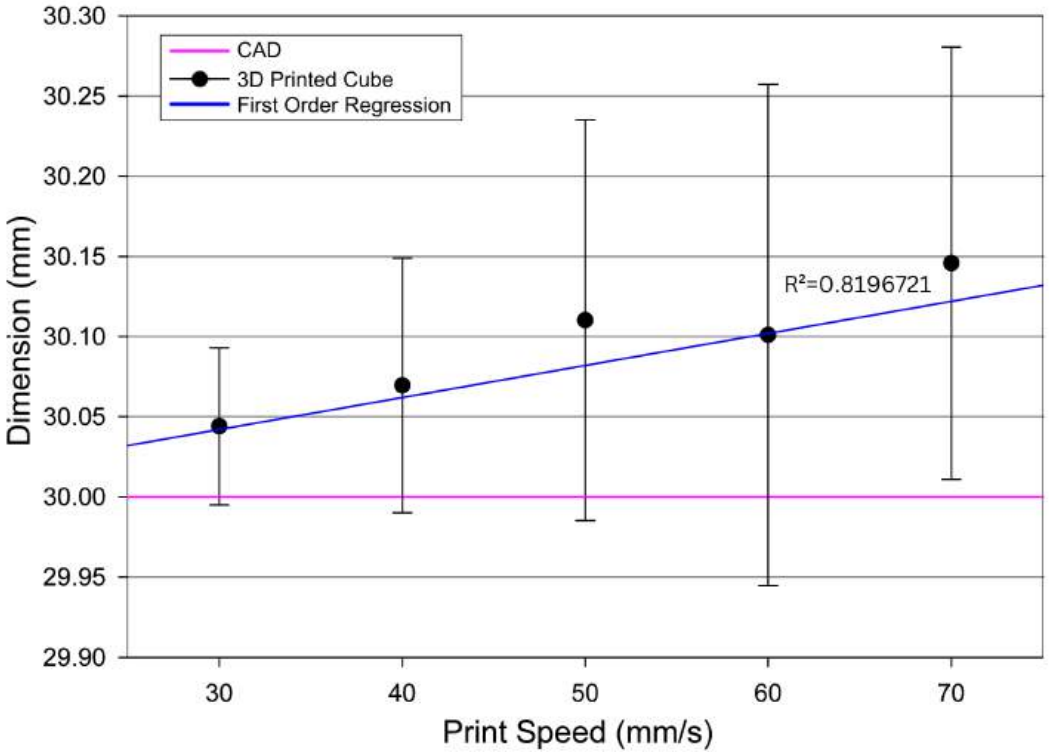

Figure 4.5: XY plane dimensions for the top face for the cube, as printing speed is varied. First order regression line (blue) $y = (29.98 \pm 0.09) + (0.002 \pm 0.002)x$ (95% confidence), $R^2 = 0.82$. Dimension for the CAD cube (pink). Error bars are standard deviations.

Statistical analysis was undertaken to examine whether the change in printed dimension was significant and able to be attributed to the change in print speed. One-Way ANOVA testing for the 5 groups suggests a significant difference between the means of at least 2 of the groups. Tukey's Honestly Significant Difference test was undertaken to find which 2 (or more) groups were significantly different from each other. Tukey's HSD suggests that the means for the groups printed at 30 mm/s and 70 mm/s are significantly different from one another and every other group combination was found to be not significant. Post-hoc testing was performed to investigate the size of the effect of the print speed on these significantly different means. The Cohen's f test suggested that the effect of the independent variable (print speed) on the outcome was small, to no effect, and the Omega Squared test suggested

that the effect of the independent variable (print speed) on the outcome was small.

Considering the dimension measurements separated into midline and maximum dimensions, two different trends were identified. The CAD cube had a midline dimension of 30 mm in all axes - this is presented as a reference line (pink) in Figure 4.6. For the printed cubes at 30, 40, 50, 60, 70 mm/s print speeds, the midline average dimension was greater than the CAD by 0.00, 0.00, 0.03, -0.13, and 0.10 % respectively.

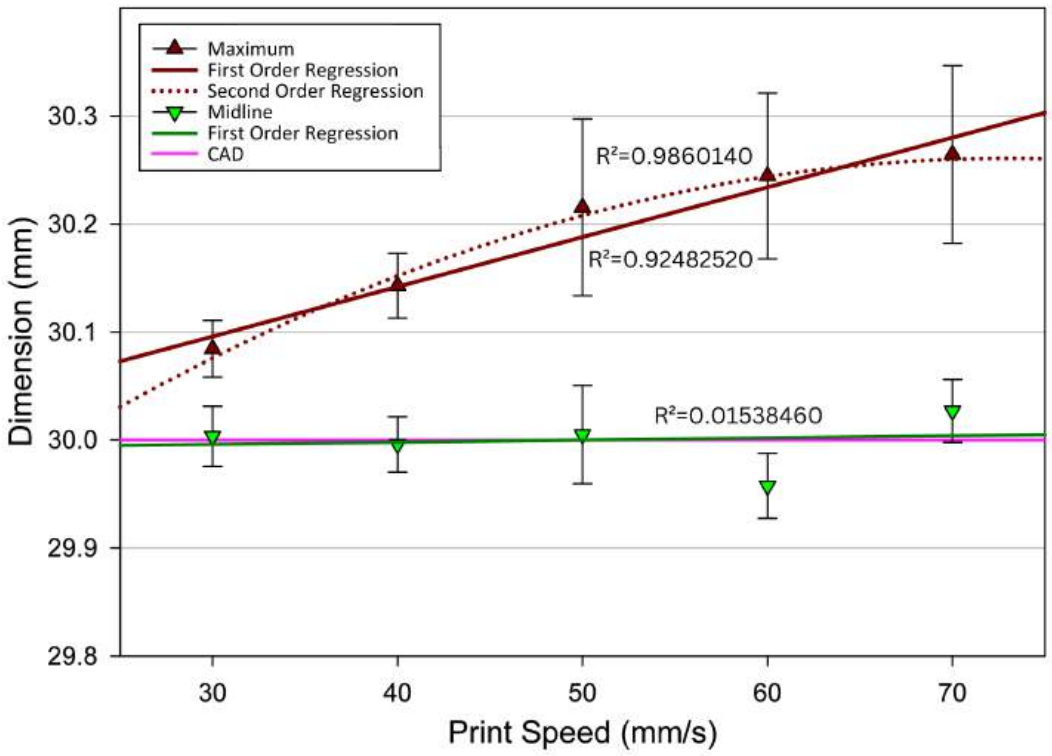

Figure 4.6: XY plane dimensions for the top face for the cube, as printing speed is varied. Mean maximum dimensions first order regression line (green), $y = (29.99 \pm 0.15) + (0.0002 \pm 0.003)x$ (95% confidence), $R^2 = 0.02$. Mean midline dimensions first order regression line (solid red), $y = (29.96 \pm 0.13) + (0.005 \pm 0.002)x$ (95% confidence), $R^2 = 0.92$. Second order regression line (dotted red), $y = (29.73 \pm 0.35) + (0.02 \pm 0.02)x + (-0.0001 \pm 0.0001)x^2$ (95% confidence), $R^2 = 0.99$. Dimension for the CAD cube (pink). Error bars are standard deviations.

Statistical analysis for the 5 groups suggested significant difference between the means of at least 2 of the sample groups, and that the mean midline dimension for the group printed at 60 mm/s was significantly different to all the other groups. Furthermore, the midline means of the groups printed at 40 mm/s and 70 mm/s were also suggested to be significantly different to each other. It was suggested that the effect of the independent variable (print speed) on the outcome was medium (Cohen's f test) to large (Omega Squared test). Due to the flat regression line presented in Figure 4.6, it could be suggested that the effect of the change in print speed is not significant until the print speed reaches 60 or 70 mm/s. Considering the trend generated by the data, it could also be suggested that the cubes printed at 60 mm/s were anomalous, and do not fit the trend due to another external factor.

The CAD cube also had a maximum dimension of 30 mm in all axes, represented by the same

reference line in Figure 4.6. The maximum printed dimension means were much greater than the midline printed dimension means, and generated a positive graphical correlation. The maximum dimension means (mm) for the top faces of the printed cubes were greater than the CAD dimension, by 0.27 (30 mm/s), 0.47 (40 mm/s), 0.73 (50 mm/s), 0.80 (60 mm/s), and 0.87 % (70 mm/s). Figure 4.6 presents a first order regression line and a second order regression line for the data.

One-Way ANOVA testing for the 5 groups suggested a significant difference between the means of at least 2 of the groups and further analysis with Tukey's HSD test suggested that: the mean maximum dimension for the group printed at 30 mm/s was significantly different from all the other groups' means, the mean maximum dimension for the group printed at 40 mm/s was significantly different from all the other groups' means, and the mean maximum dimensions for all the other groups were suggested to be not significantly different from each other. The Cohen's f and Omega Squared tests suggest that the effect of the independent variable (print speed) on this outcome is large.

4.3.2 Effect of Print Speed on Scanned Dimensions

The average dimensions of the top face of the scanned cube were compared to the average dimensions of the top face of the printed cube, and the difference between the two was investigated. Figure 4.7 presents the difference of the scanned cubes compared to the printed cubes, for each print speed (30, 40, 50, 60 and 70 mm/s).

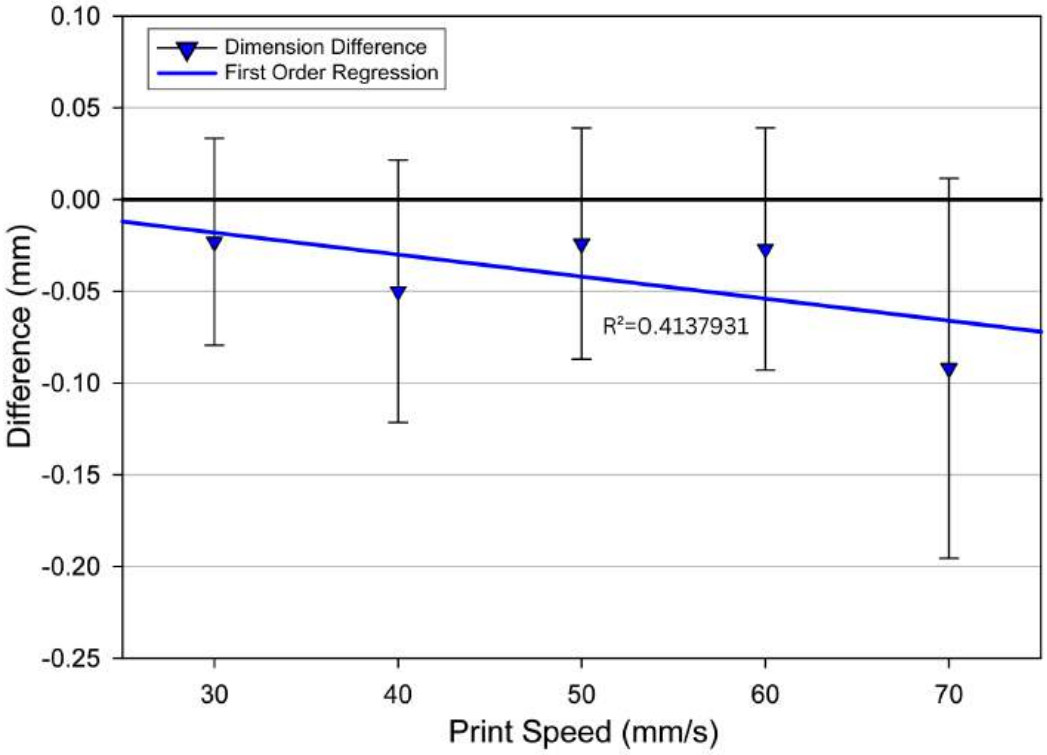

Figure 4.7: XZ plane dimensions for the top face of the cube as printing speed is varied. First order regression line (blue) $y = (0.02 \pm 0.14) + (-0.001 \pm 0.003)x$ (95% confidence), $R^2 = 0.41$. Error bars are standard deviation.

The mean dimension difference of the top faces of the scanned cubes compared to the printed cubes for each print speed were -0.02, -0.05, -0.02, -0.03, and -0.09 mm, for 30, 40, 50, 60 and 70 mm/s, respectively. The mean dimensions for the printed cubes were greater than the mean dimensions of the scanned cubes. The trendline in Figure 4.7 suggests that as the print speed was increased, the scanned dimensions came out smaller. Statistical analysis for the 5 groups suggests there is no significant difference between the means of any of the groups. Considering the absolute values of the differences also suggested no significant difference between any of the means of the groups.

Considering the dimension difference measurements separated into midline and maximum dimensions, two different trends were identified. For the cubes printed at 30, 40, 50, 60, and 70 mm/s, the midline average dimension difference was -0.06, -0.11, -0.08, -0.08, and -0.19 mm, respectively. The first order trendline (4.8, solid green) suggests as print speed is increased, the scan midline dimensions are increasingly smaller than the printed dimensions of the cube. The second order trendline (dotted green) suggests that the difference in dimensions could be steady around -0.07 mm for print speeds 30 to 60 mm/s, but for the cube printed at 70 mm/s the scanned dimension is smaller by approximately 0.20 mm and this downward trend is suggested to continue at greater print speed.

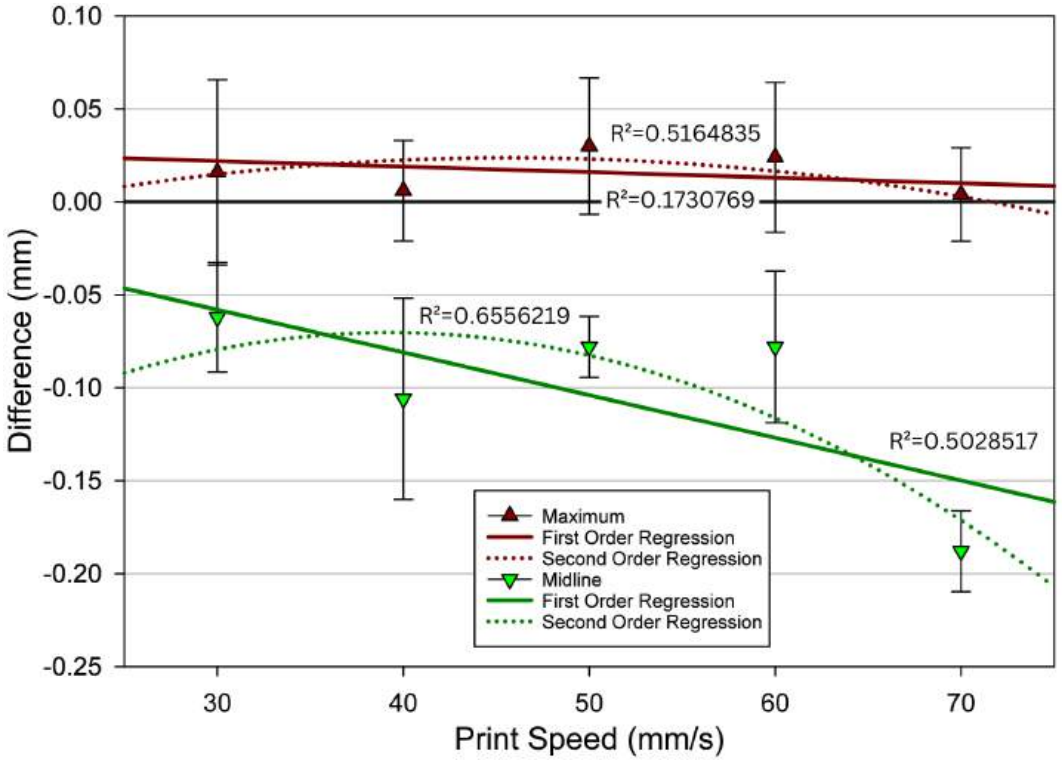

Figure 4.8: XZ plane difference in dimension of the scan compared to the printed cube for the top face as printing speed is varied. Mean midline dimension difference first order regression line (green solid), $y = (0.01 \pm 0.22) + (-0.002 \pm 0.004)x$ (95% confidence), $R^2 = 0.50$. Second order regression line (green dotted), $y = (-0.24 \pm 1.16) + (0.01 \pm 0.05)x + (-0.0001 \pm 0.0005)x^2$ (95% confidence), $R^2 = 0.66$. Mean maximum dimension difference first order regression line (red solid), $y = (0.03 \pm 0.06) + (-0.0003 \pm 0.001)x$ (95% confidence), $R^2 = 0.17$. Second order regression line (red dotted), $y = (-0.05 \pm 0.31) + (0.003 \pm 0.01)x + (-0.00004 \pm 0.0001)x^2$ (95% confidence), $R^2 = 0.52$. Error bars are standard deviation.

Statistical analysis suggested there was a significant difference between the means of at least 2 of the groups, and that the mean for the group printed at 70 mm/s was significantly different to the means of all the other groups. The effect of the independent variable (print speed) on this outcome was considered large. Considering instead the absolute values of the differences, the results of the analysis were identical to the analysis for the true differences.

The mean maximum dimension difference of the scans compared to the prints was 0.02, 0.01, 0.03, 0.02, and 0.00 mm, for the cubes printed at 30, 40, 50, 60 and 70 mm/s, respectively. The scan means were greater than the printed means, and the trendlines are presented in Figure 4.8 (red). Both trendlines display a nearly horizontal, flat pattern suggesting little to no effect of the print speed on the scan accuracy. The scan maximum dimension was an average of 0.02 mm larger than the print maximum dimension, regardless of print speed used. One-Way ANOVA and Tukey's HSD testing for the 5 groups suggest there was no significant difference between the means of any of the groups. Considering instead the absolute values of the differences no significant difference in mean was found either.

4.3.3 Effect of Printing Temperature on Printed Dimensions

Figure 4.9 presents the average dimension for the top face of the printed cubes, for each print temperature (180, 190, 200, 210 and 220 °C).

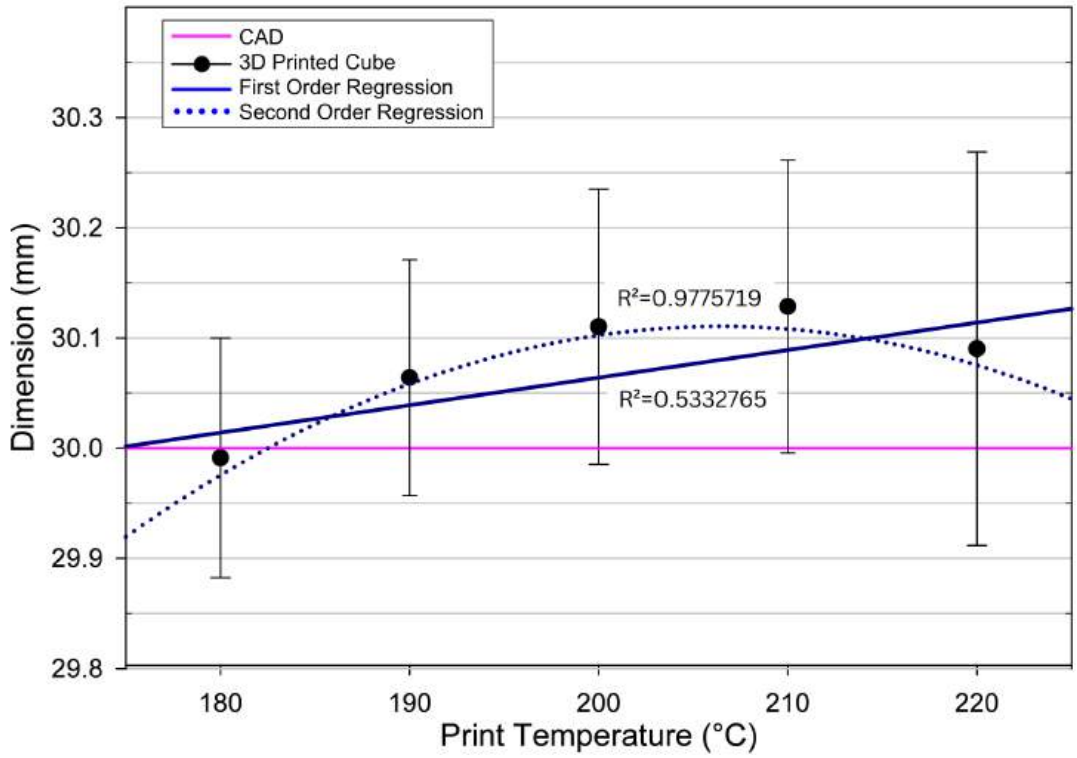

Figure 4.9: XY plane dimensions for the top face for the cube, as printing temperature is varied. First order regression line (blue solid), $y = (29.56 \pm 0.86) + (0.003 \pm 0.004)x$ (95% confidence), $R^2 = 0.53$. Second order regression line (blue dotted), $y = (21.89 \pm 5.25) + (0.08 \pm 0.05)x + (-0.0002 \pm 0.0001)x^2$ (95% confidence), $R^2 = 0.98$. Dimension for the CAD cube (pink). Error bars are standard deviation.

The mean dimension of the top faces of the printed cubes for each print temperature had a percentage difference compared to the CAD dimension (30 mm) of -0.07 % (180 °C), 0.17 % (190 °C), 0.33 % (200 °C), 0.40 % (210 °C), and 0.23 % (220 °C). The first order trendline in Fig.4.9 presents a positive correlation - as print temperature is increased, the mean dimension of the cube increased, positively diverging from the CAD dimension, whereas the second order regression line suggests an increase until a plateau, or decrease, at around 210 °C. Statistical analysis for the 5 groups suggests there was a significant difference between the means of at least 2 of the groups, and that the mean of the group printed at 180 °C is significantly different to the means of the groups printed at 200, 210, and 220 °C. The effect of the independent variable (print temperature) was suggested to be small (Cohen's f test) to medium (Omega Squared test).

Considering the dimension measurements separated into midline and maximum dimensions, two different trends were identified. For the printed cubes printed at 180, 190, 200, 210 and 220 °C, the midline average dimension was 29.90, 29.97, 30.01, 30.01, and 29.93 mm, respectively. Compared to the CAD dimension (30 mm) this was a difference of -0.33, -0.10, 0.03, 0.03, and -0.23 %, respectively. The weak trend presented by the first order regression

line (Fig. 4.10, solid green) suggests as print temperature was increased, the mean midline dimension increased, towards 30 mm. The second order regression line has a stronger alignment, and suggests the mean midline dimension increased towards a peak around 200 to 210 °C, and then decreased as the print temperature is increased further.

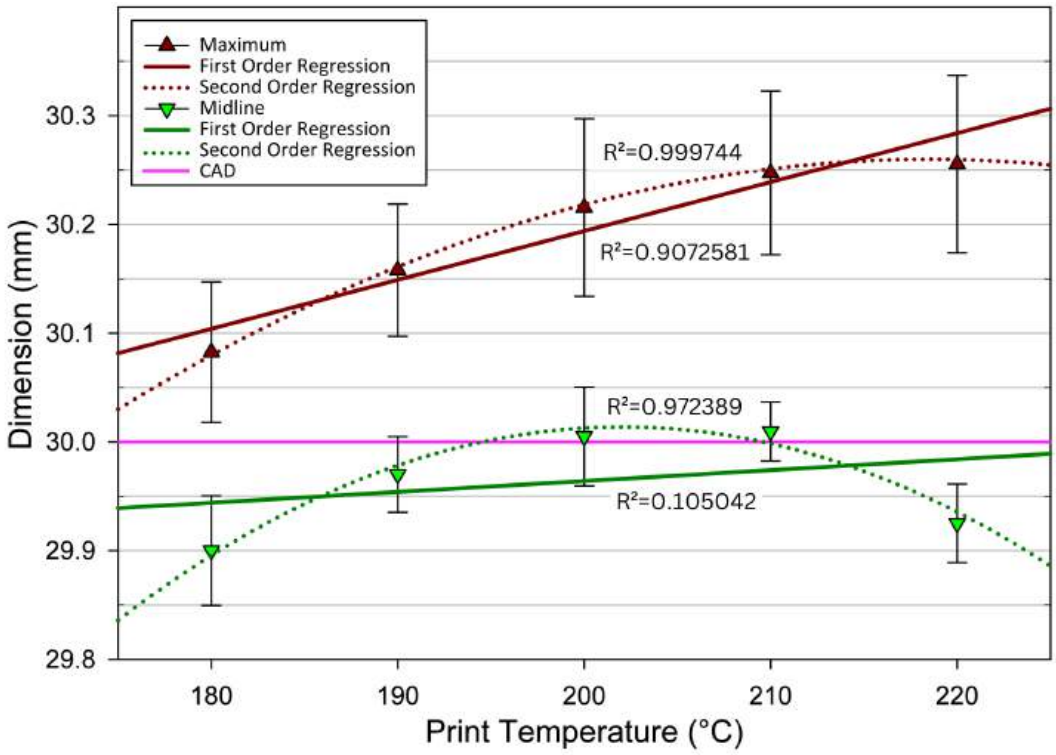

Figure 4.10: XY plane midline and maximum dimensions for the top face for the cube, as printing temperature is varied. Mean midline dimensions first order regression line (solid green), $y = (29.76 \pm 1.08) + (0.001 \pm 0.005)x$ (95% confidence), $R^2 = 0.11$. Second order regression line (dotted green), $y = (20.10 \pm 5.25) + (0.10 \pm 0.05)x + (-0.0002 \pm 0.0001)x^2$ (95% confidence), $R^2 = 0.97$. Mean maximum dimensions first order regression line (solid red), $y = (29.29 \pm 0.53) + (0.005 \pm 0.003)x$ (95 % confidence), $R^2 = 0.91$. Second order regression line (dotted red), $y = (24.46 \pm 0.77) + (0.05 \pm 0.008)x + (-0.0001 \pm 0.00002)x^2$ (95 % confidence), $R^2 = 1.00$. Dimension for the CAD cube (pink). Error bars are standard deviation.

Statistical analysis for the 5 groups suggested there was a significant difference between the means of at least 2 of the groups. It is suggested that the mean for the group printed at 190 °C was significantly different from all the other groups' means, the means for the groups printed at 180 and 220 °C were significantly different from the other groups means, and the means for the groups printed at 200 and 210 °C were significantly different from the other groups. The effect of the independent variable (print temperature) on the outcome was large.

The maximum printed dimension means were greater than the midline printed dimension means, and displayed a positive correlation. The maximum dimension means (mm) for the top face of the printed cubes were all greater than the CAD dimension, by 0.27 (180 °C), 0.53 (190 °C), 0.73 (200 °C), 0.83 (210 °C), and 0.87 % (220 °C). The first order regression line (Fig. 4.10, solid red) presents a strong trend that suggests that as the print temperature was increased, the mean maximum dimension increased further away from 30 mm. The second order regression line

has a greater R^2 and suggests that the mean maximum dimension increases as print temperature is increased, but it begins to plateau at 190 to 200 °C. Statistical analysis for the 5 groups suggests there is a significant difference between the means of at least 2 of the groups, and that the mean for the group printed at 180 °C was significantly different from all the other groups' means. The effect of the independent variable (print temperature) on the outcome was large.

4.3.4 Effect of Print Temperature on Scanned Dimensions

The average dimensions of the top face of the scanned cube were compared to the average dimensions of the top face of the printed cube, and the difference between the two was investigated. Figure 4.11 presents this difference for each print temperature (180, 190, 200, 210 and 220 °C).

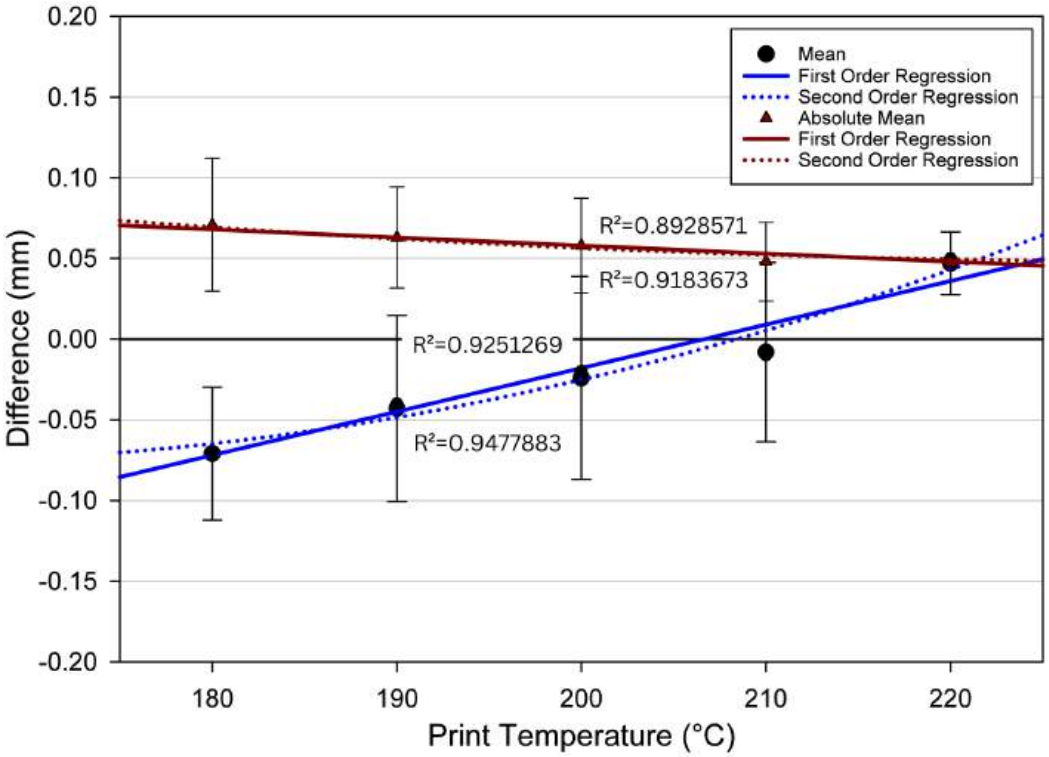

Figure 4.11: XZ plane average dimension difference for the top face for the scanned cube compared to the printed cube, as print temperature is varied. Mean dimension difference first order regression line (solid blue), $y = (-0.56 \pm 0.28) + (0.003 \pm 0.001)x$ (95% confidence), $R^2 = 0.93$. Second order regression line (dotted blue), $y = (0.86 \pm 6.56) + (-0.01 \pm 0.07)x + (0.00004 \pm 0.0002)x^2$ (95 % confidence), $R^2 = 0.95$. Mean dimension difference, absolute value first order regression line (solid red), $y = (0.16 \pm 0.06) + (-0.001 \pm 0.0003)x$ (95% confidence), $R^2 = 0.89$. Second order regression line (dotted red), $y = (0.44 \pm 1.55) + (-0.003 \pm 0.02)x + (0.00001 \pm 0.00004)x^2$ (95% confidence), $R^2 = 0.92$ Error bars are standard deviation.

The mean dimension difference of the top faces of the scanned cubes compared to the printed cubes for each print temperature were -0.07, -0.04, -0.02, -0.01, and 0.05 mm, for 180, 190, 200, 210, and 220 °C, respectively. The trendlines in Figure 4.11 (blue) suggest that as the print temperature was increased, the mean dimension difference trended from negative values towards zero from 180 to 210 °C, then increased at 220 °C to the scan measuring a mean of 0.05 mm larger.

For the true mean dimension difference, statistical analysis suggests there was a significant difference between the means of at least 2 of the groups, and that for the cubes printed at 220 °C the mean dimension difference was significantly different to the mean dimension difference for the cubes printed at 180, 190, and 200 °C, but not 210 °C. The effect of the independent variable (print temperature) on the outcome was suggested to be large.

The absolute mean dimension differences were 0.07, 0.06, 0.06, 0.05, and 0.05 mm, for the cubes printed at 180, 190, 200, 210 and 220 °C, respectively. A first order regression line (Figure 4.11, solid red) suggests a negative correlation - as print temperature is increased, the absolute difference between the mean dimensions of the scan and the printed cube decreases towards zero. The second order regression line (dotted red) follows the same presentation - as the print temperature is increased, the absolute difference between the mean dimensions of the scan and the printed cube decreases towards zero. Statistical analysis for the 5 groups considering the absolute difference suggested no significant difference between the means of any of the groups.

Considering the dimension difference measurements separated into midline and maximum dimensions, two different trends were identified. Figure 4.12 presents the measurements split into true mean midline and maximum dimension difference, and Figure 4.13 presents the absolute means. For the cubes printed at 180, 190, 200, 210, and 220 °C, the true mean midline dimension difference was -0.10, -0.08, -0.08, -0.08, and 0.05 mm, respectively. The first order trendline (Fig. 4.12, solid green) suggests as temperature is increased, the difference decreases towards zero and then increases. The second order trendline (dotted green) also suggests an increase, after remaining constant between 180 and 200 °C. Statistical analysis for the 5 groups suggests there is significant difference between the means of at least 2 of the groups, and that the mean midline difference for the group printed at 220 °C is significantly different to all the other groups. The effect of the independent variable (print temperature) on the outcome was suggested to be large.

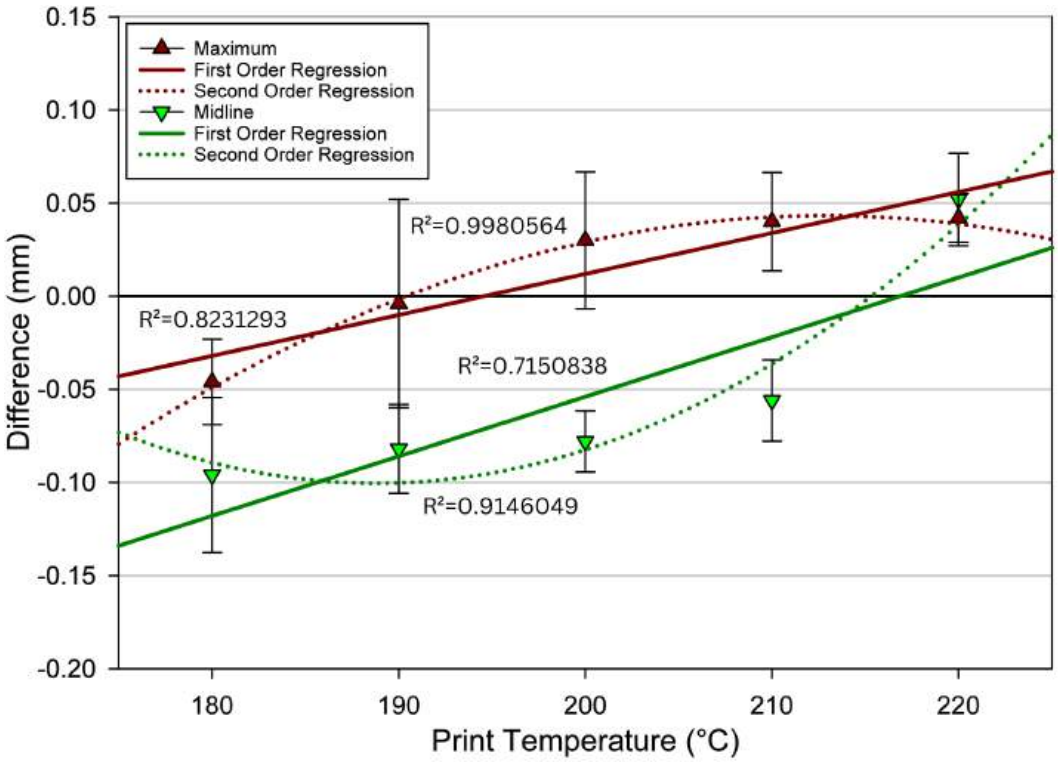

Figure 4.12: XZ plane dimensions for the top face for the scanned cube compared to XZ plane dimensions for the top face for the printed cube, as print temperature is varied. Mean midline dimension difference first order regression line (solid green), y = (–0.69±0.74)+(0.003±0.004)x (95% confidence), R^2 of 0.72. Second order regression line (dotted green), y = (4.99±11.31)+(–0.05±0.11)x+(0.0001± 0.0003)x^2 (95% confidence), R^2 = 0.91. Mean maximum dimension difference first order regression line (solid red), y = (–0.43 ± 0.38) + (0.002 ± 0.002)x (95% confidence), R^2 = 0.82. Second order regression line (dotted red), y = (–3.84 ± 1.09) + (0.04 ± 0.01)x + (–0.0001 ± 0.00003)x^2 (95% confidence), R^2 = 1.00. Error bars are standard deviation.

Considering the absolute difference between the scan and printed dimensions, the mean midline differences for each group (mm) were 0.10, 0.08, 0.08, 0.06, and 0.05 mm (for 180, 190, 200, 210, and 220 °C print temperature, respectively). A first order regression line is presented in Figure 4.13 (green) and suggests a negative correlation - as the print temperature was increased, the absolute difference of the scanned midline dimension decreased towards zero. A second order regression line did not produce a better visual fit or improved R^2 value, so is not presented. Statistical analysis for the 5 groups, considering the absolute dimension difference, suggested no significant difference between any of the groups.

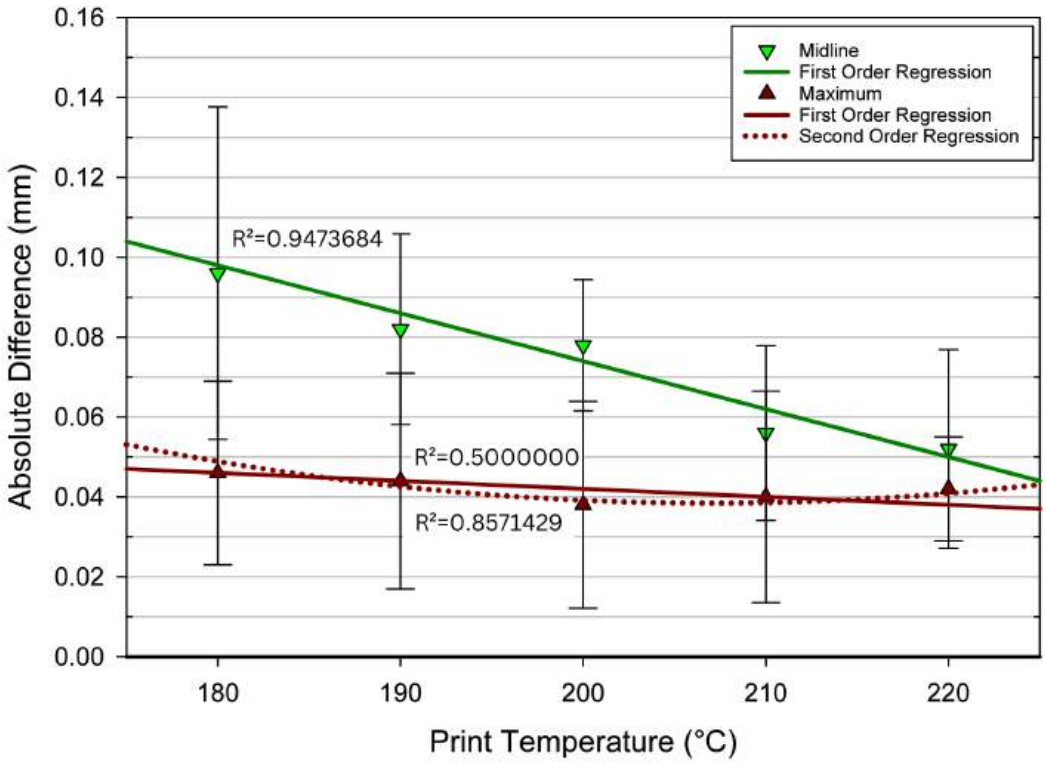

Figure 4.13: XZ plane dimensions for the top face for the scanned cube compared to XZ plane dimensions for the top face for the printed cube, as print temperature is varied, absolute values. Mean midline absolute dimension difference first order regression line (solid green). $y = (0.31 \pm 0.10) + (-0.001 \pm 0.001)x$ (95% confidence), $R^2 = 0.95$. Mean maximum absolute dimension difference first order regression line (solid red), $y = (0.08 \pm 0.07) + (-0.0002 \pm 0.0004)x$ (95% confidence), $R^2 = 0.50$. Second order regression line (dotted red), $y = (0.65 \pm 1.09) + (-0.006 \pm 0.01)x + (0.00001 \pm 0.00003)x^2$ (95% confidence), $R^2 = 0.86$. Error bars are standard deviation.

The true mean maximum dimension difference of the scans compared to the prints was -0.05, 0.00, 0.03, 0.04, and 0.04 mm for the cubes printed at 180, 190, 200, 210, and 220 °C, respectively. Statistical analysis for the 5 groups suggests there is significant difference between the means of at least 2 of the groups and that the mean maximum difference for the group printed at 180 °C is significantly different to the mean maximum differences for the groups printed at 200, 210 and 220 °C. The effect of the independent variable (print temperature) on the outcome is suggested to be large.

Considering the absolute difference between the scan and printed maximum dimensions, the means for each group were 0.05, 0.04, 0.04, 0.04, and 0.04 mm. Statistical analysis for the 5 groups suggested no significant difference between any of the groups. Thus it can be suggested that the independent variable (print temperature) had no effect on the perceived difference in mean difference of the scanned maximum dimensions compared to the printed maximum dimensions, when considering the absolute value of the difference in maximum dimension.

4.4 Discussion

4.4.1 Effect of Print Speed on Printed Dimensions

The maximum dimensions were found to be at the corners of the cube top face, where the travel path of the print head changes direction - moving in the X axis to moving in the Y axis, and vice versa. Therefore it is hypothesised that the increase in speed causes a difference in how the material is extruded at the corners. Acceleration for the walls was 2000 mm/s^2, accelerating from the corner point (0 mm/s) to the desired maximum speed, where the print head travelled at that constant speed, until decelerating towards the next corner (0 mm/s). The effect of this same acceleration value on the 5 different maximum speeds is presented graphically against the time from the starting corner of the side (Figure 4.14), and against the displacement from the starting corner (Figure 4.15).

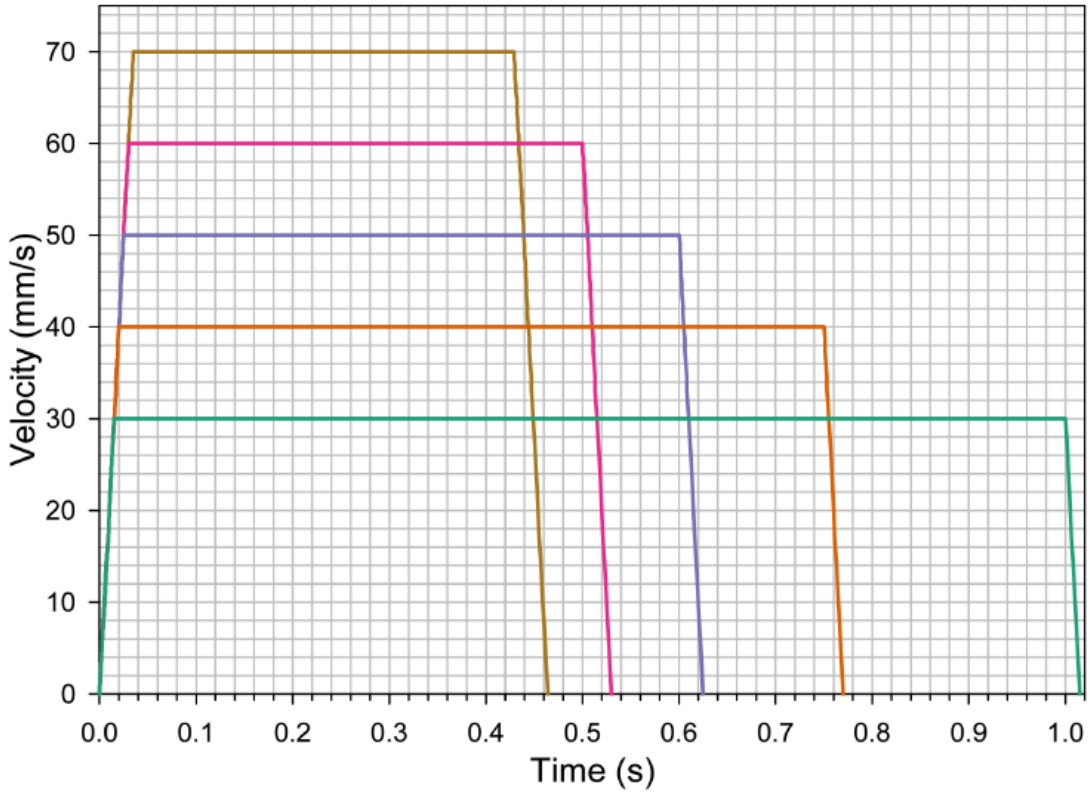

Figure 4.14: Velocity of the print head against time, for each side (wall) of the cube, for each layer, at 2000 mm/s^2 acceleration.

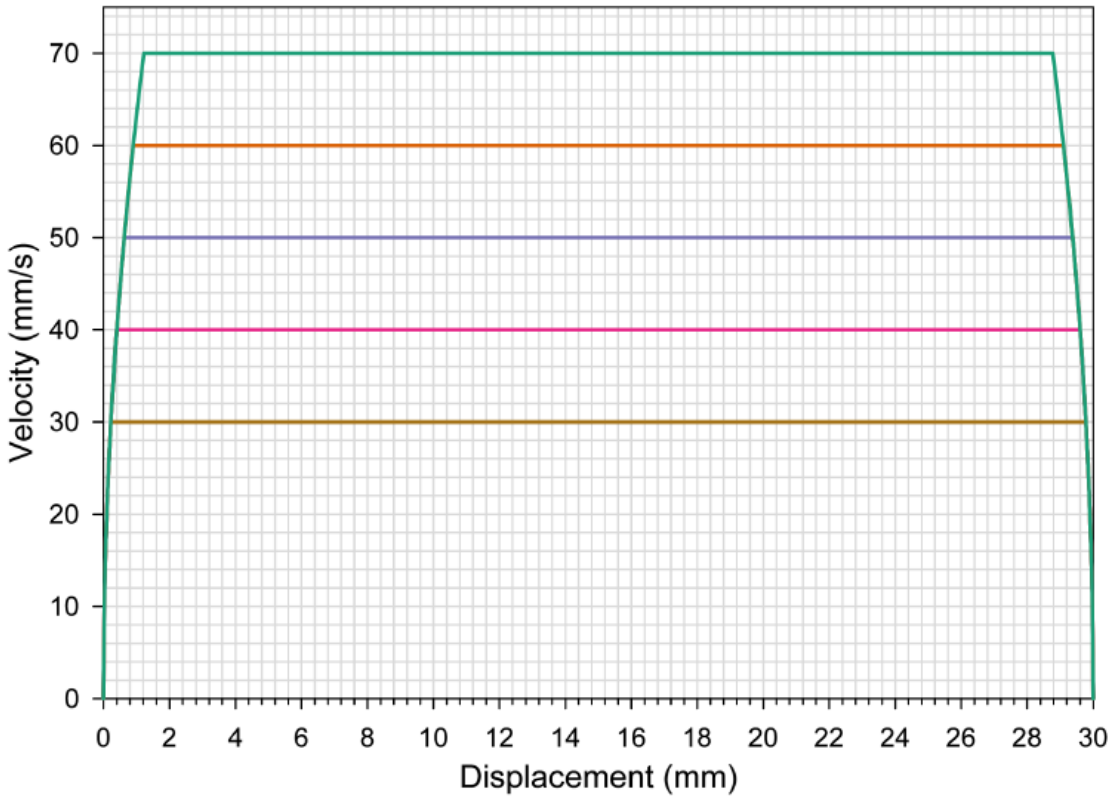

Figure 4.15: Velocity of the print head against displacement from the corner, for each side (wall) of the cube, for each layer, for 2000 mm/s^2 acceleration.

The graphical data shows as the maximum print speed is increased, the time and displacement during acceleration and deceleration increases. Levinskas (2019) discusses the effect of "corner swell" as a phenomenon displayed in high velocity FDM prints (Figure 4.16). If the print head is required to make a sharp turn (which is shown with our cubes and the 90° corner angles) the effects of residual pressure are visible in the "blobbing" at the corners. If the print head is moving too slowly relative to its maximum velocity for that line, the residual pressure inside the nozzle causes over-extrusion as the print head stops for direction change. Due to the pressure within the extrusion system lagging slightly behind the change in extrusion speed, the melted filament does not stop flowing immediately when the extruder stops, and does not start flowing immediately when the extruder starts up again. Therefore at the corners, there is an increase in the amount of material deposited as the print head moves towards the corner (deceleration), and then a decrease in the amount of material deposited as the print head moves away from the corner (acceleration). At the midline of the sides (and for the majority of the side line as it is laid), due to the constant speed (no acceleration at maximum print speed), the deposition of material is constant [133].

Figure 4.16: Representation of a straight line of printed filament starting from rest, arrow shows direction of print head travel. a) print head accelerating to the desired print speed, b) constant speed, c) print head decelerating to a stop. At the end of the printed line (c) the filament is over-extruded.

To combat this effect, Linear Advance Calibration can be used. Linear Advance Calibration is a firmware feature that anticipates and compensates for residual pressure in the nozzle when stopping and starting extrusion. While not removing the residual pressure, this calibration alters the extrusion as the print speed changes, to keep the pressure more constant. The compensation helps to print sharper corners and more consistent wall thickness, by extruding an extra length of material for every 1 mm/s of print speed. This is denoted by a "compression distance" or K-value [134]. The Linear Advance Calibration feature is not standard for slicer g-code in Cura (Ultimaker), but can be input into the start code script using the command M900, or a plugin can be downloaded [135, 136].

The effect of changing the K-value is explained visually in Figure 4.17 - uncalibrated lines start thicker, get thinner as speed is increased, remain constant during constant speed, and thicken as the nozzle speed decreases towards a stop or turn in the print. As the K-value is increased, the thickness during the acceleration/deceleration is decreased, and the line is comparatively thickened during the constant speed section (Figure 4.17, K-value 0.2 and 0.4). The K-value is altered until the acceleration/deceleration phase matches, or is very similar to, the constant speed phase in terms of thickness of printed line (Figure 4.17, K-value 0.6). If the calibration value is increased past this point, the start and end of the line become too thin and the constant speed middle section thickens excessively (Figure 4.17, K-value 0.8 and 1.0) [137]. Linear Advance Calibration is explored more in depth by Arntsonn Tronvoll et al. (2019) [138], with experimental results for 0.2 mm PLA deposition presented in Figure 4.18.

Figure 4.17: Simplified model of Linear Advance Calibration effects on filament deposition; example K-values for PLA and the effect on filament deposition as viewed from above.

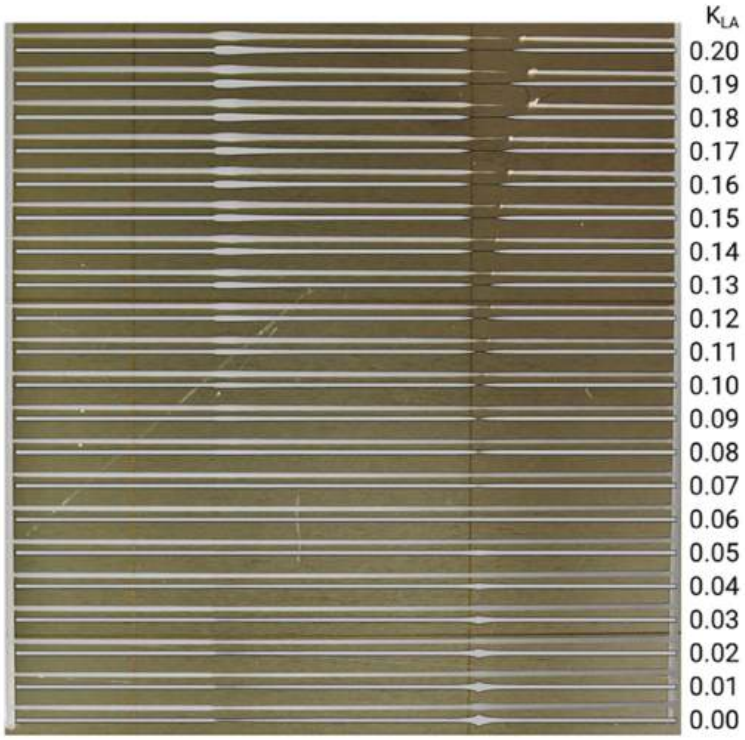

Figure 4.18: Experimental results of PLA filament deposition with Marlin Firmware Linear Advance Calibration [138].

4.4.2 Effect of Print Speed on Scanned Dimensions

Considering the mean maximum dimension difference of the scanned cube compared to the printed cube, there is suggested to be no significant difference, regardless of the print speed used, for 30 to 70 mm/s print speed. The scanned cube maximum dimensions were relatively constant at an average 0.02 mm larger than the printed cube that was scanned. As all the means for the maximum dimension difference fall within both the point distance and accuracy ranges (Figure 3.21) for the scanner, it can be suggested that any perceived differences can be attributed to the error margin of the scanner. Thus it can be suggested that the print speed had a no effect on the scan accuracy for the maximum dimensions of the printed cubes.

It can also be suggested that the mean midline dimension difference of the cubes printed at 70 mm/s was significantly different from the mean midline differences of the other groups, and thus it can be suggested that this is due to the effect of change in print speed, and that the effect on the dimension difference is large. For the scans of the cubes printed at 30 to 60 mm/s, it could be suggested there is no significant difference in the midline dimension difference, and that the scanned cube midline dimensions are constant at an average of 0.07 mm smaller than the printed dimensions. The scan midline dimensions for the group printed at 70 mm/s are significantly smaller than the printed midline dimensions.

The scanner specification [114] states a 'point distance' of 0.17 to 0.2 mm, and an 'accuracy' of 0.03 mm (Section 3.4). The means for all the sample groups for midline dimension difference fall within the scanner point distance range (-0.2 to 0.2 mm), but not within the scanner accuracy range (-0.03 to 0.03 mm) .

4.4.3 Effect of Printing Temperature on Printed Dimensions

Considering the maximum dimensions of the printed cubes, it can be suggested that the samples printed at 180 °C are significantly different in mean maximum dimension from the other sample groups, it can be suggested that this is due to the effect of the change in print temperature, and the print temperature is suggested to have had a large effect on this outcome. Considering the significantly different samples and the trends presented in Figure 4.10 (red), it could be suggested that the print temperature had a large effect when the samples were printed at 180 and 190 °C. As the temperature was increased further beyond that point, the effect became less, to a non-significant level. It could be suggested that the mean maximum dimension plateaus between 190 and 220 °C print temperature, and any perceived difference between the samples here is due to different influencing factors, or accepted levels of error within the manufacturing process.

For the material properties of the PLA filament, the range of print temperature given is the 'usable' print temperature. It is expected that the optimum print temperature would lie within this range, approximately at the median, but with room for the effects of different ambient temperatures and different printer models used. A print temperature that is too low results in the heated filament having a higher viscosity, thus flowing slower than anticipated by the G-Code, resulting in less material being extruded from the nozzle as the print head traverses the toolpath [139]. This results in under-extrusion, and it is expected the printed part would have smaller dimensions than the CAD model. Too high print temperature results in the filament having a lower viscosity and so flowing faster than expected, resulting in over-extrusion. Furthermore, the hotter the temperature of the filament as it exits the print head nozzle, the greater the temperature difference to bridge with cooling in order for the printed filament to solidify. This can result in the extruded filament deforming into a flatter, wider shape before solidifying, potentially causing the print to have greater width dimensions.

It is worth considering that, as in the investigation from Section 4.3.1, the maximum dimensions are found at the corners of the cube - where the print head changes from X axis movement to Y axis movement. The increase in dimension here could also be due to a compounded over-extrusion effect, at the corners due to residual pressure. Higher print temperatures can also cause extrusion during 'travel' movements and non-extruding sections. This is discussed in more detail in Section 4.3.1 (Figure 4.16).

A different trend is presented for the midline measurements. For the mean midline dimensions of the printed cubes, it can be suggested that there are 3 populations with significantly different means; one population printed at 190 °C, one population printed at 200 and 210 °C, and a population printed at 180 and 220 °C. The second order regression line (dotted green) presented in Figure 4.10 supports this. At the extreme ends of the print temperature range, the mean midline print dimension was furthest away from the CAD dimension, and much smaller. In the middle of the range, at around 200 and 210 °C print temperature, the mean midline dimension was closest to the CAD dimension . It can be suggested that the differences in dimension observed between these populations can be due to the large effect of the change in the print temperature.

The trend between 180 and 200 °C is supported by the known material properties of the filament. The range of print temperature given is the usable print temperature, and it is expected that the optimum print temperature would lie approximately at the median. Again, too low temperature results in the heated filament having a higher viscosity, thus flowing slower than anticipated, resulting in under-extrusion. Conversely, the mean midline dimensions decreased when printed at 220 °C. Too high print temperature should result in the filament being low viscosity and flowing faster, resulting in over-extrusion.

4.4.4 Effect of Print Temperature on Scanned Dimensions

Considering the mean midline dimension difference of the scanned cubes compared to the printed cubes as the print temperature was varied, it was suggested that the cubes printed at 220 °C were significantly different from all the other groups, and thus it can be suggested that this is due to the change in print temperature. Post-hoc tests suggested that the effect of the change in print temperature was large. Figure 4.12 presents the midline mean dimension difference (green), and considering the significance testing and the second order regression line pattern, it can be suggested that the print temperature had no significant effect on the mean midline dimension difference between 180 to 210 °C. The scans of the cubes had an average midline dimension that was around 0.08 mm smaller than the dimensions of the physical printed cube. When printed at 220 °C print temperature, the difference between the scan and the print was significantly different, with the scan mean midline dimension 0.05 mm larger than the physical printed cube. Thus, for the 220 °C group, the scans were closer in mean midline dimension than in the other groups.

Taking the absolute value of the dimension difference (Figure 4.13, green) there was found to be no significant difference between any of the groups. This suggests that the print temperature had no effect on the difference in mean midline difference of the scan compared to the print, when considering the absolute value of the difference in midline dimension. Despite the negative correlation presented in the Figure with a large R^2 value, suggesting the scan dimensions are closer to the print dimensions as the print temperature was increased, due to none of the means being significantly different, it can be proposed that the absolute mean midline difference in dimension is approximately 0.07 mm.

Considering both the real difference and absolute difference in dimension for the midline, it can be suggested that when scanned, the cubes printed at 220 °C print temperature had a more accurate midline scan dimension (the scan dimension is closer to the measured print dimension). All scanner midline dimension differences fall within the scanner 'point difference' (0.2 mm), but none fall within the scanner 'accuracy' (0.03 mm) (Figure 3.21). There is room to suggest the dimension difference could therefore be accounted for within the error margin created by the point distance of the scanner.

Conversely, for the mean maximum dimension difference, an opposing pattern was presented for Figure 4.12. The mean maximum dimension difference for the cubes printed at 180 °C print temperature was found to be significantly different to the groups printed at 200, 210, and 220 °C. It can be suggested that this significant difference was due to the print temperature, and that the effect of the change in print temperature was large. Considering this, and the second order regression line presented in Figure 4.12 (red dotted), it is suggested

that the mean maximum dimension difference of the scan compared to the print was not affected significantly between 200 and 220 °C, and averages at 0.04 mm larger. Conversely, for the cubes printed at 180 °C print temperature, the mean maximum dimension difference of the scan compared to the print was found to be significantly different, and the scan was 0.05 mm smaller.

Taking the absolute value of the mean maximum dimension difference of the scan compared to the print (Figure 4.13), there was found to be no significant difference as the print temperature was changed. The absolute mean maximum dimension difference stayed relatively constant around 0.04 mm. All the mean maximum dimension differences fall within the scanner 'point difference', but outside the scanner 'accuracy', so it could be that the difference can be stated to be within the error margin presented by the point distance of the scanner (Figure 3.21).

4.4.5 Further Discussion

Printing more cubes at smaller intervals for speed and temperature would improve the reliability of the findings, and verify or dispel the presented pattern(s) seen in this data. Furthermore, replicating the investigations with a circular print shape (no 90° corners) would enable the effect of the maximum print dimensions at the corners to be explored further, and also brings this research closer to the biomedical application of knee cartilage plugs. Research exploring the surface profiles of the cube faces is undertaken by Hawthorn et al (2024) [131]. Further research would include investigating the effect of filament colour on the accuracy and reliability of the EINSCAN-SP scanner output in the same way.

4.5 Conclusion

In conclusion, the print parameters of print speed and print temperature affected the dimensional accuracy of the 3D printed cubes, and the dimensional accuracy of the scanned models. Specifically:

- Mean maximum printed dimensions increased between print speed 30 mm/s and 50 mm/s.
- Mean midline scanned dimensions were smaller than the printed dimensions, and decreased with increase in print speed.
- As print temperature increased, the mean midline dimensions for the printed cubes appears to follow a hyperbolic trend with the most accurate dimension at 200 to 210 °C.
- As print temperature increased, the scanned mean midline dimension difference and mean maximum dimension difference both increased with change in temperature. Considering the absolute values of the differences, there was no significant change.

4.6 Summary

This chapter explored the effect of AM parameters on the dimensional accuracy of additive manufactured objects and their scanned models, and presents a possible significant effect of

print temperature and speed on certain dimensions, fulfilling the objectives stated in Section 4.1. The next chapter uses the scanned surface geometry gathered in Chapter 3 to design surface modifications and defect filling implants built onto the base geometry (considering the information from Chapter 4), and explores development of the AM toolpaths which generate the implants.

Chapter 5

Toolpath Development

5.1 Introduction

In the previous chapters, the ability of different surfaces to be accurately captured with 3D optical surface scanning was explored. This chapter details the development of the final additive manufacturing toolpaths, to print surface modifications and implants in surface defects on various surfaces. Using the bone model scanned geometry from Chapter 3, surface addition and recess-filling implants were designed. Utilising the results from Chapter 4 - considering the behaviour of the PLA AM under different printing parameters - the additive manufacturing toolpaths to create the implants were developed. The work contained in this chapter aims to fulfil the project objective 3a: generate the toolpath for in situ AM.

As discussed in Section 2.8.1, a research group in Nanjing, China has published results for several in situ AM experiments. Li et al (2017) [11] presents experimental results for in situ AM onto resin anatomic models. A full thickness AC defect and an osteochondral defect were 3D scanned, and resin models were 3D printed based on the 3D scan data. A modified Bio-Architect 3D printer filled the defects in the resin models with AM using UV cured hydrogel. The prints were considered successful in filling the defects and replicating the functional geometry, however, there was no discussion or explanation of toolpath development for in situ AM. Ma et al (2020) [12] presents the further developed process, now including robot-assisted in situ 3D printing. Again, a resin model was 3D printed, this time from 3D data acquired using micro CT of a rabbit femoral condyle with an AC defect. In situ AM to fill the defect in the resin model was completed. The procedure was repeated to fill an AC defect on a live rabbit femur. Limits to the toolpath design / registration methods are suggested by the manual positioning of the printer nozzle at the implant print origin. Furthermore, there was no explanation of the in situ AM toolpath or its development.

The aim of the work presented in this chapter was to bridge this gap in the technical knowledge base of toolpath development for in situ additive manufacture. The aim was achieved by the following objectives:

1. Design a virtual AM toolpath model for filling a simple geometric defect.
2. Evaluate methods for extracting the surface geometry of interest from 3D scan models
3. Develop an extrinsic registration method for maintaining accuracy of implant placement during the AM process

4. Design AM toolpaths for in situ AM onto various surfaces
   (a) Onto a 3D printed object
   (b) Onto a clay model approximating a surface contour of a human femoral condyle
   (c) Onto a bone model (an 'unknown' surface)

5.2 Virtual Toolpath Planning

5.2.1 Introduction

Preliminary research into in-situ 3D printing onto an objects surface was conducted via a 'virtual printer'. Repetier-Host software (Hot-World GmbH & Co. KG, Germany) [140] is a MEX-TRB AM toolpath generator, and offers more customisation and editing options than other companion softwares such as Ultimaker Cura (UltiMaker, Netherlands) [141]. Repetier can display the non-extrusion "travel" movements (orange), as well as the virtual filament deposition in purple. It can also display the filament deposition in a spectrum of colour corresponding to the speed of extrusion. The generated G-Code, which details the instructions the printer receives, is fully editable within the software itself. Furthermore, G-Code files can be opened as a .txt file and manually edited in the Windows 10 Notepad application.

5.2.2 G-Code

G-code, also known as preparatory code, is a numerical control programming language. Repetier-Host (or any other 'slicer' program) converts the STL or AMF file containing the geometry of the 3D print, into G-Code. The G-Code is made up mostly of "G" commands ("Geometric" commands) which instruct the extruder head to move within the coordinate system of the print volume. These movements can be 'G0' instructions which control movement of the extruder head without filament extrusion, or 'G1' instructions which control movement with simultaneous extrusion of the filament. In the Repetier-Host software, 'G0' is also known as "rapid move", where the extruder head moves at "fast" speed to the given position. 'G1' is known as a "controlled move", where the extruder head moves in a line to the given position.

An 'F' parameter controls the rate of the movement in 'G' commands, and during G1 (extrusion movements) the 'E' parameter controls the amount of extrusion (mm). Other basic parameters controlled in the G-Code include 'M' commands, which are non-geometric. For example, M107 turns the filament cooling fan off, and M104 sets the temperature of the filament extrusion. Parameters X, Y and Z set the Cartesian coordinates of movement of the extruder head within the print volume. For the Creality Ender 3 v2, when facing the front of the printer, the X denotes left to right positioning, Y denotes back to front position, and Z denotes the height. The default Z position is considered as relative to the bed, which is calibrated to have a position of Z 0.00. Code commands and examples of their use are included in Appendix B.

5.2.3 Virtual Base and Implant

Two CAD objects were created - a "base" and an "implant" (Figure 5.1). The base had external dimensions of height 3 mm, and a 4 mm cross section diameter, with a recess centred on the top surface. The recess represented a top surface defect of diameter 2 mm, and depth 2 mm. Articular cartilage has variable geometry depending on its location on the articulating surface, and natural variation in human anatomy. A mean that is referenced in the literature of between 2 and 3 mm depth is used for the purpose of this model. A "critical sized" human cartilage defect is defined by Onofrillo et al. as a defect of 80 μl volume (80 mm^3) [8].

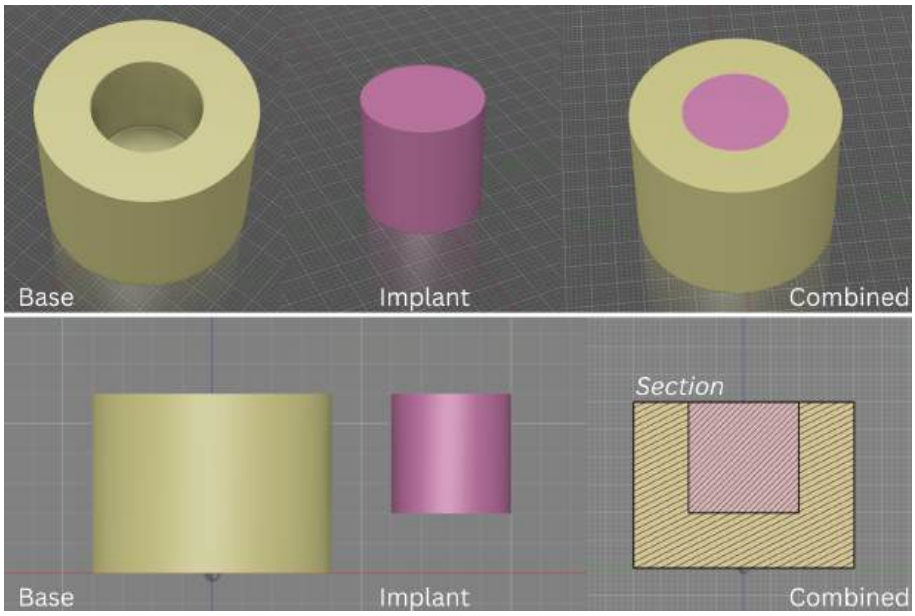

Figure 5.1: CAD models of the base and implant, and the combined model. Top: 3D perspective. Bottom: Left: side view of the base and implant. Right: Bisecting section of the implant combined with the base.

The CAD base and implant models were exported as STL files and uploaded to the slicer software, Repetier-Host. The objects were sliced with a layer height of 0.2 mm. Therefore the base print comprised of 10 layers (Figure 5.2), and the implant of 7 layers (Figure 5.3). Labelled in Figure 5.2 is the virtual toolpath print model of the base. In orange are the "travel" extruder head movements, controlled with G0 commands; in purple, the virtual modelling of the filament deposition; and on the right, the window for direct editing of the G-Code commands.

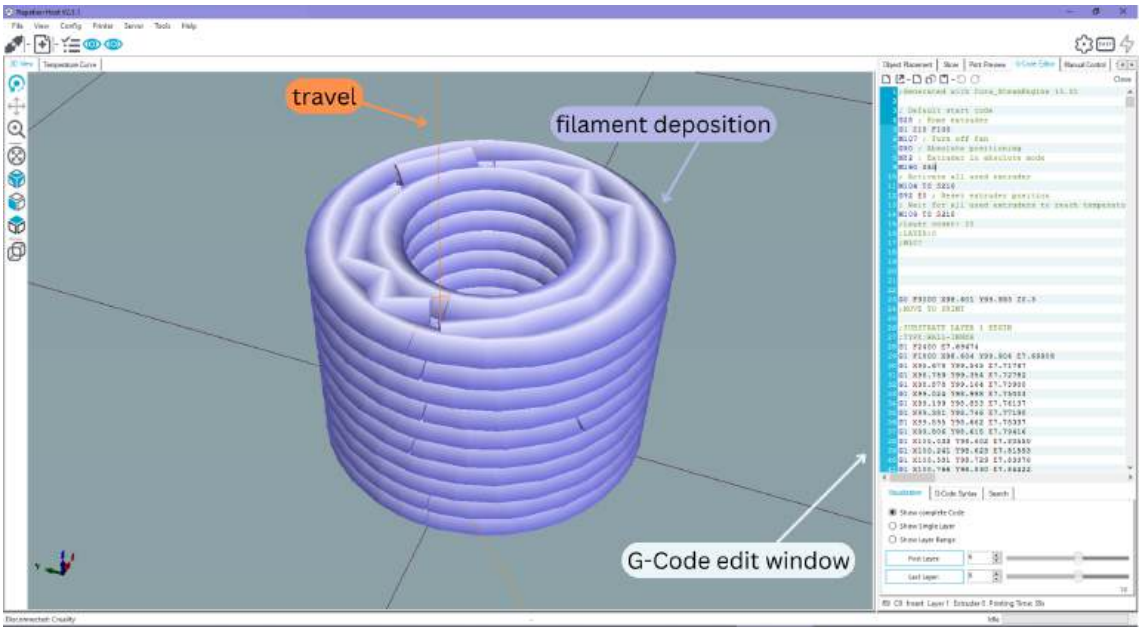

Figure 5.2: Toolpath simulation in Repetier-Host software of the base print. Dimensions: 4 mm outer diameter, 2 mm inner diameter, recess depth 2 mm.

Manual Editing of the Z Value

The implant model was also imported and virtually printed as a single object (Figure 5.3). For the preliminary method for printing the implant in the recess of the base, the start of each layer was manually edited by increasing the Z value by 1. This moved the whole print up (in the Z direction) by 1 mm. An example of the code edit for Layer 2 is presented in Figure 5.3 - after layer 2 starts, the original G0 command Z value has been changed from the generated value of Z0.600 to Z1.600.

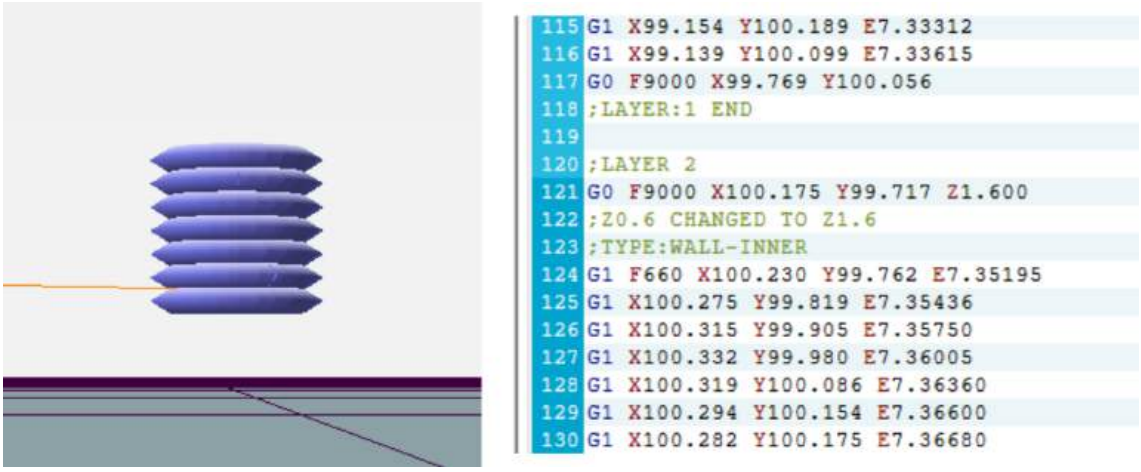

```
115 G1 X99.154 Y100.189 E7.33312
116 G1 X99.139 Y100.099 E7.33615
117 G0 F9000 X99.769 Y100.056
118 ;LAYER:1 END
119
120 ;LAYER 2
121 G0 F9000 X100.175 Y99.717 Z1.600
122 ;Z0.6 CHANGED TO Z1.6
123 ;TYPE:WALL-INNER
124 G1 F660 X100.230 Y99.762 E7.35195
125 G1 X100.275 Y99.819 E7.35436
126 G1 X100.315 Y99.905 E7.35750
127 G1 X100.332 Y99.980 E7.36005
128 G1 X100.319 Y100.086 E7.36360
129 G1 X100.294 Y100.154 E7.36600
130 G1 X100.282 Y100.175 E7.36680
```

Figure 5.3: Toolpath simulation in Repetier-Host software of the implant print. Dimensions: 2 mm diameter, 2 mm height. The print has been manually moved "up" by adding 1 mm to the slicer generated Z position at the beginning of each layer.

Dual Extrusion Simultaneous Print

The base and implant CAD were imported into the same workspace in Repetier-Host. After aligning the two objects, the combined objects were sliced with the same settings. In this model, the base and implant objects are set to be printed with different filaments. The virtual printer in this set up has two extruder heads which supply different (virtual) filaments. Filament 1 (T0 in the code, presented in purple in Figure 5.4) prints the base, and filament 2 (T1 in the code, presented in dark blue in Figure 5.4) prints the implant.

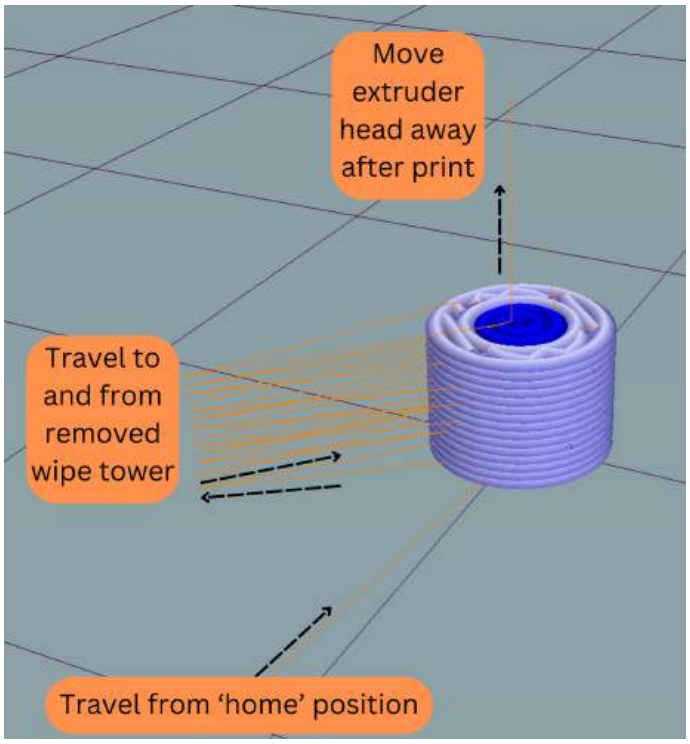

Figure 5.4: Screen-capture of the base and implant objects virtually printed together in Repetier-Host software. Both objects were printed together using different (virtual) filaments for each object. The wiping tower deposition code has been removed, leaving the travel movements between the print and the tower.

In the first iteration of development, both objects were printed simultaneously (Figure 5.4). The filament / extruder head swaps part way through each layer when both objects are being printed. The default settings for multi-filament prints includes a "wipe tower" when changing from one filament to the other. The extruder head moves away from the object and the other filament is printed in a layer in the wipe tower before the extruder head returns to the object and finishes the current layer in the object in the new filament. The next layer begins with the current filament, and then the wipe tower swap is performed again, with the original filament printing a wipe tower layer before returning to complete the object layer. In the interest of simplifying the virtual model, the wipe tower extrusion code was removed.

Dual Extrusion Print in Series

Version 1

The dual extrusion method was developed further, by combining the G-Code for the individual base and implant in series, such that the base is printed in full and then the implant is printed in full after. Unedited, the toolpath instructs the extruder head to begin the implant print with a travel movement that crosses the printed geometry of the base. This is shown in Figure 5.5 (Left), where on the left side, two orange travel lines are visible. One for the original movement from the 'home' position to the start of the base, a second for the movement from the 'home' position to the start point of the implant.

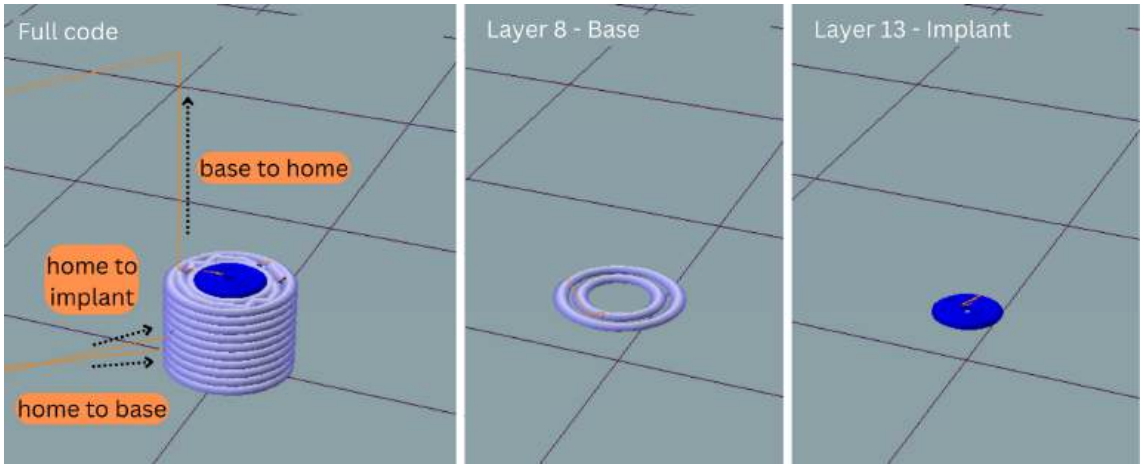

Figure 5.5: Screen-capture of the base and implant objects virtually printed in series in Repetier-Host software. The base and implant were printed using different (virtual) filaments for each object. The toolpath is unedited, so the print head moves "through" the base (Object 1) to start the implant (Object 2). Left: Full virtual print of base and implant in series. Middle: Isolated layer 8 - base layer 8. Right: Isolated layer 13 - implant layer 3.

General code structure - Version 1:

DEFAULT START CODE

Temperature settings for the bed and extruder, initiates bed levelling or use of stored bed level data, defines absolute or relative motion and extrusion, and "home" the print head. The default start code was updated from factory settings to include a "test line" print, and to turn off Power-loss Recovery. The test line means the printer settings / bed levelling can be adjusted before the full print begins if issues are presented. Power-loss recovery mode, while useful for long prints (multiple hours) in case of unexpected power failure, generates small but noticeable over-extrusion in each layer at the point where it saves the progress. As it is not needed for the short prints described in this thesis (<10 min) it is turned off to improve the print quality.

CODE FOR BASE PRINT

MOVE EXTRUDER UP AND AWAY FROM PRINT

HOME EXTRUDER

Print head returns to "Home" position.

DEFAULT START CODE (REPEATED)

The test line can be set to be repeated if there is "dwell" time in-between prints, to ensure the filament is extruding properly again before attempting the first layer of the second print.

CODE FOR Z+1 IMPLANT PRINT

END CODE

Reverse extrusion to reduce stringing after finishing the last layer. Move extruder up and away from the print. Move the bed forward to allow access to the finished print. The default end code was also customised to include an audible series of "beeps" to alert that the print is complete.

Version 2

The toolpath was edited to ensure the extruder head travel movements avoid the already generated base print when moving from the 'home' position to the start point of the implant print (Figure 5.6). The toolpath thus finishes the base print (at layer 10) and moves the extruder head to the 'home' position, the filament is swapped, and the extruder head travels up above the base print (avoiding colliding with the base geometry), before travelling straight down to the start point of the implant print, on the bottom surface of the base recess.

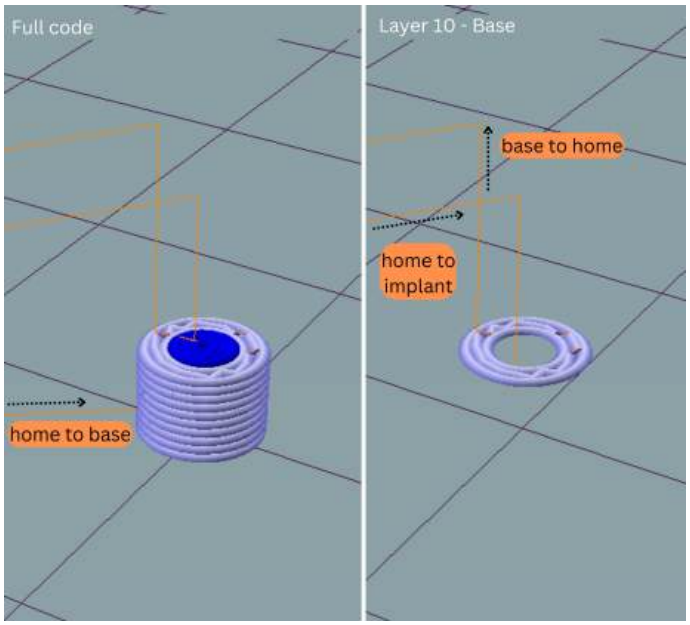

Figure 5.6: Screen-capture of the base and implant objects virtually printed in series in Repetier-Host software. The base and implant are printed using different (virtual) filaments for each object. The toolpath is edited so the print head returns to the "home" position after the first print, and moves around the printed base into the recess, to begin the implant print. Left: Full print with travel lines. Right: Isolated last layer of the base, and the subsequent travel movement of the print head to begin the first implant layer without colliding with the base.

General code structure - Version 2:

DEFAULT START CODE

Temperature settings for the bed and extruder, initiates bed levelling or use of stored bed level data, defines absolute or relative motion and extrusion, and "home" the print head. Power-loss recovery mode turned off. Test line printed.

CODE FOR BASE PRINT

MOVE EXTRUDER UP AND AWAY FROM PRINT

HOME EXTRUDER

Print head returns to "Home" position.

DEFAULT START CODE (REPEATED)

The test line can be set to be repeated if there is "dwell" time in-between prints, to ensure the filament is extruding properly again before attempting the first layer of the second print.

** Manually added in movement commands to move the print head from the "Home" position to a point centred above the top of the base print. Thus, the subsequent movement of the nozzle to the first point of the implant code is a single straight vertical movement down into the recess (rather than across from the "Home" position "through" the printed base.

CODE FOR Z+1 IMPLANT PRINT

END CODE

Reverse extrusion to reduce stringing after finishing the last layer. Move extruder up and away from the print. Move the bed forward to allow access to the finished print. An audible series of "beeps" alerts the user that the print is complete.

5.3 Preliminary In Situ Method Development

5.3.1 Extraction of 3D Scanned Surface for Design of Conformal Implant

Chapter 3 describes experimental work to determine optimal scanning settings for capturing the surface geometry of Sawbones bone models (Sawbones, USA). The dark colour truncated bone model was scanned using the EinScan-SP 3D scanner and the generated CAD models were used to investigate surface cloning and surface extraction within Autodesk Fusion 360 software (Autodesk, USA). The aim was to extract a portion of the top-most geometry of the polygon mesh surface model of the bone to use, as a NURBS surface, to build an implant CAD model onto. This implant CAD 3D solid model could then be separated from the surface, exported to AM toolpath preparation software, and used to generate an AM toolpath which could 3D print a solid object which conforms to the surface geometry of the physical bone model. Explanations of the different types of 3D modelling used in this chapter are found in Section 2.5.

The polygon mesh models generated by the 3D scan data were exported to Meshmixer software (Autodesk, USA) [52] as .3mf files. Meshmixer was used to select and extract a section of the full polygon mesh model (Figure 5.7). In the case that the extracted mesh section consisted of more than 10,000 triangles, the mesh was reduced via the 'Mesh Reduce' function, with a Triangle Budget of 10,000. The extracted section of polygon mesh model was exported as a .3mf file and opened in Fusion 360 (Figure 5.8). Fusion 360 does not support mesh/NURBS Boolean operations. In order to use the extracted section as a splitting tool on the implant CAD body, the polygon mesh model was first converted to a NURBS surface model (shown in Figure 5.9).

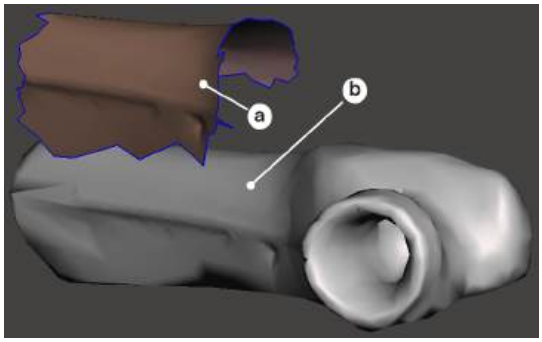

Figure 5.7: A section of the polygon mesh (a) from the full model (b) has been cloned and offset, in Meshmixer.

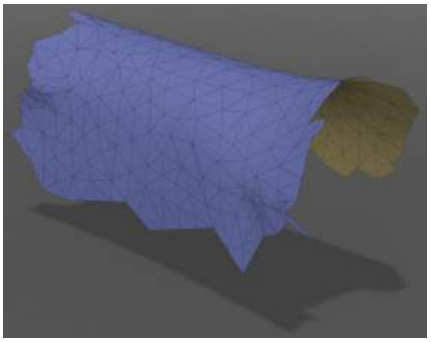

Figure 5.8: The polygon mesh section in Figure 5.7 (a), exported from Meshmixer, and imported in Autodesk Fusion 360, with the mesh arrangement visible.

To create the basic geometry of the surface modification implant, an offset plane was created at 400 mm (Z direction / vertically) from the origin. Originally a simple rectangular cross-section (200 x 125 mm) was sketched on the offset plane, and a new body was extruded from the sketch down (negative Z direction) until it fully intersected with the extracted top surface model. The new body was bisected using this intersecting surface as the 'splitting tool', creating two bodies. The top body has a rectangular cross-section and its bottom surface conforms perfectly to the top surface of the bone scan model (Figure 5.9). The

bottom body was discarded. The top body (the surface modification implant) was extracted and saved as an STL file. It had the following height measurements at the corners, measured from the horizontal top surface: 39.00, 42.90, 55.67, and 44.14 mm. The smallest height measurement was on the shortest side, of 26.48 mm.

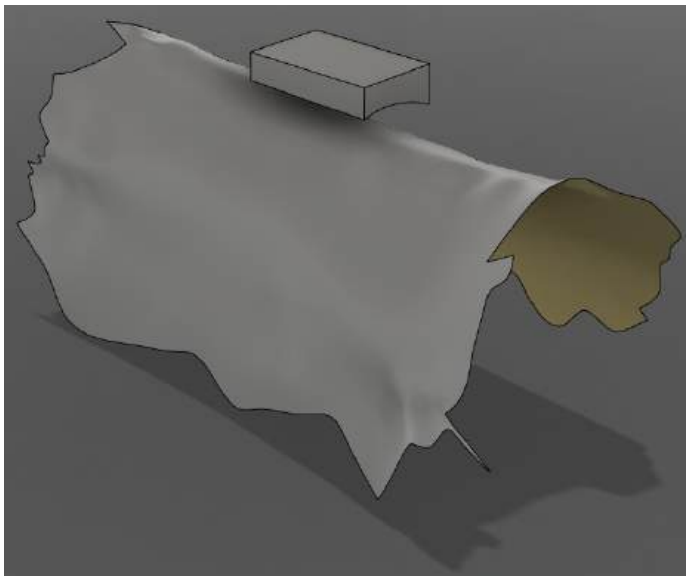

Figure 5.9: The extracted polygon mesh surface was converted in Fusion 360 to a NURBS surface, and a surface modification implant CAD model was built upon it. The implant model is offset vertically here to show the complementary surface geometries.

5.3.2 Orientation and Alignment of the Implant - Z Direction

The next step became how to orient the implant in the 3D printer print volume after it has been sliced, so that the implant toolpath would align correctly and build the implant conformally on the top surface of the bone model placed within the printer workspace. One method originally considered, demonstrated visually in Figure 5.10, was to extract a small section of the bottom surface (2) of the scanned bone model when extracting the top surface (1). Exporting them together as one mesh model, the top surface remains at a constant distance (vertically, Z direction) from the base of the CAD environment. Thus the bottom of the implant CAD model, when built onto this top surface, remains a constant distance from the print bed. When exporting the implant CAD model into the G-Code slicer (Repetier-Host), the toolpath for extrusion can be ensured to begin at this Z height. The G-Code development for this technique is discussed further in Section 5.4.

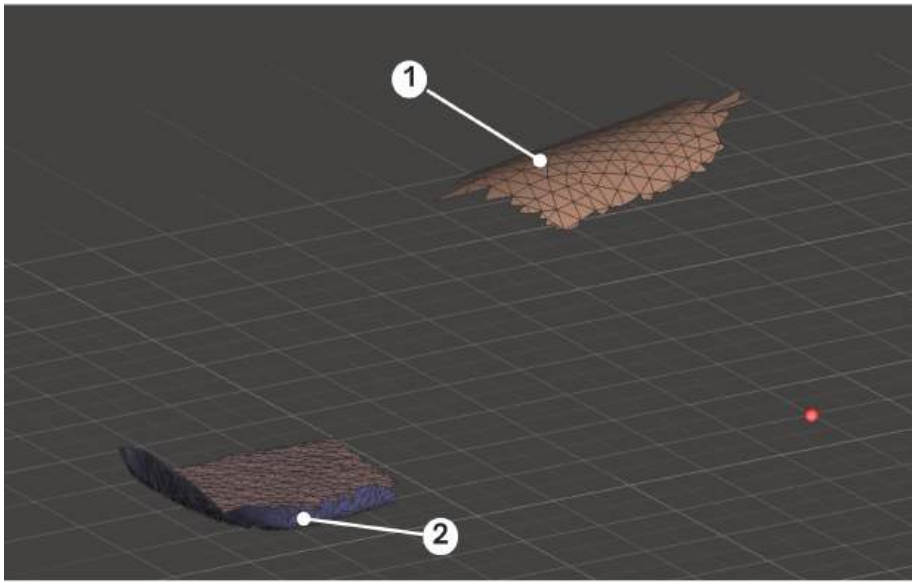

Figure 5.10: A section of polygon mesh extracted from the bone model 3D scan data. This extracted section of mesh includes a top surface geometry (1) and a section that is aligned with the floor of the virtual environment (2).

5.3.3 Orientation and Alignment of the Implant - XY Plane

The method outlined in Section 5.3.2 leaves alignment in the X and Y directions unaddressed. A solution to this is proposed in the form of a 3D printed alignment frame. Section 2.7 details current uses for frames and holders, for alignment and registration, in surgical procedures. The theory method of using an alignment frame for experiments in this thesis is presented in Figures 5.11, 5.12 & 5.13.

The alignment frame is designed (Figure 5.11a) such that it has inner dimensions that are greater than the maximum dimensions of the object to be printed onto - for example, the bone model. The dark colour bone model had overall maximum dimensions of 199.90 x 81.00 mm. The alignment frame CAD model, designed in Fusion 360, had inner dimensions of 200 x 84 mm, a wall thickness of 2 mm, and height 3 mm.

The alignment frame was converted into g-code and 3D printed (Figure 5.11b). Air drying clay [142] was pressed into the printed alignment frame, and the dark colour bone model was pressed into the clay, to create a moulded holder which fits around the bone model (Figure 5.11c). After air drying for 48 hours, the bone model and alignment frame were removed, leaving the solid clay moulded holder. For all subsequent scans of the bone model, it was placed into the clay holder to facilitate consistent orientation of the bone model (Figure 5.11d).

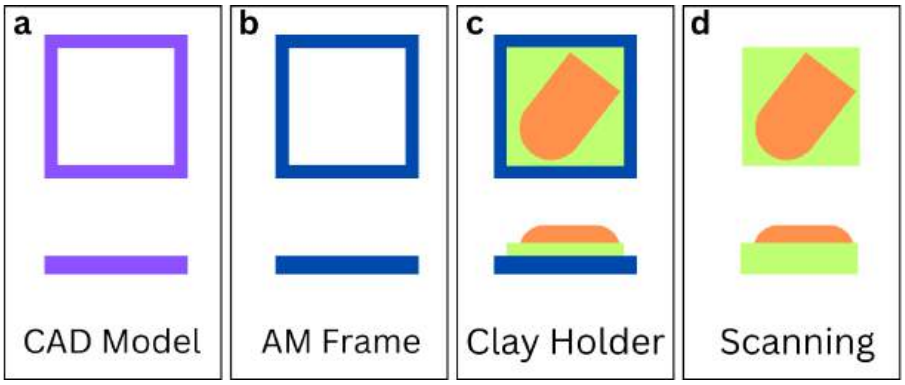

Figure 5.11: The steps for creating a holder that keeps the bone model in consistent orientation for scanning and in situ AM. (a) Design the alignment frame in Fusion 360. (b) 3D print the alignment frame. (c) Mould the clay inside the alignment frame to create the holder. (d) The bone model is placed in the holder for scanning.

The process of 3D scanning the bone model is thus modified to include the clay holder. The bone model oriented in the holder was scanned as an assembly (Figure 5.12a). The scan data point cloud (Figure 5.12b) was converted to a polygon mesh, and the surface model manipulated as described in Section 5.3.1 and Section 6.3.3. The CAD model for the alignment frame is imported into Fusion 360 along with the scanned mesh model, and they are aligned such that the scanned geometry of the holder is inside the alignment frame. The CAD model for the implant is built upon the surface model of the scanned bone (Figure 5.12c). When complete, the implant CAD model and the alignment frame CAD model are extracted and exported together as a single STL file (Figure 5.12d).

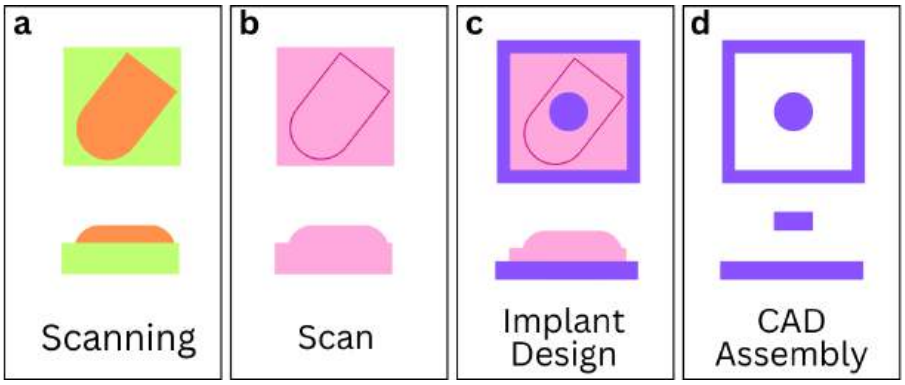

Figure 5.12: The steps for designing the implant CAD model. (a) Scan the bone model in the holder. (b) Convert the scan data to a mesh model. (c) Import the frame model and the scan model into an assembly, and build the implant CAD geometry. (d) Extract the frame and implant CAD as a single model.

The STL file is converted to g-code (Figure 5.13a). The STL model was sliced with 0.2 mm layer height in Repetier-Host and 3D printed using the Creality Ender 3 v2. The alignment frame is printed first (Figure 5.13b), then the holder and bone model are placed into the alignment frame on the print bed (Figure 5.13c). The implant is then 3D printed onto the bone model (Figure 5.13d). After the AM in situ process is complete, the bone model, complete with in situ conformal 3D print, can be removed from the print bed (Figure 5.13e).

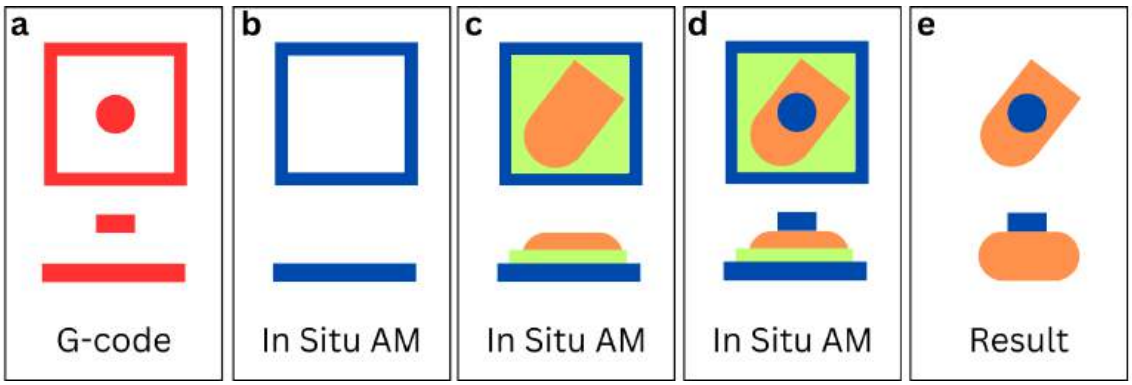

Figure 5.13: The process steps for in situ AM. (a) The STL model of the frame and implant is converted to g-code. (b) The frame is 3D printed. (c) The holder and bone model are placed inside the frame in the print volume. (d) The print for the implant is completed on the surface of the bone model. (e) After completion, the bone model can be extracted with the implant.

Converting this process to a surgical environment would require alterations to adapt to the shape of the anatomy being printed on, and to take the rest of the patient's body into account. Section 2.7 details how current registration methods are used in orthopaedic surgery to enable computer- and robot-assisted surgery with pre-planned toolpaths. Using fiducial markers on an alignment frame surrounding the patient's knee anatomy, the implant toolpath could be oriented to the frame. With the frame oriented to the patient's anatomy using optical scanning and/or medical imaging, the implant toolpath would in turn be oriented to the patient's anatomy.

5.4 G-Code Development

5.4.1 Printing onto 3D Printed bases

After virtual experiments (Section 5.2.3) to explore the methodology of designing an in situ conformal 3D print, G-Code was developed for a series of physical experiments. The first experiment included start and end G-Code development for in situ printing onto an object that has been previously 3D printed. The slicer settings are described in Chapter 6, alongside more in depth description of the various base geometries investigated. An example start and end code is presented in Appendix C, but for brevity the general structure of the code for in situ printing onto a 3D printed base is described here:

START CODE

Temperature settings for the bed and extruder.

Initiate use of stored bed level data, defines absolute extrusion mode, and power-loss recovery mode turned off.

CR-Touch probe in centre of the print bed.

Manually added in print head travel movement, to avoid colliding with the holder when travelling from centre probe point to the "home" position.

Test line printed.

Move print bed forward to allow access.

"Dwell" to allow placing of the 3D printed base into the holder attached to the print bed.

Beep to alert user to end of "dwell" period.

Return extruder to "home" position.

Move print head up 20 mm (height of the top surface of the 3D printed base).

From now on consider the current Z position as Z = 0.

CODE FOR IMPLANT PRINT

Code for implant as if it was being printed on the print bed (Z = 0).

END CODE

Relative positioning begins

Reverse extrusion (to reduce stringing after finishing the last layer).

Move extruder up and away from the print.

Move the bed forward to allow access to the finished print.

An audible series of beeps alerts the user that the print is complete.

5.4.2 Printing onto Clay bases

Developing the methodology for increasingly "unknown" surfaces, start and end G-Code was developed for in situ printing onto an object that has been moulded from air-drying clay. The slicer settings are described in Chapter 6, alongside more in depth description of the various base geometries investigated. Example start and end code is presented in Appendices D & E, but for brevity the general structure of the code is described here:

START CODE

Temperature settings for the bed and extruder.

Initiate use of stored bed level data, defines absolute extrusion mode, and power-loss recovery mode turned off.

CR-Touch probe in centre of the print bed.

Test line printed.

Cut generated code for the alignment frame (from Layer:0) and paste into code here.

Reset extruder; current extrusion is 0.

Move print bed forward to allow access.

"Dwell" to allow placing of the prepared clay base into the printed alignment frame.

Beep to alert user to end of "dwell" period.

Return extruder to "home" position.

Test line printed.

Reset extruder; current extrusion set to match last extrusion value of the frame print.

Move print head up above the height of the base, and across to the approximate XY centre of the print bed.

CODE FOR IMPLANT PRINT

Code for implant begins.

END CODE

Relative positioning.

Reverse extrusion.

Move extruder up and away from the print.

Absolute positioning.

Move the bed forward to allow access to the finished print.

An audible series of beeps alerts the user that the print is complete.

5.4.3 Printing onto Model bone

Finally, start and end G-Code was developed for in situ printing onto a bone model that has been scanned - a completely "unknown" surface; The slicer settings are described in Chapter 6, alongside more in depth description of the process. The general structure of the start and end code is the same as presented in Section 5.4.2 above. An example G-Code is included in Appendix F.

5.5 Summary

The aim of the work presented in this chapter was to bridge this gap in the technical knowledge base of toolpath development for in situ additive manufacture. This chapter detailed the development of the toolpath planning process and methodology, fulfilling chapter objective 1. Methods for extracting surface geometry from the 3D scan models were evaluated (chapter objective 2), and the extracted surface was used to design CAD models of surface-addition and recess-filling prints. In creating the general structures of the G-Code files for each type of in situ AM performed in each stage of the experimental process (chapter objective 4), a registration method for maintaining accuracy of the implant placement was developed (chapter objective 3) in the form of an AM alignment frame. Thus the theory base for the process of in situ AM is outlined. In the following chapter, the different stages of experimental prints are presented in more depth, starting with the in situ additive manufacturing onto 3D printed bases.

Chapter 6

In Situ Additive Manufacturing

6.1 Introduction

The previous chapters have covered the stages of in situ print design and preparation - using the scanned surface geometry to design a conformal print, and planning the additive manufacturing toolpath to generate the print in situ. This chapter describes the development of experimental testing of the in situ additive manufacturing techniques, starting with AM onto previously additively manufactured bases. The stages of the first experimental workflow are presented in Figure 6.2 as bases of increasing design complexity. These bases, increasingly more accurately modelling the geometry of the articular surface of the knee (Figure 6.1), were modelled in CAD (Autodesk Fusion 360) [143] and additively manufactured by the Creality Ender 3 V2 3D printer (Creality, UK) [144]. Conformal surface prints were designed in Fusion 360, and additively manufactured in situ onto the top surface of the bases. 3D printing onto a curved surface offers particular challenges to in situ additive manufacturing. The curvature of the surface that is accessible by the printer is limited to the geometry of the print head and nozzle installed. If the nozzle does not extend past the base of the print head a sufficient length, the base of the print head will collide with the higher part(s) of the curved surface during the lower layers of the print. Furthermore, the importance of accurate alignment of base structure and AM in situ print is increased. Misalignment can be greatly amplified depending on the curvature of the base top surface and the resolution of the print layers, which is limited by the printer and nozzle used.

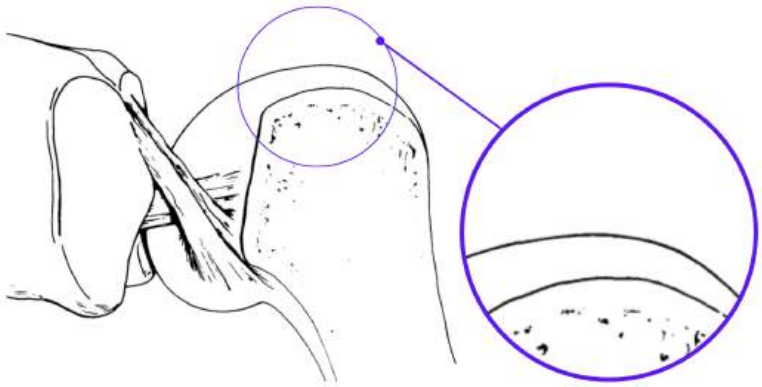

Figure 6.1: Visual of the articulating surface of the human knee, highlighting the surface contour. Original image courtesy of Blackburn & Craig (1980) [145].

The 3D printer was originally installed with the standard 0.4 mm brass nozzle, and fitted with a CR Touch bed probe (Creality, UK) [146]. All prints described in this chapter were printed in blue or red PLA filament from RS Components Ltd. (UK) [147, 148, 149, 150]. The process presented in Figure 6.2 highlighted and facilitated understanding of some of the issues to be overcome before attempting to print onto fully "unknown" surfaces. An "unknown" surface is defined as a surface which has not been designed or generated through known tool paths.

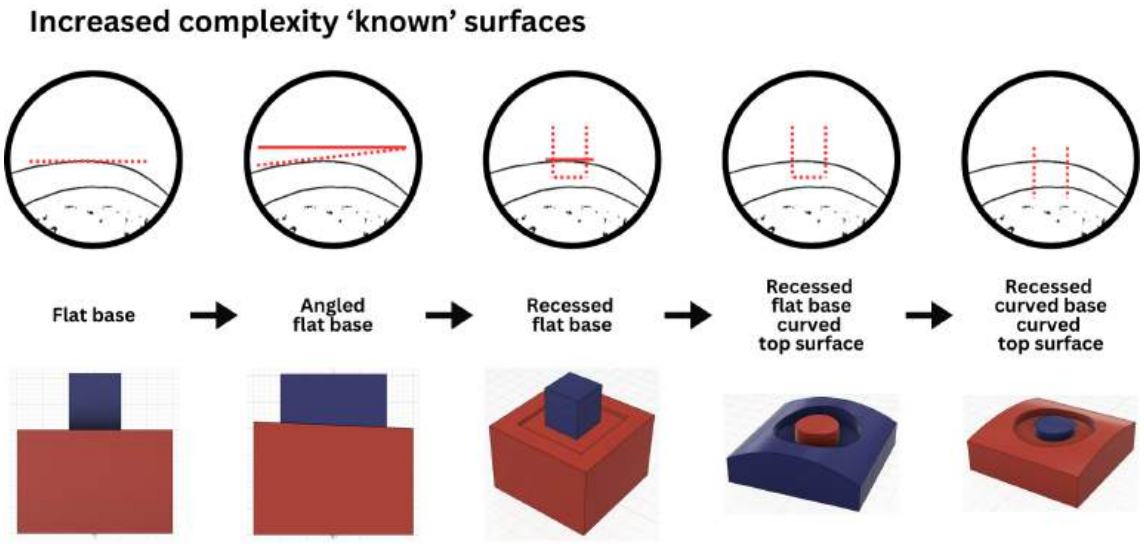

Figure 6.2: The base and implant CAD models for the first stage of the in situ AM print experiment process (Section 6.2), with reference to the anatomical surface geometry of the articular cartilage surface presented in Figure 6.1. The CAD models for the AM prints are presented from left to right, increasing in their complexity to better approximate different elements of the AC gross anatomy.

The process presented in Figure 6.2 helped to highlight and understand some of the issues to be overcome before attempting to print onto "unknown" surfaces. The experimental workflow for the increasingly more 'unknown' surfaces is presented in Figure 6.3. First, the geometry of

the articular cartilage surface contour (Section 2.2) and surgical preparation of articular cartilage defects for implant (Section 2.4) were considered, and simplified models were designed and manufactured in clay. MEX-TRB/P/PLA implants were designed and in situ additively manufactured on these models, experimentally demonstrating the theory outlined in Chapter 5, and presenting the capabilities of this theory to meet project objective 3. The final stage of proof of concept experiment was then completed; a Sawbones bone model was 3D scanned and a conformal in situ additive manufactured object was built upon the fully "unknown" top surface of the model.

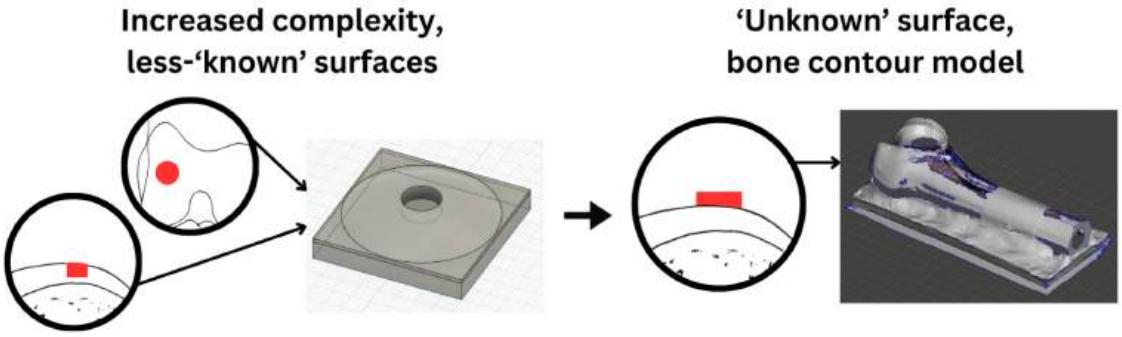

Figure 6.3: The CAD model for one of the clay bases (Section 6.3), and the mesh model of the physical bone model (Section 6.4) with reference to the anatomical surface geometry of the articular cartilage surface presented in Figure 6.1.

The aim of the work in this chapter was to experimentally validate the theory that meets project objective 4; formulate techniques to use in situ additive manufacturing for specific surgical procedure(s), for repair of articular cartilage defects in the knee. Referring to the criteria for successful proof of concept outlined in Section 2.9, the objectives to meet this aim were:

1. A PLA object additively manufactured in situ on the surface of another object
   (a) Where the base object is an AM print
   (b) Where the base object is a model approximating the contour of the articular cartilage surface
   (c) Where the base object is a fully "unknown" surface
2. A PLA implant is additively manufactured in situ into a model recess that is considered an approximation of an AC defect
3. Positioning of the nozzle at the origin of the AM in situ print is part of the automated toolpath (not manually positioned)

A successful in situ AM print is considered to have accurate implant location within 1 mm in X and Y print bed axes, visually conformal surface matching between the AM in situ print and the base object, and no damage to the base object from the nozzle due to the toolpath taken.

6.2 Additive Manufactured Bases

6.2.1 Base A - Basic Cuboid

The primary cuboid base design is developed from the cube design used in Chapter 4. The CAD model of the base (red) with the surface print (blue) is presented in Figure 6.4. The base has top face dimensions of 30 x 30 mm, and a height of 20 mm. The surface print is a cuboid of 10 x 10 x 11 mm, and is positioned on the top face of the base, in the centre of the face.

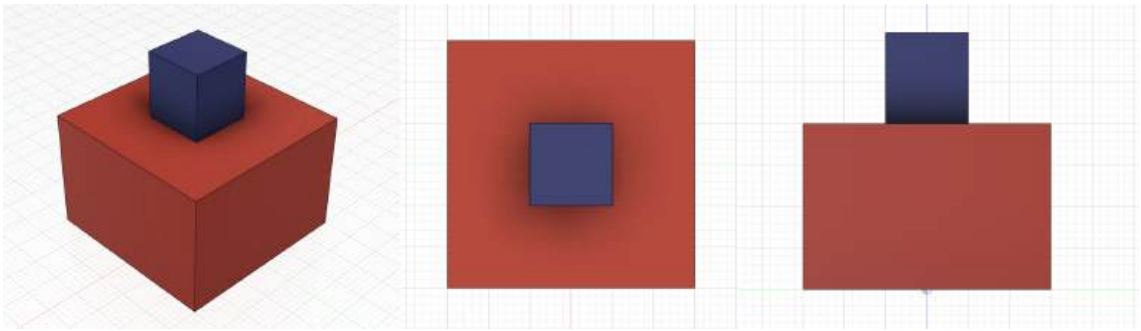

Figure 6.4: Base A (30 x 30 x 20 mm) (red) with cuboid surface print (10 x 10 x 11 mm) (blue) CAD model in Fusion 360.

The main slicer settings are presented in Table 6.1. Other settings included a solid 100% top and bottom layer infill, and the perimeter of each layer was deposited before the infill. The G-Code development for in situ AM onto this type of base is discussed in Chapter 5 Section 5.4.1. Example code for the Start and End G-Codes are given in Appendix C.

Table 6.1: Base A slicer settings

Setting	Value	Unit
Print speed	30 to 70	mm/s
Travel speed	150	mm/s
First layer print speed	30 to 70	mm/s
Outer perimeter print speed	30 to 70	mm/s
Inner perimeter print speed	30 to 70	mm/s
Infill print speed	60 to 100	mm/s
Skin infill print speed	30 to 70	mm/s
Layer height	0.2	mm
Shell thickness	1.5	mm
Top / bottom thickness	1	mm
Infill overlap	15	%
Infill pattern	Grid	-
G-code flavour	RepRap	-
Retraction settings	Default	-

Base A is printed in red PLA [149, 150], and no brim / raft / skirt was used. The position of the base of Base A was marked on the printer bed before the print was removed for measuring.

The Base A print measured 29.7 x 29.7 x 19.5 mm with digital vernier calipers. The red PLA Base A was replaced on the print bed, and the second print was performed. The second print (in blue PLA [147, 148]) of the smaller cuboid was 3D printed in situ directly onto the top surface of Base A. Shown in Figure 6.5 is the combined print after it was removed from the print bed.

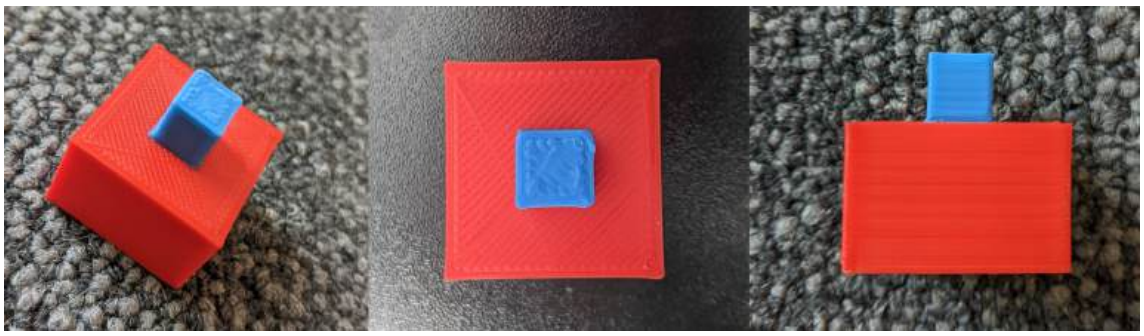

Figure 6.5: A 30 x 30 x 20 mm printed PLA cuboid (Base A) (red) with a 10 x 10 x 11 mm printed surface addition (blue).

The surface addition print adhered well to Base A. Some minor movement of the base was observed during the second print, particularly during the first few layers. This is due to the base print being removed from the printer bed for measuring - it was no longer bonded to the printer bed during the second print. The surface addition print was measured to have dimensions of 10.3 mm and 10.2 mm at the base where it joins the first print.

It was observed that the movement during the start of the second print impacted the accuracy of the deposition of the first layer - the layer is misaligned and slightly distorted. In an attempt to mitigate this, a custom holding device was designed in Fusion 360 and manufactured with MEX-TRB/P/PLA using the Creality Ender 3 v2. The CAD design for this holding device is presented in Figure 6.6. The device was designed to be secured to the print bed with tape to facilitate easy removal of it from the print bed between prints.

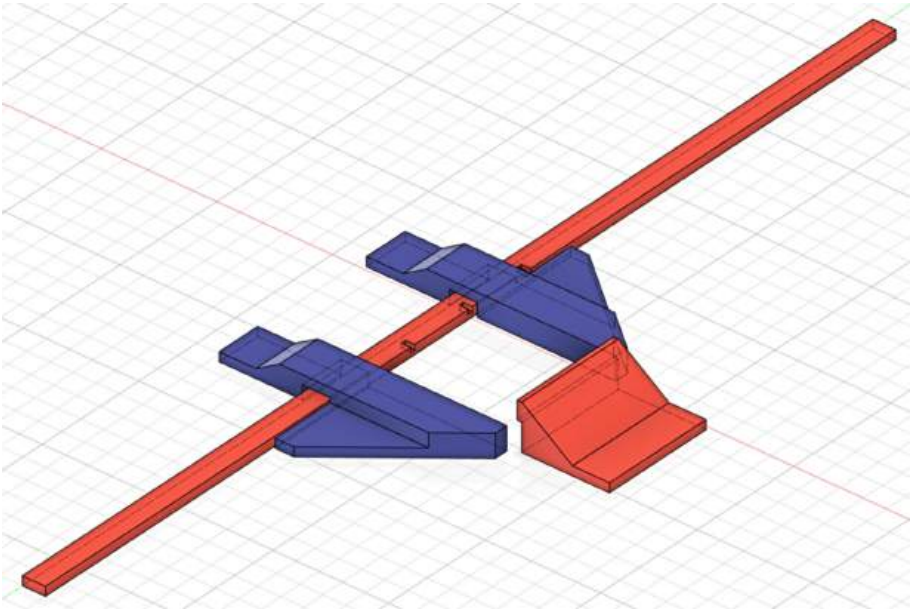

Figure 6.6: 3DP base holder CAD model in Fusion 360.

6.2.2 Base B - Angled Top Surface

The Base A design was modified with the addition of an angled top surface of 2.5°. The 2.5° was calculated as a suitable geometry for the current print head to be able to print onto, without the fan cover colliding with the taller side, during the surface addition print. The fan cover (Figure 6.7) was originally modelled as a cuboid (Figure 6.8), where the nozzle extends a certain length down below the bottom surface. The maximum width of the fan cover was measured as 63 mm, and the nozzle tip was measured at 31 mm from the left hand side of the cover (labelled 'a' in Figure 6.8). The tip of the nozzle was measured to have a diameter of 1 mm. The extruding length of the nozzle from the bottom edge of the cover was measured at approximately 1.5 mm (labelled 'b' in Figure 6.8).

Taking the inverse tangent of b/a (1.5/31), the clearance angle under the fan cover was calculated as 2.77°. Considering the width dimension of Base B (30 mm) as the maximum value of a (Figure 6.8), the angle is calculated as 2.86°. A 2.5° angle was chosen for the angled flat top as it is slightly smaller than the theoretical maximum angle that could be printed on to, thus giving a small clearance and an error margin. Therefore, the dimensions of the Base B CAD model were 30 x 30 mm with a height of 20 to 21.31 mm. Due to the acute angle of the top surface and the layer resolution of 0.2, the angled surfaces displayed clear steps rather than a smooth angled surface (Figures 6.10 & 6.11). The dimensions of the Base B prints were 29.8 x 29.9 x (20.0 to 21.3) mm. The CAD design for the implant has a horizontal top face of 20 x 10 mm. The maximum height is 10 mm, and the 2.5° angle is cut into the bottom surface of the implant, with a shortest side of height 9.13 mm.

Figure 6.7: Photograph of the fan cover on the Creality Ender 3 V2.

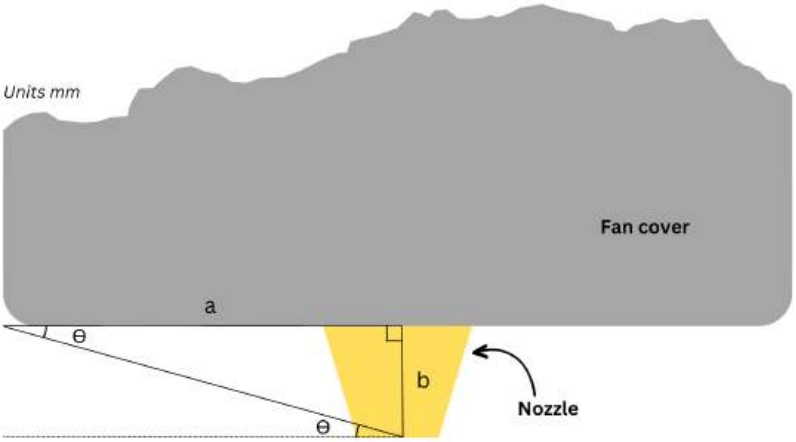

Figure 6.8: Original model of the fan cover geometry used for calculation of clearance between the bottom of the fan cover and the tip of the nozzle.

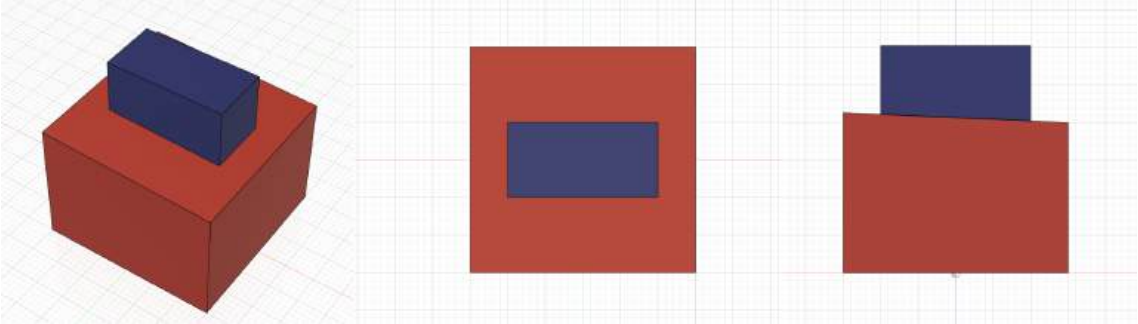

Figure 6.9: Angled top surface cube base and conformal surface print CAD design.

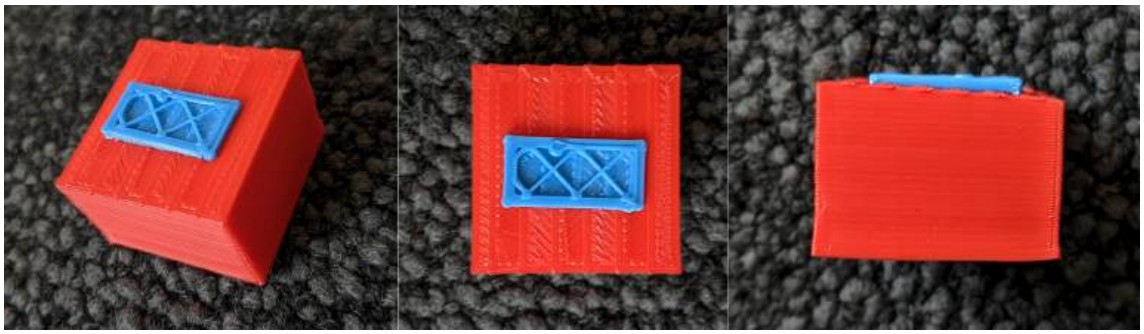

Figure 6.10: Angled top surface base (red) with attempted centre-aligned surface addition (blue) part-printed.

Realignment of the base print at this time was still through marking the print bed before removal, and the alignment was not sufficiently accurate for perfect conformal in situ printing of the surface addition. The first attempt, with the centre aligned surface print (Figure 6.10), was printed without the holding device. The base print began to move during the second printing process, so to save the print and printer from being damaged the print was cancelled part way. The dimensions of this surface print attempt were 9.9 x 20.0 x (2.1 to 1.0) mm.

The second attempt, with a side aligned surface print (Figure 6.11), was printed using the holding device (Figure 6.6) for the base during the second print. This gave better print quality, with less movement of the base during the printing process, and thus the print was able to be completed. The dimensions of this surface print attempt were 9.8 x 20.0 x (9.6 to 8.5) mm.

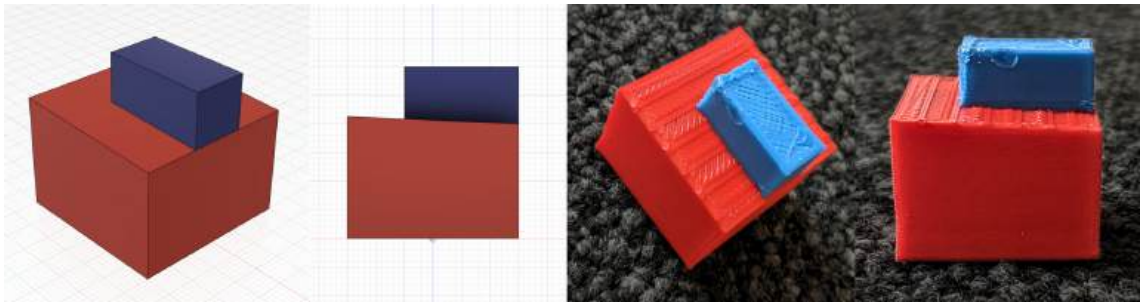

Figure 6.11: Angled top surface base with side-aligned surface print. Left: CAD model. Right: PLA print.

6.2.3 Base C - Wide Recess on Top Surface

The Base A design (30 x 30 x 20 mm) was again modified, with a wide square recess (20 x 20 x 1 mm) set into the centre of the top face. A depth of 1 mm was chosen for the recess because the clearance between the lowest point of the fan cover and the tip of the nozzle was measured at 1.5 mm. This left approximately 0.5 mm clearance between the fan cover and the top surface of Base C during the first layer of the in situ second print. The Base C print had dimensions of 30.0 x 30.0 x 19.9 mm with the recess measuring 20.0 x 20.0 x 1.1 mm.

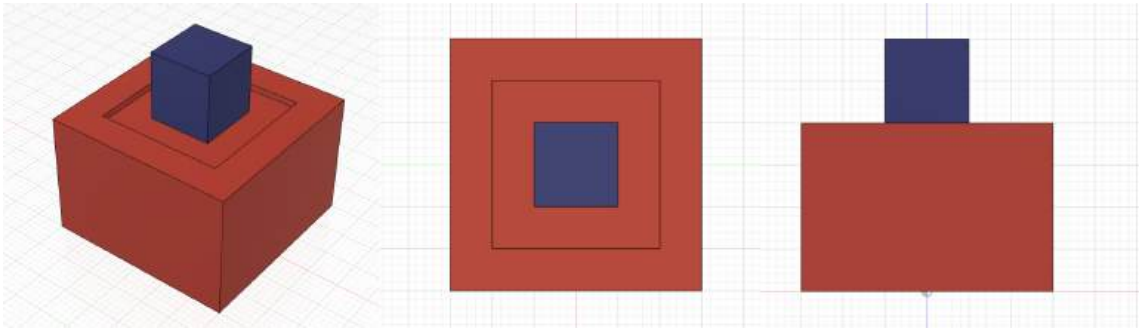

Figure 6.12: CAD model of Base C (red) with a surface print (blue) in the wide square recess.

The CAD model for the surface implant had dimensions of 10 x 10 x 11 mm, and was centred on the bottom surface of the recess. The holding device (Figure 6.6) was used to secure the Base C print during the second print process, where the surface implant was printed in situ onto the bottom surface of the recess. The measured dimensions of the in situ second print were 10.0 x 10.0 x 10.2 mm. The print was measured to be 0.8 and 0.9 mm (in each axis direction) from the centre of the top face of Base C. Realignment of the base print at this time was still through marking the print bed before removal.

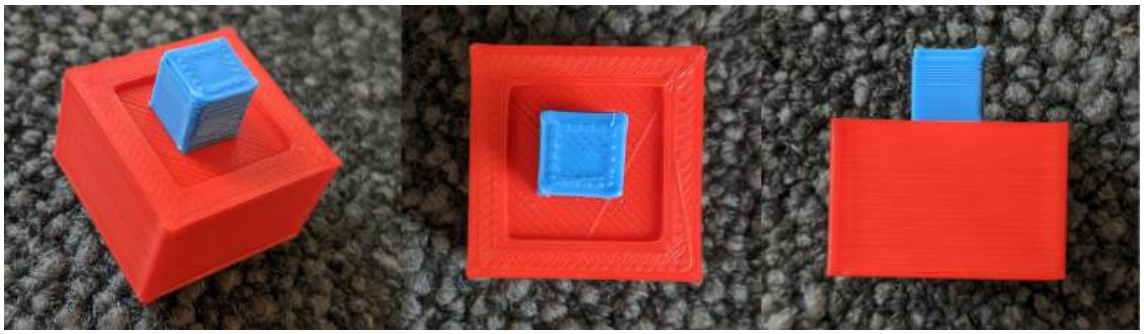

Figure 6.13: Smaller blue cube printed into the shallow square recess on the top face of a larger red cube.

6.2.4 Adapting the Print Head

Further bases which were more geometrically similar to the surface of a knee condyle were planned, but not feasible to print onto/into without more clearance around the printer nozzle. Two different types of printer nozzle were considered as options to provide more clearance for printing onto curved surfaces, and into recesses. The first type was a 'volcano' nozzle [151] which is longer than a standard nozzle (Figure 6.14a). This nozzle would increase the length of nozzle that would extend past the bottom edge of the fan cover. Unfortunately, the nozzle tip is a similar size and shape to the original nozzle - a conical / pyramid shape with a width dimension of approximately 6 mm, and non-threaded height of approximately 7.5 mm. Thus while extending the clearance of the hot end itself, enabling printing onto the bottom surface of deeper recesses on the top surface, it would still struggle with curved or angled top surface conformal printing. Furthermore, it was not clear whether the Creality Ender 3 V2 original heating element would be able to function well with this nozzle type. Due to the increased length of the nozzle after the heating element, it is not clear whether the heating element

currently installed would be able to generate a high enough temperature to ensure the molten filament remained molten by the time it was deposited from the tip of the nozzle. If not, the filament would begin to solidify inside the nozzle, causing blockages. This would result in inconsistent filament flow and layer height, and possibly block the nozzle completely, rendering it useless.

Furthermore, if the required temperature at the heating point was more than 220°C, for the filament to be molten at the desired temperature upon deposition as a layer, this would be above the recommended printing temperatures for PLA. Thus the PLA filament risks being damaged and decomposed by the heat. Therefore, the quality of the printed parts would be compromised, potentially to unusable standards.

The second nozzle type was an 'airbrush' nozzle [152] which has a similar main geometry to the original nozzle, and a long, narrow tip attachment made from stainless steel (Figure 6.14b). The original nozzle had a hexagon dimension across the flats of 6 mm, and a non-threaded length of 7.5 mm. The airbrush nozzle has a hexagon dimension across the flats of 7 mm, but the brass non-threaded length is approximately 5.8 mm. The steel tip attachment has a width of 2.33 mm (widest) to 0.7 mm (tip) and length of 4.6 mm. When attached, this gives an overall length of approximately 10.5 mm.

(a) Volcano nozzles [151] (b) Airbrush nozzle [152]

Figure 6.14: Alternative nozzles considered for *in situ* 3D printing.

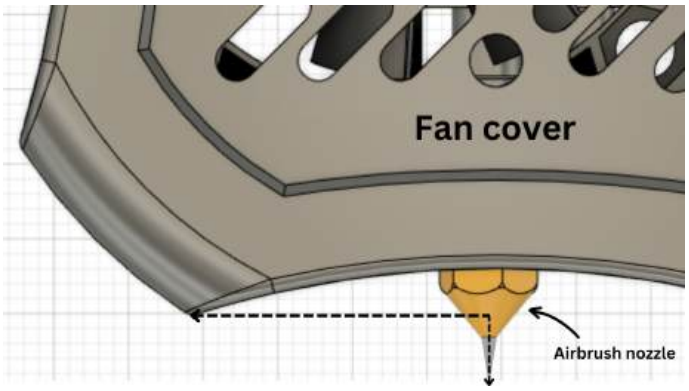

Figure 6.15: Close up image of the fan cover CAD model with the airbrush nozzle installed in the Creality Ender 3 v2. Model customised from original CAD file published online by Mo Sabri [153].

The fan cover model for the clearance calculations was updated from the original model in Figure 6.8 to the model in Figure 6.15. This new model more closely represents the geometry

of the fan cover (Figure 6.7). The geometry of the airbrush nozzle was added to the new model, and the clearance for the airbrush nozzle length was calculated. Substituting a = 19.85 and b = 4.50, the new angle is calculated as 12.77°.

Due to the nozzle attachment increasing the distance from the heating element to the tip of the nozzle, a custom spacer was designed for the touch probe bracket, and manufactured (MEX-TRB/P/PLA). The spacer was designed to be attached to the bracket for the bed levelling touch probe, lowering the touch probe, thus allowing it to be able to probe the bed with the new nozzle installed. The 3 mm spacer was the smallest dimension spacer that enabled the probe to work with the nozzle attachment. The spacer was required to lower the probe housing enough that at full probe extension the tip of the probe extended past the tip of the installed airbrush nozzle, meaning it would touch the print bed before the nozzle did, and could carry out its self-levelling function.

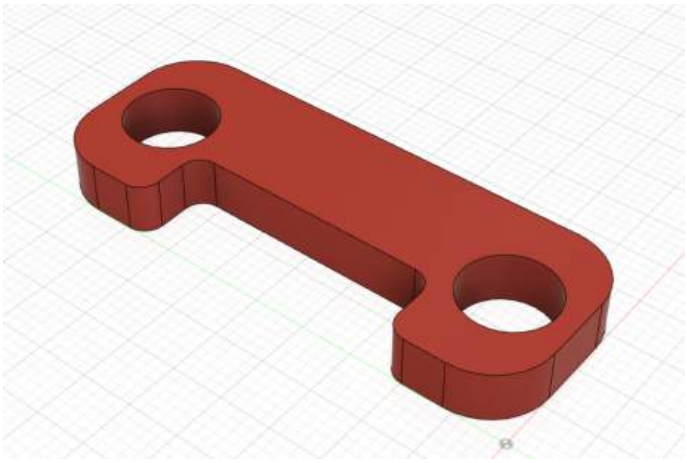

Figure 6.16: CAD model for the 3 mm probe spacer.

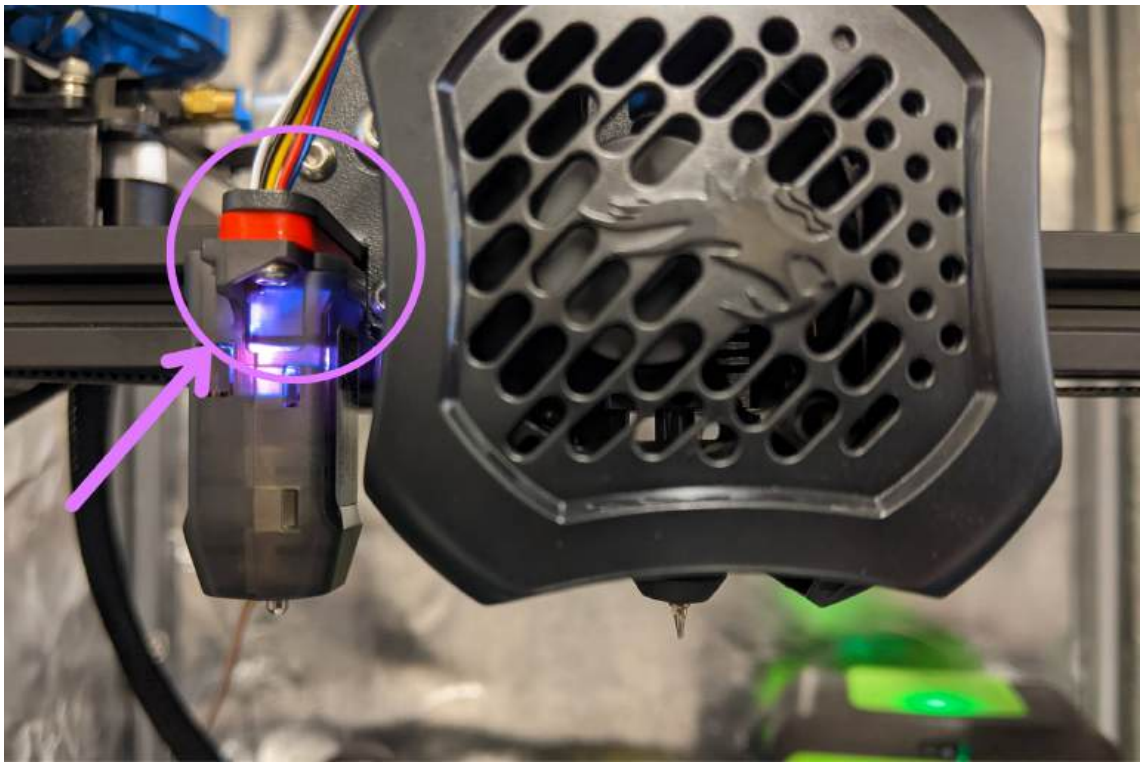

Figure 6.17: Airbrush nozzle fitted in the Creality Ender 3 v2 printer. The custom manufactured 3 mm probe spacer (red) is installed on the probe bracket.

Due to the nozzle tip extending further away from the heating element, the print temperature was increased slightly until consistent flow through the new nozzle was achieved, which was between 210 and 220°C. The part cooling fan intensity setting was also reduced. The direction of the cooling part fan usually means it is pointed at the extruded filament as it is laid down in a layer. With the airbrush nozzle installed, the part cooling fan was now pointing at the nozzle, cooling the nozzle and therefore the filament before it has left the nozzle. Therefore, the molten filament was at a lower temperature by the time it reached the tip of the nozzle. The alterations to the printing parameters slightly reduced the quality of the prints, resulting in some stringing during travel-only (non-extrusion) movements. This reduced the accuracy slightly, but it was decided to be an acceptable compromise for this preliminary stage of experimentation with in situ printing. The filament settings for printing with the airbrush nozzle are presented in Table 6.2.

Table 6.2: Filament settings for the airbrush nozzle prints.

Setting	Value	Unit
Filament diameter	1.75	mm
Flow	100	%
Print temperature	220	°C
Bed temperature	25	°C
Min. Fan Speed	10	%
Max. Fan Speed	60	%
Minimum layer time	5	s

6.2.5 Base D - Wide Recess on Top Surface

Alongside the updated print head nozzle, the models for the bases were developed further. To reduce the effect of 90 degree corners on geometry of both prints (discussed in more depth in Chapter 4), and movement of the base during printing, the recesses and implants were made circular. This also produces a closer replication of a biomedical application for in situ printing. For example, filling an articular cartilage defect. The geometry of the [transplanted] plugs is significant in healing - the defect should be remodelled to a cylindrical shape before filling, whether by donor plug or 3D printed implant [154]. Finally, the height of the cuboid base shape was shortened to 10 mm, to reduce printing time. The CAD model design of Base D (Figure 6.18) thus comprised of the updated basic cuboid base (30 x 30 x 10 mm) with the addition of a circular recess centred in the top face (20 mm diameter, 1 mm depth). An implant design of diameter 10 mm and height 4 mm was centred on the bottom surface of the recess.

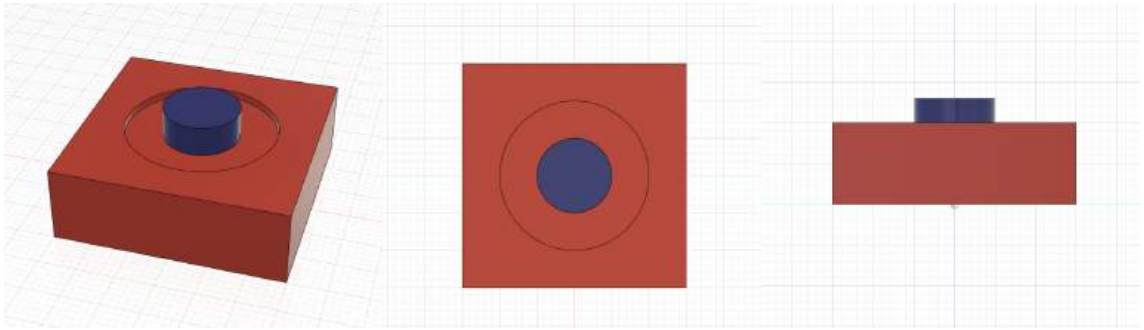

Figure 6.18: 10 mm diameter (height 4 mm) cylindrical print (blue) in situ printed onto the bottom surface of the circular recess (depth 1 mm) in the top face of the 3D printed base (red) (30 x 30 x 10 mm).

The Base D print had dimensions of 29.9 x 29.9 x 10.3 with a recess of diameter 20.0 mm and depth 1.3 mm. The second print was performed in situ onto the bottom surface of the Base D recess with the airbrush nozzle (Figure 6.19). The first attempt had printed dimensions of diameter 9.8 mm and height 4.0 mm, and was off-centre by 1.5 and 1.7 mm (in each axis direction).

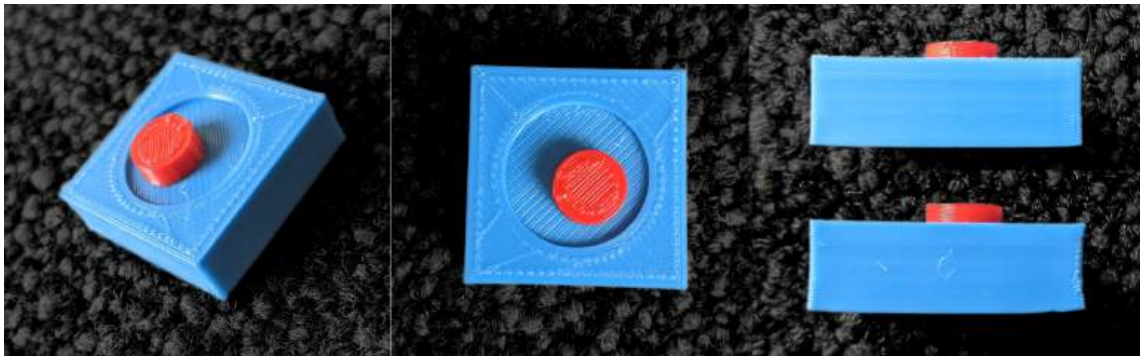

Figure 6.19: 10 mm diameter (height 4 mm) cylindrical print (red) in situ printed onto the bottom surface of the circular recess (depth 1 mm) in the top face of the 3D printed base (blue) (30 x 30 x 10 mm).

This print test was repeated (Figure 6.20) after some minor edits to the G-Code. The second attempt produced a more accurately centred in situ print (off-centre by 0.3 and 0.6 mm in each axis direction). The diameter of the print was 9.8 mm with height 4.1 mm. The following edits to the G-Code were retained for the subsequent experiments; a second test line being printed after the dwell point, and the print head moving from the 'home' position up and across to a point above the centre of the base before travelling to the start position for the second print first layer.

Figure 6.20: Second print of the 10 mm diameter (height 4 mm) cylindrical print (blue) in situ printed onto the bottom surface of the circular recess (depth 1 mm) in the top face of the 3D printed base (red) (30 x 30 x 10 mm). The surface addition print is more central.

6.2.6 Base E - Wide Recess on Top Surface

The Base D design was modified such that the circular recess is now 4 mm depth (Figure 6.22). The base CAD dimensions remain 30 x 30 x 10 mm, and the recess is centred on the top face and has a diameter of 20 mm. The recess depth now matches the height of the in situ second print. Base E has printed dimensions of 29.8 x 29.8 x 10.2 mm with the recess measuring 19.8 mm diameter and depth 4.1 mm.

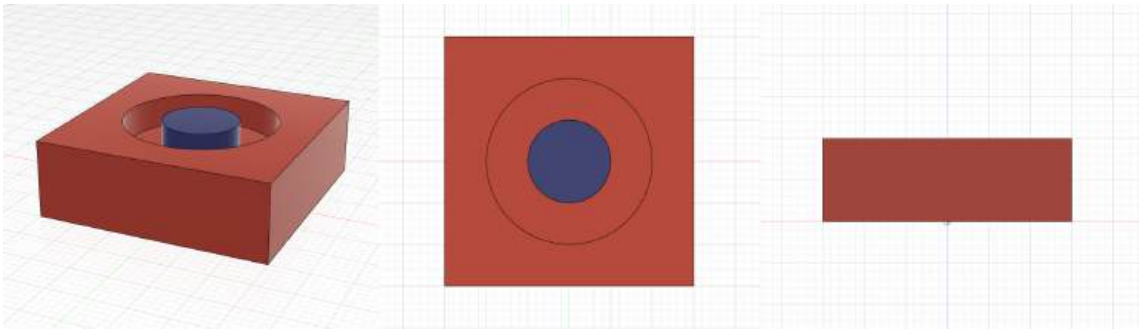

Figure 6.21: CAD model of Base E (red) with a surface print (blue) in the circular recess. The top face of the surface print is in line with the top surface of the base.

The CAD model for the surface implant remained the same at 10 mm diameter and 4 mm height, and is centred on the bottom surface of the recess. As seen in Figure 6.21, in the CAD model the top of the implant in the recess is completely in line with the top face of the

base. The measured dimensions of the in situ second print were 10.0 mm diameter and height 4.1 mm. As seen in Figure 6.22, the top of the implant print does not protrude past the top surface of the base. The print was measured to be 0.0 and 0.6 mm (in each axis direction) from the centre of the top face of Base D.

Figure 6.22: 10 mm diameter (height 4 mm) cylindrical print (red) in situ printed onto the bottom surface of the circular recess (depth 4 mm) in the top face of the 3D printed base (blue) (30 x 30 x 10 mm). The top surface of the implant is in line with the top surface of the base.

6.2.7 Base F - Curved Top Surface with Recess

The Base D base design - a cuboid of 30 x 30 x 10 mm - was modified to have a curved top surface of radius of curvature (ROC) 30 mm. Then a circular recess was created centred on the top surface, of 20 mm diameter and 4 mm depth from the apex of the top surface. This base - Base F - has printed dimensions of 29.7 x 29.8 x 10.1 mm with the recess measuring 19.8 mm diameter, with a maximum depth of 4.1 mm.

An implant was CAD modelled to have a diameter of 10 mm and a maximum height of 4 mm. The top surface of the implant was matched to the radius of curvature of the Base F top surface. Placed central on the bottom of the recess, the implant CAD model (red) top surface is inline with the top surface of the base (blue). This is shown in Figure 6.23.

The implant print was printed in situ centred on the bottom surface of the recess of Base F, and had measured print dimensions of 9.8 mm diameter and maximum height 4.0 mm. As presented in Figure 6.24, the top of the implant print does not protrude past the top surface of the base. The print was measured to be 0.4 and 0.0 mm (in each axis direction) from the centre of the top face of Base F. The effect of the airbrush nozzle temperature adaptations were more visible in the layering of the curved surfaces produced. The layers are less clean compared to the earlier prints (Sections 6.2.1 - 6.2.3).

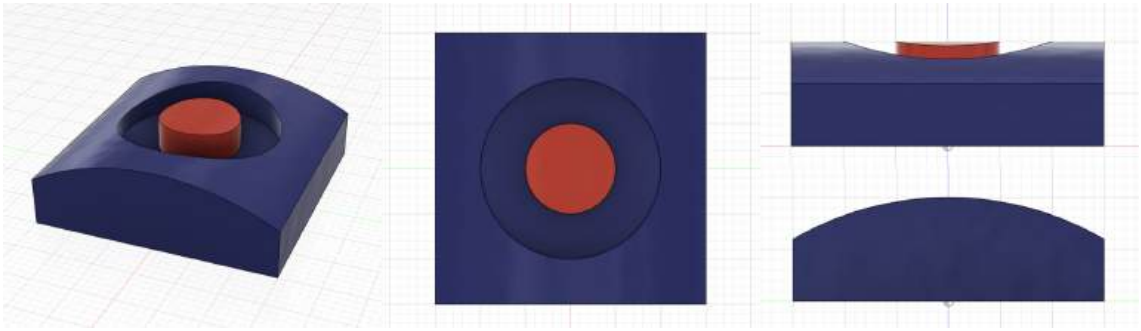

Figure 6.23: Base F with implant CAD.

Figure 6.24: 10 mm diameter (maximum height 4 mm) cylindrical print (red) in situ printed onto the bottom surface of the circular recess (20 mm diameter, maximum depth 4 mm) in the top face of the 3D printed base (blue) (30 x 30 x 10 mm with top surface radius of curvature 30 mm). The top surface of the base and of the surface addition print have the same curvature.

6.2.8 Base G - Curved Top Surface with Recess

The Base D design (30 x 30 x 10 mm) was modified once more to create Base G (Figure 6.25). The CAD model for Base G comprises of the basic cuboid base (30 x 30 mm) with a curved top surface (ROC 57 mm). A circular recess was created, centred on the top surface, of 20 mm diameter and 2 mm depth. The bottom surface of the recess is matched to the curvature of the top surface (ROC 57 mm). Base G has printed base dimensions of 29.6 x 29.8 mm, maximum height 10.3 mm, with the recess diameter 20.0 mm and depth 2.1 mm.

An implant was modelled in CAD to have a diameter 10 mm and maximum height 2 mm. The bottom surface of the implant was matched to the geometry of the bottom of the recess, and the top surface was matched to the ROC of the Base G top surface. Placed central on the bottom on the recess, the implant CAD model (blue) top surface is inline with the top surface of the base (red) (Figure 6.25).

The implant print was printed in situ centred on the bottom surface of the recess of Base G, and had measured print dimensions of diameter 9.9 mm and height 2.1 mm. As presented in Figure 6.26, the top of the implant does not protrude past the top surface of the base. The implant print was measured to be 0.2 and 0.1 mm (in each axis direction) from the geometric centre of the top face of Base G.

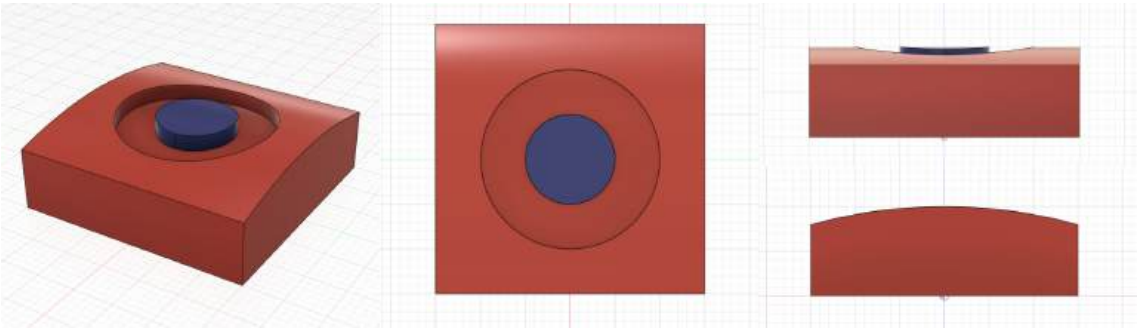

Figure 6.25: Base G with implant CAD.

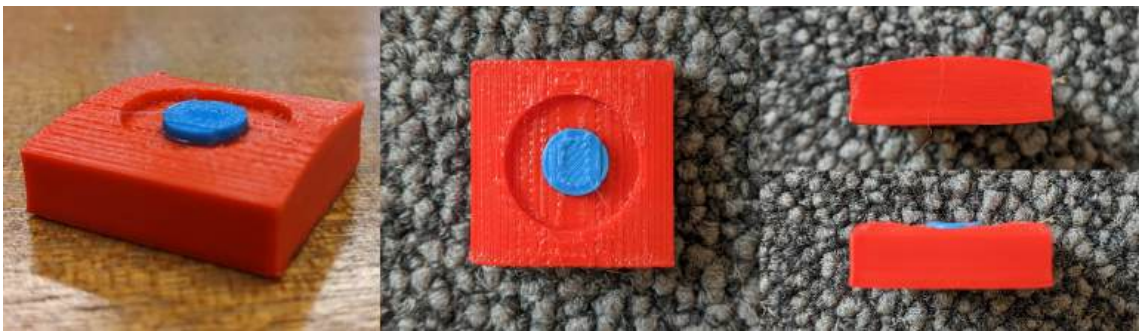

Figure 6.26: 10 mm diameter (height 2 mm) cylindrical print (blue) in situ printed onto the curved bottom surface of the circular recess (20 mm diameter, depth 2 mm) in the top face of the 3D printed base (red) (30 x 30 x 10 mm with top surface radius of curvature 57 mm). The top surface of the base, the bottom of the recess, and the top surface of the surface addition print have the same curvature.

6.3 Clay Bases

6.3.1 Designing the Clay Bases

For the design of the clay bases described in the experimental workflow in Figure 6.3, the radius of curvature of human knee condyles was investigated. Table 6.3 details mean radius of curvature measurements for data sets of the human femoral condyle. The femoral condyle is where the majority of human knee articular cartilage injuries present (Section 2.4), and is the focus of the type of surgical interventions described in Section 2.4. Thus the clay models for in situ additive manufacturing were designed to approximate the challenges faced with in situ additive manufacturing for such a surface - predominantly challenges with contour matching of the articulating surface.

Table 6.3: Radius of Curvature of Adult Human Femoral Condyle

Authors		Measurement	(mm)
Du, P. Z. et al (2018)	[155]	Medial mean±s.d.	32.5±3.6
			32.7±3.4
		Lateral mean±s.d.	26.9±3.9
			26.4±3.8
Chaurasia, A. et al (2021)	[156]	*Mean medial arcs*	
		anterior	20.77
		distal	31.42
		posterior	19.68
		Mean lateral arcs	
		anterior	21.48
		distal	64.40
		posterior	19.06
Nuño, N. and Ahmed, A. M. (2003)	[157]	medial mean	18.7
		medial mean	32.5
		lateral mean	20.1
		lateral mean	36.9
Freeman, M. A. R. and Pinskerova, V. (2005)	[158]	anterior medial mean	32
		posterior medial mean	22

All of the mean values of radius of curvature were between 19 and 41 mm (except for the distal lateral arc in Chaurasia et al. (2021) [156]) so these values were chosen as the lower and upper boundaries for the ROC of the designs for the clay condlye surfaces. The radius limits (19 and 41 mm) were tested, with the assumption that if these models were successful, the ROC values within this range should be successful as well.

For each radius modelled a model was produced with a full curved surface, and another model was produced with a 10 mm diameter cylindrical recess into the top surface. The cylindrical recess was chosen to model the geometry of a knee articular cartilage injury site after it has been debrided and made uniform with a surgical harvesting tool, as discussed in Section 2.4 and visually presented in Figure 2.5. This creates a uniform cylindrical "punch", perpendicular to the joint surface.

Four models were designed using Fusion 360 (Autodesk, USA) [143]. Each model comprised of a square base of side length 40 mm and height 5 mm, and a top surface 'dome' (Figure 6.27). Four 'dome' geometries were tested for in situ AM. The CAD dimensions for the four models were:

- A: Full top surface with a radius of curvature of 41 mm (Figure 6.28a, A).
- B: Top surface radius of curvature of 41 mm, with a 10 mm diameter recess (maximum depth 3.33 mm) (Figure 6.28a, B).
- C: Full top surface with a radius of curvature of 19 mm (Figure 6.28b, C).
- D: Top surface radius of curvature of 19 mm, with a 10 mm diameter recess (maximum depth 3.69 mm) (Figure 6.28b, D).

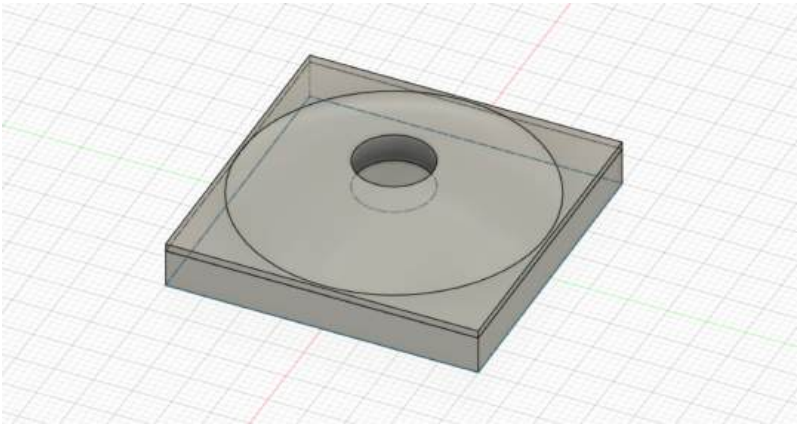

Figure 6.27: The CAD model for the 41 mm radius of curvature with a 10 mm diameter recess, mounted on an alignment base, modelled in Fusion 360.

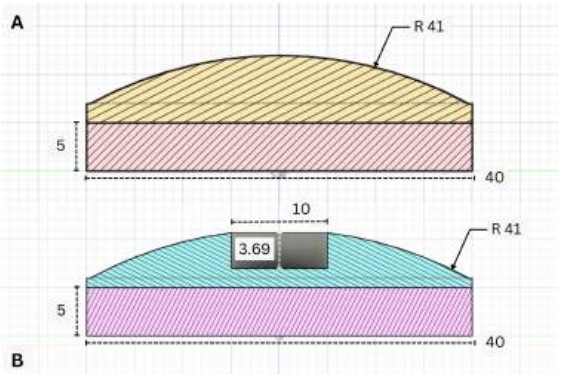

(a) CAD models with 41 mm top surface radius of curvature. Model A has a full top surface, model B has a 10 mm diameter recess.

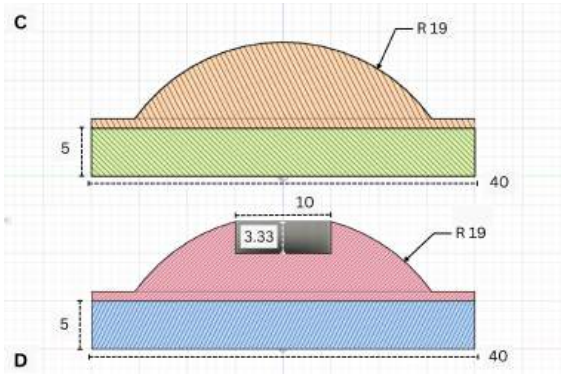

(b) CAD models with 19 mm top surface radius of curvature. Model C has a full top surface, model D has a 10 mm diameter recess.

Figure 6.28: Bisecting section views of the CAD models for the 41 mm and 19 mm radius of curvature bases (with and without a recess), modelled in Fusion 360.

The CAD designs were used to design negative moulds of the dome top sections in Fusion 360 (Figure 6.29), which were then sliced and produced by additive manufacture with the Creality Ender 3 v2 printer (Creality, UK) [144]. These moulds were designed to enable air-drying clay [142] to be pressed into the mould and left to cure. Once released from the mould, a clay 'dome' of the required dimensions is produced. An example of the 41 mm ROC clay dome section next to the PLA mould is presented in Figure 6.30.

Clay was selected as an easily accessible material which had the ability to be shaped using a PLA mould. Furthermore, the surface of the clay was non-plastic, and not thermoplastic, so the surface of the model would not be dimensionally altered by the heat of the nozzle or filament deposition. The clay produced an inflexible top surface, which would highlight (through print error) inaccuracies with the in situ positioning if the nozzle tried to breach the top surface of the model (instead of printing conformally with the surface).

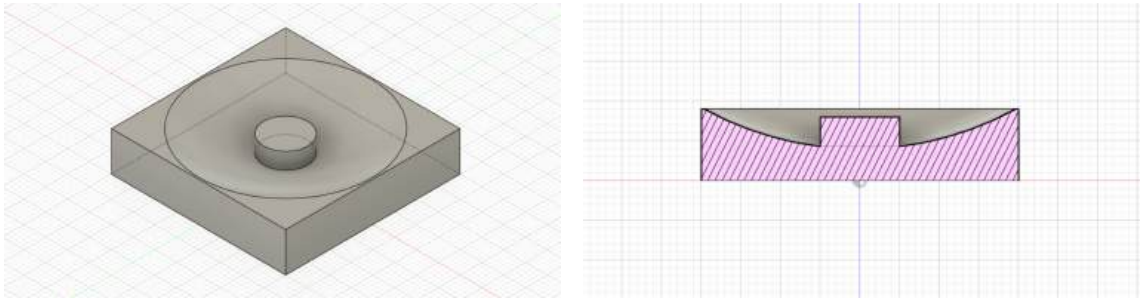

(a) Isometric view. (b) A bisecting section.

Figure 6.29: The CAD model for the 41 mm radius of curvature mould (with recess), modelled in Fusion 360.

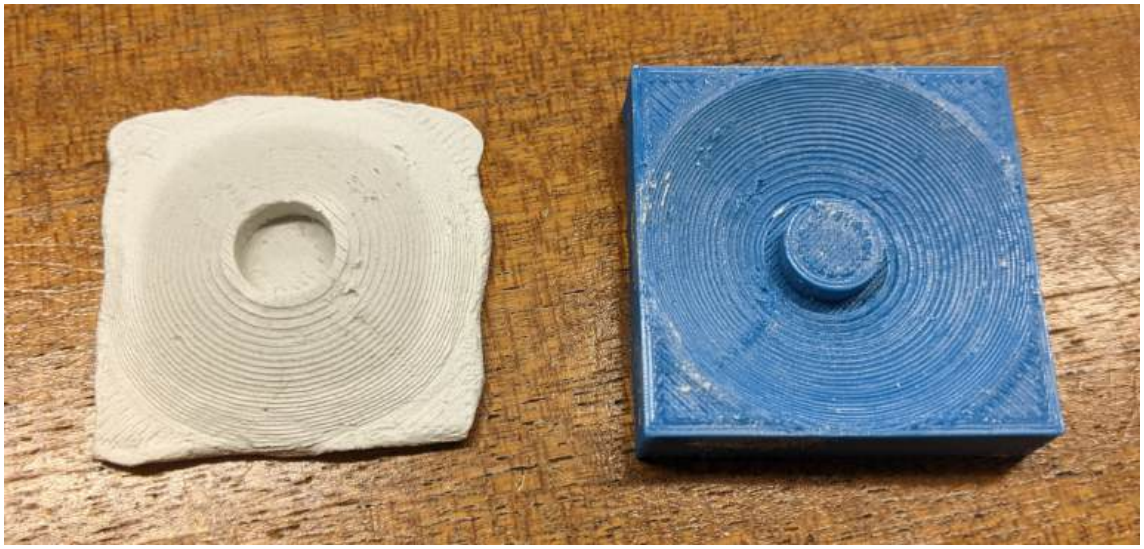

Figure 6.30: A 41 mm ROC model (left) after release from the MEX-TRB/P/PLA mould (right).

The mould design and methods were developed during the initial phase of the experiment. Originally the 19 mm ROC mould was deeper, creating a taller model in the clay. This was much more difficult to release from the mould, so the mould was shortened to a similar depth to the 41 mm ROC mould. Furthermore, in order to increase the ease of the method of release, whilst retaining good adhesion of the curved surface during the curing time, a very small amount of petroleum jelly was applied to the flat corner areas of the mould to aid in releasing the model from the mould.

To improve the alignment of the base within the print volume of the bed for in-situ printing, an alignment base and method were designed. A simple square frame was printed in PLA with internal dimensions of 40 x 40 mm, and a height of 5 mm. The bases for the models were created by using the frame as a mould for the clay (Figure 6.31). In theory, printing the frame G-Code at the beginning of the in-situ implant print would enable an alignment frame, aligned within the printers coordinate system relative to the implant. Thus the model would be placed base-first into this frame before being secured to the bed, and ideally be perfectly aligned to print the implant.

Figure 6.31: From left to right: The clay alignment base before removal from the mould, the empty mould, the cured clay alignment base.

The top surface domes were attached to bases with super glue. An example of the finished clay model for the 41 mm ROC surface with recess is presented in Figure 6.32. All the bases were measured with digital vernier calipers to record the base width and height, and the top surface geometries.

The models were constructed from separate upper and base components, as the parts had specific, differing geometry requirements. Each requirement was addressed separately, which resulted in two parts being joined into a final model with the required dimensions. The focus of the dome upper part was creation of the desired radius, with or without a recess. The focus of the base lower part was complementary geometry to the alignment frame. Together the two parts created a model with a geometry that fit within the alignment frame without movement, and a domed top surface of the required radius. The method used, of creating the two parts and combining them to create the model, was not the only method that could have been used. If continued or repeated, these models could be created using silicone moulds, or some other medium, which would enable the full required geometry to be contained in a single cast part.

(a) Top view (b) Side view

Figure 6.32: Clay model 41 mm ROC with recess, mounted on alignment base.

6.3.2 Scanning the Clay Bases

The bases were then ready to be scanned using the EinScan-SP 3D Scanner (Shining3D, China) [114], using the ExScanS V3.1.3.0 companion software. Scan settings are detailed in Table 6.4 below. The 'dot' that can be seen on the top right hand side corner of the condyle base in Figure 6.33 is an alignment marker so that the orientation of the base can be determined during the implant CAD design, and when placing the base in the printer for the in situ 3D printing process later. It was an orientation feature, due to the symmetrical geometry of the clay bases, and was recognised and aligned manually in the experiments outlined in this project. Section 6.3.4 describes this alignment method in more detail. For surgical contexts, more appropriate extrinsic or intrinsic fiducial markers would be utilised, as discussed in Section 2.7, to ensure correct alignment and orientation of the implant and patient anatomy.

Table 6.4: 3D Scanning Settings for the Condyle Bases

Setting	Value
HDR	On
Turntable	On
Alignment Mode	Coded Turntable Alignment
Turntable Steps	36
Turntable Speed	2

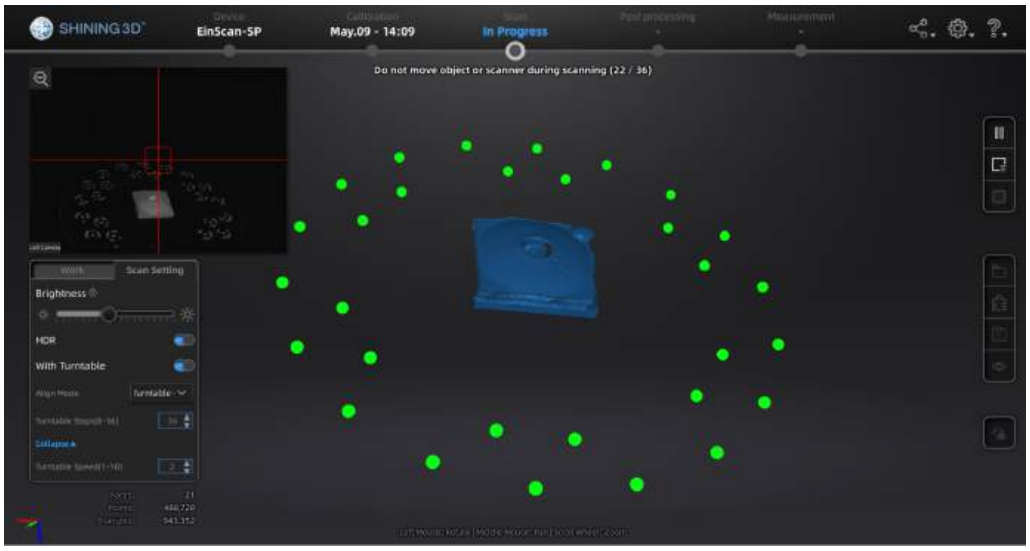

Figure 6.33: The 41 mm radius of curvature model (with recess) point cloud being compiled in the Shining 3D software.

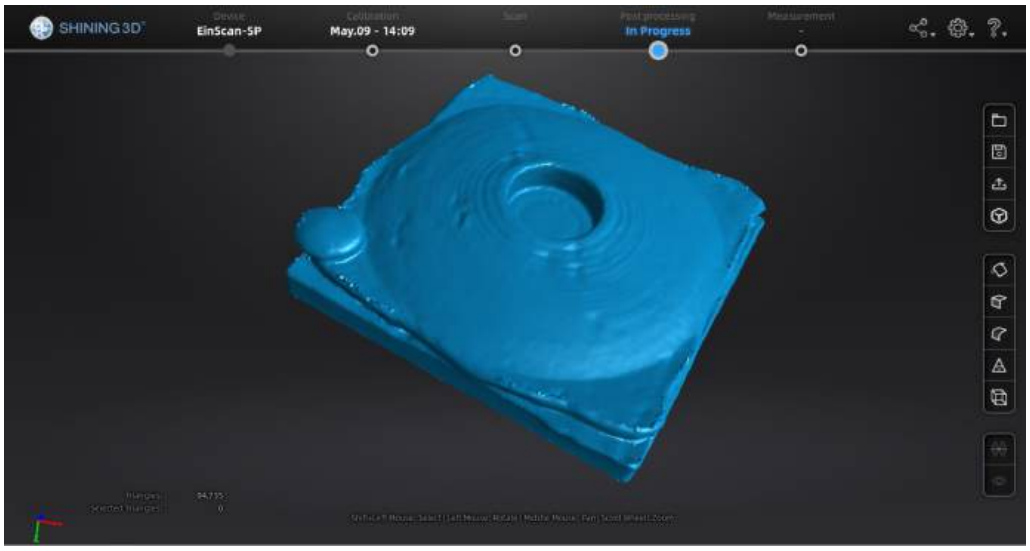

Figure 6.34: The 41 mm radius of curvature model (with recess) scan point cloud has been converted into an unwatertight mesh in the Shining 3D software.

6.3.3 Manipulating the Scan Models

The scanned models were imported into Meshmixer (Autodesk, USA) [52]. The scan models were measured in Meshmixer using the 'Dimensions' and 'point to point' measuring tools (Figure 6.35). Comparing the caliper measurements to the scans showed that the scanner consistently did not capture the lowest 2 mm of the alignment base. The CAD model was able to be shifted upwards (in the Z direction) to account for this, before the implant was built onto the top surface in the Fusion 360 software. To reduce the computing time and power required, the scan models were edited to leave only the specific sections of interest: the section of surface to be printed onto, the alignment base geometry, and the alignment dot. The workflow presented in Figure 6.36 is the overall series of steps taken in the Meshmixer

software. Step 1 in the workflow was completed before the dimension checks were undertaken.

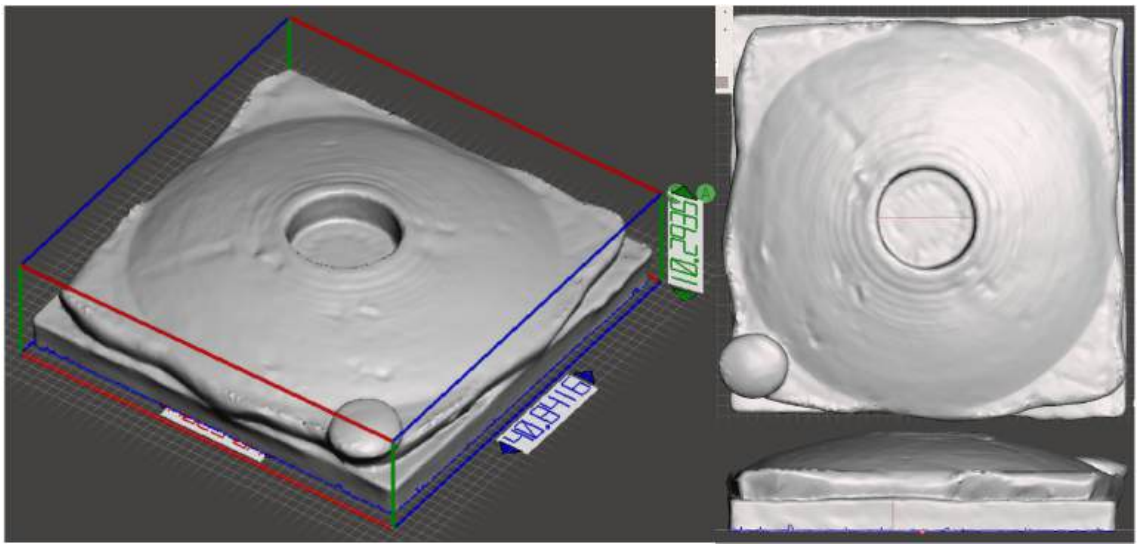

Figure 6.35: The 41 mm ROC (with recess) clay model scan model presented in Meshmixer.

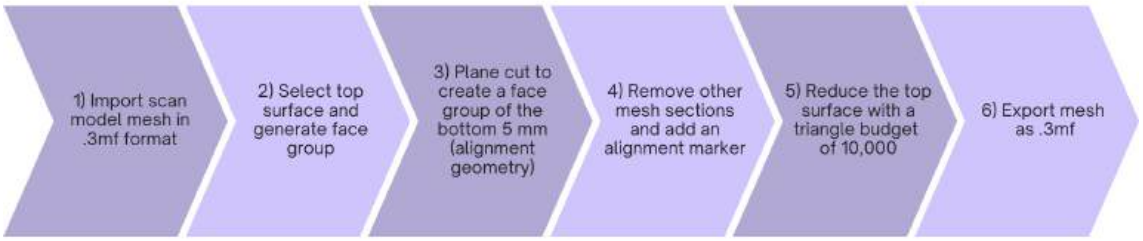

Figure 6.36: Workflow for scan mesh preparation in Autodesk Meshmixer.

Step 2 (Figure 6.36) for the clay bases was achieved using the 'plane cut' tool (cut type 'slice groups', fill type 'no fill') to select the top surface of the dome (Figure 6.37a, (1)) and section it into a separate face group. The 'plane cut' tool was repeated to complete Step 3 (Figure 6.36) and separate the alignment geometry ((Figure 6.37a, (3)) at the bottom of the clay base into its own face group. The 'brush select' tool was used to select and separate the alignment marker ((Figure 6.37a, (4)) into a separate face group. The result is presented in Figure 6.37a: the surface to be printed onto (1) (purple), the alignment base (3) (turquoise), the alignment marker (4)(green), and the removable excess geometry (2)(peach). The alignment base section is retained to enable alignment in the X, Y and Z dimensions. A large portion of the dome was kept to enable more reliable extrapolation of the full ROC top surface for the models with a recess.

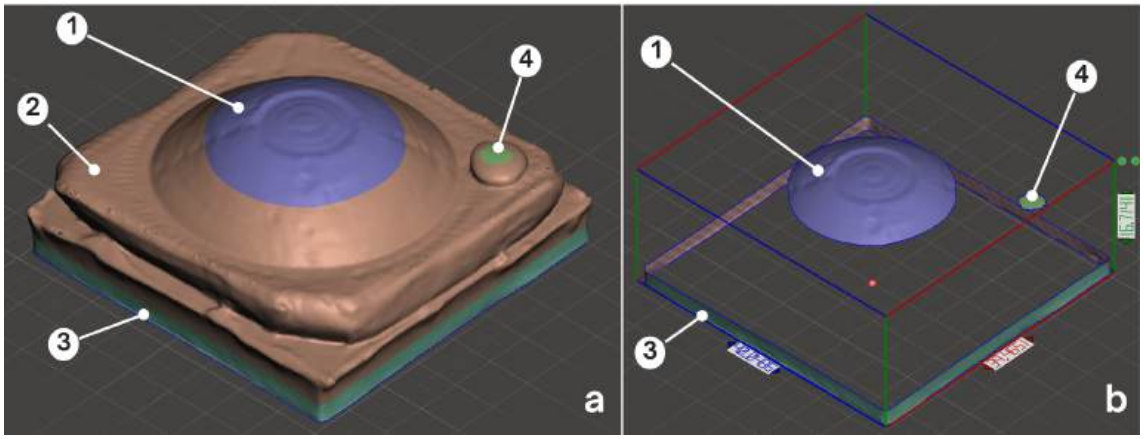

Figure 6.37: 19 mm full surface scanned model in Meshmixer. a) Plane cut face groups. b) Surplus geometry removed.

Shown in Figure 6.37b, the excess geometry (2) was erased. The top surface mesh (1) was reduced, and the resulting mesh model was exported as a .3mf file. Minimising the surface area enabled as much detail as possible to be retained when reducing the mesh (to a maximum of 10,000 triangles) for conversion and editing in Fusion 360.

6.3.4 Implant Design Workflow

The .3mf file was uploaded into Fusion 360, and the implant CAD model was created. The workflow for creating the implant CAD is outlined in Figure 6.38.

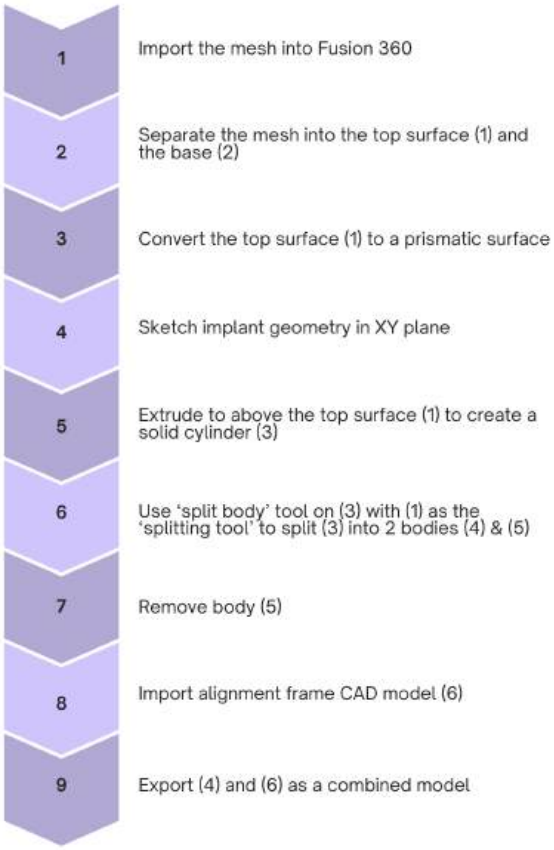

Figure 6.38: Implant design workflow.

For Step 2 for the full surface models (Figure 6.39), the full mesh was separated into the top surface (1) and the alignment base (2). Then, the top surface mesh (1) was converted into a prismatic surface (Step 3). In Step 2 for the models with a recess (Figure 6.40), the full mesh was separated into the bottom surface of the recess (1), the alignment base (2), and also the sides of the recess (S), the top surface of the model (T). Then, Step 3, the mesh for the bottom surface of the recess (1) was converted into a prismatic surface - this is considered the 'top surface' (1) in the workflow (Figure 6.38) as it is the surface the implant will be built upon.

For both types of model, at Step 4 the circular cross sectional area for the implant was sketched on the XY origin plane, and the circle sketch was aligned to the centre of the recess (or the peak of the top surface). The sketch had a diameter of 10 mm for the full surface models (Figure 6.39), and 8 mm for the recess models (Figure 6.40). The main body of the implant was thus generated (Step 5) by extruding the sketch from the XY origin plane, to approximately 4 mm above the tallest dimension of the model.

The implants for this experiment were not necessarily perfectly centred with regards to the alignment base, but for the full surface models the 10 mm implants were aligned with the peak of the dome. For the recess models the 8 mm implants were centre aligned within the recess such that the side of the implant CAD was no closer than 1 mm to the sides of the recess. This would allow some space for the nozzle width to enter the recess without damaging or colliding with the base.

The implant body was then divided into sections using the 'split body' tool (Step 6). For the models with a full top surface (Figure 6.39), the extruded body (3) was split using the top surface (1) as the 'splitting tool'. The top surface of the body remained the flat horizontal top face of the cylinder at approximately 4 mm above the height of the scanned clay model.

For the models with a recess (Figure 6.40), Step 6 had two parts: the extruded body was split once for the conformal base of the implant, and again for the matching contour of the top of the implant. Presented in 6a in the figure, the extruded body (3) was split using the surface of the bottom of the recess (1) as the 'splitting tool'. The extruded body (3) was then split using the matching contour top surface geometry (1b), as presented in 6b in the figure. The top surface geometry (1b) for the recess models was able to be created in two different ways, described in more detail in Sections 6.3.5 & 6.3.6.

For all models, in Step 7, the surplus geometry (5) of the extruded implant was removed, leaving a CAD implant. For the full top surface models, the bottom of the CAD implant conforms to the top surface of the scanned model, and has a flat top surface (Figure 6.39). For the recess models, the CAD implant conforms perfectly to the bottom surface of the recess, and the top surface has a matching contour to the projected top surface of the scanned model.

Step 8 for all models was completed by importing the alignment frame CAD model (6) into the assembly, with the frame reduced in height to 1 mm (40 x 40 inside dimensions, 42 x 42 outer dimensions) (Figure 6.39). The frame was centred at the origin, and the rest of the assembly (scanned surface model and implant CAD model) was aligned within the frame using the alignment base geometry of the scanned model (2). The alignment frame model has a round corner marker (labelled M in sub-figure 2 of Figure 6.39 & Figure 6.40), and the frame was oriented so the round corner coincided with the alignment marker on the scanned model.

In the final step in the workflow, Step 9, the alignment frame (6) and generated implant CAD (4) were extracted together from the assembly, and exported to STL as one model. Sub-figures 9 in Figure 6.39 and Figure 6.40 show the final assembly for a full top surface clay model, and a model with a recess, respectively.

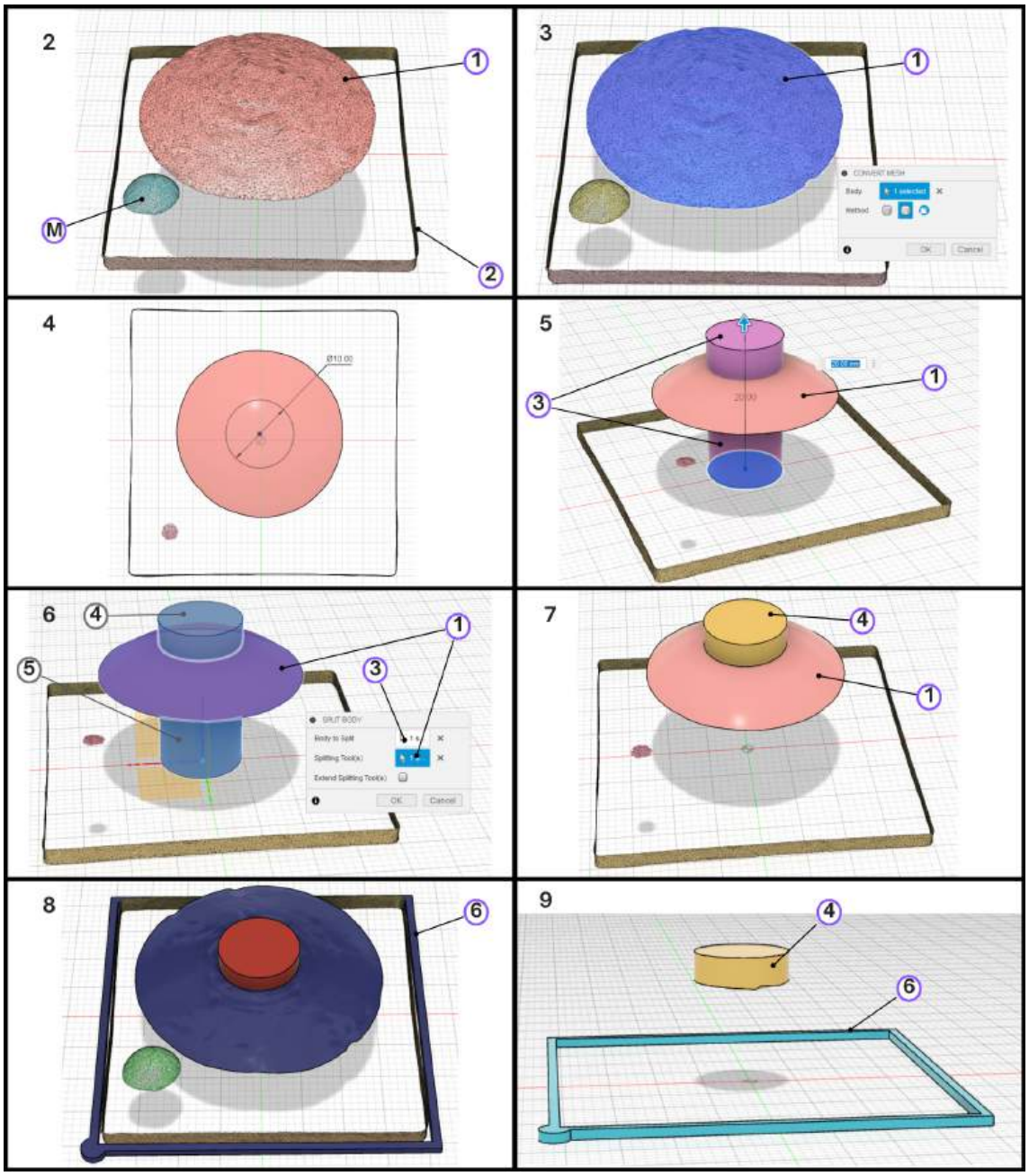

Figure 6.39: Screenshots from Fusion 360 of the stages of the implant CAD design process for the clay models with full top surface. Sub-figure numbers and labels correspond to the workflow stages in Figure 6.38.

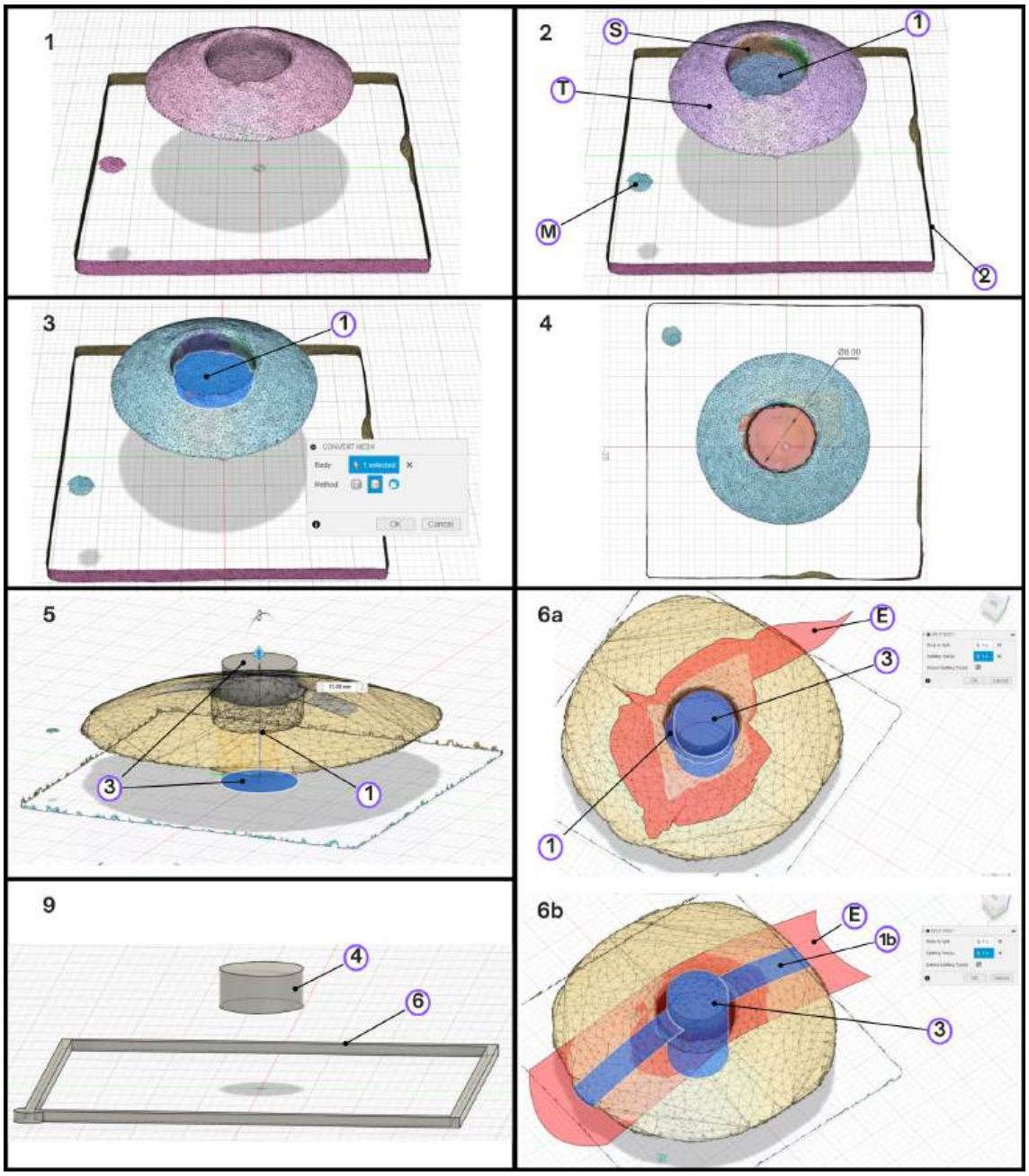

Figure 6.40: Screenshots from Fusion 360 of the stages of the implant CAD design process for the clay models with a recess in the top surface. Sub-figure numbers and labels correspond to the workflow stages in Figure 6.38.

In Figure 6.40 6a & 6b, the 'splitting tool' for each 'split body' operation has been 'extended' (labelled E). This is an option in Fusion 360 which temporarily extends the surface geometry of the surface which is selected as the 'splitting tool'. The extended surface is an estimation of how the geometry would continue if the selected surface was a section of a larger surface.

In sub-figure 6a, the surface at the bottom of the recess was extended during the split body operation, however this was not required as the extended geometry did not intersect with the body being split - only the original surface was required. In sub-figure 6b, the top surface

matching contour (1b) (used as the 'splitting tool') was generated using the manual top surface generation method outlined in Section 6.3.5. The surface was selected as the 'splitting tool' and extended to split the body (3). The amount that the splitting tool surface is extended appears to be arbitrary, and the surface extrapolation techniques / algorithms that Fusion 360 employs are not published. For future research, specific surface extrapolation techniques could be explored to evaluate their utility in creating an extended surface that continues the required contour(s).

6.3.5 Manual Top Surface Design

One method of generating the top surface of the implant for the models with a recess, is to extend the curve of the top surface to cover the hole. After importing the scanned model as a mesh, the same process of separating the sections of mesh occurs as outlined in Section 6.3.4. Using the 'sketch mesh section' tool, profiles of the cross section of the top surface of the scanned model can be generated. For this application, a profile was generated in the XZ plane through the origin, and at 1 mm intervals along the X axis, to the edge of the recess. An example of this, for the 41 mm ROC with recess model is presented in Figure 6.41.

Using the 'loft' tool a solid surface can be generated by joining the profiles together. An example of this surface can be seen in surface (1b) in Figure 6.40, sub-figure 6b. Depending on the frequency of the points taken along the sketch profile, and the length of the sketch profile, varying degrees of successful surfaces can be generated. Furthermore, more sketch profiles, closer together, can generate a more accurate representation of the curved surface. Ideally this would produce a more reliable extrapolation of the top surface curve over the top of the recess. Intervals of 1 mm between the sketch profiles generated a similar enough surface for filing the recess such as to be acceptable for the low resolution purposes of proof of concept for in situ conformal additive manufacturing.

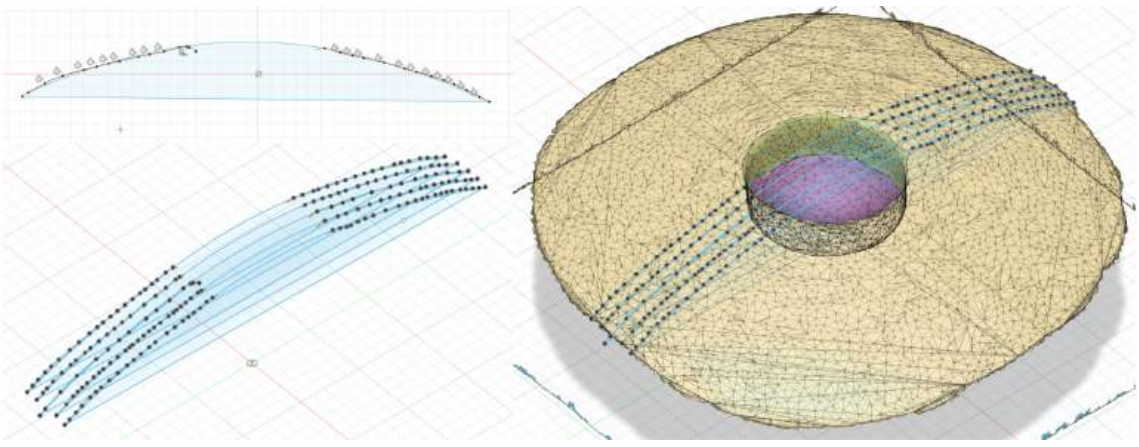

Figure 6.41: 'Mesh sketch' for extending the top surface of the 41 mm ROC condyle over the recess. Top left: XZ plane view of the isolated sketch profiles. Bottom left: Isometric view of the isolated sketch profiles. Right: sketch profiles combined with the top surface mesh they are sketched from.

6.3.6 Boolean Top Surface Design

The second method of generating the top surface of the implant for the models with a recess, is using the geometry of the respective full top surface model. The model with the recess is imported into Fusion 360 and the steps are followed as described in Section 6.3.4, up to the implant cylinder being split by the top surface geometry (step 6b). To create this geometry, the full top surface model with the same ROC is imported into Fusion 360 as a mesh. The mesh is separated into its sections in the same way, and the top surface dome section is converted to a prismatic solid surface. This surface is extracted and imported into the assembly file where the implant is being designed. This surface is able to be aligned with the top surface of the model with the recess, as shown in Figure 6.42a. Thus, this surface can be used as the 'splitting tool' to create the top surface of the implant (Figure 6.42b,c). Figure 6.43 presents a close up of the top surface section of the implant in situ in the 19 mm ROC with recess model in Fusion360. The image shows that using the full surface CAD as the top surface splitting tool generates a good continuation of the curved top surface.

The limits to the continuity of the implant top surface at the sides of the recess were the size of the print nozzle, and that the sides of the recess were not wholly vertical or smooth. This was due to the method of production of the clay models. A more accurate model replication would be possible by obtaining a full surface in an appropriate material, and using a surgical 'punch tool' to create the recess. This full surface could be the same dimensions of the dome surfaces utilised in this investigation, manufactured in a hydrogel-based material that aims to replicate articular cartilage. Furthermore, it could be a bovine knee sample.

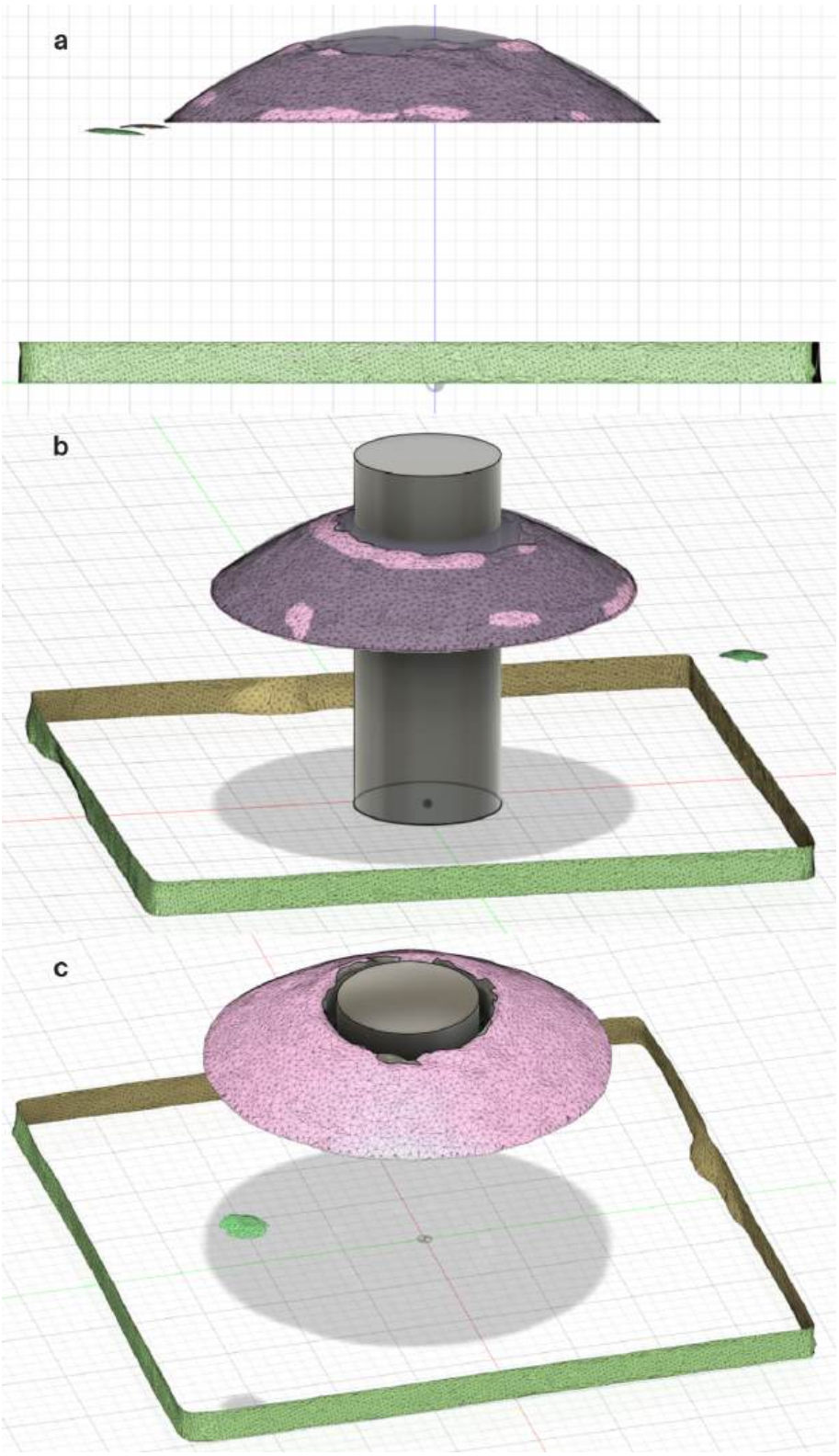

Figure 6.42: a) Side view of the scanned mesh model of the 19 mm ROC with recess clay model, overlaid with the solid surface generated from the scanned model mesh of the 19 mm ROC full surface. The solid surface has reduced opacity. b) The general implant cylinder geometry extruded from the XY plane. c) The excess sections of the implant cylinder removed after the body was split using the top and bottom surfaces. This leaves the conformal implant in situ in the recess.

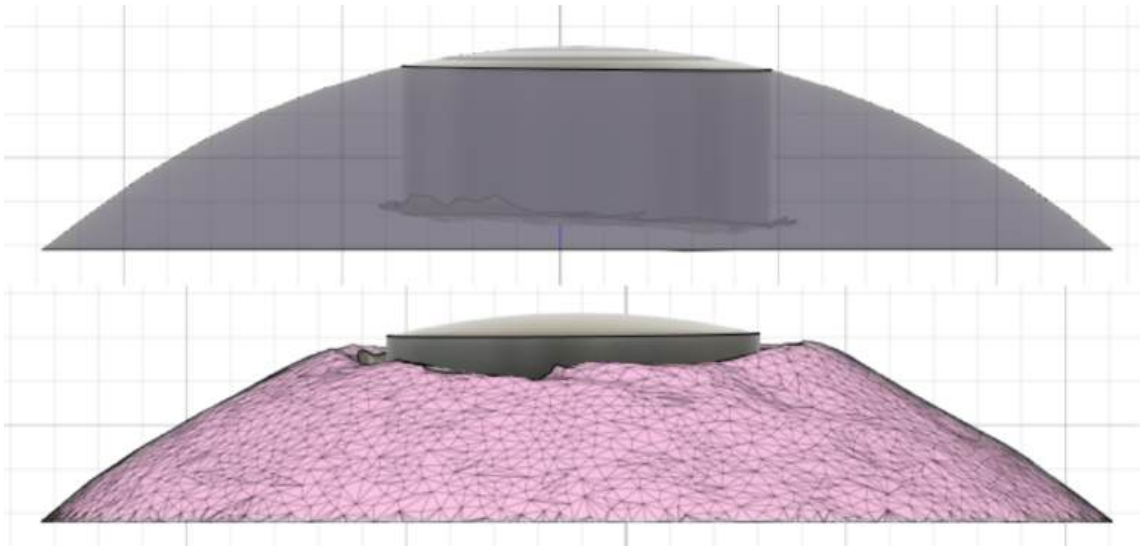

Figure 6.43: Expanded view of the top surface dome of the 19 mm ROC with recess model. Top: Isolated implant, recess bottom surface, and the imported surface of the 19 mm ROC full surface model. Bottom: Isolated top surface with recess mesh, and implant CAD in situ.

6.3.7 Preparing the Implant G-Codes

The implant was sliced in Repetier-Host software [140]. The process of editing the G-Code for the in situ 3D printing onto the clay bases is presented in more detail in Chapter 5.

6.3.8 In Situ Additive Manufacturing of the Implants

The inner surfaces of the recess (or the top surface of the full surface models) were dampened slightly, and a small amount of multi-purpose glue was rubbed onto the surface. This reduces the effect of the slightly dusty surface of the clay, and enhances the adhesion of the first layer of the print. As the clay model is not PLA / thermoplastic, there is not the adhesion of the molten PLA filament on the PLA top surface.

As discussed in Chapter 5, the G-Code prints the alignment frame and then moves the print bed forward for access, and 'dwells' the printer for a set amount of time (Figure 6.44a). During the dwell time, the test print line is removed from the print bed, and the clay model is placed into the alignment frame. The model is then secured to the print bed (Figure 6.44b). The model is secured with tape to the print bed due to it being lightweight. During printing, when the subsequent PLA layers are printed after the initial layer onto the clay surface, thermoplastic bonding of these layers can result in the model being lifted up with the nozzle movement. This results in the filament being laid inaccurately and can cause damage to the machine and the model. Otherwise, the position of the model within the frame remained consistent. Considering the medical application of in situ additive manufacturing, it is not unreasonable to design for the area being printed on to be immobilised during the procedure, but also to consider that the effects observed due to thermoplastic bonding of the layers would not be present with hydrogel- based additive manufacture.

The printer continues the print after the dwell point, and the implant is 3D printed into the recess, or onto the full top surface (Figure 6.45). This process is repeated for all four clay

models, and the results are presented visually in Figure 6.46. The use of the alignment frame appears to result in better alignment of the in situ 3D print in the XY directions, compared to the results in Chapter 6, with average deviance from the planned locations of the prints of less than 0.2 mm.

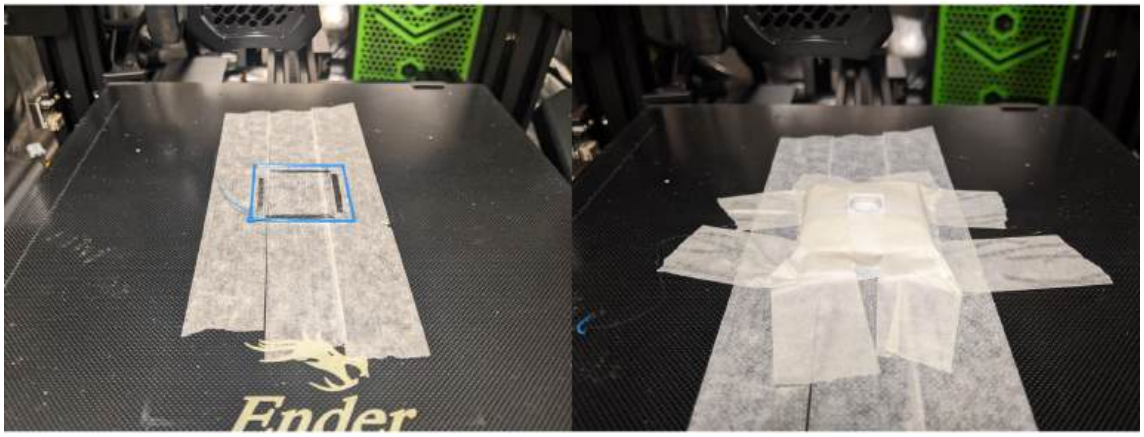

Figure 6.44: The stages of the in situ additive manufacturing onto the clay models. Images are of the 41 mm ROC with recess model. 1) The alignment frame is 3D printed, and the printer is in 'dwell'. 2) The clay model is placed into the alignment frame and secured to the print bed.

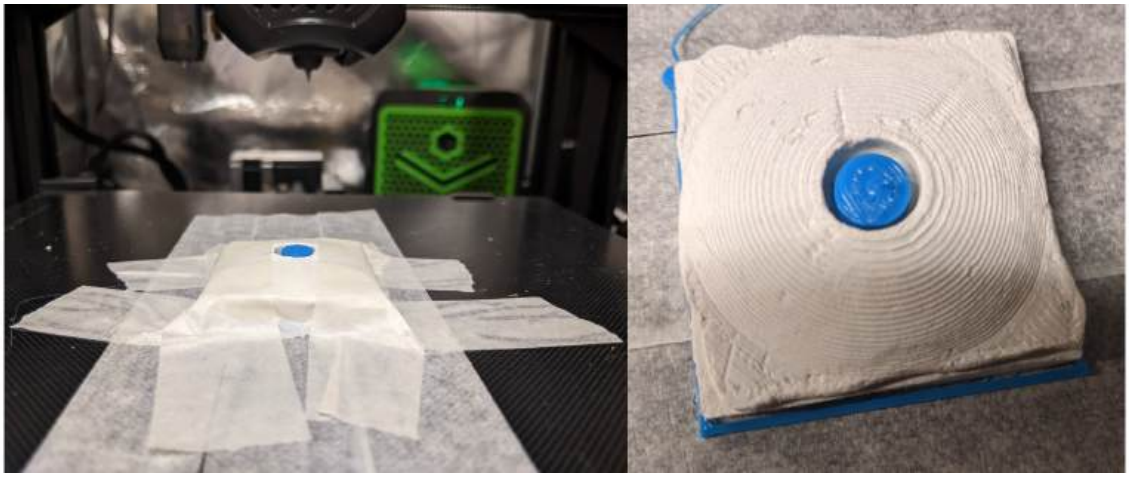

Figure 6.45: The stages of the in stages of the in situ additive manufacturing onto the clay models. Images are of the 41 mm ROC with recess model. 3) The in situ 3D print has been completed. 4) The securing tape has been removed to show the implant print in the recess of the clay model, which is in the printed alignment frame.

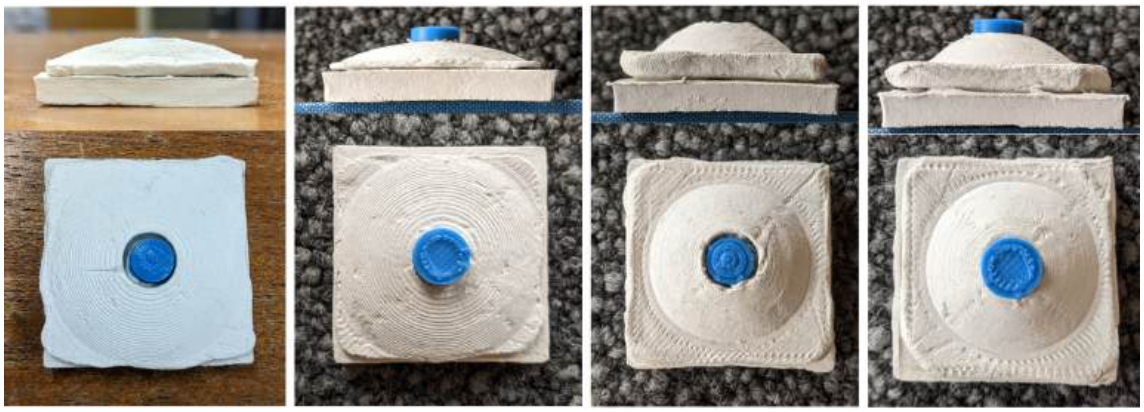

Figure 6.46: The four clay models with their corresponding in situ printed implants / surface additions (side and top views). Left to right: 41 mm ROC with recess, 41 mm ROC full surface, 19 mm ROC with recess, 19 mm ROC full surface.

6.4 Bone Model

6.4.1 Introduction

The next step, a fully 'unknown' surface to meet the chapter objective 1c: A PLA object additively manufactured in situ on the surface of another object, where the base object is a fully "unknown" surface with anatomical bone surface contour geometry. A Sawbone bone model was scanned and a surface addition print was designed and 3D printed in situ onto the surface of the model. This is a proof of concept experiment for in situ additive manufacture of a conformal print onto an 'unknown' surface.

6.4.2 Holding Frame

In order to maintain consistent orientation of the Sawbone bone model during scanning and printing, a holding frame was designed and created. The design theory is outlined in Section 5.3.3. Similar to the clay model alignment bases, a rectangular frame was designed in Fusion 360. The frame had internal dimensions of 84 x 200 mm, outer dimensions of 88 x 204 mm, and height of 10 mm. The frame was 3D printed in the blue PLA [147, 148].

Air-drying clay [142] was moulded into the frame, and then the bone model was pressed into the clay. More clay was built around the sides of the model to assist with secure positioning and alignment. The model bone was taped into position during the curing time, and the assembly was left for 24 hours to cure. The bone model was then removed and the mould was left to cure for a further 24 hours. Once cured, the mould was removed from the 3D printed PLA frame. The bone model was placed in the mould during the scanning and in situ 3D printing processes to ensure consistent orientation and alignment of the bone model. While visually the holder base does not appear to be completely flat, it remained stable and of constant alignment during the scanning and AM printing processes.

Figure 6.47: Creation of the holding mould for the Sawbone bone model. Top: The bone model secured in the mould during curing. Bottom: The empty holding mould during the curing time.

6.4.3 Scanning the Bone Model

The bone model was placed into the holder, and the combined assembly was placed on the turntable of the EinScan-SP 3D scanner (Shining3D, China) [114] inside the darkbox. The scan settings are detailed in Table 6.5. The scan data was processed in ExScanS V3.1.3.0 and exported as an unwatertight mesh in .3mf file format. The exported scanned model was imported into Autodesk Meshmixer software (Figure 6.48a) for editing in a similar way to the clay models, to remove excess geometry. The mesh preparation workflow presented for the clay models was followed for the bone model (Figure 6.36). Step 1 - importing the mesh into Meshmixer - completed, the required top surface area (Figure 6.48b, (1)) was selected with the 'brush tool' and a separate face group generated for this area (Step 2).

Table 6.5: 3D Scanner settings for bone model scan for in situ surface print.

Setting	Value
Scan type	Non-Texture Scan
HDR	On
With Turntable	On
Align Mode	Turntable Coded Align
Turntable Steps	18
Turntable Speed	1
Turntable Turns	One

The mesh model was sectioned (Step 3) using the 'plane cut' tool with the cut type as 'slice groups' and the fill type 'no fill', to create a face group of the bottom 5 mm of the alignment base geometry (Figure 6.48b, (2)). The surplus mesh sections were removed (Step 4); due to the model being asymmetrical, an alignment marker was not required, but could have been

included for confidence. The top surface section mesh was reduced with a triangle budget of 10,000 (Step 5), and the mesh model (Figure 6.48b) was exported as a .3mf file (Step 6).

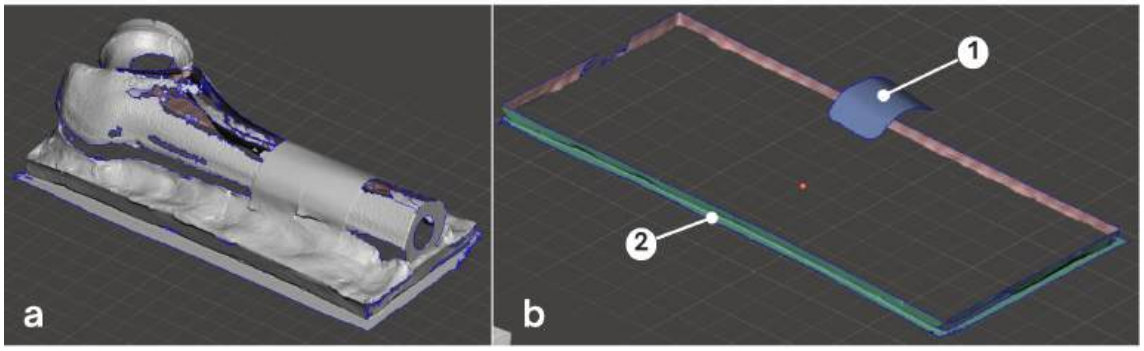

Figure 6.48: The bone model scan mesh in Meshmixer. a) Original scan mesh imported into Meshmixer. b) The mesh exported as a .3mf file.

6.4.4 Implant Design

The .3mf mesh file was uploaded into Autodesk Fusion 360, and the implant CAD model was created following the workflow presented in Figure 6.38. Similar to the method of designing the implants for the clay models, in Step 2 the mesh is separated into the top surface (1), and the alignment base (2) (Figure 6.49, sub-figure 2). The top surface mesh section (1) was then converted to a prismatic surface (Figure 6.49, sub-figure 3).

The cross section of the surface addition print is sketched on the XY origin plane (Figure 6.49, sub-figure 4). For the printed experiment, the sketch was a circle of diameter 10 mm, and was aligned to the approximate centre of the selected top surface section. The main body of the surface addition implant is thus generated by extruding the sketch from the XY origin plane to approximately 3 mm above the top surface (Figure 6.49, sub-figure 5). The implant CAD has a flat horizontal top surface. The top surface was designed to be flat as the top surface matching the contours of the bone model was not the aim of this specific experiment. The aim was for a conformal bottom surface which matched the contour of the bone model. The top flat surface also added the opportunity for more visual validation of the print path - if the lower layers of the print, which were of the most interest in this experiment, were distorted, this was easier to observe visually against flat horizontal neighbouring layers.

The 'split body' tool was used, with the top surface prismatic surface (1) as the 'splitting tool', to bisect the cylinder (3) (Figure 6.49, sub-figure 6). The excess section of the cylinder (5) was removed, leaving a surface addition object (4) that has a bottom surface that conforms to the top surface of the bone model (Figure 6.49, sub-figure 7). The alignment frame CAD (6) was added to the assembly, and reduced in height to 2 mm. The frame was aligned to the base geometry (2) of the scanned model (Figure 6.49, sub-figure 8). A round corner marker was added to the assembly, which coincided with the end of the model closest to the surface addition. This ensured that the bone model was placed in the alignment frame in the correct orientation during the printing process. The frame (6) and generated surface

addition CAD (4) were extracted together from the assembly, and exported to STL as one model (Figure 6.49, sub-figure 9).

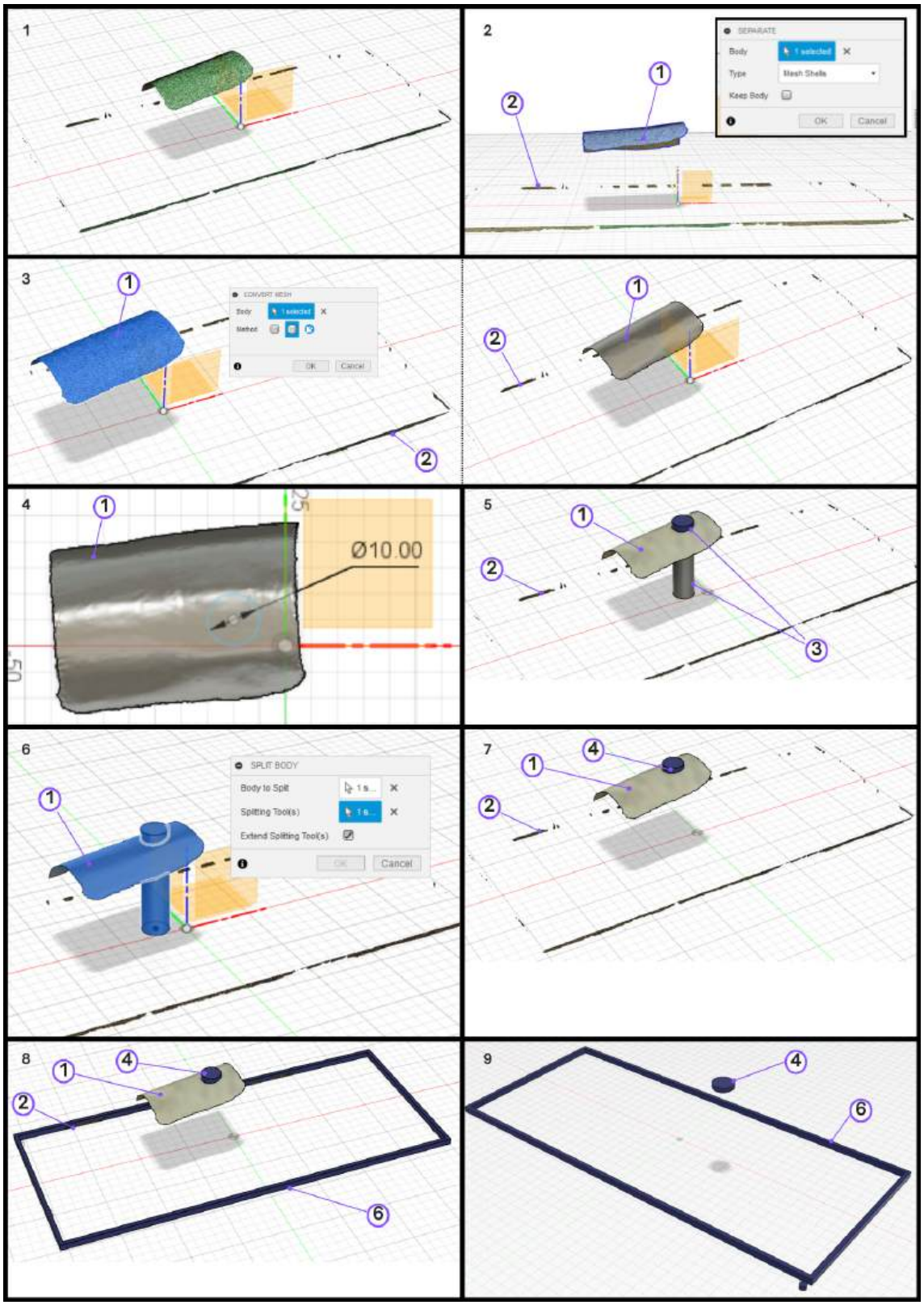

Figure 6.49: Screenshots from Fusion 360 of the stages of the surface implant CAD design process for the bone model. Sub-figure numbers correspond to the workflow stages in Figure 6.38.

6.4.5 Preparing the Implant Toolpath

The surface addition and alignment frame were imported into Repetier-Host for slicing, and generation of G-Code. Figure 6.50 presents the surface addition section of the toolpath modelled in Repetier-Host, showing the conformal bottom surface. The process of editing the G-Code for the in situ 3D printing onto the bone model is presented in more detail in Chapter 5. The example code for this print is presented in Appendix F.

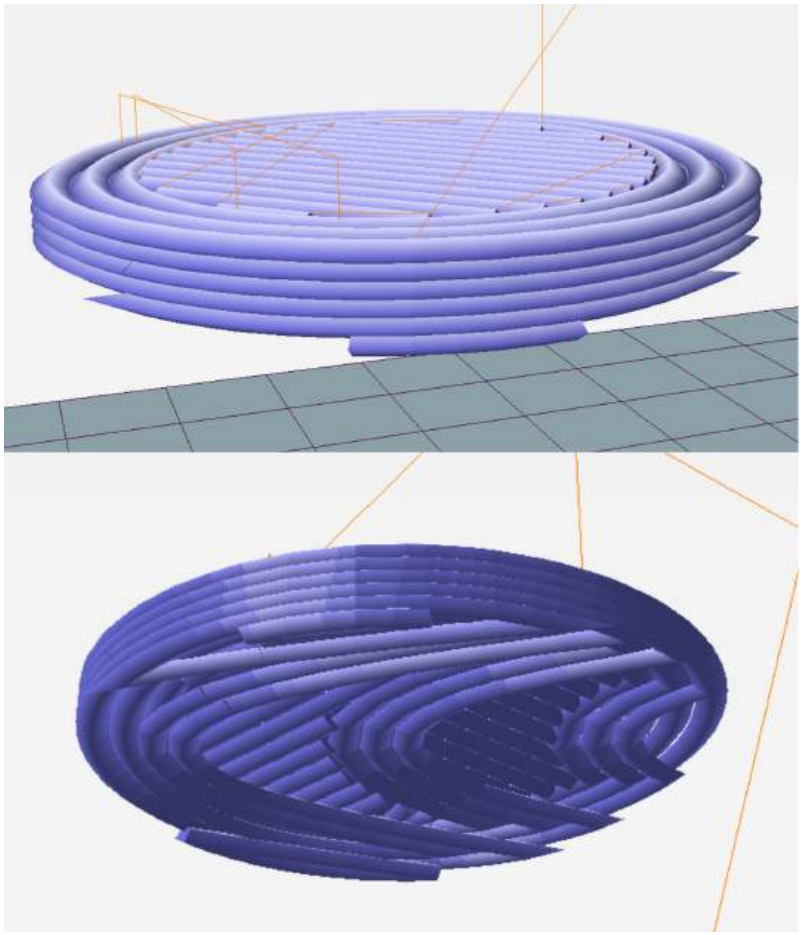

Figure 6.50: Virtual model of the toolpath for the bone model surface addition print. The flat top surface and conformal bottom surface are presented.

6.4.6 In Situ Additive Manufacturing

A thin temporary surface was taped to the section of the top surface of the bone model where the surface addition was to be 3D printed. This was to enable the surface print to be removed for repeat experiments without damaging the surface of the bone model. A spray adhesive was applied to the section of the top surface where the surface addition was to be printed. This is to enhance the adhesion of the first layer of the print, as there is not the thermal bonding adhesion between the layers of PLA filament with the first layer. As discussed in Chapter 5, the G-Code prints the alignment frame and then dwells the printer for placement of the bone model in the frame. After the dwell, the 3D printer continues the print and in situ 3D printing of the conformal surface addition is completed (Figure 6.51).

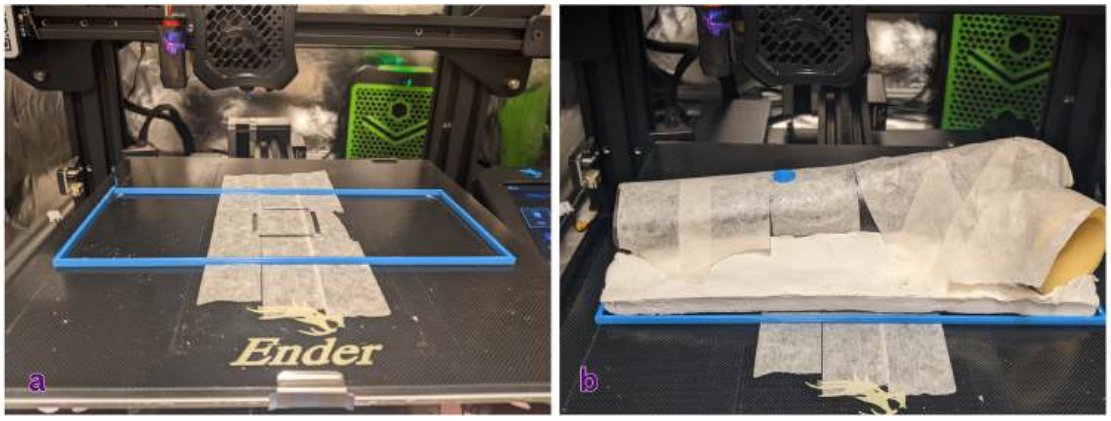

Figure 6.51: The stages of in situ 3D printing onto the bone model. a) The alignment frame is printed. b) The moulded holder has been placed in the frame, and the bone model has been placed in the holder. The print has been completed on the top surface of the bone model. The bone model has been covered to keep the spray adhesive off the rest of the model.

The in situ conformal additive manufacture of the CAD designed surface addition was considered successful. The first layer of the print adhered to the bone model (temporary) surface. As shown in Figure 6.52c, there is no damage to the surface under the temporary surface. This suggests conformal printing without the nozzle colliding with the surface. The print has a diameter measurement of 10.0 mm, and a maximum height of approximately 2.6 mm.

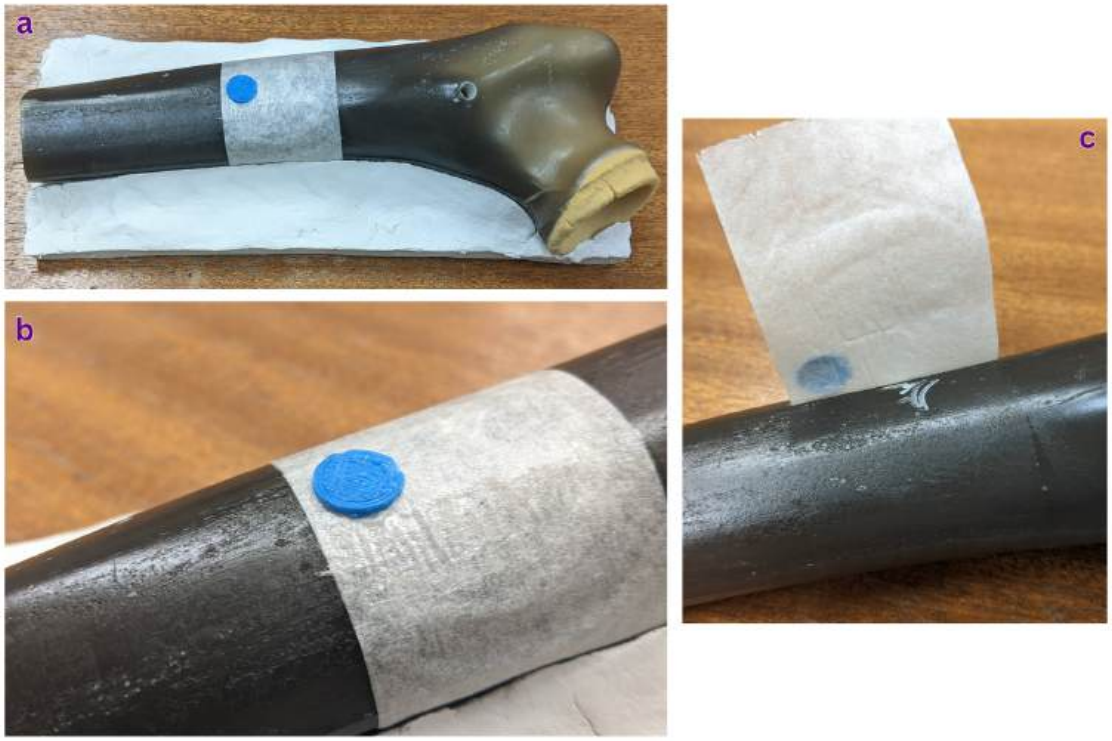

Figure 6.52: The in situ conformal 3D print as printed onto the top surface of the bone model. a) Top view of the bone model with surface addition print. b) Close up of the surface addition print. c) The temporary surface has been partially pulled away from the bone model surface to show the underside of the in situ print. The top surface of the model underneath is unchanged by the print process.

6.5 Summary

In this chapter, the full process of in situ additive manufacturing was brought together - various surfaces of increasingly 'unknown' status were scanned, and had implants CAD designed and then in situ 3D printed onto these surfaces.

Section 6.2 outlined a process of 3D printing onto a series of 3D printed bases of varying geometries. Successful in situ AM prints were completed, starting with the most basic cuboid base, to the final AM base which presented matching contours for both the top and bottom surfaces of the implant. These prints are considered proof of concept for AM onto "known" surfaces with relatively simple geometry alignment, and fulfil chapter objective 1a. The design and creation of a set of clay bases which approximated the contours of the human femoral condyles, and subsequent in situ conformal AM of implants onto their surfaces (Section 6.3) fulfilled chapter objective 1b. Furthermore, chapter objective 2 was achieved with successful in situ AM prints of implants into recesses which were approximate models of articular cartilage defects. Section 6.4 outlined the steps for in situ AM of a conformal surface addition print onto a fully "unknown" surface, to fulfil chapter objective 1c. The anatomical bone contour of the model used in this experiment furthermore supports in situ AM for articular cartilage regeneration by providing experimental validation on a surface with a similar radius to parts of some human femoral condyles. All in situ AM prints presented in Section 6.3 and Section 6.4 were considered successful, with accurate implant locations within the bounds

stated in Section 6.1, visually conformal surface matching between the AM in situ prints and their respective base objects, and no observed damage to the base objects.

The experiments described in this chapter are considered proof of concept of a methodology developed for in situ conformal MEX-TRB/P/PLA. The results presented in this chapter not only corroborate the results presented by Li et al (2017) [11] and Ma et al (2021) [12] (Section 2.8.1), but experimentally validate the toolpath theory presented in Chapter 5, thus filling a current gap in the field knowledge of in situ additive manufacturing. This in turn satisfies the aim of the chapter, to experimentally validate the theory that satisfies project objective 4. Furthermore, the results experimentally demonstrate in situ AM nozzle print origin positioning as part of the toolpath g-code (rather than manual nozzle positioning at the print origin [11, 12]), satisfying chapter objective 3.

Chapter 7

Overall Discussion

The aim of this research project was to develop a technique for additive manufacturing in situ based on the developments of biomedical applications of AM in the human body. The objectives were to evaluate methods of imaging the geometry that will be 3D printed upon, develop methods for AM onto a non-flat surface, and formulate techniques to use in-situ AM for the specific surgical procedure of repair of articular cartilage defect in the knee.

The contents of this thesis describe proof of concept for in situ conformal material extrusion additive manufacturing; achieved on additive manufactured bases, manufactured clay bases, and an 'unknown' surface of a bone model. The workflow described in Chapter 1 was reproduced with the surfaces undergoing 3D optical scanning to capture the geometry, the virtual models used to design conformal AM prints, the CAD models of the prints sliced and the toolpaths generated, and the workflow completed with the successful completion of in situ AM prints on a series of different bases.

As outlined in Chapter 2, critical sized articular cartilage defects will not heal fully without intervention, and current interventions generate fibrocartilage to replace the lost hyaline cartilage, or require implantation of donor hyaline cartilage. The inferior mechanical properties of fibrocartilage under normal joint loading, articular surface contour mismatch, and graft-host mismatch, are the main factors limiting the effectiveness of current interventions. Additive manufacturing, combined with 3D scanning, has been used to manufacture implants for low load bearing medical interventions. Furthermore, current in situ additive manufacturing research has developed a unique 'filament' for articular cartilage repair in the form of the Biopen Shell/Core system. While some research has presented proof of concept in vivo 3D printing of biocompatible hydrogel-based implants in situ for repair of articular cartilage defects, gaps remain in this research regarding the steps between scanning the cartilage defect to the implant being manufactured in situ via additive manufacturing. There is a lack of clarity in the underlying theory and mechanics of the in situ process. Little to no information is presented in the literature on: how the scan data is developed into the 3D printer toolpath or how the printer(s) were modified for the experiments undertaken. Furthermore, this research employed manual initial positioning of the print head at the print origin.

Considering the combination of additive manufacturing and surgical implants towards conformal bioprinting, the need for a standardised repeatable workflow became abundant. Filling the aforementioned gaps is significant in enabling a solid foundation for the development of patient-specific, customisable, in situ AM implants for the repair of human

articular cartilage defects. The work presented in this thesis contributes towards standardisation of the process of in situ additive manufacture onto unknown surfaces, helping to bridge that gap and fulfil the novel aspect of the PhD requirements.

The content of Chapter 3 fulfils the project objective 1; evaluate methods for imaging the geometry that will be printed upon. The development of a method for imaging the geometry of the surface to be printed onto found that all turntable step frequencies produced scan dimensional accuracy within 2 mm. The best dimensional accuracy was observed at a step frequency of 90 steps per 360 degree turn. Furthermore there was an observed difference in dimensional accuracy between the objects of a lighter surface colour and a darker surface colour, with the lighter object surface captured more completely and thus contributing to an increased dimensional accuracy. Further research, possibly exploring the diffuse structured light method [124] presented in Chapter 3, is required to investigate the significance of the surface colour in the observed results.

Considering the effect of the print parameters of print speed and print temperature on print dimensions, the maximum deviation was 0.3 mm for both parameters. The results suggest 40 mm/s print speed and 200 °C were the parameter values that would generate the best dimensional accuracy. Optical scanning of the same prints found maximum deviation of the scan dimensions compared to the prints of 0.1 mm (print temperature) and 0.2 mm (print speed). The results suggest a print speed of 30 - 60 mm/s, and print temperature of 200 °C to produce scans with the best dimensional accuracy compared to the physical prints. Behzadnasab et al (2020) [159] state that the mechanical properties of PLA AM prints are particularly affected by the processing conditions of AM, because of the semi-crystalline nature of PLA. Semi crystalline thermoplastics observe more severe cooling shrinkage than amorphous polymers, which can affect parts needing specific dimensional accuracy. The crystalline regions also result in increased stiffness and strength of the printed part compared to amorphous polymer prints. Many studies have observed higher crystallinity in PLA printed samples compared to their constituent PLA filament pre-printing [160]. Lay et al (2019) [161] suggest that this results from thermal cycling produced by movement of the heated nozzle across the same points in the print as the layers are deposited. Thermal cycling is suggested to induce formation of multiple smaller crystals (instead of a single larger crystal) [162]. Furthermore, Srinivas et al (2018) [163] suggest heat retention within the printed part increases crystallinity - the highest crystallinity for PLA was observed in the central layers, with the surrounding PLA layers insulating them, maintaining a higher temperature. Levenhagen et al (2017) [164] suggest the higher crystallinity is the result of shear-induced crystallisation from the high shear rates experienced by the molten PLA during extrusion through the nozzle. In contrast, some studies present low crystallinity, suggesting the cooling rates experienced during the AM process is too fast for crystallisation in PLA, as it is typically slow to form crystals [165, 166, 167]. Thus crystallinity of PLA AM prints is very variable - this could be explained by the use of different AM printers, print settings, environmental temperatures across the variety of studies. Furthermore, different PLA filaments from different suppliers [168] and even in different colours from the same supplier [169, 170] have presented varying crystallinity with the same print parameters. Behzadnasab et al (2020) [159] suggests that higher nozzle temperature during AM of PLA increases the interlayer adhesion, and that the movement of the nozzle during AM further affects the properties of the resulting print due to the temperature variations. Different patterns of filament deposition result in different temperature gradients and cooling times for individual layers, affecting the interlayer bonding

[159]. Shear rates experienced by the molten polymer as it is extruded through the AM nozzle has been shown to influence the orientation of the microstructures within the bulk extrudate [160]. The macromolecular chains have been observed to orient and align with the direction of the flow upon experiencing the shear rates [171, 172, 173]. Increased shear rates also present enhanced formation of microfibres within polymer blends [174, 175, 176], and orienting of reinforcing fibres within composites in the direction of the flow [177].

The generic AM process, which was used throughout this project, is multi-step (Figure 1.1). Each stage of design and conversion introduces errors, and is limited by the individual software limitations. Future research developing the methodologies presented in this thesis could utilise the concepts of explicit print-path definition presented in FullControl GCode Designer [178]. This software allows the user to define each step of the manufacturing process, and edit individual parameters at each segment of the print path, for full control of the AM toolpath from conception of the gross AM print design. This software aims to address the issues presented in Section 4.4 with manufacturing process-informed design. AM printing limitations on the G-Code level are considered and mitigated during simultaneous design of the overall AM structure geometry.

The logical next step in the development of the presented methodology is to use hydrogels; this software (FullControl) and the consideration of specific toolpath behaviour of hydrogels is important. The issues seen with additive manufacturing by MEX-TRB/P/PLA appear to be amplified with hydrogel bioprinting - for example the effect of temperature. Investigation into the behaviour of hydrogels during in situ AM for the applications discussed in this thesis is necessary. A gelatin–methacrylamide/hyaluronic acid–methacrylate hydrogel with UV curing was used by O'Connell at al (2016) [33] to generate the structures of their AM scaffolds when developing the BioPen. Abdollahiyan et al (2020) [179] reviews current developments in hydrogel-based bioinks for cartilage tissue engineering via additive manufacturing. Natural and synthetic hydrogels are both available for AM of articular cartilage, with poly(ε-caprolactone) (PCL) highlighted as for its suitability for modification to enhance its mechanical, physical and chemical properties [180, 181].

Furthermore, there is the added complication of 3D scanning a hydrogel construct for implant design and comparison to the CAD model, due to many hydrogels ranging from transparent to translucent. Optical scanning could be possible with an opaque hydrogel, or the use of an aerosolised, biocompatible masking spray which could temporarily cover the surface prior to scanning, and be rinsed away if the hydrogel surface was required for in situ additive manufacturing. Again, diffuse structured light 3D scanning could be investigated - Gupta (2013) presents it as a possibility for scanning of transparent objects [122].

As discussed in Chapter 2, scaffolds for surgical chondral repair have been pre-manufactured using AM in the laboratory and subsequently implanted during surgery [4, 5, 6, 7]. The scaffold lattice geometries and their mechanical properties have been explored for application to additive manufacturing of articular cartilage [182]. While homogeneous AM can create porosity by reducing the percentage fill within the body of the AM print, single- material Functionally Graded AM (FGAM) [183] can be used to adjust the internal geometry to better mimic the internal anatomy of articular cartilage. Multi-material FGAM can further customise the internal structure of the AM print and potentially aid the transition from implant to native hyaline cartilage structure [183]. Consideration of the lattice unit cell, the smallest

element of a lattice, is required to ensure biocompatibility (see Section 2.8) regarding cell expansion and replication of the mechanical functions of the native articular cartilage [182]. Combined with the development of software such as FullControl, specific customisation on a macro and micro scale could be achieved for closer approximations of the functional structure and mechanical properties of native articular cartilage.

Further development of synthesised articular cartilage for surgical applications should explore the tribological behaviour of the articulating surface and how this is facilitated within the human body. A significant property of articular cartilage is that it can provide an articular surface with a coefficient of friction between 0.002 and 0.01 [184]. Complex interactions between the articular cartilage and the synovial fluid, particularly the components lubricin and hyaluronic acid, are suggested to be key in effective joint function [15, 185, 186]. Development of synthetic lubricin-like nanostructured polymers is being researched and its relevance to articular cartilage implant design should be considered [185, 187].

The development of methods for in situ additive manufacturing onto non-flat surfaces comprised a series of experiments with different surfaces. First, in situ AM onto basic geometric surfaces previously 3D printed. These surfaces and their specific toolpaths were known, and used to prepare the toolpaths for the surface addition prints. Following on, clay surfaces were manufactured in house, optically scanned, and the toolpaths for in situ surface addition prints developed using the scan geometries. The clay models displayed radius of curvatures approximate to healthy human knee articular surfaces, and defects representing articular cartilage defects after surgical debridement. In situ AM successfully printed surface addition and defect-filling prints onto these surfaces. Finally, a surface of unknown manufacturing process(es) was scanned, and a surface addition print designed using the scanned geometry. A toolpath was generated for in situ additive manufacturing of a surface addition print, and the print was successfully performed onto the top surface of the object, with no observed damage to the surface, and a conformal shape was present at the adjoining surfaces. Although not covered in this work, the immediate next development of the in situ AM print experimental validation process would have been the combination of the full "unknown" surface and the model of the surgically debrided articular cartilage defect. Further experiments comprising milled defects into the bone model being filled with in situ AM implants would be a next step. It would also be beneficial to update the bone model to include the femoral condyles, for a more representative geometry.

Moving to more accurate representations of the human femoral condyle articular cartilage, bovine knee condyles would be used as a base model, with defects created through the same instruments used during surgical debridement of human AC defects before implantation (described in Chapter 2). These bovine knee condyles would be 3D scanned, with and without created defects, and the scanned models used to generate toolpaths for the condyles to be filled in the same method as presented in Chapter 6. The use of CT or MRI scanning for capture of the pre-defect articular cartilage surface geometry could be explored here, for investigation of medical utility compared to optical 3D scanning. Following on from the proof-of-concept of the technique in bovine models, the methodology should be combined with the latest innovations in hydrogel compositions and AM internal lattice research for mimicking human knee articular cartilage. Together, the technology can be developed for translation to human surgical intervention.

The research presented in this thesis confirms and elevates the in situ additive manufacturing processes presented by Li et al [11, 12], and, combined with the Biopen co-axial extrusion technology (Section 2.8.1), could transform the surgical repair of articular cartilage defects in the human knee. This methodology can also be developed further for different applications. Combined with the most up-to-date materials and scaffolding techniques, in situ conformal additive manufacturing could be the next step in the development of additive manufacturing technology.

7.1 Conclusion

Through a series of virtual and physical experiments, a method was developed, and experimentally validated, for additive manufacturing in situ onto "known" and "unknown" surfaces. Objects were 3D scanned using the EinScan-SP 3D scanner, and in situ AM prints onto the surfaces of these objects were completed. Successful prints were demonstrated on previously additive manufactured top-surface geometries, clay models representing the radius of curvature of human condyles and approximate geometries of articular cartilage debrided defects, and the "unknown" surface of a Sawbones bone model. The techniques developed through this work are able to be modified and developed through further research to facilitate in situ additive manufacturing for repair of articular cartilage defects, towards human surgical use.

Overall conclusions:

- Surfaces of a lighter colour are captured better with 3D optical scanners than darker surfaces.
- The print parameters of print speed and print temperature affect the dimensional accuracy of both printed parts and the scanned models of the parts.
- Alignment frames contained within the G-Code of the implant prints increase accuracy of the alignment of the implant.
- In situ additive manufacture of conformal implant and surface addition prints is possible, and perfect filling of defects was primarily limited by the size of the print head nozzle.

In conclusion, this thesis provides in depth proof-of-concept for the development of a technique for additive manufacturing in situ for conformal additive manufacturing onto 'unknown' surfaces. Furthermore, applications of the methodologies developed in this thesis extend far further than in situ AM of biomedical surgical implants. The techniques presented are versatile and can be modified for applications of surface addition part upgrades, retrofitting, defect repair of non-medical surfaces, and other applications which utilise the fundamental techniques behind material extrusion additive manufacturing.

References

[1] Cornelissen, D-K. *et al.* "Current developments in 3D bioprinting for tissue engineering". In: *Current Opinion in Biomedical Engineering* 2 (2017). [online] [Accessed 3 October 2019]. DOI: https://doi.org/10.1016/j.cobme.2017.05.004.

[2] Lui, Y. *et al.* "Recent Progress in Cartilage Tissue Engineering — Our Experience and Future Directions". In: *Engineering* 3 (2017). [online] [Accessed 22 August 2023]. DOI: https://doi.org/10.1016/J.ENG.2017.01.010.

[3] Daly, A. C. *et al.* "3D Bioprinting for Cartilage and Osteochondral Tissue Engineering". In: *Advanced Healthcare Materials* 6 (2017). [online] [Accessed 3 October 2019]. DOI: https://doi.org/10.1002/adhm.201700298.

[4] Di Bella, C. *et al.* "3D Bioprinting of Cartilage for Orthopedic Surgeons: Reading between the Lines". In: *Frontiers in Surgery* 2 (2015). [online] [Accessed 22 August 2023]. DOI: https://doi.org/10.3389/fsurg.2015.00039.

[5] Iwasa, J. *et al.* "Clinical application of scaffolds for cartilage tissue engineering". In: *Knee Surgery, sports Traumatology, Arthroscopy* 17 (2009). [online] [Accessed 22 August 2023]. DOI: https://doi.org/10.1007/s00167-008-0663-2.

[6] Kang, H-W. *et al.* "Bioprinted Scaffolds for Cartilage Tissue Engineering". In: *Cartilage Tissue Engineering* (2015). [online] [Accessed 22 August 2023]. DOI: https://doi.org/10.1007/978-1-4939-2938-2_11.

[7] Rai, V. *et al.* "Recent strategies in cartilage repair: A systemic review of the scaffold development and tissue engineering". In: *Journal of Biomedical Materials Research Part A* 105 (2017). [online] [Accessed 22 August 2023]. DOI: https://doi.org/10.1002/jbm.a.36087.

[8] Onofrillo, C. *et al.* "Biofabrication of human articular cartilage: a path towards the development of a clincal treatment". In: *Biofabrication* 10 (2018). [online] [Accessed 16 October 2019]. DOI: https://doi.org/10.1088/1758-5090/aad8d9.

[9] Koh, J.L. *et al.* "The Effect of Graft Height Mismatch on Contact Pressure following Osteochondral Grafting: A Biomechanical Study". In: *The American Journal of Sports Medicine* 32 (2004). [online] [Accessed 22 August 2023]. DOI: https://doi.org/10.1177/0363546503261730.

[10] International Organization for Standardization. *Additive manufacturing. General principles. Fundamentals and vocabulary*. BS EN ISO/ASTM 52900:2021. [online] [Accessed 5 May 2023]. The British Standards Institution, 2021. URL: https://bsol.bsigroup.com/Bibliographic/BibliographicInfoData/000000000030448424.

[11] Li, L. *et al.* "*In situ* repair of bone and cartilage defects using 3D scanning and 3D printing". In: *Scientific Reports* 7 (2017). [online] [Accessed 21 October 2021]. DOI: https://doi.org/10.1038/s41598-017-10060-3.

[12] Ma, K. *et al.* "Application of robotic-assisted *in situ* 3D printing in cartilage regeneration with HAMA hydrogel: An *in vivo* study". In: *Journal of Advanced Research* 23 (2020). [online] [Accessed 21 October 2021]. DOI: https://doi.org/10.1016/j.jare.2020.01.010.

[13] Moyad, T.F. "Cartilage Injuries in the Adult Knee: Evaluation and Management". In: *Cartilage* 2 (2010). [online] [Accessed 3 October 2019]. DOI: https://doi.org/10.1177/1947603510383973.

[14] Bose, S. *et al.* "Additive Manufacturing of biomaterials". In: *Progress in Materials Science* 93 (2018). [online] [Accessed 16 October 2019]. DOI: https://doi.org/10.1016/j.pmatsci.2017.08.003.

[15] Buckwalter, J.A. "Mechanical Injuries of Articular Cartilage". In: *The Iowa Orthopaedic Journal* (1992). [online] [Accessed 16 October 2019]. URL: https://www.ncbi.nlm.nih.gov/pmc/articles/PMC2328735/.

[16] Fox, A. J. S. *et al.* "The Basic Science of Articular Cartilage: Structure, Composition, and Function". In: *Sports Health* 1 (2009). [online] [Accessed 12 July 2024]. DOI: https://doi.org/10.1177%2F1941738109350438.

[17] Maroudas, A. *et al.* "The effect of osmotic and mechanical pressures on water partitioning in articular cartilage". In: *Biochimica et Biophysica Acta (BBA) - General Subjects* 1073 (1991). [online] [Accessed 12 July 2024]. DOI: https://doi.org/10.1016/0304-4165(91)90133-2..

[18] Moore, D.W. *Articular Cartilage*. [online] [Accessed 14 June 2023]. 2022. URL: https://www.orthobullets.com/basic-science/9017/articular-cartilage.

[19] Kabir, W. *et al.* "Assessment of Native Human Articular Cartilage: A Biomechanical Protocol". In: *Cartilage* 13 (2020). [online] [Accessed 31 August 2023]. DOI: https://doi.org/10.1177/1947603520973240.

[20] Lyyra, T. *et al.* "In vivo characterization of indentation stiffness of articular cartilage in the normal human knee". In: *Journal of Biomedical Materials Research* 48 (1999). [online] [Accessed 29 September 2023]. DOI: https://doi.org/10.1002/(SICI)1097-4636(1999)48:4<482::AID-JBM13>3.0.CO;2-M.

[21] Jurvelin, J.S. *et al.* "Mechanical anisotropy of the human knee articular cartilage in compression". In: *Proceedings of the Institution of Mechanical Engineers, Part H: Journal of Engineering in Medicine* 217 (2003). [online] [Accessed 29 September 2023]. DOI: https://doi.org/10.1243/095441103765212712.

[22] Antons, J. *et al.* "Zone-dependent mechanical properties of human articular cartilage obtained by indentation measurements". In: *Journal of Materials Science: Materials in Medicine* 29 (2018). [online] [Accessed 29 September 2023]. DOI: https://doi.org/10.1007/s10856-018-6066-0.

[23] Hoemann, C. *et al.* "International Cartilage Repair Society (ICRS) Recommended Guidelines for Histological Endpoints for Cartilage Repair Studies in Animal Models and Clinical Trials". In: *Cartilage* 2 (2011). DOI: https://doi.org/10.1177/1947603510397535.

[24] Fridbie, D.D. *et al.* "A comparative study of articular cartilage thickness in the stifle of animal species used in human pre-clinical studies compared to articular cartilage thickness in the human knee". In: *Veterinary and Comparative Orthopaedics and Traumatology* (2006). [online] [Accessed 14 June 2023]. URL: https://pubmed.ncbi.nlm.nih.gov/16971996/.

[25] Madry, H. *et al.* "The basic science of the subchondral bone". In: *Knee Surgery, Sports Traumatology, Arthroscopy* 18 (2010). [online] [Accessed 24 October 2024]. DOI: https://doi.org/10.1007/s00167-010-1054-z.

[26] Duncan, H. *et al.* "The tibial subchondral plate. A scanning electron microscopic study". In: *The Journal of Bone & Joint Surgery* 69 (1987). [online] [Accessed 24 October 2024]. URL: https://pubmed.ncbi.nlm.nih.gov/3667650/.

[27] Layton, M. W. *et al.* "Examination of subchondral bone architecture in experimental osteoarthritis by microscopic computed axial tomography". In: *Arthritis and rheumatism* 31 (1988). [online] [Accessed 24 October 2024]. DOI: https://doi.org/10.1002/art.1780311109.

[28] Malekipour, F. *et al.* "Shock absorbing ability of articular cartilage and subchondral bone under impact compression". In: *Journal of the Mechanical Behavior of Biomedical Materials* 26 (2013). [online] [Accessed 24 October 2024]. DOI: https://doi.org/10.1016/j.jmbbm.2013.05.005.

[29] Radin, E. L. & Rose, R. M. "Role of subchondral bone in the initiation and progression of cartilage damage". In: *Clinical orthopaedics and related research* 213 (1986). [online] [Accessed 24 October 2024]. URL: https://journals.lww.com/clinorthop/abstract/1986/12000/role_of_subchondral_bone_in_the_initiation_and.5.aspx.

[30] Coon, M. S. & Best, B. J. "Distal Femur Fractures." In: (2023). [online] [Accessed 24 October 2024]. URL: %7Bhttps://www.ncbi.nlm.nih.gov/books/NBK551675/%7D.

[31] Aneja, A. & Graves, M. L. "Distal Femur Fractures". In: *Encyclopedia of Trauma Care* (2015). [online] [Accessed 24 October 2024]. DOI: https://doi.org/10.1007/978-3-642-29613-0_646.

[32] Di Bella, C. *et al.* "*In situ* handheld three-dimensional bioprinting for cartilage regeneration". In: *Journal of Tissue Engineering and Regenerative Medicine* 12 (2017). [online] [Accessed 3 October 2019]. DOI: https://doi.org/10.1002/term.2476.

[33] O'Connell, C.D. *et al.* "Development of the Biopen: a handheld device for surgical printing of adipose stem cells at a chondral wound site". In: *Biofabrication* 8 (2016). [online] [Accessed 3 October 2019]. DOI: https://doi.org/10.1088/1758-5090/8/1/015019.

[34] Coulter, F.B. *et al.* "Bioinspired Heart Valve Prosthesis Made by Silicone Additive Manufacturing". In: *Matter* 1 (2019). [online] [Accessed 16 October 2019]. DOI: https://doi.org/10.1016/j.matt.2019.05.013.

[35] Conley, S. *et al.* "The Female Knee: Anatomic Variations". In: *Journal of the American Academcy of Orthopaedic Surgeons* 15 (2007). [online] [Accessed 16 October 2019]. DOI: https://doi.org/10.5435/00124635-200700001-00009.

[36] Katagiri, H. *et al.* "Definition of a Critical Size Osteochondral Knee Defect and its Negative Effect on the Surrounding Articular Cartilage in the Rat". In: *Osteoarthritis and Cartilage* 25 (2017). [online] [Accessed 3 October 2019]. DOI: https://doi.org/10.1016/j.joca.2017.05.006.

[37] Browne, J.E. & Branch T.P. "Surgical Alternatives for Treatment of Articular Cartilage Lesions". In: *Journal of the American Academy of Orthopaedic Surgeons* 8 (2000). [online] [Accessed 14 June 2023]. DOI: https://doi.org/10.5435/00124635-200005000-00005.

[38] Husen, M. *et al.* "Size of cartilage defects and the need for repair: a systematic review". In: *Journal of Cartilage & Joint Preservation* 2 (2022). [online] [Accessed 14 June 2023]. DOI: https://doi.org/10.1016/j.jcjp.2022.100049.

[39] van der Meijden, O. *et al.* "Glenohumeral Joint Preservation: A Review of Management Options for Young, Active Patients with Osteoarthritis". In: *Advances in Orthopedics* 1 (2012). [online] [Accessed 12 July 2024]. DOI: https://doi.org/10.1155/2012/160923.

[40] Ondresik, M. *et al.* "Management of knee osteoarthritis. Current status and future trends". In: *Biotechnology and Bioengineering* 114 (2016). [online] [Accessed 3 October 2019]. DOI: https://doi.org/10.1002/bit.26182.

[41] Steadman, J.R. *et al.* "Microfracture technique forfull-thickness chondral defects: Technique and clinical results". In: *Operative Techniques in Orthopeadics* 7 (1997). [online] [Accessed 29 June 2023]. DOI: https://doi.org/10.1016/S1048-6666(97)80033-X.

[42] Mithoefer, K. et al. *Chondral Resurfacing of Articular Cartilage Defects in the Knee with the Microfracture Technique*. [online] [Accessed 30 June 2023]. 2006. DOI: 10.2106/JBJS.F.00292. URL: https://journals.lww.com/jbjsjournal/Fulltext/2006/09001/Chondral_Resurfacing_of_Articular_Cartilage.13.aspx.

[43] Moiduddin, K. *et al.* "Structural and mechanical characterization of custom design cranial implant created using additive manufacturing". In: *Electronic Journal of Biotechnology* 29 (2017). [online] [Accessed 16 October 2019]. DOI: https://doi.org/10.1016/j.ejbt.2017.06.005.

[44] Epec Engineered Technologies. *Differences Between Solid Modeling and Surface Modeling*. [online] Available at: https://blog.epectec.com/differences-between-solid-modeling-and-surface-modeling [Accessed 25 October 2024]. 2022.

[45] Dassault Systemes. *Glossary - Solid Modeling*. [online] Available at: https://www.spatial.com/resources/glossary/what-is-solid-modeling [Accessed 25 October 2024]. 2024.

[46] Solid Solutions Management Ltd. *Surface Modelling: How to Convert Surfaces to Solid Bodies in SOLIDWORKS*. [online] Available at: https://www.solidsolutions.co.uk/blog/2023/08/surface-modelling-how-to-convert-surfaces-to-solid-bodies-in-solidworks/#:~:text=Asopposedtosolidmodelling,thickness,andareentirelyweightless. [Accessed 25 October 2024]. 2023.

[47] Dassault Systemes. *The Essentials of surface modeling explained*. [online] Available at: https://www.3ds.com/store/cad/surface-modeling [Accessed 25 October 2024]. 2024.

[48] Precise 3D Metrology & Design Solutions Pvt. Ltd. *Difference between Nurbs surface and Parametric surface in 3D Reverse Engineering*. [online] Available at: https://precise3dm.com/blogs/difference-between-nurbs-surface-and-parametric-surface-in-3d-reverse-engineering/#:~:text=InthefieldofCAD,bycontrolpointsandknots. [Accessed 25 October 2024]. 2021.

[49] Danthree Studio. *What Is A 3D Mesh Model? (Definition & Examples)*. [online] Available at: https://www.danthree.studio/en/blog-cgi/what-is-a-3d-mesh-model-definition-examples [Accessed 25 October 2024]. no date.

[50] Rack, S. *What is the difference between NURBs model and a mesh?* [online] Available at: https://holocreators.com/blog/what-is-the-difference-between-a-nurbs-model-and-a-polygon-mesh/#:~:text=ANURBSmodelconsistsof,ormillionsofsmalltriangles. [Accessed 25 October 2024]. 2020.

[51] Materialise nv. *3D Printing With Rhino: Preparing Your Rhinoceros 3D Model for 3D Printing*. [online] Available at: https://i.materialise.com/blog/en/3d-printing-with-rhino//#:~:text=InRhino,youcreatean,howthemodelismeshed. [Accessed 25 October 2024]. 2024.

[52] Autodesk. *Autodesk Meshmixer*. [online] [Accessed 18 Jan 2023]. URL: https://meshmixer.com/.

[53] Dassault Systemes. *Understanding the power of parametric modeling*. [online] Available at: https://www.3ds.com/store/cad/parametric-modeling [Accessed 25 October 2024]. 2024.

[54] DDDimension. *What is the difference between mesh models and parametric 3D models?* [online] Available at: https://www.ddd-imension.com/en/post/what-is-the-difference-between-mesh-models-and-parametric-3d-models#:~:text=Mesh-based3Dmodelsare,usedforproduction:3Dprinting. [Accessed 25 October 2024]. no date.

[55] Roy, S. *Nurbs: An Introduction*. [online] Available at: https://professional3dservices.com/blog/nurbs-modeling.html [Accessed 25 October 2024]. 2023.

[56] Robert McNeel & Associates. *What are NURBS?* [online] Available at: https://www.rhino3d.com/features/nurbs/ [Accessed 25 October 2024]. 2024.

[57] Nevercenter. *Using subdivision surfaces in Silo.* [online] Available at: https://nevercenter.com/silo3d/Tutorials/Subdivision_Surfaces/Subdivision_Surfaces.html [Accessed 25 October 2024]. 2024.

[58] Shiue, L-J, A. *CGAL 6.0.1 - 3D Surface Subdivision Methods*. [online] Available at: https://doc.cgal.org/latest/Subdivision_method_3/index.html#:~:text=Asubdivisionmethodrecursivelyrefines,homeomorphictoa2Ddisk. [Accessed 25 October 2024]. no date.

[59] Ma, W. "Subdivision surfaces for CAD—an overview". In: *Computer-Aided Design* 37 (2005). [online] [Accessed 25 October 2024]. DOI: https://doi.org/10.1016/j.cad.2004.08.008.

[60] Siber, B. *Blender: Reduce Polygons – Simply Explained*. [online] Available at: https://all3dp.com/2/blender-how-to-reduce-polygons/ [Accessed 25 October 2024]. 2022.

[61] Dassault Systemes. *A simple guide to the basics of subdivision surfaces modeling*. [online] Available at: https://www.3ds.com/store/cad/subdivision-modeling [Accessed 25 October 2024]. 2024.

[62] Catmull, E & Clark, J. "Recursively generated B-spline surfaces on arbitrary topological meshes". In: *Computer-Aided Design* 10 (1978). [online] [Accessed 25 October 2024]. DOI: https://doi.org/10.1016/0010-4485(78)90110-0.

[63] Kemiyatorn, B. *Catmull-Clark-subdivision-of-4-planes.png*. [online] Available at: https://en.wikipedia.org/wiki/File:Catmull-Clark_subdivision_of_4_planes.png [Accessed 25 October 2024]. 2009.

[64] Thomas-Seale, L.E.J. *et al.* "The barriers to the progression of additive manufacture: Perspectives from UK industry". In: *International Journal of Production Economics* 198 (2018). [online] [Accessed 30 August 2023]. DOI: https://doi.org/10.1016/j.ijpe.2018.02.003.

[65] Wiria, F.E. *et al.* "Printing of Titanium implant prototype". In: *Materials & Design* 31 (2010). [online] [Accessed 16 October 2019]. DOI: https://doi.org/10.1016/j.matdes.2009.12.050.

[66] Singh, S. & Ramakrishna, S. "Biomedical applications of additive manufacturing: Present and future". In: *Current Opinion in Biomedical Engineering* 2 (2017). [online] [Accessed 16 October 2019]. DOI: http://dx.doi.org/10.1016/j.cobme.2017.05.006.

[67] Wong, K.V. & Hernandez, H. "A Review of Additive Manufacturing". In: *International Scholarly Research Notices* (2012). [online] [Accessed 16 October 2019]. DOI: https://doi.org/10.5402/2012/208760.

[68] Frunzaverde, D. *et al.* "The Influence of the Printing Temperature and the Filament Color on the Dimensional Accuracy, Tensile Strength, and Friction Performance of FFF-Printed PLA Specimens". In: *Polymers* 14 (2022). [online] [Accessed 23 March 2023]. URL: https://doi.org/10.3390/polym14101978.

[69] Alsoufi, M. *et al.* "Experimental Characterization of the Influence of Nozzle Temperature in FDM 3D Printed Pure PLA and Advanced PLA+". In: *American Journal of Mechanical Engineering* 7 (2019). [online] [Accessed 23 March 2023]. DOI: 10.12691/ajme-7-2-1.

[70] Hatz, C. *et al.* "Can an entry-level 3D printer create high-quality anatomical models? Accuracy assessment of mandibular models printed by a desktop 3D printer and a professional device". In: *International Journal of Oral and Maxillofacial Surgery* 49 (2020). [online] [Accessed 23 March 2023]. DOI: https://doi.org/10.1016/j.ijom.2019.03.962.

[71] Msallem, B. *et al.* "Evaluation of the Dimensional Accuracy of 3D-Printed Anatomical Mandibular Models Using FFF, SLA, SLS, MJ, and BJ Printing Technology". In: *Journal of Clinical Medicine* 9 (2020). [online] [Accessed 23 March 2023]. DOI: https://doi.org/10.3390/jcm9030817.

[72] He, G. *et al.* "Report on a novel bone registration method: A rapid, accurate, and radiation-free technique for computer- and robotic-assisted orthopedic surgeries". In: *Journal of Orthopaedics* 23 (2021). [online] [Accessed 27 March 2023]. DOI: https://doi.org/10.1016/j.jor.2021.01.010.

[73] Lievendag, N. *SHINING 3D EINSCAN-SE & EINSCAN-SP REVIEW & COMPARISON*. [online] [Accessed 29 June 2023]. 2017. URL: https://3dscanexpert.com/shining-3d-einscan-se-einscan-sp-review-comparison/.

[74] Taubin, G. *et al. 3D Scanning for Personal 3D Printing: Build Your Own Desktop 3D Scanner*. [online] Available at: http://mesh.brown.edu/desktop3dscan/SG14-byod3d.pdf [Accessed 28 October 2024]. 2014.

[75] Bose, S. *et al.* "Surface modification of biomaterials and biomedical devices using additive manufacturing". In: *Acta Biomaterialia* 66 (2018). [online] [Accessed 16 October 2019]. DOI: https://doi.org/10.1016/j.actbio.2017.11.003.

[76] Cohen, D.L. *et al.* "Additive manufacturing for *in situ* repair of osteochondral defects". In: *Biofabrication* 2 (2010). [online] [Accessed 16 October 2019]. DOI: https://doi.org/10.1088/1758-5082/2/3/035004.

[77] Jardini, A.L. *et al.* "Cranial reconstruction: 3D biomodel and custom-built implant created using additive manufacturing". In: *Journal of Cranio-Maxillofacial Surgery* 42 (2014). [online] [Accessed 16 October 2019]. DOI: https://doi.org/10.1016/j.jcms.2014.07.006.

[78] Petrovic, V. *et al. Additive Manufacturing Solutions for Improved Medical Implants*. Biomedicine. [online] [Accessed 16 October 2019]. InTech, 2012. ISBN: 978-953-51-0352-3. URL: http://www.intechopen.com/books/biomedicine/additive-manufacturing-solutions-for-improved-implants.

[79] Koptyug, A. *et al.* "Additive Manufacturing Technology Applications Targeting Practical Surgery". In: *International Journal of Life Science and Medical Research* 3 (2013). [online] [Accessed 16 October 2019]. DOI: http://dx.doi.org/10.5963/LSMR0301003.

[80] Jammalamadaka, U. *et al.* "Recent Advances in Biomaterials for 3D Printing and Tissue Engineering". In: *Journal of Functional Biomaterials* 9 (2018). [online] [Accessed 16 October 2019]. DOI: https://doi.org/10.3390/jfb9010022.

[81] Ciocca, L. *et al.* "CAD/CAM and rapid prototyped scaffold construction for bone regenerative medicine and surgical transfer of virtual planning: A pilot study". In: *Computerized Medical Imaging and Graphics* 33 (2009). [online] [Accessed 16 October 2019]. DOI: https://doi.org/10.1016/j.compmedimag.2008.10.005.

[82] Salmi, M. *et al.* "Accuracy of medical models made by additive manufacturing (rapid manufacturing)". In: *Journal of Cranio-Maxillofacial Surgery* 41 (2013). [online] [Accessed 16 October 2019]. DOI: https://doi.org/10.1016/j.jcms.2012.11.041.

[83] Singh, S. *et al.* "Material issues in additive manufacturing: A review". In: *Journal of Manufacturing Processes* 25 (2017). [online] [Accessed 16 October 2019]. DOI: https://doi.org/10.1016/j.jmapro.2016.11.006.

[84] Peltola, M.J. *et al.* "Novel composite implant in craniofacial bone reconstruction". In: *European Archives of Oto-Rhino-Larynology* 269 (2012). [online] [Accessed 16 October 2019]. DOI: https://doi.org/10.1007/s00405-011-1607-x.

[85] Chua, C.K. *et al.* "1 - Introduction to rapid prototyping of biomaterials". In: *Rapid Prototyping of Biomaterials (Second Edition): Techniques in Additive Manufacturing* (2020). [online] [Accessed 16 October 2019]. DOI: https://doi.org/10.1016/B978-0-08-102663-2.00001-0.

[86] Youssef, A. *et al.* "Additive manufacturing of polymer melts for implantable medical devices and scaffolds". In: *Biofabrication* 9 (2017). [online] [Accessed 16 October 2019]. DOI: https://doi.org/10.1088/1758-5090/aa5766.

[87] Salmi, M. *et al.* "Patient-specific reconstruction with 3D modeling and DMLS additive manufacturing". In: *Rapid Prototyping Journal* 18 (2012). [online] [Accessed 16 October 2019]. DOI: https://doi.org/10.1108/13552541211218126.

[88] Singare, S. *et al.* "Design and fabrication of custom mandible titanium tray based on rapid prototyping". In: *Medical Engineering & Physics* 26 (2004). [online] [Accessed 16 October 2019]. DOI: https://doi.org/10.1016/j.medengphy.2004.06.001.

[89] Bausch, N. *et al.* "3D Printing onto Unknown Uneven Surfaces". In: *IFAC-PapersOnLine* 49 (2016). [online] [Accessed 16 October 2019]. DOI: https://doi.org/10.1016/j.ifacol.2016.10.664.

[90] Perez, A.N. *et al.* "Ex vivo 3D scanning and specimen mappping in anatomic pathology". In: *Journal of Pathology Informatics* 14 (2023). [online] [Accessed 23 March 2023]. DOI: https://doi.org/10.1016/j.jpi.2022.100186.

[91] He, G. *et al.* "A novel bone registration method using impression molding and structured-light 3D scanning technology". In: *Journal of Orthopaedic Research* 40 (2022). [online] [Accessed 23 March 2023]. DOI: https://doi.org/10.1002/jor.25275.

[92] Schlaier, J. *et al.* "Registration Accuracy and Practicability of Laser-Directed Surface Matching". In: *Computer Aided Surgery* 7 (2002). [online] [Accessed 28 March 2023]. DOI: https://doi.org/10.3109/10929080209146037.

[93] Drost, B. *et al.* "Model Globally, Match Locally: Efficient and Robust 3D Object Recognition". In: *IEEE Computer Society Conference on Computer Vision and Pattern Recognition* San Francisco, CA, USA (2010). [online] [Accessed 27 March 2023]. DOI: https://doi.org/10.1109/CVPR.2010.5540108.

[94] Lea, J. T. *et al.* "Registration and immobilization in robot-assisted surgery". In: *Journal of Image Guided Surgery* 1 (1995). [online] [Accessed 28 October 2024]. DOI: https://doi.org/10.1002/(sici)1522-712x(1995)1:2%3C80::aid-igs2%3E3.0.co;2-h.

[95] Lui, J. L. *et al.* "Image Registration in Medical Robotics and Intelligent Systems: Fundamentals and Applications". In: *Advanced Intelligent Systems* 1 (2019). [online] [Accessed 28 October 2024]. DOI: https://doi.org/10.1002/aisy.201900048.

[96] Sheriff, J. *et al.* "Computer-readable Image Markers for Automated Registration in Correlative Microscopy – "autoCRIM"". In: *Ultramicroscopy* 228 (2021). [online] [Accessed 28 October 2024]. DOI: https://doi.org/10.1016/j.ultramic.2021.113322.

[97] Habermehl, D. *et al.* "Evaluation of different fiducial markers for image-guided radiotherapy and particle therapy". In: *Journal of Radiation Research* 54 (2013). [online] [Accessed 30 October 2024]. DOI: http://dx.doi.org/10.1093/jrr/rrt071.

[98] Alam, F. *et al.* "A Review on Extrinsic Registration Methods for Medical Images". In: *Technical Journal of University of Engineering & Technology Taxila* 21 (2016). [online] [Accessed 30 October 2024]. URL: https://www.researchgate.net/publication/313160195_A_Review_on_Extrinsic_Registration_Methods_for_Medical_Images.

[99] Hongwei, Z. *et al.* "Accuracy of Fiducial Marker Based Multimodal Image Registration in Image Guided Surgery". In: *IFMBE proceedings* 31 (2010). [online] [Accessed 30 October 2024]. DOI: http://dx.doi.org/10.1007/978-3-642-14515-5_392.

[100] Simonetti, A. B. "Planning and Registration Techniques for Image-Guided Robotic Spinal Surgery". Dissertation submitted for the Degree of Doctor of Philosophy, University of Navarra. 2012. URL: https://core.ac.uk/download/83577986.pdf.

[101] Patravale, V. *et al.* "3 - Characterization techniques for nanoparticulate carriers". In: *Nanoparticulate Drug Delivery* (2012). [online] [Accessed 12 July 2024]. DOI: https://doi.org/10.1533/9781908818195.87.

[102] Ramakrishna, S. & Huang, Z-M. "Bioengineering". In: *Comprehensive Structural Integrity* 9 (2003). [online] [Accessed 12 July 2024]. DOI: https://doi.org/10.1016/B0-08-043749-4/09064-9.

[103] Niaounakis, M. "7 - Medical, Dental, and Pharmaceutical Applications". In: *Biopolymers: Applications and Trends* (2015). [online] [Accessed 21 October 2024]. DOI: https://doi.org/10.1016/B978-0-323-35399-1.00007-7.

[104] Ferris, C.J. *et al.* "Biofabrication: an overview of the approaches used for printing of living cells". In: *Applied Microbiology and Biotechnology* 97 (2013). [online] [Accessed 16 October 2019]. DOI: https://doi.org/10.1007/s00253-013-4853-6.

[105] Ligon, S.C. *et al.* "Polymers for 3D Printing and Customized Additive Manufacturing". In: *Chemical Reviews* 117 (2017). [online] [Accessed 16 October 2019]. DOI: https://doi.org/10.1021/acs.chemrev.7b00074.

[106] Wendel, B. *et al.* "Additive Processing of Polymers". In: *Macromolecular Materials and Engineering* 293 (2008). [online] [Accessed 16 October 2019]. DOI: https://doi.org/10.1002/mame.200800121.

[107] Chung, J.H.Y. *et al.* "Bio-ink properties and printability for extrusion printing living cells". In: *Biomaterials Science* 1 (2013). [online] [Accessed 16 October 2019]. DOI: https://doi.org/10.1039/C3BM00012E.

[108] Duchi, S. *et al.* "Handheld Co-Axial Bioprinting: Application to *in situ* surgical cartilage repair". In: *Scientific Reports* 7 (2017). [online] [Accessed 3 October 2019]. DOI: https://doi.org/10.1038/s41598-017-05699-x.

[109] Christensen, K. *et al.* "Effects of printing-induced interfaces on localized strain within 3D printed hydrogel structures". In: *Materials Science and Engineering: C* 89 (2018). [online] [Accessed 30 August 2023]. DOI: https://doi.org/10.1016/j.msec.2018.03.014.

[110] Yoon, D. *et al.* "Design and characterization of 3-D printed hydrogel lattices with anisotropic mechanical properties". In: *Journal of the Mechanical Behavior of Biomedical Materials* 138 (2023). [online] [Accessed 30 August 2023]. DOI: https://doi.org/10.1016/j.jmbbm.2023.105652.

[111] Hunziker, E.B. *et al.* "Quantitative structural organization of normal adult human articular cartilage". In: *Osteoarthritis and Cartilage* 10 (2002). [online] [Accessed 29 August 2023]. DOI: https://doi.org/10.1053/joca.2002.0814.

[112] Shining3D. *EinScan Pro HD SPECS*. [online] Available at: https://www.einscan.com/handheld-3d-scanner/einscan-pro-hd/einscan-pro-hd-specs/ [Accessed 16 July 2024].

[113] Shining3D. *EinScan H2 SPECS*. [online] Available at: https://www.einscan.com/handheld-3d-scanner/einscan-h/einscan-h2-specs/ [Accessed 16 July 2024].

[114] Shining3D. *EinScan-SP SPECS Desktop 3D Scanner*. [online] Available at: https://www.einscan.com/desktop-3d-scanners/einscan-sp/einscan-sp-specs/ [Accessed 9 May 2022].

[115] Sawbones Europe AB. *Sawbones*. [online] [Accessed 29 June 2023]. URL: https://www.sawbones.com/.

[116] Gupta, M. *et al.* "Structured Light in Sunlight". In: *2013 IEEE International Conference on Computer Vision* (2013). [online] [Accessed 29 October 2024]. DOI: 10.1109/ICCV.2013.73.

[117] Bada, S. *"Watertight" and "Unwatertight" meshes*. [online] Available at: https://support.einscan.com/en/support/solutions/articles/60000687687--watertight-and-unwatertight-meshes [Accessed 29 September 2023]. 2022.

[118] Bonneau, D. *et al.* "Surface Reconstruction for Three-Dimensional Rockfall Volumetric Analysis". In: *ISPRS International Journal of Geo-Information* 8 (2019). [online] [Accessed 29 September 2023]. DOI: https://doi.org/10.3390/ijgi8120548.

[119] Pribanic, T. *et al.* "Efficient multiple phase shift patterns for dense 3D acquisition in structured light scanning". In: *Image and Vision Computing* 28 (2010). [online] [Accessed 28 October 2024]. DOI: https://doi.org/10.1016/j.imavis.2010.01.003.

[120] Selotkin, V. & Kobein, I. *Structured-Light Imaging: What's in It?* [online] Available at: https://www.softserveinc.com/en-us/blog/structured-light-imaging [Accessed 28 October 2024]. 2020.

[121] Kalisperakis, I. *et al.* "A STRUCTURED-LIGHT APPROACH FOR THE RECONSTRUCTION OF COMPLEX OBJECTS". In: *Geoinformatics FCE CTU* 6 (2011). [online] [Accessed 28 October 2024]. DOI: https://doi.org/10.14311/gi.6.32.

[122] Gupta, M. *et al.* "A Practical Approach to 3D Scanning in the Presence of Interreflections, Subsurface Scattering and Defocus". In: *International Journal of Computer Vision* 102 (2013). [online] [Accessed 29 October 2024]. DOI: https://doi.org/10.1007/s11263-012-0554-3.

[123] Tan, R. T. "Specularity, Specular Reflectance". In: *Computer Vision* (2021). [online] [Accessed 29 October 2024]. DOI: https://doi.org/10.1007/978-3-030-63416-2_538.

[124] Nayar, S. K. & Gupta, M. "Diffuse Structured Light". In: *2012 IEEE International Conference on Computational Photography (ICCP)* (2012). [online] [Accessed 29 October 2024]. DOI: 10.1109/ICCPhot.2012.6215216.

[125] Aurenhammer, F. "Voronoi diagrams - a survey of a fundamental geometric data structure". In: *ACM Computing Surveys* 23 (1991). [online] [Accessed 29 October 2024]. DOI: https://doi.org/10.1145/116873.116880.

[126] Li, Z. *et al.* "DIGITAL TERRAIN MODELING Principles and Methodology". In: (2005). [online] [Accessed 29 October 2024]. URL: https://nguyenduyliemgis.wordpress.com/wp-content/uploads/2014/11/digital-terrain-modeling-principles-and-methodology_2005.pdf.

[127] MathWorks. *Working with Delaunay Triangulations*. [online] Available at: https://uk.mathworks.com/help/matlab/math/delaunay-triangulation.html [Accessed 29 October 2024]. 2024.

[128] Gallier, J. "Chapter 8 - Dirichlet–Voronoi Diagrams and Delaunay Triangulations". In: *In: Geometric Methods and Applications* 38 (2011). [online] [Accessed 29 October 2024]. DOI: https://doi.org/10.1007/978-1-4613-0137-0_9.

[129] Red Blob Games. *Delaunay + Voronoi on a sphere*. [online] Available at: https://www.redblobgames.com/x/1842-delaunay-voronoi-sphere/ [Accessed 25 October 2024]. 2018.

[130] UltiMaker B. V. *Technical Data Sheet PLA*. [online] [Accessed 27 Jan 2023]. 2016. URL: https://docs.rs-online.com/030e/0900766b815911d6.pdf.

[131] Hawthorn, B. *et al.* "Tailoring surface roughness through the temporal variation of additive manufacturing process parameters". In: *The International Journal of Advanced Manufacturing Technology* 132 (2024). [online] [Accessed 21 October 2024]. DOI: https://doi.org/10.1007/s00170-024-13532-9.

[132] Ultimaker B. V. *Ultimaker S5*. [online] [Accessed 23 Nov 2022]. URL: https://ultimaker.com/3d-printers/s-series/ultimaker-s5/.

[133] Levinskas, L. "Research of dimensional accuracy and surface quality dependency on printing speed of FDM 3D printed parts". Master's Final Degree Project, Kaunas University of Technology, Kaunas. 2019. URL: https://epubl.ktu.edu/object/elaba:38308616/.

[134] O'Connell, J. *How to Set Up Linear Advance in Marlin*. [online] [Accessed 8 Feb 2023]. 2021. URL: https://all3dp.com/2/linear-advance-cura-marlin/.

[135] Prusa Research. *Linear Advance*. [online] [Accessed 8 Feb 2023]. 2022. URL: https://help.prusa3d.com/article/linear-advance_2252.

[136] Davies, M. *How to Use Linear Advance in Cura? (In-Depth Explanation)*. [online] [Accessed 8 Feb 2023]. 2023. URL: https://www.3dprintbeast.com/cura-linear-advance/.

[137] Dwamena, M. *What is Linear Advance & How to Use It – Cura, Klipper*. [online] [Accessed 8 Feb 2023]. 2022. URL: https://3dprinterly.com/what-is-linear-advance-how-to-use-it-cura-klipper/.

[138] Arntsonn Tronvoll, S. *et al.* "Investigating pressure advance algorithms for filament-based melt extrusion additive manufacturing: theory, practice and simulations". In: *Rapid Prototyping Journal* 25 (2019). [online] [Accessed 22 October 2024]. DOI: http://dx.doi.org/10.1108/RPJ-10-2018-0275.

[139] Gilbert, M. *Brydson's Plastics Materials: Chapter 4 - Relation of Structure to Thermal and Mechanical Properties*. 8th edition. [online] [Accessed 29 March 2023]. Butterworth-Heinemann, 2017. ISBN: 9780323358248. DOI: https://doi.org/10.1016/B978-0-323-35824-8.00004-9.

[140] Hot-World GmbH & Co. KG. *Repetier-Host*. [online] [Accessed 18 Sept 2023]. URL: https://www.repetier.com/.

[141] Ultimaker B.V. *UltiMaker*. [online] [Accessed 18 Sept 2023]. URL: https://ultimaker.com/software/ultimaker-cura/.

[142] DAS. *1kg White Modelling Clay*. The Works. 2023. URL: https://www.theworks.co.uk/p/modelling-clay/das-1kg-white-modelling-clay/8000144074105.html.

[143] Autodesk Inc. *Fusion 360*. [online] [Accessed 27 Jan 2023]. 2021. URL: https://www.autodesk.co.uk/products/fusion-360/.

[144] Creality. *Creality Ender 3 V2*. [online] [Accessed 20 Sept 2023]. URL: https://www.crealityofficial.co.uk/products/ender-3-v2-3d-printer.

[145] Blackburn, T. A. & Craig, E. "Knee Anatomy: A Brief Review". In: *Physical Therapy* 60 (1980). [online] [Accessed 22 October 2024]. DOI: https://doi.org/10.1093/ptj/60.12.1556.

[146] Creality. *CR Touch*. [online] [Accessed 20 Sept 2023]. URL: https://www.crealityofficial.co.uk/products/ender-cr-touch-kit-uk.

[147] RS. *RS PRO 1.75mm Blue PLA 3D Printer Filament, 1kg*. [online] [Accessed 11 Feb 2022]. (RS Stock No.8320226). URL: https://uk.rs-online.com/web/p/3d-printing-materials/8320226?searchId=5949fcb4-f214-433b-87bb-2493941b9899&gb=s.

[148] RS. *RS PRO 1.75mm Blue PLA 3D Printer Filament, 1kg*. [online] [Accessed 11 Feb 2022]. URL: https://docs.rs-online.com/bf49/A700000007511197.pdf.

[149] RS. *RS PRO 1.75mm Red PLA 3D Printer Filament, 1kg*. [online] [Accessed 11 Feb 2022]. (RS Stock No.8320220). URL: https://uk.rs-online.com/web/p/3d-printing-materials/8320220?searchId=2bbc44c1-728f-453e-80ed-1fff30b57b70&gb=s.

[150] RS. *RS PRO 3D Printing Materials - 1.75mm Red PLA 3D Printer Filament, 1kg*. [online] [Accessed 11 Feb 2022]. URL: https://docs.rs-online.com/bc1c/A700000007511189.pdf.

[151] Creality 3D. *K8 Brass Volcano Nozzles*. Available online. 2022. URL: https://onecall.farnell.com/creality-3d/4007010083/k8-brass-volcano-nozzle/dp/3813243?ost=volcano+nozzle.

[152] Two Trees. *V6 Airbrush Nozzle*. Available online. 2022. URL: https://uk.vicedeal.com/products/3d-printer-m6-v5-v6-nozzle-airbrush-adapter-set-0-2-0-3-0-4-0-5mm-removable-stainless-steel-tips-for-e3d-v6-hotend-ender-3-cr10?gclid=EAIaIQobChMIraCCoM769wIV4u3mCh2alwl_EAQYAiABEgIihfD_BwE&variant=UHJvZHVjdFZhcmlhbnQ6MjY2NjE4Njg2.

[153] Mo Sabri. *Creality Ender 3-V2*. [online] [Accessed 6 October 2023]. 2022. URL: https://grabcad.com/library/creality-ender-3-v2-4.

[154] Hangody, L. *et al.* "Autologous osteochondral grafting - Technique and long-term results". In: *Injury* 39 (2008). [online] [Accessed 29 August 2023]. DOI: https://doi.org/10.1016/j.injury.2008.01.041.

[155] Du, P.Z. *et al.* "Differences in the Radius of Curvature Between Femoral Condyles: Implications for Osteochondral Allograft Matching". In: *The Journal of Bone and Joint Surgery* 100 (2018). [online] [Accessed 28 April 2023]. DOI: http://dx.doi.org/10.2106/JBJS.17.01509.

[156] Chaurasia, A. *et al.* "Morphologic Features of the Distal Femur and Proximal Tibia: A Cross-Sectional Study". In: *Cureus* 13 (2021). [online] [Accessed 28 April 2023]. DOI: https://doi.org/10.7759/cureus.12907.

[157] Nuño, N. & Ahmed, A.M. "Three-dimensional morphometry of the femoral condyles". In: *Clinical Biomechanics* 18 (2003). [online] [Accessed 28 April 2023]. DOI: https://doi.org/10.1016/s0268-0033(03)00172-4.

[158] Freeman, M.A.R. & Pinskerova, V. "The movement of the normal tibio-femoral joint". In: *Journal of Biomechanics* 38 (2005). [online] [Accessed 28 April 2023]. DOI: https://doi.org/10.1016/j.jbiomech.2004.02.006.

[159] Behzadnasab, M. *et al.* "Effects of processing conditions on mechanical properties of PLA printed parts". In: *Rapid Prototyping Journal* 26 (2020). [online] [Accessed 4 November 2024]. DOI: http://dx.doi.org/10.1108/RPJ-02-2019-0048.

[160] Vaes, D. & Van Puyvelde, P. "Semi-crystalline feedstock for filament-based 3D printing of polymers". In: *Progress in Polymer Science* 118 (2021). [online] [Accessed 8 November 2024]. DOI: https://doi.org/10.1016/j.progpolymsci.2021.101411.

[161] Lay, M. *et al.* "Comparison of physical and mechanical properties of PLA, ABS and nylon 6 fabricated using fused deposition modeling and injection molding". In: *Composites Part B: Engineering* 176 (2019). [online] [Accessed 8 November 2024]. DOI: https://doi.org/10.1016/j.compositesb.2019.107341.

[162] Song, Y. *et al.* "Measurements of the mechanical response of unidirectional 3D-printed PLA". In: *Materials & Design* 123 (2017). [online] [Accessed 8 November 2024]. DOI: https://doi.org/10.1016/j.matdes.2017.03.051.

[163] Srinivas, V. *et al.* "Correlating molecular and crystallization dynamics to macroscopic fusion and thermodynamic stability in fused deposition modeling; a model study on polylactides". In: *Polymer* 142 (2018). [online] [Accessed 8 November 2024]. DOI: https://doi.org/10.1016/j.polymer.2018.03.063.

[164] Levenhagen, N. P. & Dadmun, M. D. "Bimodal molecular weight samples improve the isotropy of 3D printed polymeric samples". In: *Polymer* 122 (2017). [online] [Accessed 8 November 2024]. DOI: https://doi.org/10.1016/j.polymer.2017.06.057.

[165] Verbeeten, W. M. H. *et al.* "Anisotropic rate-dependent mechanical behavior of Poly(Lactic Acid) processed by Material Extrusion Additive Manufacturing". In: *Additive Manufacturing* 31 (2020). [online] [Accessed 8 November 2024]. DOI: https://doi.org/10.1016/j.addma.2019.100968.

[166] Wach, R. A. *et al.* "Enhancement of Mechanical Properties of FDM-PLA Parts via Thermal Annealing". In: *Macromolecular Materials and Engineering* 303 (2018). [online] [Accessed 8 November 2024]. DOI: https://doi.org/10.1002/mame.201800169.

[167] Wijnen, B. *et al.* "Improved model and experimental validation of deformation in fused filament fabrication of polylactic acid". In: *Progress in Additive Manufacturing* 3 (2018). [online] [Accessed 8 November 2024]. DOI: https://doi.org/10.1007/s40964-018-0052-4.

[168] Cicala, G. *et al.* "Polylactide (PLA) Filaments a Biobased Solution for Additive Manufacturing: Correlating Rheology and Thermomechanical Properties with Printing Quality". In: *Materials* 11 (2018). [online] [Accessed 8 November 2024]. DOI: https://doi.org/10.3390/ma11071191.

[169] Wittbrodt, B. & Pearce, J. M. "The effects of PLA color on material properties of 3-D printed components". In: *Additive Manufacturing* 8 (2015). [online] [Accessed 8 November 2024]. DOI: https://doi.org/10.1016/j.addma.2015.09.006.

[170] Spina, R. "Performance Analysis of Colored PLA Products with a Fused Filament Fabrication Process". In: *Polymers* 11 (2019). [online] [Accessed 8 November 2024]. DOI: https://doi.org/10.3390/polym11121984.

[171] Mackay, M. E. "The importance of rheological behavior in the additive manufacturing technique material extrusion". In: *Journal of Rheology* 62 (2018). [online] [Accessed 8 November 2024]. DOI: https://doi.org/10.1122/1.5037687.

[172] Mackay, M. E. *et al.* "The performance of the hot end in a plasticating 3D printer". In: *Journal of Rheology* 61 (2017). [online] [Accessed 8 November 2024]. DOI: https://doi.org/10.1122/1.4973852.

[173] McIlroy, C. & Olmsted, P. D. "Disentanglement effects on welding behaviour of polymer melts during the fused-filament-fabrication method for additive manufacturing". In: *Polymer* 123 (2017). [online] [Accessed 8 November 2024]. DOI: https://doi.org/10.1016/j.polymer.2017.06.051.

[174] Leng, J. *et al.* "Preparation of Thermoplastic Polyurethane Parts Reinforced with in Situ Polylactic Acid Microfibers during Fused Deposition Modeling: The Influences of Deposition-Induced Effects". In: *Industrial & Engineering Chemistry Research* 58 (2019). [online] [Accessed 8 November 2024]. DOI: 10.1021/acs.iecr.9b04285.

[175] Jiang, Y. *et al.* "Reinforced and toughened PP/PS composites prepared by Fused Filament Fabrication (FFF) with in-situ microfibril and shish-kebab structure". In: *Polymer* 186 (2020). [online] [Accessed 8 November 2024]. DOI: https://doi.org/10.1016/j.polymer.2019.121971.

[176] Zhou, Y-G. *et al.* "Deposition-induced effects of isotactic polypropylene and polycarbonate composites during fused deposition modeling". In: *Rapid Prototyping Journal* 23 (2017). [online] [Accessed 8 November 2024]. DOI: http://dx.doi.org/10.1108/RPJ-12-2015-0189.

[177] Heller, B. P. *et al.* "Effects of extrudate swell and nozzle geometry on fiber orientation in Fused Filament Fabrication nozzle flow". In: *Additive Manufacturing* 12 (2016). [online] [Accessed 8 November 2024]. DOI: https://doi.org/10.1016/j.addma.2016.06.005.

[178] Gleadall, A. "FullControl GCode Designer: Open-source software for unconstrained design in additive manufacturing". In: *Additive Manufacturing* 46 (2021). [online] [Accessed 4 November 2024]. DOI: https://doi.org/10.1016/j.addma.2021.102109.

[179] Abdollahiyan, P. *et al.* "Hydrogel-Based 3D Bioprinting for Bone andCartilage Tissue Engineering". In: *Biotechnology Journal* 15 (2020). [online] [Accessed 4 November 2024]. DOI: https://doi.org/10.1002/biot.202000095.

[180] Malikmammadov, E. *et al.* "PCL and PCL-based materials in biomedical applications". In: *Journal of Biomaterials Science, Polymer Edition* 29 (2017). [online] [Accessed 4 November 2024]. DOI: https://doi.org/10.1080/09205063.2017.1394711.

[181] Kundu, J. *et al.* "An additive manufacturing-based PCL–alginate–chondrocyte bioprinted scaffold for cartilage tissue engineering". In: *Journal of Tissue Engineering and Regenerative Medicine* (2013). [online] [Accessed 4 November 2024]. DOI: https://doi.org/10.1002/term.1682.

[182] Ataollahi, S. "A review on additive manufacturing of lattice structures in tissue engineering". In: *Bioprinting* 35 (2023). [online] [Accessed 4 November 2024]. DOI: https://doi.org/10.1016/j.bprint.2023.e00304.

[183] Hsiang Loh, G. *et al.* "An overview of functionally graded additive manufacturing". In: *Additive Manufacturing* 23 (2018). [online] [Accessed 4 November 2024]. DOI: https://doi.org/10.1016/j.addma.2018.06.023.

[184] Oungoulian, S.R. *et al.* "Wear and Damage of Articular Cartilage with Friction Against Orthopaedic Implant Materials". In: *Journal of Biomechanics* 48 (2015). DOI: https://doi.org/10.1016/j.jbiomech.2015.04.008.

[185] Bayer, I. S. "Advances in Tribology of Lubricin and Lubricin-Like Synthetic Polymer Nanostructures". In: *Lubricants* 6 (2018). [online] [Accessed 4 November 2024]. DOI: https://doi.org/10.3390/lubricants6020030.

[186] Gleghorn, J. P. *et al.* "Boundary mode lubrication of articular cartilage by recombinant human lubricin". In: *Journal of Orthopaedic Research* 27 (2009). [online] [Accessed 4 November 2024]. DOI: https://doi.org/10.1002/jor.20798.

[187] Lee, Y. *et al.* "Regulation of lubricin for functional cartilage tissue regeneration: a review". In: *Biomaterials Research* 22 (2018). [online] [Accessed 4 November 2024]. DOI: https://doi.org/10.1186/s40824-018-0118-x.

[188] SPSS Tutorials. *ANOVA - Super Simple Introduction*. [online] [Accessed 2 Dec 2022]. 2022. URL: https://www.spss-tutorials.com/anova-what-is-it/.

[189] SPSS Tutorials. *Effect Size - A Quick Guide*. [online] [Accessed 2 Dec 2022]. 2022. URL: https://www.spss-tutorials.com/effect-size/.

[190] SPSS Tutorials. *Effect Size - A Quick Guide, ANOVA - (Partial) Eta Squared*. [online] [Accessed 2 Dec 2022]. 2022. URL: https://www.spss-tutorials.com/effect-size/#anova-partial-eta-squared.

[191] Cohen, J. *Statistical Power Analysis for the Behavioral Sciences*. 2nd ed. [online] [Accessed 2 Dec 2022]. Lawrence Erlbaum Associates, 1988. URL: https://www.utstat.toronto.edu/~brunner/oldclass/378f16/readings/CohenPower.pdf.

[192] anon. *G-Code*. [online] [Accessed 6 October 2023]. 2023. URL: https://reprap.org/wiki/G-code.

Appendix A

Statistical Analysis

A.1 One Way ANOVA

ANOVA ("Analysis of Variance") tests if population means are equal. One-Way ANOVA compares 2+ groups for one independent variable.

The null hypothesis for an ANOVA test is that all the population means are exactly equal. If our sample means differ significantly, this suggests they are from different populations, and we would reject our null hypothesis that our samples are from the same population.

The F value compares the Between Group Variability ("sum of squares between", $SS_{between}$) (the sum of the standard deviations between the sample means and the overall mean) (variability assumed due to the effect of the independent variable), and the Within Group Variability (variability within the group - not due to the effect of the independent variable). The F value is compared to the Critical F Value, and if F is greater than Fcrit then you can reject the null hypothesis, and suggests that there is a significant difference between AT LEAST TWO groups.

ANOVA assumptions: a normal distribution in each sample set (necessary for small sample sizes n<20), homogeneity (equal variance within all sample sets (only needed if sample sizes are unequal - the sample sizes here are equal).

Between group variability:

$$SS_{between} = \Sigma n_j(\bar{X}_j - \bar{X})^2 \tag{A.1}$$

$$MS_{between} = \frac{SS_{between}}{DF_{between}} \tag{A.2}$$

$$DF_{between} = k - 1 \tag{A.3}$$

Within group variability:

$$SS_{within} = \Sigma(\bar{x}_i - \bar{x}_j)^2 \tag{A.4}$$

$$MS_{within} = \frac{SS_{within}}{DF_{within}} \tag{A.5}$$

$$DF_{within} = N - k \tag{A.6}$$

Where $SS_{between}$ is the sum of squares between the groups, $\bar{X}_j$ is a sample group mean, $\bar{X}$ is the overall mean, n_j is the sample group size, $DF_{between}$ is the degrees of freedom between the sample groups, k is the number of sample group means

SS_{within} is the sum of squares within the groups, $(\bar{x}_i - \bar{x}_j)^2$ is the difference between each sample and the sample group mean, DF_{within} is the degrees of freedom within the sample group, N is the total number of samples. [188]

A.2 Post Hoc Test

Method 1: Running One Way ANOVA for each pair within the experiment. This method is essentially the same as doing a t-test for each pair, however each t-test has the chance of suggesting an incorrect conclusion.

Method 2: Tukey's HSD (Honestly Significant Difference) procedure suggests which means are significantly different.

$$q_{tukey} = \frac{|\bar{x}_{j1} - \bar{x}_{j2}|}{\sqrt{\frac{MS_{within}}{n}}} \tag{A.7}$$

Tukey's HSD is completed for each pair of sample groups. If the q value is smaller than the q_{crit} value then they are suggested to be not significantly different.

A.3 Effect Size Measures for ANOVA

A.3.1 (Partial) Eta Squared

(Partial) Eta Squared test - η^2 - suggests what percentage of the difference found was due to the approach used, i.e. due to the effect of the Independent Variable. A small effect is > 0.01, a medium effect is > 0.06, and a large effect is > 0.14 [188]. For One-Way ANOVA, partial eta squared is equal to eta squared [189].

$$\eta_p^2 = SS_{between}/(SS_{between} + SS_{within}) \tag{A.8}$$

Where η_p^2 is partial eta squared, and the other variables are defined in Equations A.1, A.4. reference [190].

A.3.2 Cohen's f

Cohen's f test. Uses partial eta squared. A value of 0.1 suggests a small effect, 0.25 a medium effect, and 0.4 a large effect [191] [189].

$$f = \sqrt{\frac{\eta_p^2}{1-\eta_p^2}} \tag{A.9}$$

Where η_p^2 is partial eta squared (Equation A.8).

A.3.3 Omega Squared

Omega Squared (ω^2). Omega Squared is suggested to be less biased than (partial) eta squared test. A value of 0.01 suggests a small effect, 0.06 a medium effect, and 0.14 a large effect [189].

$$\omega^2 = \frac{SS_{between} - (DF_{between})(MS_{within})}{SS_{between} + SS_{within} + MS_{within}} \tag{A.10}$$

Variables defined in Equations A.1, A.3 A.5, A.4.

Appendix B

G-Code Commands

Extracted from Repetier-Host software [140] and RepRap.org [192].

Table B.1: G-Code Commands

Code	Name	Description	Example
Xnnn Ynnn Znnn	Coordinates	X, Y and Z position coordinates	
Fnnn	Feedrate	Speed of print head movement in mm per minute	F2400 ;print head travel speed 2400
Ennn	Length of extrudate	Length of filament to extrude	E65.69976 ;extrude to 65.69976 mm
Tnnn	Select tool	Select a nozzle, if machine has more than one	T0 ;nozzle 1 (extrudes filament 1)
Snnn	Command parameter	e.g time in seconds, temperature	
Gnnn	Standard G-Code command	e.g G0, G1, G28, etc	
Mnnn	RepRap-defined command	e.g turn on cooling fan	
G0	Rapid move	Move fast to the given position	G0 F9000 X89.467 Y89.474 Z0.200
G1	Controlled Move	Move in a line to the given position	G1 F1800 X89.592 Y89.374 E0.00666
G4	Dwell	"pause" for a set amount of time	G4 P1000 ;wait for 1 s
G28	Home all axes	if CR Touch installed, this probes the middle of the bed	
G90	Absolute positioning	Coordinates are absolute to origin	
G91	Relative positioning	Coordinates are relative to last position	
G92	Set position	Set current position to coordinates given	G92 E0 ;reset extrusion to zero

Table B.1: G-Code Commands

Code	Name	Description	Example
M82	Disable extruder relative mode	Absolute extrusion mode	
M84	Disable motors	Disable stepper motors	
M104	Set extruder temperature (fast)	Sets target temperature and returns immediately	M104 S220 ;start heating extruder to 220 °C
M105	Report temperature	read and report the current temperature	
M106	Fan on	Turns the fan on (speed 0 to 225)	M106 S12
M107	Fan Off	Turns the fan off	
M109	Set extruder temperature	Sets target temperature and waits until the temperature is reached	M109 S220 ;wait for extruder to reach 220 °C
M140	Set bed temperature (fast)	Start heating the bed to the stated temperature	M140 S25 ;heat bed to 25 °C
M190	Set bed temperature	Sets target temperature for the bed and waits for bed to reach target temperature	M190 S25 ;wait until the bed reaches 25 °C
M300	Play frequency	Make an audible 'beep'	M300 S400 P500 ;play frequency 400 Hz for 0.5 sec
M413	Power-Loss Recovery	Enable or disable power-loss recovery	M413 S0 ;power-loss recovery turned off

Appendix C

G-Code: In Situ Additive Manufacturing onto Base A

```
; START G-CODE BEGINS

; TEMPERATURE SETTINGS

M140 S25 ; START HEATING BED TO TEMP 25 C
M105 ; REPORT TEMP
M190 S25 ; WAIT UNTIL BED REACHES 25 C

M104 S200 ; START HEATING EXTRUDER TO 200 C
M105 ; REPORT TEMP
M109 S200 ; WAIT FOR EXTRUDER TO REACH 200 C

; 2 BEEP FOR TEMP - 400 HZ FOR 0.5 SEC WITH 0.2 SEC PAUSE
M300 S400 P500
G4 P200
M300 S400 P500
G4 P200

M420 S1 ; USES STORED BED LEVEL

M82 ; ABSOLUTE EXTRUSION MODE

; ENDER 3 CUSTOM START G-CODE
M413 S0 ; POWER-LOSS RECOVERY TURNED OFF

G92 E0 ; RESET EXTRUDER

G28 ; HOME ALL AXES - PROBE

; BEEP FOR G28 - 400 HZ FOR 0.5 S
M300 S400 P500
; WAIT 1 SEC
```

```
G4 P1000

; AVOID HOLDER AFTER PROBE
G1 Z30 F3000.0 ; MOVE IN A STRAIGHT LINE VERTICALLY TO 30 MM
G1 X10 F3000.0 ; MOVE IN A STRAIGHT LINE ALONG X AXIS TO 10 MM
G1 Y10 F3000.0 ; MOVE IN A STRAIGHT LINE ALONG Y AXIS TO 10 MM

; 2 BEEP FOR POST-PROBE AT 440 HZ FOR 0.5 S
M300 S440 P500
G4 P1000
M300 S440 P500
G4 P5000 ; WAIT 5 SEC

; PRINT TEST LINE
G1 Z2.0 F3000 ; MOVE Z AXIS UP LITTLE TO PREVENT SCRATCHING OF HEAT BED
G1 X0.1 Y20 Z0.3 F5000.0 ; MOVE TO START POSITION
G1 X0.1 Y200.0 Z0.3 F1500.0 E15 ; DRAW THE FIRST LINE
G1 X0.4 Y200.0 Z0.3 F5000.0 ; MOVE TO SIDE A LITTLE
G1 X0.4 Y20 Z0.3 F1500.0 E30 ; DRAW THE SECOND LINE
G92 E0 ; RESET EXTRUDER
G1 Z2.0 F3000 ; MOVE Z AXIS UP LITTLE TO PREVENT SCRATCHING OF HEAT BED
G1 X5 Y20 Z0.3 F5000.0 ; MOVE OVER TO PREVENT BLOB SQUISH

; WAIT FOR 2 SEC
G4 P2000

; BEEP FOR TEST LINE - 300 HZ FOR 0.5 S
M300 S300 P500
; WAIT 1 SEC
G4 P1000

; MOVE BED OUT TO ALLOW ACCESS
G1 Z30 F5000.0 ; MOVE UP TO Z AT 30 MM
G1 Y200 F5000.0 ; MOVE "BACK" TO Y 200 MM

; DWELL TO ALLOW PLACING OF BASE
G4 S300 ; DWELL FOR 300 SEC / 5 MIN

; 2 BEEP FOR DWELL - 300 HZ FOR 0.5 S
M300 S300 P500
G4 P1000
M300 S300 P500
G4 P1000

; MOVE BACK TO HOME POSITION
G1 Y20 F5000.0 ; MOVE "FORWARD" TO Y 20 MM
G1 X5 Y20 Z0.3 F5000.0 ; RETURN TO POST-ENDER3-CUSTOM CODE POSITION
```

```
; BEEP FOR HOME - 300 HZ FOR 0.5 S
M300 S300 P500
G4 P1000

;SHIFTS EVERYTHING UP 20 MM
G1 Z20 ;MOVE TO 20 MM UP
G92 Z0 ;FROM NOW ON CONSIDER THIS POSITION AS 0 MM UP

; BEEP FOR SHIFT UP - 300 HZ FOR 0.5 S
M300 S300 P500
G4 P1000

; START G-CODE ENDS

; END G-CODE BEGINS

G91 ;RELATIVE POSITIONING
G1 E-2 F2700 ;RETRACT A BIT
G1 E-2 Z0.2 F2400 ;RETRACT AND RAISE Z
G1 X5 Y5 F3000 ;WIPE OUT
G1 Z10 ;RAISE Z MORE
G90 ;ABSOLUTE POSITIONING

; MOVE BED OUT TO ALLOW ACCESS TO BED
G1 Z50 F5000.0 ; MOVE UP TO Z AT 50 MM
G1 Y200 F5000.0 ; MOVE "BACK" TO Y 200 MM

; 4 BEEPS FOR END - 300 HZ FOR 0.5 S
M300 S300 P500
G4 P200
M300 S300 P500
G4 P200
M300 S300 P500
G4 P200
M300 S300 P500
G4 P200

; END G-CODE ENDS
```

Appendix D

G-Code: Surface Addition In Situ AM Print onto 41 mm ROC Clay Base

```
;GENERATED WITH CURA_STEAMENGINE 15.01

; START G-CODE BEGINS

; TEMPERATURE SETTINGS

M140 S25 ; START HEATING BED TO TEMP 25 C
M105 ; REPORT TEMP
M190 S25 ; WAIT UNTIL BED REACHES 25 C

M104 S220 ; START HEATING EXTRUDER TO 220 C
M105 ; REPORT TEMP
M109 S220 ; WAIT FOR EXTRUDER TO REACH 220 C

; 2 BEEP FOR TEMP - 400 HZ FOR 0.5 SEC WITH 0.2 SEC PAUSE
M300 S400 P500
G4 P200
M300 S400 P500
G4 P200

M420 S1 ; USES STORED BED LEVEL

M82 ; ABSOLUTE EXTRUSION MODE

; ENDER 3 CUSTOM START G-CODE
M413 S0 ; POWER-LOSS RECOVERY TURNED OFF

G92 E0 ; RESET EXTRUDER

G28 ; HOME ALL AXES - PROBE
```

```
; BEEP FOR G28 - 400 HZ FOR 0.5 S
M300 S400 P500
; WAIT 1 SEC
G4 P1000

; AVOID HOLDER AFTER PROBE
G1 Z30 F3000.0 ; MOVE IN A STRAIGHT LINE VERTICALLY TO 30 MM
G1 X10 F3000.0 ; MOVE IN A STRAIGHT LINE ALONG X AXIS TO 10 MM
G1 Y10 F3000.0 ; MOVE IN A STRAIGHT LINE ALONG Y AXIS TO 10 MM

; 2 BEEP FOR POST-PROBE AT 440 HZ FOR 0.5 S
M300 S440 P500
G4 P1000
M300 S440 P500
G4 P5000 ; WAIT 5 SEC

; PRINT TEST LINE 1
G1 Z2.0 F3000 ; MOVE Z AXIS UP LITTLE TO PREVENT SCRATCHING OF HEAT BED
G1 X0.1 Y20 Z0.3 F5000.0 ; MOVE TO START POSITION
G1 X0.1 Y200.0 Z0.3 F1500.0 E15 ; DRAW THE FIRST LINE
G1 X0.4 Y200.0 Z0.3 F5000.0 ; MOVE TO SIDE A LITTLE
G1 X0.4 Y20 Z0.3 F1500.0 E30 ; DRAW THE SECOND LINE
G92 E0 ; RESET EXTRUDER
G1 Z2.0 F3000 ; MOVE Z AXIS UP LITTLE TO PREVENT SCRATCHING OF HEAT BED
G1 X5 Y20 Z0.3 F5000.0 ; MOVE OVER TO PREVENT BLOB SQUISH

; WAIT FOR 2 SEC
G4 P2000

; BEEP FOR TEST LINE - 300 HZ FOR 0.5 S
M300 S300 P500
; WAIT 1 SEC
G4 P1000

; CUT PASTE PRINT FOR FRAME HERE
    ;LAYER:0
    M107
    G1 F2400 E-4.00000
    G0 F9000 X130.252 Y129.298 Z0.200
    ;TYPE:WALL-INNER
    G1 F2400 E0.00000
    G1 F1800 X130.378 Y129.357 E0.00578
    %—CONTINUED FRAME CODE—%
    G1 X89.252 Y89.252 E66.33239
    G1 X89.252 Y129.752 E68.01618
    G1 X129.752 Y129.752 E69.69998
```

```
G92 E0 ; RESET EXTRUDER

; MOVE BED OUT TO ALLOW ACCESS
G1 Z30 F5000.0 ; MOVE UP TO Z AT 30 MM
G1 Y200 F5000.0 ; MOVE "BACK" TO Y 200 MM

; DWELL TO ALLOW PLACING OF BASE
G4 S200 ; DWELL FOR 200 SEC / 4 MIN

; 2 BEEP FOR DWELL - 300 HZ FOR 0.5 S
M300 S300 P500
G4 P1000
M300 S300 P500
G4 P1000

; MOVE BACK TO HOME POSITION
G1 Y20 F5000.0 ; MOVE "FORWARD" TO Y 20 MM
G1 X5 Y20 Z0.3 F5000.0 ; RETURN TO POST-ENDER3-CUSTOM CODE POSITION

; BEEP FOR HOME - 300 HZ FOR 0.5 S
M300 S300 P500
G4 P1000

; PRINT SECOND TEST LINE
G1 Z2.0 F3000 ; MOVE Z AXIS UP LITTLE TO PREVENT SCRATCHING OF HEAT BED
G1 X0.1 Y20 Z0.3 F5000.0 ; MOVE TO START POSITION
G1 X0.1 Y200.0 Z0.3 F1500.0 E15 ; DRAW THE FIRST LINE
G1 X0.4 Y200.0 Z0.3 F5000.0 ; MOVE TO SIDE A LITTLE
G1 X0.4 Y20 Z0.3 F1500.0 E30 ; DRAW THE SECOND LINE
G92 E0 ; RESET EXTRUDER
G1 Z2.0 F3000 ; MOVE Z AXIS UP LITTLE TO PREVENT SCRATCHING OF HEAT BED
G1 X5 Y20 Z0.3 F5000.0 ; MOVE OVER TO PREVENT BLOB SQUISH

G92 E69.69998 ; RESET EXTRUDER TO AVOID SPLURGE - LAST E OF FRAME

; BEEP - 300 HZ FOR 0.5 S
M300 S300 P500
G4 P1000

;MOVES NOZZLE UP ABOVE BASE IN APPROX CENTRE OF BED
G1 Z30
G1 F9000 X110 Y110

; START G-CODE ENDS

%—— CODE FOR FRAME CUT FROM HERE ——%

; PRINT IMPLANT
```

```
;LAYER COUNT: 70
;LAYER:52
M106 S153
G1 F2400 E65.69998
G0 F9000 X111.145 Y111.890 Z10.600
;TYPE:WALL-OUTER
G1 F2400 E69.69998
G1 F540 X110.943 Y111.997 E69.70948
G1 X110.800 Y112.101 E69.71683
%—CONTINUED IMPLANT CODE—%
G1 F1800 X113.479 Y108.905 E174.14132
G0 F9000 X113.296 Y109.795
G1 F1800 X111.077 Y112.014 E174.27179

M107

G1 F2400 E170.27179
G0 F9000 X111.077 Y112.014 Z19.000

; END G-CODE BEGINS

G91 ;RELATIVE POSITIONING
G1 E-2 F2700 ;RETRACT A BIT
G1 E-2 Z0.2 F2400 ;RETRACT AND RAISE Z
G1 X5 Y5 F3000 ;WIPE OUT
G1 Z10 ;RAISE Z MORE
G90 ;ABSOLUTE POSITIONING

; MOVE BED OUT TO ALLOW ACCESS TO BED
G1 Z50 F5000.0 ; MOVE UP TO Z AT 50 MM
G1 Y200 F5000.0 ; MOVE "BACK" TO Y 200 MM

; 4 BEEPS FOR END - 300 HZ FOR 0.5 S
M300 S300 P500
G4 P200
M300 S300 P500
G4 P200
M300 S300 P500
G4 P200
M300 S300 P500
G4 P200

; END G-CODE ENDS
```

Appendix E

G-Code: Implant In Situ AM Print into Recess of 41 mm ROC Clay Base

```
;GENERATED WITH CURA_STEAMENGINE 15.01

; START G-CODE BEGINS

; TEMPERATURE SETTINGS

M140 S25 ; START HEATING BED TO TEMP 25°C
M105 ; REPORT TEMP
M190 S25 ; WAIT UNTIL BED REACHES 25°C

M104 S220 ; START HEATING EXTRUDER TO 220°C
M105 ; REPORT TEMP
M109 S220 ; WAIT FOR EXTRUDER TO REACH 220°C

; 2 BEEP FOR TEMP - 400 HZ FOR 0.5 SEC WITH 0.2 SEC PAUSE
M300 S400 P500
G4 P200
M300 S400 P500
G4 P200

M420 S1 ; USES STORED BED LEVEL

M82 ; ABSOLUTE EXTRUSION MODE

; ENDER 3 CUSTOM START G-CODE
M413 S0 ; POWER-LOSS RECOVERY TURNED OFF

G92 E0 ; RESET EXTRUDER

G28 ; HOME ALL AXES - PROBE
```

```
; BEEP FOR G28 - 400 HZ FOR 0.5 S
M300 S400 P500
; WAIT 1 SEC
G4 P1000

; AVOID HOLDER AFTER PROBE
G1 Z30 F3000.0 ; MOVE IN A STRAIGHT LINE VERTICALLY TO 30 MM
G1 X10 F3000.0 ; MOVE IN A STRAIGHT LINE ALONG X AXIS TO 10 MM
G1 Y10 F3000.0 ; MOVE IN A STRAIGHT LINE ALONG Y AXIS TO 10 MM

; 2 BEEP FOR POST-PROBE AT 440 HZ FOR 0.5 S
M300 S440 P500
G4 P1000
M300 S440 P500
G4 P5000 ; WAIT 5 SEC

; PRINT TEST LINE
G1 Z2.0 F3000 ; MOVE Z AXIS UP LITTLE TO PREVENT SCRATCHING OF HEAT BED
G1 X0.1 Y20 Z0.3 F5000.0 ; MOVE TO START POSITION
G1 X0.1 Y200.0 Z0.3 F1500.0 E15 ; DRAW THE FIRST LINE
G1 X0.4 Y200.0 Z0.3 F5000.0 ; MOVE TO SIDE A LITTLE
G1 X0.4 Y20 Z0.3 F1500.0 E30 ; DRAW THE SECOND LINE
G92 E0 ; RESET EXTRUDER
G1 Z2.0 F3000 ; MOVE Z AXIS UP LITTLE TO PREVENT SCRATCHING OF HEAT BED
G1 X5 Y20 Z0.3 F5000.0 ; MOVE OVER TO PREVENT BLOB SQUISH

; WAIT FOR 2 SEC
G4 P2000

; BEEP FOR TEST LINE - 300 HZ FOR 0.5 S
M300 S300 P500
; WAIT 1 SEC
G4 P1000

; PRINT 40X40 FRAME
    ;LAYER:0
    M107 ;FAN OFF
    G1 F2400 E-4.00000
    G0 F9000 X89.467 Y89.474 Z0.200
    ;TYPE:WALL-INNER
    G1 F2400 E0.00000
    G1 F1800 X89.592 Y89.374 E0.00666
    G1 X89.691 Y89.318 E0.01138
    G1 X89.828 Y89.272 E0.01739
    G1 X89.952 Y89.254 E0.02260
    G1 X90.109 Y89.262 E0.02914
    G1 X90.245 Y89.295 E0.03496
    G1 X90.364 Y89.349 E0.04039
```

```
    %—CONTINUED FRAME CODE—%
    G1 X130.748 Y130.748 E66.33217
    G1 X130.748 Y90.248 E68.01596
    G1 X90.248 Y90.248 E69.69976

G92 E0 ; RESET EXTRUDER

; MOVE BED OUT TO ALLOW ACCESS
G1 Z30 F5000.0 ; MOVE UP TO Z AT 30 MM
G1 Y200 F5000.0 ; MOVE "BACK" TO Y 200 MM

; DWELL TO ALLOW PLACING OF BASE
G4 S200 ; DWELL FOR 200 SEC / 4 MIN

; 2 BEEP FOR DWELL - 300 HZ FOR 0.5 S
M300 S300 P500
G4 P1000
M300 S300 P500
G4 P1000

; MOVE BACK TO HOME POSITION
G1 Y20 F5000.0 ; MOVE "FORWARD" TO Y 20 MM
G1 X5 Y20 Z0.3 F5000.0 ; RETURN TO POST-ENDER3-CUSTOM CODE POSITION

; BEEP FOR HOME - 300 HZ FOR 0.5 S
M300 S300 P500
G4 P1000

; PRINT SECOND TEST LINE
G1 Z2.0 F3000 ; MOVE Z AXIS UP LITTLE TO PREVENT SCRATCHING OF HEAT BED
G1 X0.1 Y20 Z0.3 F5000.0 ; MOVE TO START POSITION
G1 X0.1 Y200.0 Z0.3 F1500.0 E15 ; DRAW THE FIRST LINE
G1 X0.4 Y200.0 Z0.3 F5000.0 ; MOVE TO SIDE A LITTLE
G1 X0.4 Y20 Z0.3 F1500.0 E30 ; DRAW THE SECOND LINE
G92 E0 ; RESET EXTRUDER
G1 Z2.0 F3000 ; MOVE Z AXIS UP LITTLE TO PREVENT SCRATCHING OF HEAT BED
G1 X5 Y20 Z0.3 F5000.0 ; MOVE OVER TO PREVENT BLOB SQUISH

G92 E69.69976 ; RESET EXTRUDER TO AVOID SPLURGE

;SHIFTS EVERYTHING UP 20 MM
;G1 Z20 ;MOVE TO 20 MM UP
;G92 Z0 ;FROM NOW ON CONSIDER THIS POSITION AS 0 MM UP

; BEEP FOR SHIFT UP - 300 HZ FOR 0.5 S
M300 S300 P500
G4 P1000
```

```
;MOVES NOZZLE UP ABOVE BASE IN APPROX CENTRE OF BED
G1 Z20
G1 F9000 X110 Y110

; START G-CODE ENDS

;PRINT IMPLANT
M106 S153 ;FAN
G1 F2400 E65.69976
G0 F9000 X108.632 Y108.079 Z8.200
;TYPE:WALL-INNER
G1 F2400 E69.69976
G1 F720 X108.833 Y107.891 E69.71120
G1 X109.014 Y107.754 E69.72064
G1 X109.403 Y107.527 E69.73936
G1 X109.701 Y107.404 E69.75276
G1 X110.157 Y107.288 E69.77233
G1 X110.547 Y107.251 E69.78861
G1 X110.861 Y107.263 E69.80168
G1 X111.175 Y107.313 E69.81490
G1 X111.620 Y107.448 E69.83423
%——CONTINUED IMPLANT CODE——%
G1 F1140 X110.447 Y110.877 E148.78308

M107

G1 F2400 E144.78308
G0 F9000 X110.447 Y110.877 Z16.927

; END G-CODE BEGINS

G91 ;RELATIVE POSITIONING
G1 E-2 F2700 ;RETRACT A BIT
G1 E-2 Z0.2 F2400 ;RETRACT AND RAISE Z
G1 X5 Y5 F3000 ;WIPE OUT
G1 Z10 ;RAISE Z MORE
G90 ;ABSOLUTE POSITIONING

; MOVE BED OUT TO ALLOW ACCESS TO BED
G1 Z50 F5000.0 ; MOVE UP TO Z AT 50 MM
G1 Y200 F5000.0 ; MOVE "BACK" TO Y 200 MM

; 4 BEEPS FOR END - 300 HZ FOR 0.5 S
M300 S300 P500
G4 P200
M300 S300 P500
G4 P200
M300 S300 P500
```

```
G4 P200
M300 S300 P500
G4 P200

; END G-CODE ENDS
```

Appendix F

G-Code: Surface Addition In Situ AM Print onto 'Unknown' Surface (Bone Model)

```
;GENERATED WITH CURA_STEAMENGINE 15.01

; START G-CODE BEGINS

; TEMPERATURE SETTINGS
M140 S25 ; START HEATING BED TO TEMP 25 C
M105 ; REPORT TEMP

M190 S25 ; WAIT UNTIL BED REACHES 25 C
M104 S220 ; START HEATING EXTRUDER TO 220 C
M105 ; REPORT TEMP
M109 S220 ; WAIT FOR EXTRUDER TO REACH 220 C

; 2 BEEP FOR TEMP - 400 HZ FOR 0.5 SEC WITH 0.2 SEC PAUSE
M300 S400 P500
G4 P200
M300 S400 P500
G4 P200

M420 S1 ; USES STORED BED LEVEL

M82 ; ABSOLUTE EXTRUSION MODE

; ENDER 3 CUSTOM START G-CODE

M413 S0 ; POWER-LOSS RECOVERY TURNED OFF

G92 E0 ; RESET EXTRUDER
```

```
G28 ; HOME ALL AXES - PROBE

; BEEP FOR G28 - 400 HZ FOR 0.5 S
M300 S400 P500
; WAIT 1 SEC
G4 P1000

; AVOID HOLDER AFTER PROBE
G1 Z30 F3000.0 ; MOVE IN A STRAIGHT LINE VERTICALLY TO 30 MM
G1 X10 F3000.0 ; MOVE IN A STRAIGHT LINE ALONG X AXIS TO 10 MM
G1 Y10 F3000.0 ; MOVE IN A STRAIGHT LINE ALONG Y AXIS TO 10 MM

; 2 BEEP FOR POST-PROBE AT 440 HZ FOR 0.5 S
M300 S440 P500
G4 P1000
M300 S440 P500
G4 P5000 ; WAIT 5 SEC

; PRINT TEST LINE 1
G1 Z2.0 F3000 ; MOVE Z AXIS UP LITTLE TO PREVENT SCRATCHING OF HEAT BED
G1 X0.1 Y20 Z0.3 F5000.0 ; MOVE TO START POSITION
G1 X0.1 Y200.0 Z0.3 F1500.0 E15 ; DRAW THE FIRST LINE
G1 X0.4 Y200.0 Z0.3 F5000.0 ; MOVE TO SIDE A LITTLE
G1 X0.4 Y20 Z0.3 F1500.0 E30 ; DRAW THE SECOND LINE
G92 E0 ; RESET EXTRUDER
G1 Z2.0 F3000 ; MOVE Z AXIS UP LITTLE TO PREVENT SCRATCHING OF HEAT BED
G1 X5 Y20 Z0.3 F5000.0 ; MOVE OVER TO PREVENT BLOB SQUISH

; WAIT FOR 2 SEC
G4 P2000

; BEEP FOR TEST LINE - 300 HZ FOR 0.5 S
M300 S300 P500
; WAIT 1 SEC
G4 P1000

; CUT-PASTE CODE FOR FRAME TO HERE
    ;LAYER:0
    M107
    G1 F2400 E-4.00000
    G0 F9000 X9.208 Y64.475 Z0.200
    ;TYPE:WALL-INNER
    G1 F2400 E0.00000
    G1 F1800 X211.697 Y66.595 E8.41898
    %—CONTINUED FRAME CODE—%
    G1 X10.198 Y65.484 E1439.13496
    G1 X9.312 Y149.980 E1442.64809
```

```
    G0 F9000 X9.061 Y149.979

G92 E0 ; RESET EXTRUDER

; MOVE BED OUT TO ALLOW ACCESS
G1 Z30 F5000.0 ; MOVE UP TO Z AT 30 MM
G1 Y200 F5000.0 ; MOVE "BACK" TO Y 200 MM

; DWELL TO ALLOW PLACING OF BASE
G4 S200 ; DWELL FOR 200 SEC / 4 MIN

; 2 BEEP FOR DWELL - 300 HZ FOR 0.5 S
M300 S300 P500
G4 P1000
M300 S300 P500
G4 P1000

; MOVE BACK TO HOME POSITION
G1 Y20 F5000.0 ; MOVE "FORWARD" TO Y 20 MM
G1 X5 Y20 Z0.3 F5000.0 ; RETURN TO POST-ENDER3-CUSTOM CODE POSITION

; BEEP FOR HOME - 300 HZ FOR 0.5 S
M300 S300 P500
G4 P1000

; PRINT SECOND TEST LINE
G1 Z2.0 F3000 ; MOVE Z AXIS UP LITTLE TO PREVENT SCRATCHING OF HEAT BED
G1 X0.1 Y20 Z0.3 F5000.0 ; MOVE TO START POSITION
G1 X0.1 Y200.0 Z0.3 F1500.0 E15 ; DRAW THE FIRST LINE
G1 X0.4 Y200.0 Z0.3 F5000.0 ; MOVE TO SIDE A LITTLE
G1 X0.4 Y20 Z0.3 F1500.0 E30 ; DRAW THE SECOND LINE
G92 E0 ; RESET EXTRUDER
G1 Z2.0 F3000 ; MOVE Z AXIS UP LITTLE TO PREVENT SCRATCHING OF HEAT BED
G1 X5 Y20 Z0.3 F5000.0 ; MOVE OVER TO PREVENT BLOB SQUISH

G92 E1442.64809 ; RESET EXTRUDER TO AVOID SPLURGE - LAST E OF FRAME

; BEEP - 300 HZ FOR 0.5 S
M300 S300 P500
G4 P1000

;MOVES NOZZLE UP ABOVE BASE IN APPROX CENTRE OF BED
G1 Z80
G1 F9000 X110 Y110

; START G-CODE ENDS
```

%—*CODE FOR FRAME CUT FROM HERE*—%

```
; IMPLANT PRINT
;LAYER COUNT: 220
;LAYER:208
M106 S153
G1 F2400 E1438.64809
G0 F9000 X78.541 Y106.461 Z41.800
;TYPE:WALL-OUTER
G1 F2400 E1442.64809
G1 F540 X78.674 Y106.398 E1442.65421
G1 X79.144 Y106.229 E1442.67497
```

%—*CONTINUED IMPLANT CODE*—%

```
G1 F1800 X81.257 Y114.257 E1465.18821
G0 F9000 X82.464 Y113.757
G1 F1800 X83.492 Y112.729 E1465.24865

M107

G0 F9000 X83.458 Y112.763 Z49.000

; END G-CODE BEGINS

G91 ;RELATIVE POSITIONING
G1 E-2 F2700 ;RETRACT A BIT
G1 E-2 Z0.2 F2400 ;RETRACT AND RAISE Z
G1 X5 Y5 F3000 ;WIPE OUT
G1 Z10 ;RAISE Z MORE
G90 ;ABSOLUTE POSITIONING

; MOVE BED OUT TO ALLOW ACCESS TO BED
G1 Z50 F5000.0 ; MOVE UP TO Z AT 50 MM
G1 Y200 F5000.0 ; MOVE "BACK" TO Y 200 MM

; 4 BEEPS FOR END - 300 HZ FOR 0.5 S
M300 S300 P500
G4 P200
M300 S300 P500
G4 P200
M300 S300 P500
G4 P200
M300 S300 P500
G4 P200

; END G-CODE ENDS
```